TU Clausthal

Optimization of hydraulic fracturing in tight gas reservoirs with alternative fluid

Doctoral Thesis

(Dissertation)

to be awarded the degree

Doctor of Engineering (Dr.-Ing.)

Submitted by

M.Sc. Faisal Mehmood

from Sialkot, Pakistan

approved by the faculty of Energy and Economic Sciences,

Clausthal University of Technology

Date of oral examination

29 June 2021

Dean

Prof. Dr. mont. Leonhard Ganzer

Chairperson of the Board of Examiners

Prof. Dr. rer. nat. Hans-Jürgen Gursky

Supervising Tutor

Prof. Dr.-Ing. habil. Michael Zhengmeng Hou

Reviewer

Prof. Dr.-Ing. habil. Olaf Kolditz

Acknowledgements

I would like to express my sincere and deepest gratitude to my supervisor Prof. Dr. -Ing. habil. Michael Zhengmeng Hou for his continuous guidance, support, and motivation. His untiring engagement helped me in completing this thesis. I am extremely thankful to Prof. Dr. -Ing. habil. Olaf Kolditz for accepting to review this work and for his valuable advice and suggestions.

I would like to thank DGMK and industrial partners of DGMK-project 814. Many thanks to Dr. Dominik Soyk (DGMK, Hamburg), Dr. Susanne Kuchling (DGMK, Hamburg), Dipl.-Geophys. D. Leuchtmann (Wintershall Dea GmbH, Hamburg), Dipl.-Ing. M. Zinterl (ExxonMobil Production Germany GmbH, Hanover), M. Berling (Neptune Energy Deutschland GmbH, Lingen) and Dipl.-Ing. J. Sommer (Wintershall Dea GmbH, Kassel) for enlightening discussions and critical reviews.

I gratefully acknowledge the scholarship "HRDI-MS Leading to PhD Program of Faculty Development for UESTP/UETs (Phase-1) Batch-IV", from Higher Education Commission Pakistan and also thank DAAD.

I would like to extend my gratitude to all my colleagues for their cooperation and wonderful time. It was a pleasure working with them. Special thanks to Dr.-Ing. Jianxing Liao for all the discussions and help in complex technical problems. My sincere appreciation to Mrs. Karin Peya for her administrative support.

Last but not the least, I am indebted to my family and friends for their unparalleled love and support. Especially, I wish to thank my wife. Her moral and emotional support have been a source of continuous encouragement in this journey.

Faisal Mehmood

Clausthal Zellerfeld, April 2021

Abstract

Due to the finite nature of petroleum resources and depletion of conventional reservoirs, the exploitation of unconventional resources has been a key to meeting world energy needs. Natural gas, a cleaner fossil fuel compared to oil and coal, has an increasing role in the energy mix. It is expected that the peak global natural gas production will remain between 3.7-6.1 trillion m^3 per year between 2019 and 2060. Therefore, addressing the technical challenges posed by reservoir exploitation technologies in an environmentally responsible manner is critical for efficient energy production and energy secure of the world.

Hydraulic stimulation is the first means of choice for improving productivity from tight gas reservoirs by creating highly conductive flow paths with the injection of high-pressure fluid. Millions of hydraulic fracture operations have been performed with water-based fluid which have caused environmental concerns such as water availability and ground water quality degradation due to surface handling and flowback water disposal. Moreover, in lower permeability gas reservoirs, the support agents (proppants) settle at the bottom of fracture due to delayed fracture closure, and slow flowback and water blockage cause hindrance to natural gas flow leading to inefficient fracturing operation.

The solution is to replace existing water-based frac-fluids with alternative frac-fluids. Therefore, fracturing with light n-alkanes consisting of pentane, hexane, heptane, octane, nonane and decane is proposed. A single component fluid, or a mixture of components in different proportions can be designed according to reservoir conditions. The characteristics of hydrocarbon nature and significantly lower density and viscosity compared to water can help achieve the objectives of quick fracture closure for better proppant placement, expeditious flowback and reduced phase trapping. Thus, in addition to creating better conductivity fractures, environmental issues associated with water-based fluids can be minimized.

To perform hydraulic fracturing with the alternative fluid, a multiphase multicomponent simulator for hydraulic fracturing and fluid flow in fracture and matrix based on popular thermo-hydro-mechanical (THM) FLAC3D-TOUGH2MP/TMVOC framework is utilized. After verification, the model is applied to case study of LPG application in a tight gas reservoir of Canada for hydraulic fracturing operation. Simulations with different frac-fluids such as water, propane and n-heptane have been performed and their fracturing performance including the proppant settling behavior have been compared. The application of proposed alternative fluid for hydraulic fracturing optimization of wellbore yx1 in a tight gas reservoir of Germany showed that fractures with better conductivity in consideration of borehole-fracture connection can be created. Sensitivity analysis through numerous simulations for parameters such as injection rate, fluid viscosity and permeability were performed. The flowback analysis demonstrated that most of the injected alternative frac-fluid can be recovered within one week of fracturing which results in better clean up and early start of natural gas production.

The fracture permeability and conductivity are dependent upon proppants. Conventionally, spherical proppants have been utilized, however, rod-shaped proppants offer higher porosity and permeability compared with spherical proppants. To analyze their performance, a production model for proppants with different shapes and sizes is implemented in FLAC3D-TMVOCMP framework. The simulations for production forecast with spherical and rod-shaped proppant fractures have been performed considering mechanical properties contrast between proppant and formation under the influence of closure stress with developed model. The application of model to wellbore yx1 showed that 7% more recovery can be achieved from aspect ratio 1 rod-shaped proppant compared to same diameter spherical proppant over a period of ten years.

Based upon this work, proposed alternative fluid and rod-shaped proppants are recommended for efficient stimulation of tight gas reservoirs.

Contents

List of figures

List of tables

1 Introduction

1.1 Motivation and objectives

Petroleum is going to play a major role in the worldwide energy mix for the years to come with the coexistence of alternative energy such as renewable in industrial, residential, commercial, transport sectors etc. As the production of petroleum from conventional resources is declining, the unconventional resources are going to play an important role to meet the energy demands. The inclusion of unconventional resources will also extend the hydrocarbon industry life by many decades and increase the production to meet the increasing energy demands. Conventional reservoirs are characterized by high porosity and permeability rocks having accumulations of hydrocarbons which migrate from source rock and are stored due to structural or stratigraphic traps. Whereas, unconventional reservoirs accumulate over large area having low/ultra-low porosity and permeability, therefore, commercial production without stimulation is not possible. Unconventional reservoirs can also be defined as reservoirs which need change in permeability-viscosity ratio to provide commercial production. The development of unconventional resources on commercial scale especially unconventional hydrocarbon revolution in North America has resulted in increasing the recoverable reserves of petroleum (Cander, 2012; Leimkuhler and Leveille, 2012; C. Zou et al., 2013; Zou et al., 2014; C. N. Zou et al., 2013).

The conventional oil and gas production for more than one century including estimated 1732×10^8 t oil and 79×10^{12} m^3 gas has led to the industrial development. Due to lower recoveries, substantial resources enough to supply energy for a long period of time, remain underground. While, unconventional oil resources are considered equivalent to conventional resources, the unconventional gas resources are vastly abundant compared to conventional gas resources (Jia, 2017). The high-quality resource of conventional reservoirs, easy to extract, is limited. Whereas around 80% of total resources are unconventional and can be characterized as tight oil, tight gas, coal-bed methane, shale gas, shale oil gas hydrates etc. (Holditch, 2006; C. Zou et al., 2013).

Tight gas reservoirs are unconventional reservoirs which mainly produce dry natural gas. Due to lower permeability of equal to or less than 0.1 mD ($<1*10^{-4}$ μm^2) and less than 10% matrix porosity, well stimulation techniques are applied to enhance production. However, the production remains considerably low compared to conventional reservoirs. Therefore, the need for more wells, less well spacing compared to conventional reservoirs arises. In addition to tight sandstones, significant production is also taken from shales, carbonates, and coal-bed methane (Bahadori, 2014; Caineng et al., 2015; Dai et al., 2012; Guo and Gou, 2015; Holditch, 2006; Prud'homme, 2013).

Natural gas is a cleaner fossil fuel compared to oil and coal with fewer emissions and pollutants due to lower CO_2-to-energy-content ratio. It produces only 117 lbs CO_2 per million British thermal units (Btu)

in comparison with 161 lb CO_2 per million Btu and 205 lb CO_2 per million Btu for diesel and coal (bituminous), respectively (US EIA). Natural gas is not as clean as renewable energy but can serve as a bridging technology for transition to renewable energy. According to global energy review 2019 (IEA, 2019), the decline in power sector related CO_2 emissions can be attributed to shifting to natural gas from coal in addition to increased renewable energy resources and higher nuclear power output. Natural gas as a bridge fuel can provide with climate benefits in comparison with coal-based energy systems however it is important to minimize its leakage rate (Zhang et al., 2016). Mena-Carrasco et al., (2012) estimated the reduction in air pollution and resulting health benefits due to natural gas usage in transport and heating. The public concern over environmental issues will also increase its role in the energy mix (Economides and Martin, 2007). Reducing the greenhouse gas (GHG) emissions and improving air quality through efficient extraction and evolution of natural gas system can help in achieving transition towards renewable energy systems. Therefore, utilizing natural gas in an environmentally responsible manner can become pathway to a sustainable energy future (Mac Kinnon et al., 2017). Thus, the role of natural gas in energy transition is of critical importance considering global climate challenges and carbon neutrality goals (Rogelj et al., 2016).

Most of the world's energy demand is met through petroleum resources or fossil fuel in a broader sense. Natural gas production and consumption from conventional and unconventional reservoirs has been on the rise due to its application in different sectors such as industry, residential, commercial etc. Figure 1.1 explains the natural gas share in the global energy mix for 2010, 2015 and 2019, respectively. An increase in the natural gas share to 23% with rising energy demand along with renewable energy at 10% with a subsequent decrease in the coal share can be observed from 2010-2019 (IEA, 2020).

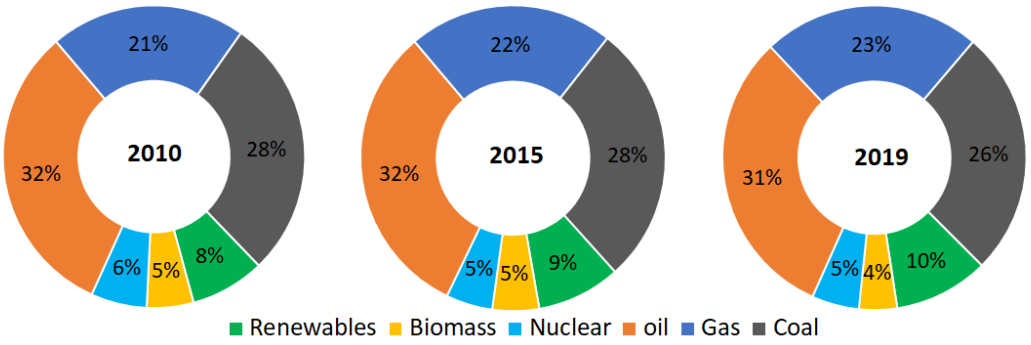

Figure 1.1: share of different energy sources in primary energy demand (IEA, 2020).

In the year 2019, the natural gas consumption increased by 78 billion m^3 (bcm), owing to increased demands of 27 bcm from US and 24 bcm from China, whereas gas production increased by 132 bcm (BP, 2020). The increase in worldwide natural gas consumption from 1970-2019, during which the gas demand grew from around 1 trillion m^3 (tcm) to about 4 tcm, can be observed from Figure 1.2. The highest gas consumption was recorded for North America, Asia Pacific, CIS (Commonwealth of Independent States), Middle East, Europe, South and Central America and Africa, respectively.

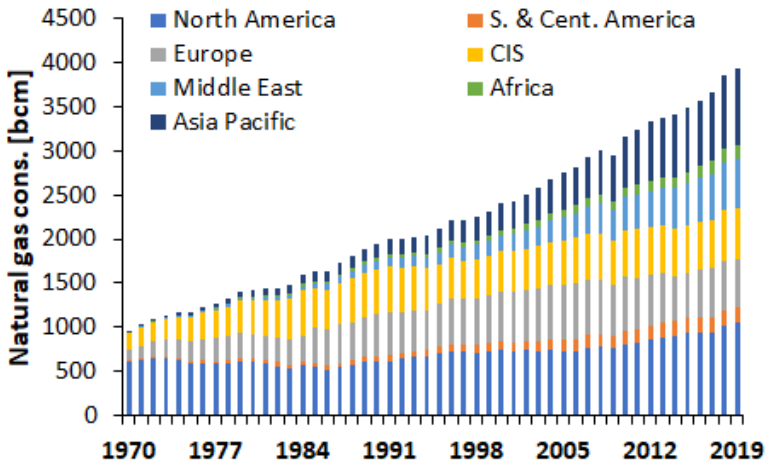

Figure 1.2: increase in gas consumption for different regions since 1970 (BP, 2020).

The trends of oil and gas production since 1970 can be observed from Figure 1.3. In 1986, the natural gas production of CIS region increased from North America. Whereas, due to unconventional hydrocarbon production especially in early 2000's, North America became highest producer of natural gas. Highest gas producer regions can be listed in the following order as North America, CIS, Middle East, Asia Pacific, Africa, Europe and South and Central America, respectively.

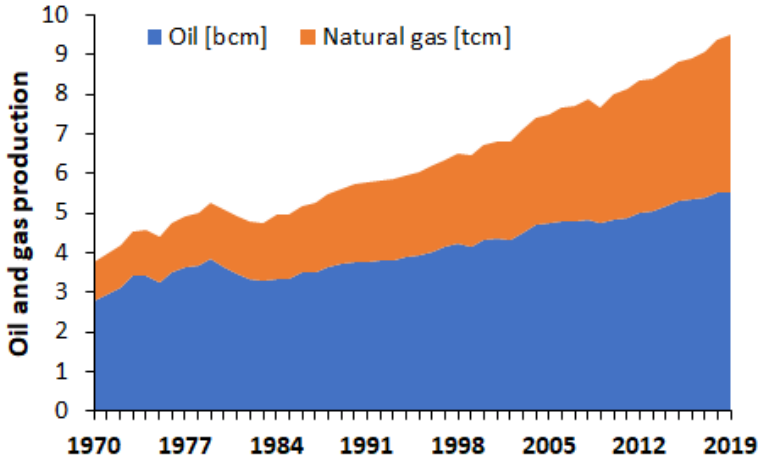

Figure 1.3: increase in global oil and gas production since 1970 (BP, 2020).

The world energy consumption increased by more than 3 times in the last fifty years growing from 192.86 exajoules to 583.9 exajoules (BP, 2020). It is expected that the peak global gas production will remain from 3.7 to 6.1 trillion m^3 (tcm) per year between 2019 and 2060 (Wang and Bentley, 2020; Zou et al., 2016). According to international energy outlook, an increase of more than 40% in global gas consumption is expected between 2018 and 2050 (US EIA, 2019). The global proved gas reserves amount to around 200 trillion m^3. The distribution of proven reserves in different regions is presented in Figure 1.4.

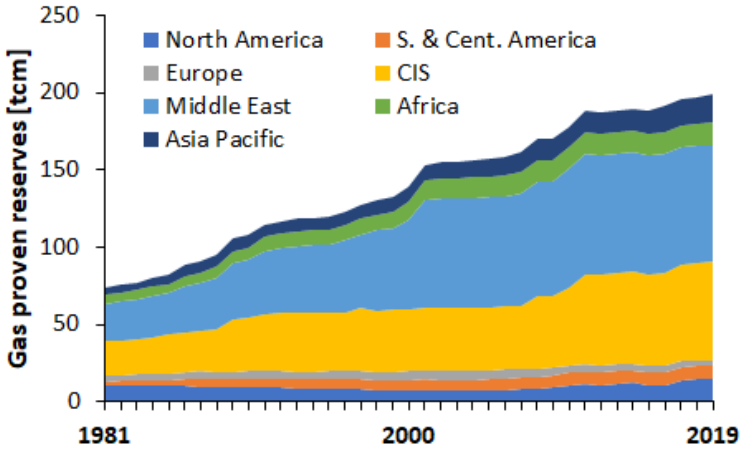

Figure 1.4: proven natural gas reserves of the world (BP, 2020).

Continued development of new technologies and methodologies has resulted in better development of unconventional reservoirs, leading to efficient and expeditious production of petroleum resources. The increased petroleum production is attributed to advanced technologies of horizontal well drilling and hydraulic fracturing in tight and ultra-tight reservoirs. Hydraulic fracturing has resulted in producing 50% of the natural gas and accounts for 33% of petroleum production in the US. Horizontal drilling and multi-stage hydraulic fracturing with optimized well spacing is the solution to enhance petroleum production (Alexander et al., 2011; Economides, 2007; Howarth et al., 2011; Hughes, 2013; Li and Zhang, 2019; Liu et al., 2018; Montgomery and Smith, 2010; Prud'homme, 2013; Rahm, 2011). According to Hughes (Hughes, 2013), around 61% of the wells in US are horizontal which in 2004 were less than 10%. Horizontal and vertical wellbores with hydraulic fracture are presented in Figure 1.5.

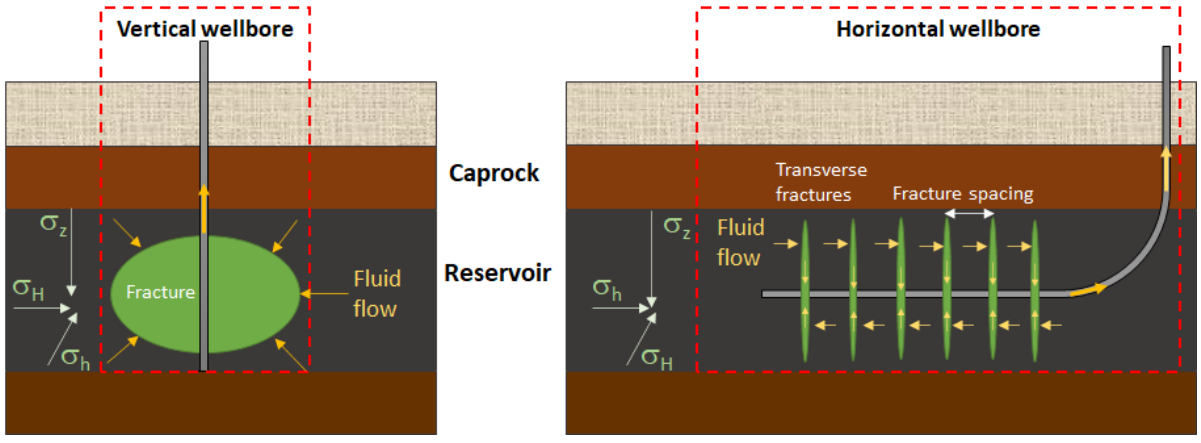

Figure 1.5: vertical and horizontal boreholes with vertical transverse fractures.

Well stimulation can be divided into two basic categories of acidizing and hydraulic fracturing. Due to surface handling issues, health and safety concerns and applicability to specific formation types such as carbonates, acidizing has limited applicability. Hydraulic fracturing on the other hand, as discussed

earlier has been widely and extensively applied. In hydraulic fracturing, the injection of fluid into the formation is done at a higher rate compared to the rate at which fluid escapes into the formation i.e., leakoff. Perforce, the pressure rises and when it reaches the limit of formation break down pressure, fracture is initiated normal to the minimum horizontal stress due to tensile failure. With continued injection at a rate higher than leakoff, the fracture propagates further towards a path of least resistance. However, as fracture grows, the leakoff increases due to exposure of more area for injected fluid to escape. In vertical wells, generally a fracture is created along the wellbore axis perpendicular to the least in-situ stress which is normally the minimum horizontal stress. But for horizontal fractures, the geometry is more complicated. Normally, a horizontal well is drilled in the minimum horizontal stress direction so that transverse fractures can be created with optimized spacing. If well trajectory follows maximum in-situ horizontal stress direction, then longitudinal fractures are created (Economides, 2007; Economides et al., 1994; Economides and Nolte, 2000; Guo et al., 2007).

The actual practice of hydraulic fracturing is only a small part of the overall process of drilling, completing, and producing an oil and gas well. Hydraulic fracturing resulting in highly conductive flow paths has been in business since late 1940s. The designing of hydraulic fracture job requires prior knowledge of reservoir and surrounding formation including pressure, stress state, physical properties such as permeability, porosity, mechanical properties such as elastic modulus, bulk modulus, shear modulus, Poisson's ratio etc. The injection of fracturing fluid containing chemicals and proppants is carried out through high pressure rating equipment on the well site. The fluid flows through the production well to the target formation. The pressure of the fluid is increased until the formation breaks down. The break down pressure and closure stress are found before the main fracturing operation through mini-frac tests and fall-off tests. Fracturing can be divided into two stages i.e., pad stage and slurry stage. During the pad stage, fracturing fluid is injected to create the fracture, whereas proppant carrying slurry is injected during the slurry stage. Proppants are injected in order to keep the fracture open under the effect of closure stress after the pumping is stopped. As the closure takes place due to fluid leakoff to surrounding formations, the width of the fracture decreases, and proppants come in contact with the walls of the fracture. These artificially created highly conductive flow paths kept open with proppants (support agents) are essential especially for commercial production from low permeability reservoirs, which were previously abandoned due to poor production. The post fracture testing and performance determines the fracture conductivity and resulting effect on well deliverability based upon the created fracture geometry (Clark, 1949; Economides and Nolte, 2000; Fisher and Warpinski, 2012; Koplos et al., 2014; Montgomery and Smith, 2010; Pang et al., 2016; Prud'homme, 2013).

Hydraulic fracturing is generally performed with water-based fluids. Although it has resulted in increased energy production, the use of water-based frac-fluid have caused problems. Lower support of

upper part of fracture in tight/ultra-tight reservoirs, phase trapping especially in sub-irreducible water saturation formations, swelling in water sensitive clays and poor fracture cleanup have resulted in inefficient fracturing operation. In addition, due to the large injection volume requirements, the water availability especially in areas of water scarcity and wastewater disposal have become critical issues. Due to environmental issues, there have been serious concerns of the public over fracking.

Fracturing operations are not conducted in Germany at industrial levels due to such environmental issues. The sandstones of upper Rotliegend, characterized by lower permeability in a high pressure and temperature environment, are the main source of gas production in Germany. The upper Rotliegend consists of series of sandstones, siltstones and shale formations. Due to the depositional environment, permeability anisotropy of 1/10 can be present within the sandstone formations. Thus, through hydraulic fracturing, not only vertical flow barriers within formations were bridged but also horizontal connectivity of the layers were improved. Massive hydraulic fracturing operations were performed such as in Soehlingen Z4 in the year 1982 with 2,582 m^3 frac-fluid and 546,000 kg proppants. Then the technology of multi-stage hydraulic fracturing in horizontal well was successfully applied to Soehlingen Z10 in 1994 (Koehler, 2005). Later, in 2005, horizontal well with multiple transverse fracture was drilled in Leer, where it was found that one of the fractures was not contributing to production due to no support for the upper half of fracture as the proppants fell to the bottom because of delayed fracture closure (Li, 2018). However, due to the large number of fracking operations and associated risks, questions were raised on the safety and environmental stability of fracking technology especially on the storage, transport and disposal of wastewater in Germany (Borschardt, 2012; Olsson et al., 2013). Later, fracking was prohibited for commercial projects especially in consideration of water protection and conservation regulations through environmental impact assessment (Bundesgesetzblatt, 2016; Die Bundesregierung, 2017).

Therefore, alternative frac-fluids need to be analyzed as a solution to the environmental concerns by minimizing the water usage and addressing the associated technical problems. In this work, numerical modeling has been utilized to investigate the applicability and effectiveness of alternative frac-fluid technology in tight gas reservoir case studies from Canada and Germany. Moreover, as the fracture permeability is dependent upon properties of proppant, especially its shape. The effect of changing the proppant shape from conventionally used spherical to rod-shaped on fracture conductivity and long-term performance need to be studied.

1.2 Thesis outline

To minimize the technical and environmental issues of conventional water-based fluid fracking, light alkanes (n-heptane to n-decane) as alternative frac-fluid are proposed. The development, verification, and application of multiphase multicomponent (MM) numerical model for simulation with alternative

frac-fluid based upon popular THM framework FLAC3D^{plus}-TMVOCMP is presented. In addition, the implementation of post fracture performance model in FLAC3D^{plus}-TMVOCMP for conventional i.e., spherical and unconventional i.e., rod-shaped proppants under the influence of stress state and mechanical properties contrast between proppant and formation is also presented. The following contents are part of this research work.

Chapter 2 explains why there is a need for alternative frac-fluid. It discusses the major environmental and technical issues associated with conventional water-based fluids utilized in the petroleum industry. In the environmental problems section, issues such as water availability, quality degradation due to chemical additives with details about some major components of frac-fluid and induced seismicity due to wastewater disposal in deep injection wells are discussed. Then the technical problems such as delayed fracture closure, clay swelling, fluid phase trapping, lower frac-fluid flowback are discussed for water-based fluid. Due to the environmental problems, the issue of public disapproval of hydraulic fracturing operation has emerged leading to ban in many countries. Later, alternative fluids for fracturing such as oil-based, gas-based, foam-based are reviewed highlighting their advantages and disadvantages.

Chapter 3 presents the proposed alternative water-less frac-fluid consisting of light alkanes from n-pentane to n-decane. The thermodynamic properties and the PVT behavior of proposed fluid are discussed. Then simulation in a fictive model is carried out to observe the phase change of the fluid under appropriate conditions. A brief introduction about the multiphase multicomponent (MM) fluid flow simulator TMVOC is also included. The phase behavior in terms of appearance and disappearance of light alkanes in liquid and gas phase is discussed.

Chapter 4 is related to the development and implementation of numerical model for MM thermo-hydro-mechanically coupled stimulation with proposed fluid. After a brief introduction of the coupling concept, hydraulic fracturing mechanics is discussed in light of fracture initiation, propagation, orientation etc. Then the numerical model is discussed which is divided into several sections explaining the mass and energy balance, space and time discretization, fracture propagation mechanism, fluid flow in fracture and formation, fluid viscosity calculation etc.

Chapter 5 is based upon the verification of developed model with literature and application to LPG-based frac-fluid stimulation case study of McCully tight gas field, New Brunswick, Canada. The verification is performed to examine the ability of developed model to simulate fracture initiation and propagation and MM fluid flow in isothermal and non-isothermal conditions. Then the application to a case study of McCully tight gas reservoir is explored. In this section, analysis for the hydraulic fracturing performance of propane (LPG)-based, water-based and n-heptane-based fluid are performed. The proppant settling behavior, flowback and production performance for different frac-fluids is also presented.

Chapter 6 covers the stimulation tests for optimization of wellbore yx1 with proposed fluid. Firstly, the model is verified through pressure history match with previously conducted frac-job data. Then the effect of most fluid important parameters such as fluid viscosity, injection rate, injection time is analyzed. Based upon numerous simulations and sensitivity analysis, hydraulic fracturing designs with alternative fluid are proposed and compared with previous fracture jobs.

Chapter 7 introduces rod-shaped proppants as an alternative to spherical proppants for improved fracture conductivity. After a brief literature review, numerical modelling for a production model is discussed incorporating different proppants. Then the influence of different factors such as effective stress, formation and proppant properties, proppant size in a generic model is discussed. Finally, the developed model is applied to wellbore yx1 well for production optimization using different aspect ratio rod-shaped proppants in different design proposals.

2 Need for alternative frac-fluid

Hundreds of thousands of fracturing operations have been performed with water as main fracturing base-fluid. Since 1949, nearly 2.5 million fracking operations have been performed leading to not only increasing the well productivity but also increasing the recoverable reserves. Whereas, until 2010 one million wells were stimulated with fracturing in the US only. A large number of fracturing jobs are also attributed to horizontal well drilling, where a number of frac-stages are performed or to multilateral wells where a number of wells are drilled from a single platform (Gallegos et al., 2015; Kondash and Vengosh, 2015; Montgomery and Smith, 2010; Rubinstein and Mahani, 2015; Gallegos and Varela, 2015). Apart from advantages, several environmental and technical disadvantages are associated with conventional frac-fluid fracking. These issues will be discussed in next sections.

2.1 Environmental problems

The main functions of frac-fluid include initiation and elongation of fracture, proppant transport through mixing tanks and surface pumping equipment to the fracture and placing them in desired location in the fracture (Economides, 2007). Most of the hydraulic fracturing treatment is performed with water-based fluids. The hydraulic fracturing water cycle can be observed from Figure 2.1.

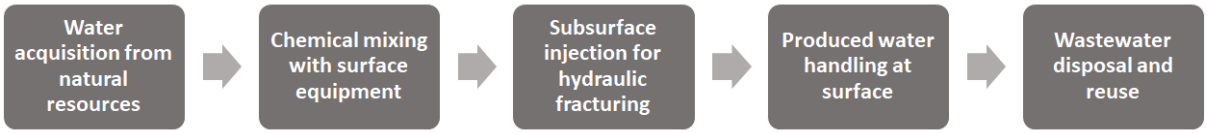

Figure 2.1: water cycle (US EPA, 2016).

During the water cycle for hydraulic fracturing acute environmental issues such as water availability issues especially in areas of water scarcity and declining water table, surface and ground water quality degradation due to wastewater disposal, induced seismicity due to injection of wastewater into deep disposal wells are caused (Jacobs, 2014; Kondash and Vengosh, 2015; Rahm, 2011; US EPA, 2016).

2.1.1 Water availability

The use of water for tapping the unconventional resources utilizing hydraulic fracturing is higher than conventional resources (Zhang and Yang, 2015). In horizontal wells in the US, average annual volumes per well between 15,275 m^3 and 19,425 m^3 water are utilized (Gallegos et al., 2015; Rahm, 2011). According to a study from 2012 to 2014, 116 billion litres annually for shale gas and 66 billion litres annually for unconventional oil were used for fracking in the US alone (Kondash and Vengosh, 2015). The transition from conventional to unconventional resource exploitation leading to high hydraulic fracturing density has increased the water usage per well up to 770% (Kondash et al., 2018).

Due to large water usage for hydraulic fracturing, the public water resources and aquatic ecology are affected. The availability of water for population, agriculture and climate can be seriously impacted especially in areas where susceptibility to droughts is high (Gallegos et al., 2015; Howarth et al., 2011; Jacobs, 2014; Vengosh et al., 2014). It has been reported that huge volumes of water extraction in some regions have resulted in significant depletion of consumptive water resources. Therefore, it is imperative to reduce strain on the water resources (Kondash et al., 2018). In addition, the water use intensity is less compared to other energy extraction methods. The water consumption on per well and total field basis, in major unconventional gas plays in the US can be observed from Figure 2.2.

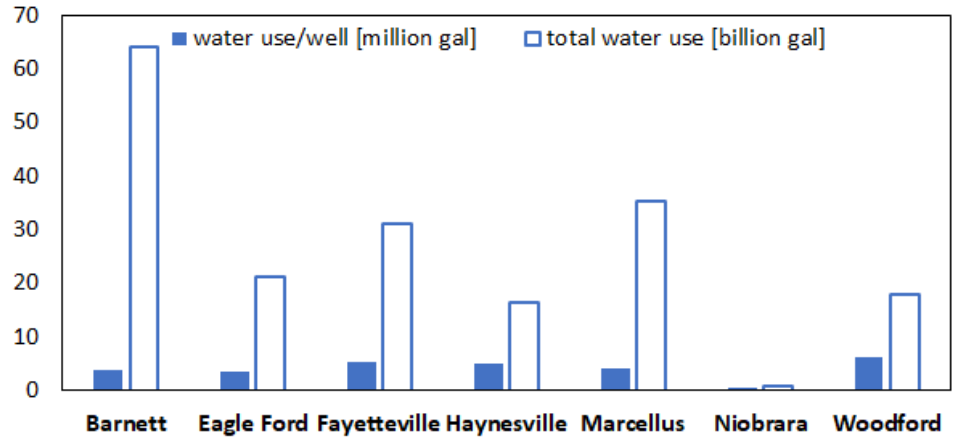

Figure 2.2: water consumption statistics for major unconventional gas plays in US (Kondash and Vengosh, 2015; US EPA, 2015).

2.1.2 Water quality

The contamination of drinking water table by chemicals added to frac-fluids due to spills or leakages, disposal of improperly treated wastewater etc. has been a growing concern. The water-based frac-fluid comprises of toxic and non-toxic components (Elliott et al., 2017). Numerous health problems are associated with these chemicals due to their toxicity. The wastewater management varies in different regions such as evaporation of wastewater and disposal of solid particles as dry waste, processing in wastewater treatment plants or reinjection into disposal wells. The waste fluid from flowback can also cause contamination through leakage or spills, direct discharge without treatment or insufficient treatment. The reinjection at shallow depths can contaminate the fresh water. One solution can be to reuse the wastewater for subsequent fracturing operation, but the scale forming components can block the fractures (Gallegos et al., 2015; Kargbo et al., 2010; Vengosh et al., 2014). Only 4% and 14% of the total volume injected for fracturing operation was reused fracturing wastewater in Marcellus shale (Susquehanna River Basin) and Barnett shale, respectively (US EPA, 2016). In addition, the wastewater volume due to flowback and produced water have increased up to startling 550% from 2011-2016 (Kondash et al., 2018).

A hydraulic fracturing fluid should have sufficient properties to perform fracturing and proppant transport efficiently (Economides and Nolte, 2000). Therefore, sufficient viscosity for fracture creation, propagation and proppant transport, formation compatibility to avoid formation damage, gel breaking ability to ensure proppant placement and fracture closure to maximize conductivity are essential (Economides, 2007). Generally, the fracturing fluid is 99% water, however, to perform its functions, several chemical additives such as acids, biocides, surfactants, scale inhibitors etc. are used with water-based fluids (Howarth et al., 2011; Rahm, 2011). A brief discussion about the chemical additives and their functions is listed below.

2.1.2.1 Gelling agents

To transport proppant and avoid fluid loss, natural polymers such as guar, starches and cellulose derivatives are added as gelling agents to viscosify water. However, to enhance the stability of gel, borate or zirconate crosslinked gels are used. In addition, due to their higher stability, carboxymethyl guar (CMG) or carboxymethyl hydroxypropyl guar (CMHPG) are used. Moreover, surfactant and viscoelastic gels without polymer have also been developed (Economides, 2007). Additionally, to reduce shear degradation and pumping pressure requirements, fluid chemistry is manipulated to delay the crosslinking process (Economides and Nolte, 2000). Fracturing fluid viscosity typically varies from 50-1000 mPa.s to transport proppants (Gallegos and Varela, 2015).

2.1.2.2 Breakers

The high viscosity fluid such as crosslinked guar gel can transport the proppants from surface to reservoir. This gelled fluid, when present in the fracture and nearby zones, can severely block the flow of reservoir fluids such as oil and gas by reducing the effective permeability and seriously damaging fracture conductivity. Therefore, breakers such as oxidizers, enzymes and acids are added to the fluid to reduce or break the gel viscosity by breaking the chemical bond and splitting the polymer into small molecular weight segments, once the proppants have been placed in the fracture. Therefore, they help in proppant pack and filter cake cleaning. Both oxidizers and enzymes have their own abilities in terms of performance at high temperature, gel breaking ability and duration and sensitivity to other chemicals used in frac-fluids (Economides and Nolte, 2000). Persulfate oxidizers such as sodium/potassium persulfates are commonly used. Polymer specific enzymes are used for a better clean-up compared to oxidizers (Economides, 2007).

2.1.2.3 Biocides

Bacteria dwell excellently on the most common water-based frac-fluid gelling agents i.e., polysaccharides. Biocides or bactericides prevent the degradation of gel from these bacteria. Therefore,

biocides such as glutaraldehyde, chlorophenates, quaternary amines etc., are added to prevent the growth of bacteria in natural polymer gelling agents (Economides, 2007; Economides and Nolte, 2000).

2.1.2.4 Fluid loss additives

For an efficient fracturing operation, fluid loss should be controlled. During the hydraulic fracturing operation, frac-fluid filtrate escapes into the matrix zone and polymers such as guar filter out on the surface of the fracture in low permeability reservoirs creating filter-cake. Depending upon the requirement of fracturing job and type of formation encountered such as low or high permeability, different types of additives can be utilized. Dispersed fluids such as oil-in-water can be used for low permeability reservoirs. Silica flour with largest aspect ratio particles can be a good fluid loss agent (Economides and Nolte, 2000).

2.1.2.5 Clay stabilizers

To minimize clay hydration and swelling in water sensitive clays, clay stabilizers are utilized. Potassium chloride and ammonium chloride are commonly used as temporary clay protection agent. Whereas, for permanent clay protection, higher molecular weight amines and cationic polymers have been utilized effectively to prevent relative permeability damage (Economides, 2007).

2.1.2.6 Stabilizers

Stabilizers are used to prevent degradation of polysaccharide gels at high temperatures. Chemicals such as methanol and sodium thiosulphate are used for this purpose. The rapid gel degradation due to dissolved oxygen can be barred as they are known to act as oxygen scavengers (Economides and Nolte, 2000).

2.1.2.7 Buffers

For proper hydration of polymers through appropriate dispersion in water, buffers are used. The crosslinking and fluid stability depend on pH, and buffers adjust and control it by withstanding the variation in hydrogen and hydroxide ions concentration due to addition of other chemicals such as acid or base. They consist of weak acid and its conjugate base such as acetic acid-sodium hydroxide or conversely, weak base and its conjugate acid such as ammonia-hydrochloric acid (Economides, 2007).

2.1.2.8 Surfactants

To minimize fluid retention in the fracture and nearby zones after fracturing operation, surfactants are used. By reducing surface tension, the injected fluid recovery becomes easier. Additionally, by decreasing surface tension between water-based fluid and formation gas, more fracturing fluid can be recovered and relative permeability to gas can be restored. Otherwise, the trapped injected fluid

especially in the near wellbore area can damage the well productivity by reducing relative permeability to reservoir fluids. They are also used for changing the wettability, stabilizing foams, act as clay controlling agents and biocides and prevent or break emulsions (Economides, 2007).

2.1.2.9 Friction reducers

Friction reducers are utilized to reduce the surface injection pressure requirements and to reduce the wear and tear of the equipment due to high injection rates. Viscoelastic surfactant systems with additives have been utilized to lower friction in turbulent flows such as those encountered during fracturing operation (Economides, 2007).

In addition to the discussed additives, other proprietary chemicals are also used by companies according to fracturing job needs. Between 2005-2013, around 1,084 chemicals in different fracturing operations were used in the US. Methanol, hydrochloric acid and light petroleum distillates were reported to have been used in more than 65% of the wells (US EPA, 2016). The untreated disposal or spill of frac-fluid containing these chemicals can cause contamination issues.

2.1.3 Induced seismicity

Due to unconventional petroleum resources exploitation and production boom, a large amount of water has been injected into the formations for hydraulic fracturing operations, similarly huge increase in flowback and produced wastewater have been observed (Kondash and Vengosh, 2015; Kondash et al., 2018; US EPA, 2016; US EPA, 2015). Apart from large injection fluid volumes, the flowback fluid volumes are also high (Figure 2.3). Whereas the water produced at surface after hydraulic fracturing is called flowback water and water (connate water) produced during the life of a well is called produced water (Clark et al., 2013).

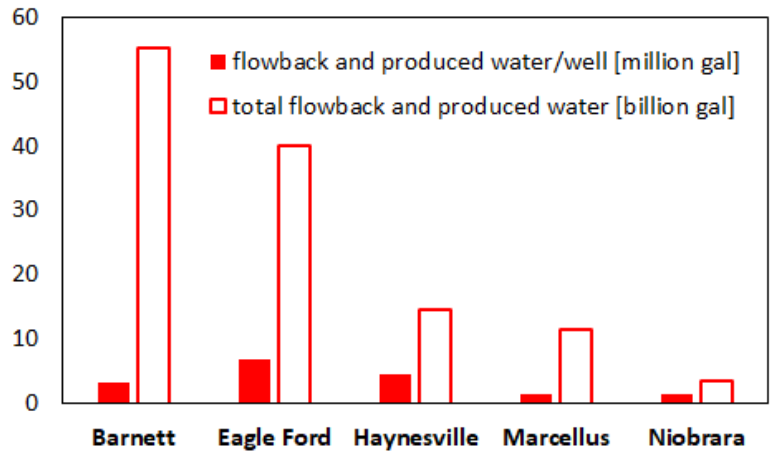

Figure 2.3: flowback and produced water from major unconventional plays in the US (Kondash and Vengosh, 2015; US EPA, 2015).

As can be observed from Figure 2.3, billions of gallons of wastewater are produced. Wastewater disposal in deep injection wells is also considered a source of induced seismicity (Doglioni, 2018; Hincks et al., 2018; Hornbach et al., 2016; Rubinstein and Mahani, 2015). According to Rubinstein and Mahani (Rubinstein and Mahani, 2015), there were approximately 35000 active waste injection wells in the US. Due to density of the fluid, gravity, and depth of the deep injection well, the injection fluid pressure rises and can cause felt earthquakes such as M 5.3 and M 5.0 seismic events in the Raton Basin. Wastewater injection is considered to be the major reason behind rise in seismic events in Oklahoma (Hincks et al., 2018). Due to wastewater injection in Ellenberger carbonate formation, a high rise in seismic events have been observed (Hornbach et al., 2016). The extent of an anthropogenic seismic event generally depends upon the local geology, stress environment, rock mechanical properties etc. The presence of large faults, stress reorientation and large pressure differentials can increase the chances of seismicity (Lei et al., 2017; Rubinstein and Mahani, 2015; Rutqvist et al., 2013). It is estimated that 5-40% flowback of the water injected during fracturing operation is achieved, therefore water handling at surface becomes a big issue, and deep well injection disposal is considered as the cheapest option (Clark et al., 2013; Gallegos et al., 2015; Gregory et al., 2011). If injection takes place close to the fault zones, then chances of induced seismicity are high (Jacobs, 2014). With the increase in unconventional resources exploitation, the environmental challenges posed by water-based fluids are also going to increase, therefore it is important to address these issues.

2.2 Technical problems

In tight and ultra-tight reservoirs, due to delayed fracture closure, less propped fracture height because of proppant settling at the bottom may result in partial or complete loss of hydraulic connection with the injection zone. In addition, clay swelling, and water entrapment poses a big problem in water sensitive clays as the relative permeability for the petroleum fluids is reduced affecting the ultimate recovery. Low flowback of injected fluid leads to more fluid left in the reservoir aggravating the problem (Bennion et al., 1996; Leblanc et al., 2011; Li and Zhang, 2019; Sanaei et al., 2018; Zhang et al., 2016).

2.2.1 Less propped fracture height

It has been observed especially in tight -ultra-tight reservoirs that after pumping proppants into the formation, they fall to the bottom of the fracture depriving the upper half of the fracture of the proppants. And due to fracture closure, the hydraulic connection between the fracture and formation especially near the perforations is lost. This happens because the leakoff rate of water-based fluids is low especially in tight reservoirs, which causes delayed fracture closure. Therefore, the productivity of the well may not increase as expected or may not increase at all due to loss of borehole-fracture hydraulic connection because of absence of proppants (Li, 2018). Slick-water has been utilized for such problems, but due to

lower viscosity, the proppant carrying ability is not up to the mark. In conventional hydraulic fracturing treatments, slow flow back of injection fluid results in delayed fracture closure and poor proppant placement, and the flowback may last over a year (Leblanc et al., 2011; Tudor et al., 2009). Figure 2.4 shows the settling of proppants to the bottom of fracture below the perforation level and the upper half of fracture completely closes due to absence of proppants.

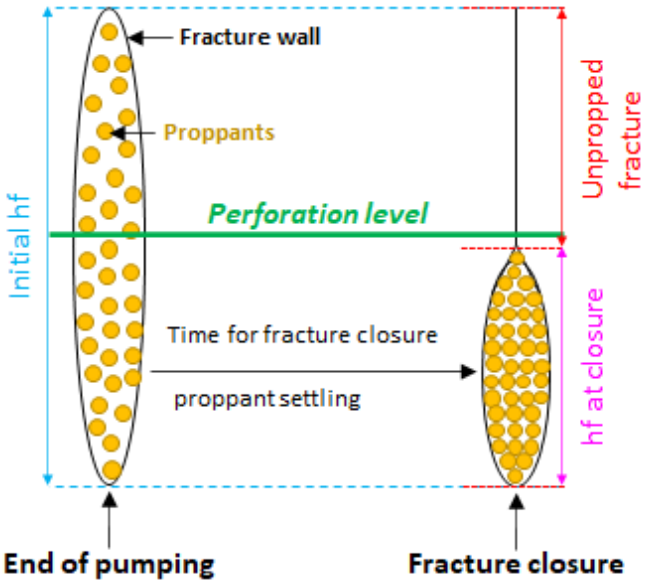

Figure 2.4: inefficient proppant placement (Mehmood et al., 2021).

2.2.2 Phase trapping

Due to processes such as desiccation, compaction and genesis, sub-irreducible saturation commonly exists in tight gas reservoirs (Bennion et al., 1999; Economides, 2007). Gas expansion near wellbore can cause evaporation of water, reducing the water saturation in tight gas sand or shale where capillary is high causing subnormal saturations (Mahadevan et al., 2007). Most ultra-tight gas reservoirs fall into the category of sub-normally saturated or desiccated reservoirs. And due to high capillary pressure energy, fluid imbibition and entrapment takes place in porous media (Abaa et al., 2013). During hydraulic fracturing operation, mostly aqueous-base fluid is used due to its cost effectiveness, accessibility and suitability (Middleton et al., 2015). The formations having lower permeability are largely candidates for stimulation and vulnerable to fluid entrapment, as the injected fluid can go to the unpropped fracture, propped fracture, or matrix (Jacobs, 2014). The issue of phase trapping is severe in reservoirs with sub-irreducible water saturations, low permeability and higher invasion depths of injected fluid such as encountered in fracturing operations (Bennion et al., 1996; Holditch, 1979). Due to lower pore throat size, capillary suction is high and leads to fluid retention in pores. Water invasion and phase trapping can damage the formation (Figure 2.5).

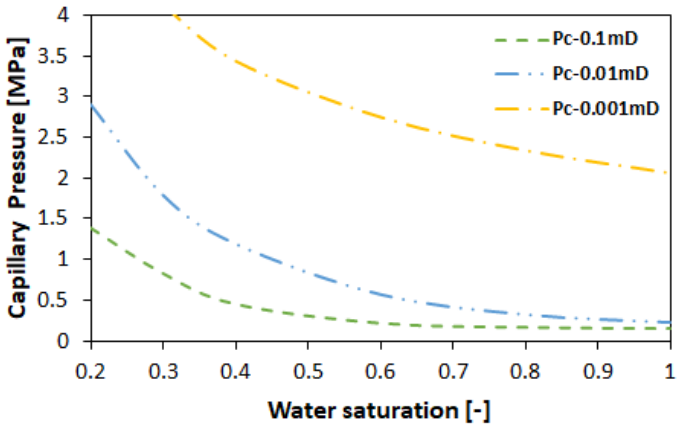

Figure 2.5: capillary pressure variation for different formation permeabilities (Economides, 2007).

Water retention in the pores can greatly reduce the flowing ability/relative permeability to reservoir fluids, affecting the fractured tight gas well deliverability. Water entrapment may cause serious damage in tight formations having sub-normal water saturation, as injected water flows to matrix due to fluid leakoff during a hydraulic fracturing operation (Abaa et al., 2013; Bahrami et al., 2012). The trapped water will reduce the permeability in the invaded zone. The impacts of increase in water phase saturation leads to decreasing gas/oil phase saturation due to aqueous phase trapping which consequently causes hydrocarbon flow blockage by reducing the permeability. Since the effective flow path is blocked by residual water, higher drawdown pressures, reducing the interfacial tension or even evaporation or heat treatment may be required to resolve the issue of phase trapping (Bennion et al., 1996; Zhang et al., 2016). The trapped water cannot flowback, becoming a constant hindrance to flow. Therefore, the hydraulic fracturing operations may not be successful due to water-based fluids and expected productivity may not be achieved (Abaa et al., 2013; Bahrami et al., 2012; Bennion et al., 1996; Li and Zhang, 2019; Ortiz and McLane, 1986; Zhang et al., 2016). Figure 2.6 shows the sharp decline in relative permeability to gas as water saturation increases due to imbibition.

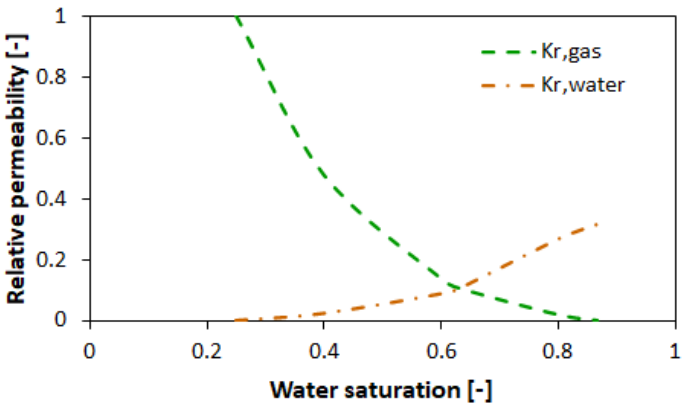

Figure 2.6: decline in gas phase relative permeability due to water imbibition (Economides, 2007).

2.2.3 Clay swelling

Minerals such as kaolinite, illite, mica and smectite are major constituents of clay created by decaying and erosion of igneous rocks. The interaction between injection fluid and rock matrix can lead to clay swelling and particle migration which can severely affect the fracture conductivity. Due to considerable amount of water sensitive minerals such as kaolinite and illite in sandstone, clay particle migration can be the dominant phenomenon behind reduced permeability. In experiments conducted on sandstone core samples, as low as 1% damage permeability due to swelling of clays was observed and the extent of damage depends upon the clay content. The phenomenon of clay swelling is dependent upon rock mineralogy, frac-fluid composition, and formation brine salinity. (Khilar and Fogler, 1983; Sanaei et al., 2018; Zhang et al., 2016). Reduction in pore opening due to clay swelling reduces absolute permeability and subsequently effective permeability to oil and gas (Bahrami et al., 2012; Li and Zhang, 2019). Therefore, the injection of aqueous-based fluids for hydraulic fracturing in clay-laden tight sandstones leads to formation damage. The use of KCL in water-based fluids to mitigate this issue has not been as successful as expected. The accomplishment of fracturing treatment lies upon efficient proppant placement in the fracture without damaging the matrix. However, the permeability impairment is a serious setback in this case (Holditch, 1979; Jacobs, 2014; Ortiz and McLane, 1986). Hence, aqueous-based fluids such as slick-water are not suitable for water sensitive formations. Due to leakoff of water, its saturation increases around the fracture. The clays swell and plug the pores creating hindrance for the petroleum to flow from matrix to fracture as well. During drilling, stimulation, or completion stages, clays such as smectite and illite swell due to contact with a different salinity water (Kong et al., 2017). Therefore, it is imperative that the injected fluid should be compatible with the formation.

2.2.4 Low flowback and poor fracture clean-up

Another issue that aqueous-based frac-fluids have is the low flowback of injected fluid to the surface. Flow back fluid can be defined as the produced water phase within three weeks of hydraulic fracturing operation. In Marcellus shale (north-eastern west Virginia), lower recoveries from 2-26% were observed of injection fluid. And the recovered water has shown high salt concentrations which have both technical and environmental implications (Barbot et al., 2013; Zhou et al., 2016). There are two major reasons of low fluid flowback in case of water-based fluid: (1) water entrapment (2) high density. The issue of water entrapment has been discussed in detail in the previous section. The second reason of water being a high-density fluid make the flowback even more difficult from subsurface formation to surface. To achieve maximum reservoir fluid flow after stimulation, it may require several months of flowback of injected fluid in some reservoirs due to water blockage and poor clean-up and in some reservoirs further gas production may not be possible due to complete blockage. In addition, nitrogen

lift is normally required to initiate the production operation after fracturing (Economides, 2007; Holditch, 1979; Leblanc et al., 2011).

According to estimates, 5-40% of injected fluid returns to surface. Which means a significant amount of injected fluid remains in the reservoir creating problems of phase trapping and clay swelling in water sensitive formations. The water if remains in the reservoir creates technical issues, whereby it reduces relative permeability leading to lower productivity or even no productivity at all due to formation damage especially in the near wellbore zones and near fracture zones where the injected fluid leaks off. Therefore, not only relative permeability but also effective permeability to reservoir fluids is lessened. The portion of fluid returning to surface creates environmental issues, which if not recycled is pumped into injection or disposal wells (Clark et al., 2013; Gallegos et al., 2015; Gregory et al., 2011; Jacobs, 2014).

2.3 Problem with public acceptance

The development of unconventional petroleum resources has not only increased the energy supply and economic growth but is also facilitating the low carbon energy transition from high carbon coal-based energy. However, due to the adverse effects on the environment as discussed earlier and consequently on health, the public acceptance of exploitation techniques such as hydraulic fracturing has declined (Boudet et al., 2014; Howarth et al., 2011; Hughes, 2013; Vengosh et al., 2014; Zhang and Yang, 2015). The major challenges can be addressed through minimizing the use of water by utilizing alternative frac-fluids. In the next section, different alternative frac-fluids are discussed.

2.4 Alternative frac-fluids

In the light of above discussion, alternative frac-fluids have been proposed and used to address the issues caused by conventional water-based frac-fluids. Foam-based fluids (water-based, acid-based, alcohol-based, CO_2-based) reduce water usage but on the other hand have the disadvantages of lower fracture conductivity, higher costs, difficult rheological characterization, and higher surface pumping pressure requirement. Acid based fluids have limited application in carbonate reservoirs with drawbacks of surface handling issues and proppant-less fractures. Cryogenic fluids (liquid CO_2 and N_2) have the disadvantages of surface handling issues (special equipment required), corrosive nature of CO_2, difficulty in implementation especially for N_2 etc. (Kong et al., 2017; Li and Zhang, 2019; Ortiz and McLane, 1986; Gandossi and Estorff, 2015). LPG-based frac-fluids have been utilized for fracking operations, but have the shortcomings of gaseous nature, high flammability, and difficulty to safely handle at surface conditions (Leblanc et al., 2011; Gandossi and Estorff, 2015; Tudor et al., 2009).

A brief description on different frac-fluids including the conventional water-based fluids is provided in the following sections.

2.4.1 Water-based fluids

The most commonly and widely used water-based fluids can be divided into three categories: linear fluids, crosslinked fluids and slick water. In low permeability formations, the fluid loss reduction and proppant carrying ability enhancement are done through the addition of polymers such as guar and its derivatives such as hydroxypropyl guar (HPG), hydroxyethyl cellulose, double derivatized carboxymethyl hydroxypropyl guar (CMHPG) and carboxymethyl hydroxyethyl cellulose (CMHEC) (US EPA, 2004). To give the guar gel stability in higher temperature and high shear environments and to avoid fluid loss in higher permeability formations, the previously discussed polymers are crosslinked with water through borate, zirconate, titanate, aluminium etc. ions. They improve the performance of gel without increasing the concentration of gelling agent. Depending upon the type of crosslinking, they are characterized as borate crosslinked, organometallic or metallic ion crosslinked, or delayed crosslinked systems. Whereas for application in unconventional reservoirs (tight and ultra-tight), slick water or friction reduced water with low viscosity are used. In this case long fractures can be created with large volumes of injected water, containing friction reducer, at higher injection rates and lower proppant concentrations. Their proppant carrying ability is poor and sometimes their injection is followed by gelled fluid for a better proppant transport (Barati and Liang, 2014; Economides, 2007; Economides and Nolte, 2000; Gandossi and Estorff, 2015).

2.4.2 Foam/emulsion-based fluids

Foams or emulsions can be defined as two phase fluids with second phase contributing to viscosity enhancement (Economides, 2007). There are many types of foam-based fluids such as water-based foams with water as base fluid and N_2 or CO_2 and foamer, acid-based foams with acid, N_2 and foamer, alcohol-based foams including methanol, foamer and N_2, and CO_2-based foams having liquid CO_2 and N_2. They are utilized in water sensitive formations and considered appropriate for shale gas reservoirs (Gupta, 2009). Due to their high viscosity and low liquid content, they have been used to stimulate petroleum reservoirs. Reducing water usage and minimizing damage to water sensitive clays are the major advantages.

However, higher costs, difficult rheological characterization, higher hydraulic horsepower requirements at the surface due to low density and most of all poor proppant carrying ability leading to lower conductivity fracture are major disadvantages of this technique. In addition, the flowback of recovered fluid as foam can be problematic for surface equipment (Barati and Liang, 2014; Economides, 2007; Gandossi and Estorff, 2015).

2.4.3 Energized fluids

The substantial increase in tight and ultra-tight reservoir exploitation having considerable clay content have attracted research in the energized systems with larger gas and smaller water fractions. The damage

caused by water blockage can be reduced in addition to decreasing the amount of water utilized during conventional fracturing operations. Different energized frac-fluid systems mainly composed of CO_2 and N_2 such as Nitrogen + HPG + foaming agent, CO_2 + HPG + foaming agent, foaming of the viscoelastic gels with N_2 and CO_2 etc. The performance of CO_2-based fluids has been reported to be better than other energized fluids (Barati and Liang, 2014; Harris, 1987, 1985).

N_2 is chemically inert and cheaper than CO_2. But due to very low density, it can easily separate itself from the fluid it is pumped with, therefore, flowback issues may arise as N_2 will be produced leaving the other fluid in the reservoir. Also, due to high compressibility, the job design may be difficult. CO_2 at injection conditions is normally in the liquid or supercritical state has a density close to water and therefore, no significant changes in hydraulic horsepower may be required. Due to its solubility in fluids, the fluid recovery is better than for the case of N_2 based fluids (Economides, 2007).

However, it is difficult to model and understand the phase behavior of energized fluids. Also, potential safety concern is a major issue. CO_2 can form dry ice plugs upon pressure reduction. Trucking, higher costs, proppant placement issues, higher injection rate requirement leading to higher friction losses and hydraulic horsepower requirements are the concerns reported (Barati and Liang, 2014). CO_2 is reactive and therefore cannot be used with fluids such as borate fluids, viscoelastic fluids, aqueous solutions, certain oil gels etc. (Economides, 2007).

Although water use is minimized and rapid fracture clean-up can be achieved, but proppant placement issue, transportation, and storage conditions (2 Mpa, and 243.15 K (-30 °C)), corrosive nature and higher costs are the potential disadvantages of CO_2. Whereas special equipment requirement for N_2 handling, higher costs and difficult practical application in liquid phase while losing the ability to place proppant are the major demerits of N_2 (Gandossi and Estorff, 2015).

2.4.4 Oil-based fluids

Due to their compatibility with formation and less damaging to water sensitive clays compared with water-based fluids, they were initially used in hydraulic fracturing operations. Aluminum phosphate ester chemistry is considered suitable for gelling and viscosifying the oil-based fluids for increasing proppant carrying capability. Iron salts replaced aluminum salts at later stages (Smith and Persinski, 1997). The gel break can be achieved by addition of calcium/magnesium oxides or carbonates. However, gel stability can be impaired due to interaction between asphaltic components of crude and iron (Economides, 2007; Economides and Nolte, 2000). In addition, soap colloids dispersion by delivering organic fatty acid have also been utilized for generating stable gelled system (Economides, 2007; Grantham and McLaurine, 1986). Several diesel-based frac-fluids can be designed. Although water usage and formation damage in water sensitive formations can be minimized but higher costs and

surface handling issues are major drawbacks (Economides and Nolte, 2000; Gandossi and Estorff, 2015).

2.4.5 LPG based fluid

Over 1500 fracking operations were performed by GasFrac using LPG in Canada and USA, since they started using it in 2007. eCorpStim also developed the waterless frac-fluid technology such as pure propane stimulation, non-flammable propane stimulation and light alkanes stimulation (Gandossi and Estorff, 2015; ecorpStim). Hydraulic fracturing was performed in the McCully gas field (New Brunswick, Canada) with liquefied petroleum gas (LPG), mainly propane, as the fracking fluid (Leblanc et al., 2011; Tudor et al., 2009). According to their findings, propane (LPG) fracking was more successful in the McCully field than the previously done water-based fracking. A comparison between LPG-based fractures and water-based fractures is provided in Figure 2.7 (comparison based upon single fracture per well and comparable fracture job size).

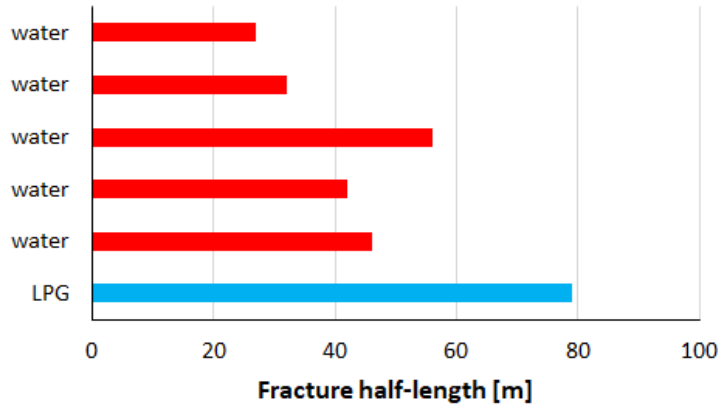

Figure 2.7: comparison between LPG and water-based fluid fracture for different wells with single fracture in McCully gas field.

The flowback of injected fluid in the case of propane-based fluid fracking was much quicker compared to water-based fluid fracking; the complete flowback of propane only took up to 10 days for all wells. Their results show a considerable increase in recovery from wells using propane-based fracking: around 1.5 times compared with water-based fracking and 3.8 times compared to when no fracking was carried out. However, the problems with LPG-based fluid include the surface handling of propane, which exists as a gas at surface conditions and is highly flammable and higher investment required for conducting the job (Gandossi and Estorff, 2015).

2.4.6 Light Alkane Stimulation

In 2015, eCORP Stimulation Technologies, LLC introduced Light Alkanes Stimulation (LAS) using mineral oil for stimulation (ecorpStim, 2015). Table 2.1 summarizes the properties of mineral oil.

Table 2.1: properties of mineral oil.

	Average molecular weight	**Carbon number**	**Boiling point**	**specific gravity**
World Health Organization (WHO) Food and Agriculture Organization (FAO) (FAO/WHO, 2012)	480-500	Not less than 25 at 5% distillation point	>664.15 K (391 °C)	
Europian Food Safety Authority (EFSA) (EFSA, 2012)	300-500+	12-40		
Conservation of Clean Air and Water in Europe (Hedelin, 2013)		15-50		
International Agency for Research on Cancer (IARC) (IARC, 2012)		>15	573.15-873.15 K (300-600 °C)	
United States Environment Protection Agency (US EPA, 2009, US EPA)	Lower molecular weight (C9-C32): <480	Lower molecular weight: 15-50		0.83-0.905

Mineral oil has a density generally higher than 800 kg/m^3, and consists of heavier components, therefore it is possible that it may develop flowback issues and its flowback may not be as quick as that of gaseous phase or lighter alkane components.

After the detailed analysis of alternative fluids, their brief review stating their potential advantages and disadvantages is presented in Table 2.2.

Table 2.2: brief review of alternative fluid technology.

	Advantages	**Disadvantages**
Foam-based (water-based foams Acid-based foams Alcohol-based foams CO_2-based foams)	Reduced water usage Suitable for water sensitive clays Better cleanup	Difficult rheological characterization Lower fracture conductivity due to lower proppant carrying ability Higher hydraulic horsepower requirement Safety issues Higher cost
Energized fluid (N_2+ HPG + foaming agent CO_2 + HPG + foaming agent)	Reduced water usage Reduced damage to formation	Flowback issues for N_2 based fluid CO_2 can form dry ice plugs upon pressure reduction Difficult to model phase behavior Proppant placement issues Higher costs

Liquid CO_2	Reduced/eliminated water usage Few or no chemical additives Reduced formation damage Rapid cleanup	Decreased fracture conductivity due to lower proppant carrying ability Transportation and storage issues Corrosive nature Reactive, therefore cannot be used with borate, viscoelastic fluids, aqueous solutions, certain oil gels Potentially higher costs
Liquid N_2	Reduced/eliminated water usage No chemical additives Reduced formation damage	Special equipment required for handling Higher costs Difficult application Poor proppant transport ability
Oil-based	Minimize water usage Fewer chemical additives Formation compatibility Better cleanup	Safety issues Higher costs
LPG-based	Reduced/eliminated water-usage Fewer or no chemical additives Reduced truck traffic Increased productivity Reduced phase trapping Rapid cleanup	Flammable and hence riskier Higher costs
Light alkane stimulation (Mineral oil/baby oil)	Reduced/eliminated water usage No chemical additives Non-flammable Non-toxic	Higher costs Density generally higher than 800 kg/m^3 (may develop flowback issues due to higher density)

3 Light alkanes (C_5-C_{10})

All fracturing fluids can cause some damage to the reservoir matrix, however this damage can be reduced by using clean fluids that are compatible with the formation and formation fluids (Holditch, 1979). The fluid discussed in previous sections have their own merits and demerits. The gas-based fluids are difficult to handle at surface conditions, can have issues with proppant transport, difficult rheological characterization etc. The fluids in liquid state have their own drawbacks such as formation compatibility issues leading to formation damage and fluid entrapment and retention, higher density resulting in lower flowback, surface handling issues etc. Therefore, an alternative fluid which can be handled as liquid at surface conditions, is compatible with formation and has lower viscosity and density for quick fracture closure for better proppant placement especially in the upper half of fracture and faster flowback for efficient fracture clean-up can help optimize the hydraulic fracturing operation in tight and ultra-tight reservoirs.

Frac-fluid consisting of light n-alkanes (C_nH_{2n+2}): n-pentane, n-hexane, n-heptane, n-octane, n-nonane and n-decane is proposed as alternative fluid in this regard (Hou and Mehmood, 2018; Mehmood et al., 2020). These alkanes are heavier than gas-based petroleum fluid i.e., LPG and lighter than the mineral oil and are formation compatible due to their hydrocarbon nature. The phase behavior of proposed fluid can be observed from Figure 3.1. It can be observed that although the components are light alkanes, the fluid can exist as liquid at surface conditions and high-pressure fracturing conditions in the reservoir. Upon lowering the pressure after fracturing, the components of proposed fluid may change their phase to gaseous phase depending upon their own properties and bottomhole and reservoir conditions. The phase behavior of individual components can be observed from Figure 3.2.

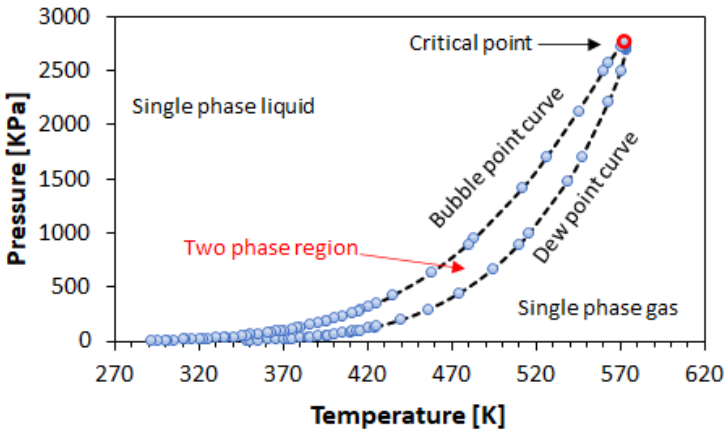

Figure 3.1: phase behavior of light n-alkanes mixture (Petex).

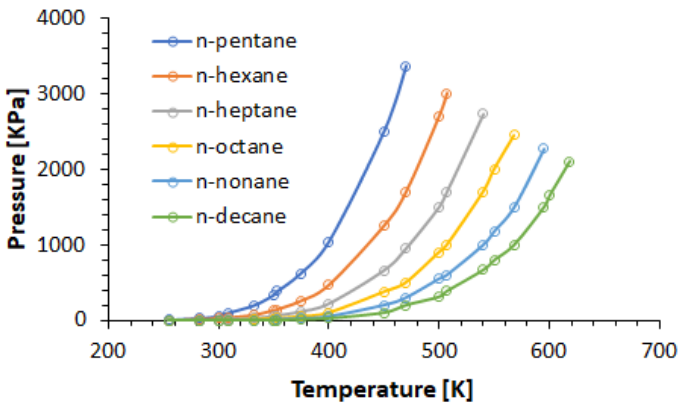

Figure 3.2: phase behavior of individual n-alkanes (last point on curve represents critical point) (Petex).

The critical properties and viscosity and density of different mixtures of light alkanes with and without propane are presented in Appendix A.

3.1 Properties of alternative fluid

To model stimulation operations, it is important to understand the properties of light alkanes. The individual components have boiling points ranging from 309.22 K to 447 K. The density of components is considerably lower than water and ranges from 626-730 kg/m^3, therefore even if the heaviest component n-decane is chosen the density will be less than mineral oil and water. Table 3.1 presents individual component properties of proposed fluid such as critical temperature, critical pressure, viscosity etc.

Table 3.1: proposed fluid properties: n-alkanes (API, 2016).

Property	**n-pentane**	**n-hexane**	**n-heptane**	**n-octane**	**n-nonane**	**n-decane**
C_nH_{2n+2}	C_5H_{12}	C_6H_{14}	C_7H_{16}	C_8H_{18}	C_9H_{20}	$C_{10}H_{22}$
T_{CRITAL}, K	469.7	507.6	540.2	568.7	594.6	617.7
P_{CRIT}, MPa	3.37	3.02	2.74	2.49	2.29	2.11
$T_{Boiling}$, K	309.22	341.88	371.57	398.82	423.97	447.3
M. Weight, g/mol	72.15	86.177	100.204	114.231	128.258	142.285
Density, kg/m^3	626	664.446	689.48	706.6	721.343	730
T_{DENREF}, K	293	288.706	288.706	288.706	288.706	293
Viscosity, mPa.s	0.206	0.2757	0.3479	0.4496	0.5827	0.7212
T_{VISREF}., K	310.928	310.928	310.928	310.928	310.928	310.928

3.1.1 Fluid density and viscosity

Fluid density and viscosity are very critical in hydraulic fracturing operation. These properties of proposed fluid mixture have been determined from the API recommended correlations (API, 2016). The reference mixture density (generally at standard conditions) can be found as

$$\rho_{l0} = \frac{\sum_{1=1}^{n} x_i M_i}{\sum_{i=1}^{n} \frac{x_i M_i}{\rho_i^0}} \quad (3.1)$$

Increasing pressure increases the density of the mixture. The density at increases pressure p is calculated by the following relation

$$\rho_p = \rho_{l0} \left(\frac{C_2}{C_1}\right) \quad (3.2)$$

Whereas, C_1 and C_2 are correlation factors for density calculation according to the conditions of ρ_{l0} and ρ_p and found by the following polynomial equations

$$C = A_0 + A_1 T_r + A_2 T_r^2 + A_3 T_r^3 \quad (3.3)$$

$$A_i = B_{0i} + B_{1i} P_r + B_{2i} P_r^2 + B_{3i} P_r^3 + B_{4i} P_r^4 \quad (3.4)$$

Where, ρ_{l0}: reference density of the mixture [lb/ft^3]; ρ_i^o: density of pure component [lb/ft^3]; x_i: mole fraction of component i; n: number of components in the mixture; M_i: molecular mass of component i; ρ_p: mixture density at pressure p [lb/ft^3]; T_r: reduced temperature [-]; P_r: reduced pressure [-]; A, B: correlation coefficients. The correlation coefficient B_{ji} values are provided in Table 3.2.

Table 3.2: values of correlation coefficient B.

i	B_{0i}	B_{1i}	B_{2i}	B_{3i}	B_{4i}
0	1.6368	-0.04615	2.1138	-0.7845	-0.6923
1	-1.9693	0.21874	-8.0028	-8.2823	5.2604
2	2.4638	-0.36461	12.8763	14.8059	-8.6895
3	-1.5841	0.25136	-11.3805	9.5672	2.1812

The density of the mixture is based upon the individual density of components at standard conditions and mole fraction of component in the mixture. Whereas viscosity is found according to the individual component viscosities and their mole fracture. Therefore, the fluid density and viscosity are influenced by the amount of a particular component in the mixture.

$$\mu_{mp} = \left(\sum_{i=1}^{n} x_i \mu_{ip}^{1/3}\right)^{\frac{1}{3}} \quad (3.5)$$

Where, μ_{mp}: mixture viscosity at pressure p [cp]; μ_{ip}: viscosity of component *I* at pressure p [cp].

The viscosity of individual component at high pressure p is given by

$$\mu_{ip} = \mu_r \mu_c \quad (3.6)$$

Where, μ_c: critical viscosity and the reduced viscosity μ_r is found as

$$\mu_r = \mu_r^0 + \omega \mu_r^1 \quad (3.7)$$

Whereas μ_r^0 is the reduced viscosity for pure fluid according to reduced pressure and reduced temperature given by

$$\mu_r^0 = A_1 log P_r + A_2 (log P_r)^2 + A_3 P_r + A_4 P_r^2 + A_5 \quad (3.8)$$

$$A_n = a_n T_r^{b_n} + c_n T_r^{d_n} + e_n \quad (3.9)$$

And μ_r^1: is the correction factor for acentricity ω, given by

$$\mu_r^1 = B_1 P_r + B_2 ln P_r + B_3 \quad (3.10)$$

Whereas, $A_n, a_n, b_n, c_n, d_n, e_n$ are constants.

The viscosity and density of proposed fluid at 288 K and varying pressure can be observed from Figure 3.3. The fluid viscosity and density rise with increasing pressure; however, it is considerably less than water.

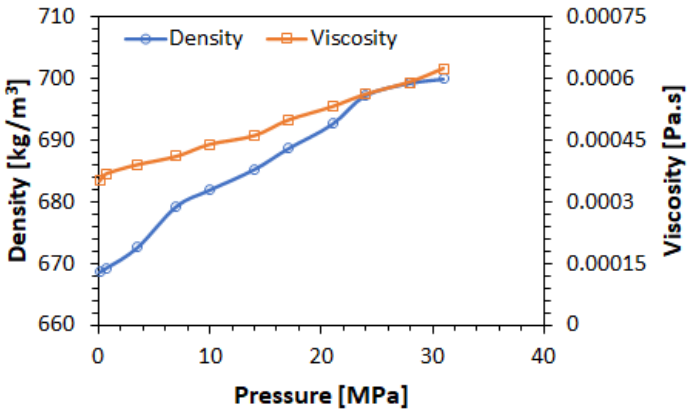

Figure 3.3: light alkanes mixture density and viscosity variation with reference to pressure.

However, to find the pure fluid viscosity as a function of temperature, following correlation (Equation (3.11) is presented.

$$\mu_{iT} = 1000 exp\left(A + \frac{B}{T} + ClnT + DT^E\right) \quad (3.11)$$

Where, μ_{iT}: pure fluid viscosity for different temperatures [cp]; T: temperature [°R]; A, B, C, D, E: constants for a specific fluid.

3.1.2 Biodegradation

As discussed in section 2.1.2.3, bacteria dwell excellently on water-based fluids, therefore biocides have been utilized. However, studies have shown that not all bacteria could be eliminated. Most of the water-based fluid remains in the reservoir which could result in harmful microbial processes. The storage of water in man-made ponds before utilization for fracturing increases bacterial contamination due to exposure to the environment (Johnson et al., 2008; Struchtemeyer and Elshahed, 2012). The larger the time fluid spends in the reservoir, the higher the microbial activity (Struchtemeyer and Elshahed, 2012). Alkanes are nonpolar and chemically inert, have a very low solubility in water, and the solubility decreases as the molecular weight increases. Thus, alkanes are not preferred substrates for bacteria (Labinger and Bercaw, 2002; Rojo, 2009). However, hydrocarbons can be degraded by hydrocarbonoclastic bacteria (Wang and Shao, 2013; Yakimov et al., 2007). But the lower solubility of alkanes in water and quick flowback ability (spending less time in the reservoir), reduce the likelihood of considerable biodegradation. The flowback ability of n-heptane will be discussed and compared with water-based fluid in sections 5.4.4 and 6.6.

3.1.3 Fluid rock interaction

Sandstone reservoirs are generally water-wet in comparison to neutral/oil-wet carbonates (Ruidiaz, 2017). The wettability of carbonates can be changed from oil-wet to water-wet through saline water injection for improved recovery. The wettability alteration is a complex phenomenon and can be attributed to the presence of monovalent and divalent ions (Lashkarbolooki et al., 2017; Yang et al., 2016). The type of fluid injected in the reservoir together with type and concentration of brine, temperature conditions and aging can affect the formation wettability due to fluid rock interaction. Crude oil has several polar and non-polar components, where the cations in the brine phase can promote the adsorption of polar components. This can consequently change the sandstone from water-wet to intermediate-wet or oil-wet. However, light alkanes (proposed in this work) are non-polar and experimental results have shown that formation remained in the water-wet regime in the presence of alkanes in varying brine concentrations (Kakati and Sangwai, 2018).

3.2 Simulation in a fictive model to investigate phase behavior

The phase behavior of proposed fluid shows that it will change its phase under higher temperature and lower pressure conditions. The density of fluid is also considerably low compared to conventional water-based fluid. The density of fluid is also temperature and pressure dependent and change to gaseous phase under relevant conditions can further reduce it. The flowback of proposed fluid due to lower density will assist in quick fracture cleanup. In this section, simulation is performed to observe

the phase behavior of proposed fluid in a porous medium containing reservoir fluid. To carry out simulation, TMVOC simulator is utilized which is discussed in the next section.

3.2.1 TMVOC: multiphase multicomponent (MM) fluid flow simulator

Considering a gas reservoir and injecting proposed fluid which consist of light alkanes requires MM fluid flow modeling in porous media. For this purpose, TMVOC which belongs to the family of famous TOUGH2 program is utilized. TMVOCMP is a numerical simulator for multi-phase (three-phase) multi-component non-isothermal flow of hydrocarbons; it has the capability to simulate multi-phase hydrocarbon flow. The three phases include water, non-condensable gases (NCG) and non-aqueous phase liquids (NAPLs). The flow behavior can be modelled for all combinations of three phases (Figure 3.4) including a maximum of 8 gases, 18 NAPLs and water. Since the effect of temperature and pressure are considered for determining the fluid properties. And parameters such as saturation, relative permeability, viscosity, density, specific enthalpy, capillary pressure, and diffusion for every phase are considered and updated at each successful Newton-Raphson iteration, the appearance and disappearance of phases and components in different phases is modeled with reasonable accuracy. Therefore, fluid flow modeling of volatile organic chemicals (VOCs) in the presence of formation gases and water using the concept of three-phase relative permeability is possible considering isothermal and non-isothermal conditions. The light alkanes discussed earlier as proposed fluids can be modelled using the 'CHEMP' section in the TMVOC infile as a third fluid phase as NAPLs (Pruess et al., 1999; Pruess and Battistelli, 2002).

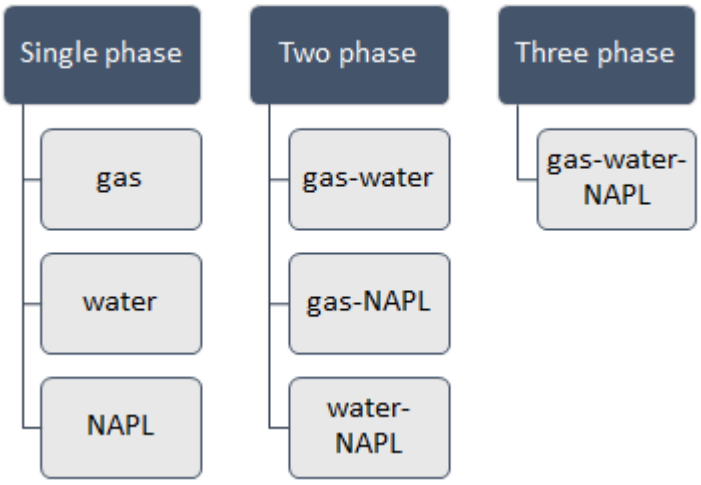

Figure 3.4: single, two and three phase fluid flow modeling options in TMVOCMP.

In order to be able to simulate the behavior of proposed fluid in porous media, the properties of utilized fluid need to be provided to the CHEMP section of TMVOC infile after initiating the number of components to be used in a particular simulation. The non-condensable gases (NCG) are predefined therefore, their names only need to be mentioned as components. However, for defining the proposed fluid, properties are summarized in the following Table 3.3 (API, 2016; Poling et al., 2001; Pruess and

Battistelli, 2002; Reid et al., 1987). Whereas Table 3.4 provides details of numbered properties in Table 3.3.

Table 3.3: proposed fluid properties to be used in infile of TMVOC.

Properties	**n-pentane**	**n-hexane**	**n-heptane**	**n-octane**	**n-nonane**	**n-decane**
C_nH_{2n+2}	C_5H_{12}	C_6H_{14}	C_7H_{16}	C_8H_{18}	C_9H_{20}	$C_{10}H_{22}$
1	469.7	507.6	540.2	568.7	594.6	617.7
2	33.7	30.25	27.4	24.9	22.9	21.1
3	0.268	0.264	0.261	0.259	0.257	0.256
4	0.252	0.3	0.35	0.399	0.445	0.49
5	309.22	341.88	371.57	398.82	423.97	447.3
6	-7.30698	-7.53998	-7.77404	-8.04937	-8.32886	-8.56523
7	1.53679	1.624944	1.713098	1.801252	1.889404	1.97756
8	-3.08367	-3.63088	-4.17809	-4.72529	-5.2725	-5.81971
9	-1.02456	-0.87961	-0.73466	-0.58972	-0.44477	-0.29982
10	72.15	86.177	100.204	114.231	128.258	142.285
11	-3.63	-4.486	-5.342	-6.198	-7.054	-7.91
12	4.87E-01	0.5818	0.6766	0.7714	0.8662	9.61E-01
13	-2.58E-04	-3.12E-04	-3.66E-04	-4.21E-04	-4.75E-04	-5.29E-04
14	5.31E-08	6.51E-08	7.71E-08	8.90E-08	1.01E-07	1.13E-07
15	626	664.446	689.48	706.6	721.343	730
16	293	288.706	288.706	288.706	288.706	293
17	7.70E-06	8.16E-06	8.62E-06	9.08E-06	9.54E-06	1.00E-05
18	273.1	293	293	293	293	293
19	1.52	1.536	1.552	1.568	1.584	1.6
20	311	368	428	492	555	624
21	9.97E-08	1.56E-07	2.12E-07	2.68E-07	3.24E-07	3.80E-07
22	0.635	1.908	3.181	4.454	5.727	7

Table 3.4: details of fluid properties according to Table 3.3.

Property #	**Detail**
1	Critical temperature, K
2	Critical pressure, bar
3	Critical compressibility
4	Pitzer's acentric factor
5	Normal boiling point, K

6	Vapour pressure constant
7	Vapor pressure constant
8	Vapor pressure constant
9	Vapour pressure constant
10	Molecular weight, g/mole
11	Ideal gas heat capacity
12	Ideal gas heat capacity
13	Ideal gas heat capacity
14	Ideal gas heat capacity
15	Reference non-aqueous phase liquid (NAPL) density, kg/m^3
16	Reference temperature for density, K
17	Binary diffusivity of volatile oil component in air, m^2/sec
18	Reference temperature for gas diffusivity, K
19	Exponent for chemical diffusivity
20	Critical volume, $cm^3/mole$
21	Chemical solubility constant in water
22	Organic carbon partition coefficient, m^3/kg

The simulations can be performed for a variety of three phase combinations of fluids (Pruess and Battistelli, 2002). To investigate the behavior of fluid under reservoir conditions, a fictive model is utilized (Figure 3.5).

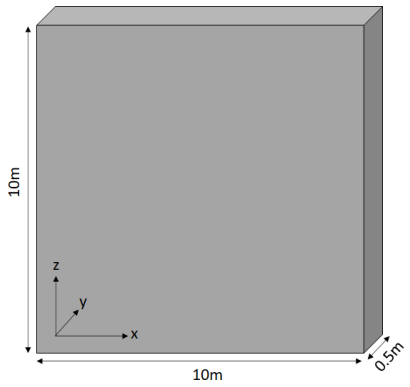

Figure 3.5: fictive model to observe phase behavior of light alkanes.

The model is given a small y-dimension of 0.5 m as the width of hydraulic fracture is generally small. The properties of the fictive model can be found in Table 3.5. There are 4 grid-blocks per meter in the x-direction and in the z-direction 2 grid blocks per meter. Whereas these grid-blocks have a width of 0.5 m which is in y-direction. As can be observed from Figure 3.1 and Figure 3.2, for the fluid mixture to change phase higher reservoir temperature and lower pressure are required. Therefore, model is given

a temperature of 425 K as the boiling points of mixture components i.e., n-pentane to n-decane, range from 339 K to 447 K. Generally, the pressure is lowered using nitrogen lift at the end of hydraulic fracturing operation for fracture cleanup and flowback of injected fluid to start reservoir fluid production. So, a special scenario of 420 KPa pressure is considered. However, it should be noted that not all the fluid components will change their phase to gas under these conditions.

Table 3.5: properties of fictive model.

Number of grid blocks (xyz)	40×1×20 = 800
Reservoir fluid	Gas (methane 95 %, ethane 5 %)
Porosity	35 %
Permeability	1.0×10^{-14} m^2

Considering the reservoir to be at its initial state with reservoir gases, 97.2 kg of proposed fluid mixture is injected at an injection rate of 2.7×10^{-3} kg/sec. The fluid is injected at a lower rate and no fracturing is considered. After the injection duration of ten hours, the fluid remains in the reservoir and changes its phase under reservoir conditions. The simulation is continued until fifteen days without production. The results of the simulation are presented in the next sections.

3.2.2 Phase behavior of alternative fluid in porous media

The initial density of reservoir fluid i.e., gas at reservoir conditions is only 1.98 kg/m^3. Then the proposed fluid is injected. The proposed fluid occurs in liquid state at standard conditions of temperature and pressure. The injection fluid, which is a mixture of light alkanes, at the considered reservoir conditions will change its phase from liquid to gas. The change to gaseous phase increases the gas phase density. Since only 97 kg of fluid is injected, therefore it remains in the near injection zone. The lighter components of the fluid preferentially change to gaseous phase. Hence the gas phase density increases from its initial value of 1.98 kg/m^3 to 15.56 kg/m^3 in the near injection zone. The change in density in the zones where the fluid has reached can be observed from Figure 3.6 at different times.

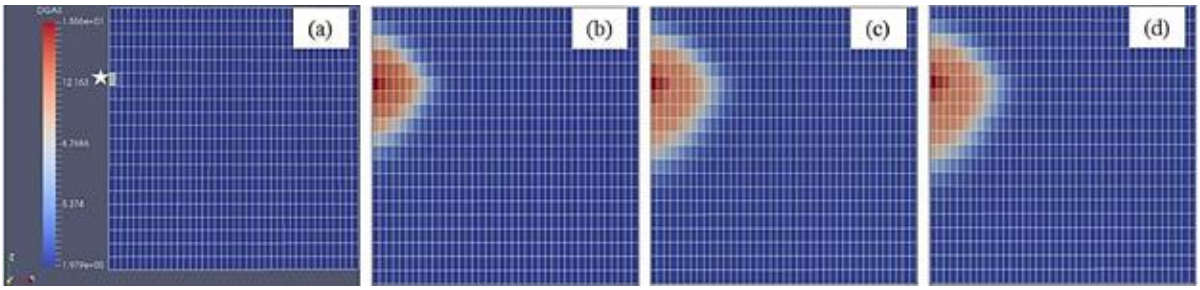

Figure 3.6: change in gas phase density (in the near injection zone) due to phase change of proposed fluid (DGAS: gas density), star shows injection zone, (a) beginning of injection, (b) end of injection, (c) 7 days (d) 15 days (Hou and Mehmood, 2018).

Initially, the reservoir contains only the gaseous phase. However, the injection of light alkanes will reduce the gas saturations in the zones they reach initially. This will increase the liquid saturation in the near injection zones. Due to higher reservoir temperature, the heat transfer from reservoir to fluid will increase the temperature of injected fluid. The components in the fluid mixture will start to change to gaseous phase as the fluid temperature rises and their boiling points reach. Therefore, the gas phase saturation once again increases due to injected fluid vaporization. This will automatically decrease the liquid phase saturation in the nearby zones of injection. The zones away from injection are not affected as the light alkanes did not reach that far. The gas phase saturation reduced initially from 100% to less than 10% initially and then increased again to more than 50% in the injection zone showing phase change (Figure 3.7a-d). Similarly, the liquid phase saturation decreased from higher saturations of 70%-90% to between 25% to 50% in the regions reached by injected fluid (Figure 3.8a-d).

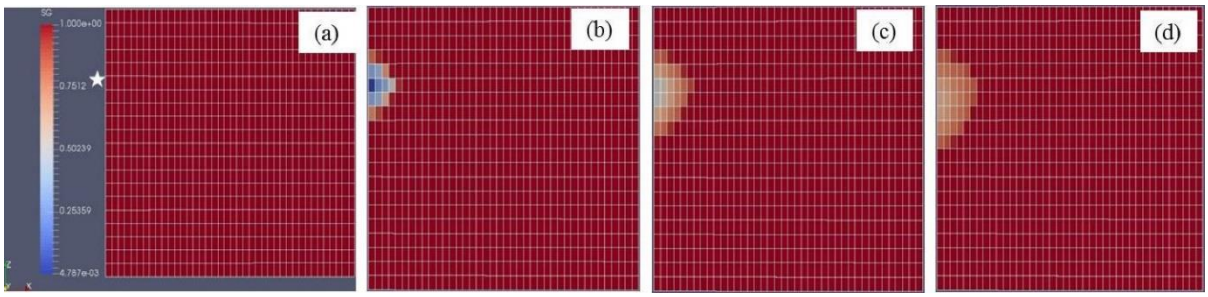

Figure 3.7: variation in gas phase saturation due to injection and vaporization of injected alternative fluid (SG: gas phase saturation), star shows injection zone, (a) beginning of injection, (b) end of injection, (c) 7 days (d) 15 days (Hou and Mehmood, 2018).

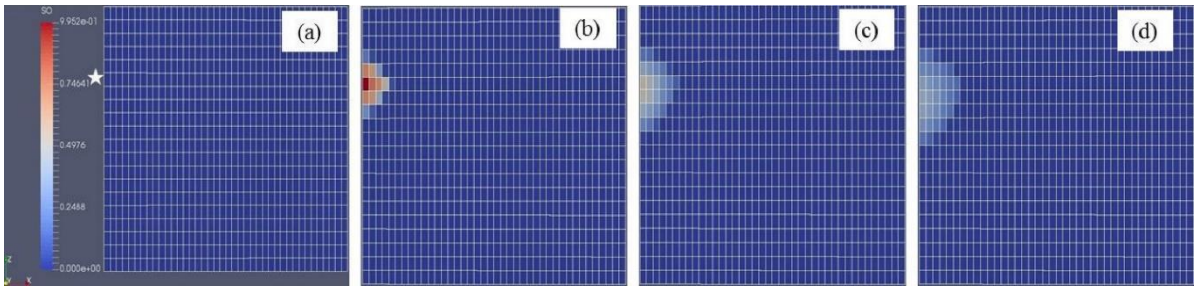

Figure 3.8: variation in saturation of injected fluid at different times (SO: liquid phase saturation), star shows injection zone, (a) beginning of injection, (b) end of injection, (c) 7 days (d) 15 days (Hou and Mehmood, 2018).

The results in terms of injected fluid individual component mole fractions in gaseous and liquid phase can be observed from Figure 3.9 and Figure 3.10. As is obvious from light alkanes properties from Table 3.1, the lighter fluid i.e., n-pentane shows the maximum phase change and the heavier i.e., n-decane undergoes minimum phase change since the reservoir temperature is still below its boiling point. As the fluid temperature rises, n-pentane is the first to vaporize as its boiling point is only 309.22 K. Therefore, a variety of injection fluid combinations or individual fluid component can be utilized for hydraulic fracturing operation based upon reservoir conditions.

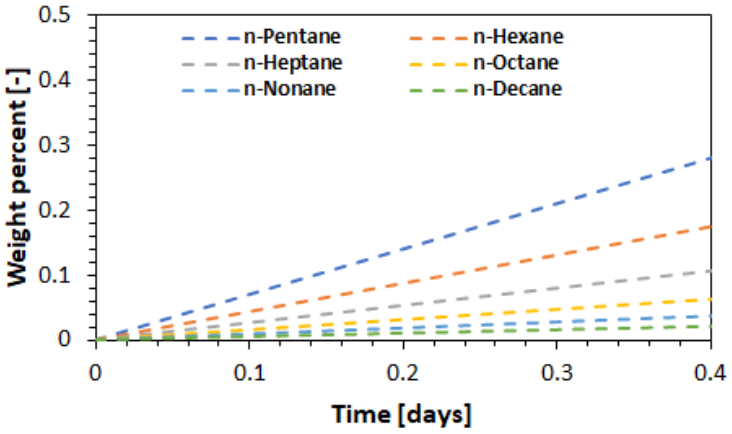

Figure 3.9: rise in the weight percent of injected fluid in gaseous phase due to phase change.

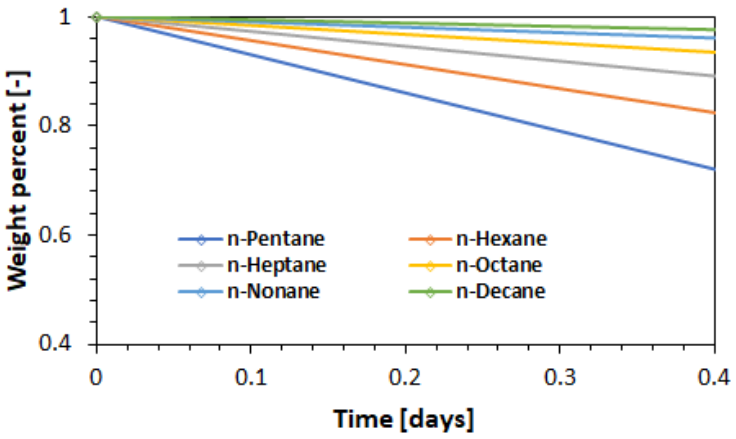

Figure 3.10: decline in weight percent of light alkanes in liquid phase due to phase change to gas.

As the reservoir pressure and temperature conditions do not reflect the single-phase gaseous conditions according to Figure 3.1, therefore complete phase change of fluid cannot be achieved. The results indicate that fluid flow behavior with the appearance and disappearance of components in different phases can be modeled with TMVOC.

Where the reservoir temperature is up to 373 K, lighter fluids such as n-pentane, n-hexane and n-heptane can be utilized. For reservoirs having a temperature around 423 K, n-heptane and n-octane can be used and similarly for reservoirs having temperatures of around 473 K, heavier components of proposed fluid can be used. The phase change and density and viscosity reduction can help in quicker flowback of fluid after the fracturing operation which will help in achieving good fracture cleanup, quick fracture closure and early start of reservoir fluid production. The lower density and phase change will help in efficient fracture cleanup. Since the viscosity of proposed fluid is low, the fluid leakoff will result in quick fracture closure and better proppant placement especially in the upper half of fracture. The difference of boiling point between the lightest component i.e., n-pentane and methane through propane is huge. Therefore, the fluid can be separated at the surface and reused for subsequent fracturing operation for

better economics. The use of proposed fluid will not only address technical issues but will also reduce environmental hazards associated with water-based fluids.

To achieve aforementioned advantages, n-heptane is utilized as alternative frac-fluid for case studies in this work. The phase behavior of n-heptane can be observed from Figure 3.11.

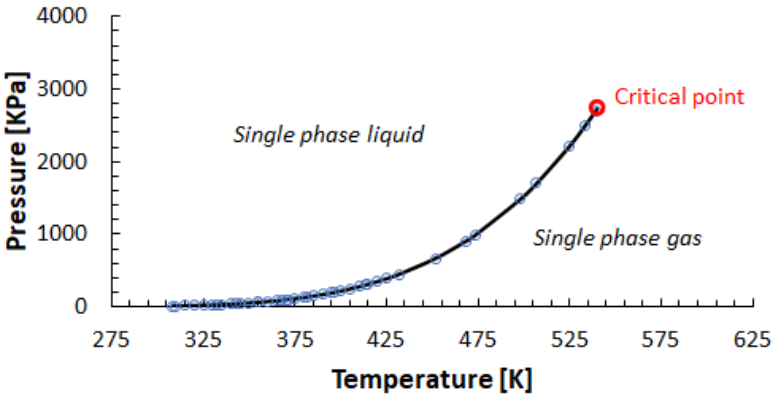

Figure 3.11: phase behavior of n-heptane.

The density of n-heptane at standard pressure of 101352.9 Pa and 288.706 K is 689.48 kg/m^3, which is considerably lower than water and higher than gas-based fluids. The viscosity at 101352.9 Pa and 311 K is 0.348 mPa.s. The application of n-heptane in tight gas reservoirs is also advantageous in terms of injected fluid separation from reservoir gas at the surface. The boiling point of n-heptane is 371.57 K which is much higher than boiling point of reservoir gases such as methane and ethane. The viscosity variation of fluid as a function of temperature is plotted in Figure 3.12 according to API (Equation (3.11) and TMVOC (Equation (3.12)) (API, 2016; Poling et al., 2001; Pruess and Battistelli, 2002).

$$ln\mu_{iT} = A' + \frac{B'}{T} \qquad (3.12)$$

Where T: temperature [K]; A', B': constants.

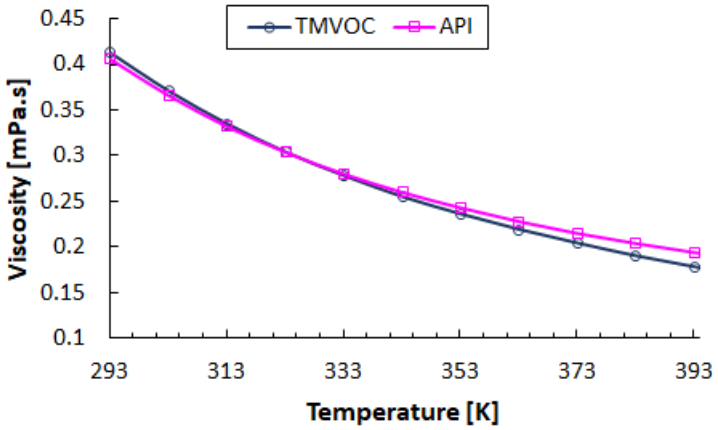

Figure 3.12: decline in n-heptane viscosity with increase in temperature.

4 Hydraulic fracture modeling

Numerical modelling is used to investigate the potential application of this innovative waterless light-alkanes fracking fluid. Therefore, fracture model, MM flow model and gelled fluid proppant transport model are implemented in FLAC3D^{plus}-TMVOCMP framework (Gou et al., 2015). The mechanical simulation is performed by full 3D thermo-hydro-mechanical (THM) coupled FLAC3D^{plus} which is an in-house upgraded version of FLAC3D (Itasca, 2009). Whereas MM flow simulation is performed by TMVOCMP which has been discussed in section 3.2.1.

FLAC3D (Fast Lagrangian analysis of continua in 3D) is a numerical modeling software which utilizes explicit finite volume method to solve wide variety of geotechnical problems. Since, FLAC3D is based upon continuum mechanics, a new numerical 3D-model based upon tensile fracture (discontinuous media) criterion in the presence of 3D stress state and hydromechanical coupling between fracture and matrix was developed (Zhou and Hou, 2013). The effects of stress redistribution after the tensile failure and fluid leak-off to matrix were all numerically modelled. To model proppant through gelled fluid, the solid-liquid two phase flow in the fracture was integrated based upon proppant concentration, shear rate, fluid viscosity, proppant and fluid densities etc. (Zhou et al., 2014). These developed models for incompressible fluid were integrated into FLAC3D. The effect of reservoir heterogeneity on fracture orientation was also investigated in tight gas reservoirs using XFEM and FVM (Zhou et al., 2015). To numerically study the heat transport in the fracture and heat exchange between the fracture and formation, a new thermal module was added to FLAC3D (Feng et al., 2016). To model the THM processes in a MM flow environment, two well established numerical simulators FLAC3D and TOUGH2 were coupled to exchange data with non-linear coupling functions (Rutqvist, 2011; Rutqvist et al., 2002). TOUGH2 is a numerical simulator with a number of different equations of states to solve different non-isothermal MM flow problems (Pruess et al., 1999). The in-house upgraded version of FLAC3D called FLAC3d^{plus} was then coupled with TOUGH2MP to model hydraulic fracturing in different reservoirs (Gou et al., 2015; Li et al., 2018).

In the next sections, a brief background of fracture mechanics is discussed before the numerical modeling.

4.1 Brief overview of hydraulic fracturing

The fracture propagation models generally utilize the concept of linear elasticity and plane state of strain. Elastic modulus is the most important parameter in linear elastic models which influences the fracture geometry and thus net pressure. Another important parameter is the Poisson's ratio which can be defined as the ratio of longitudinal to axial (transverse) strain. Experimental testing of representative core samples of formations through uniaxial or triaxial also known as static testing are considered the most reliable. Although log-derived or ultrasound testing of samples known as dynamic testing are also

performed to find these elastic parameters. In triaxial testing, axial loading and confining pressure are applied to the samples in a Hoek cell. The resulting strain/deformation against the triaxial stress condition is measured for different stress cycles by varying the confining stress. From the experimental results, elastic modulus and Poisson's ratio can be determined. In case of heterogenous formations, a reasonable number of samples should be tested from different depths so that reliable approximations can be made. In addition, cohesion and friction angle can also be determined from triaxial testing. When stress is applied on a material, it deforms initially in the elastic region. The material regains its original shape if stress is removed in the elastic region. However, if stress application is continued, the material goes into plastic deformation which means that it will not regain its initial shape after the removal of stress. A typical stress strain curve can be observed from Figure 4.1 (Economides and Nolte, 2000; Fjær et al., 1992a).

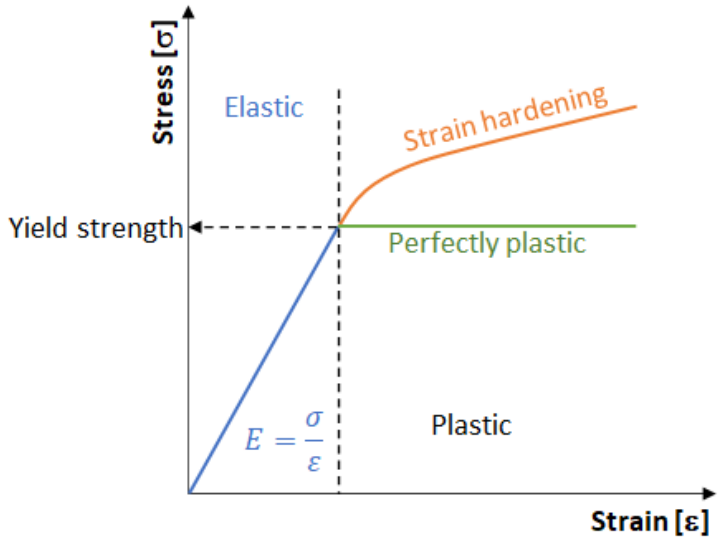

Figure 4.1:stress-strain behavior of ductile materials.

4.1.1 Fracture initiation and propagation

The splitting of the rock due to tensile failure is caused when the rise in injected fluid pressure exceeds the combined effect of smallest principal stress and tensile strength. The fracture propagates perpendicular to the least principal stress which generally is the minimum horizontal stress leading to vertical fracture. Considering the pore pressure in the formation, and compressive stress to be positive, the failure criteria therefore can be explained as:

$$Stress_{minimum} - Pressure_{fracture} < -Tensile_{strength}$$

Therefore, the pore pressure should increase to a level where it is more than the combined effect of normal stress and tensile strength of rock (Economides and Nolte, 2000; Fjær et al., 1992b). The tensile failure criteria is expressed by Equation (4.1)

$$f_t = P_m - \sigma_n - \sigma_t \quad (4.1)$$

Where, f_t: tensile criterion of hydraulic fracturing; σ_n is normal stress [Pa]; σ_t is tensile strength [Pa]; P_m: pore pressure in rock formation [Pa].

Initially the fluid is compressed in the borehole which then leads to fracture initiation reaching the peak pressure (Figure 4.2) (Fjaer et al., 1992). The pressure drops after fracture initiation due to unstable fracture growth which after continuous injection becomes stable. The pressure during this phase also steadies. Once the fracture is created, the tensile strength of the rock can be ignored for refracturing since a crack already exists. Mohr failure is another criterion which is based upon shear failure of formation as expressed by the following Equation (4.2) (Fjær et al., 1992c; Fjær et al., 2008).

$$f_m = N_\emptyset \sigma_3 + 2c\sqrt{\frac{1+sin\emptyset}{1-sin\emptyset}} \quad (4.2)$$

Where, f_m: Mohr failure criterion; $N_\emptyset$: triaxial factor $N_\emptyset = \frac{1+sin\emptyset}{1-sin\emptyset}$; c: cohesion.

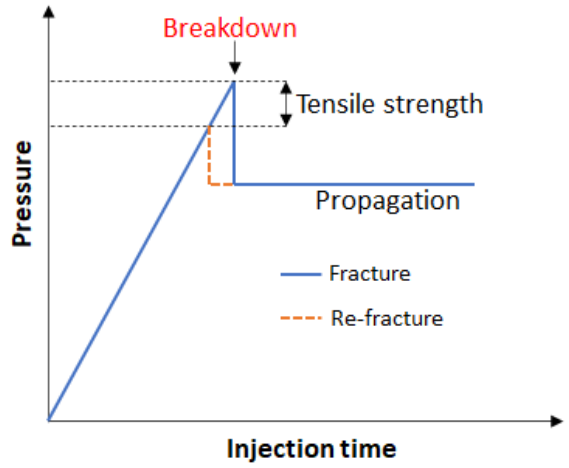

Figure 4.2: bottomhole pressure response for fracture initiation and propagation in impermeable rock.

4.1.2 Fracture orientation

The direction of fracture propagation is greatly stress dependent. Therefore, it is important to identify the in-situ stresses. The vertical stress also known as overburden stress is usually the maximum stress due to the weight of overlying rocks. Whereas two more stresses exist in the horizontal directions which in the absence of tectonic stresses are equal. Generally, the existence of tectonic stresses, folding and faulting make one stress bigger than the other, so they are defined as minimum and maximum horizontal stress. The in-situ stress condition can be defined according to fault regimes categorized as normal fault, thrust fault and strike-slip fault. The three discussed stresses vary in magnitude in these fault regimes. For the normal fault case vertical stress is the maximum stress. Thrust fault represents stress state opposite to normal fault. While strike-slip fault is generated when the magnitude of vertical stress is

lower than maximum horizontal stress but greater than minimum horizontal stress. The discussed fault regimes can be further understood with the help of Figure 4.3. Two other stress states may also exist: one of them is the lithostatic stress state where all the stresses are equal such as those encountered in salt formations, and the other one represents equal horizontal stresses with maximum principal stress as the overburden stress (Li, 2018).

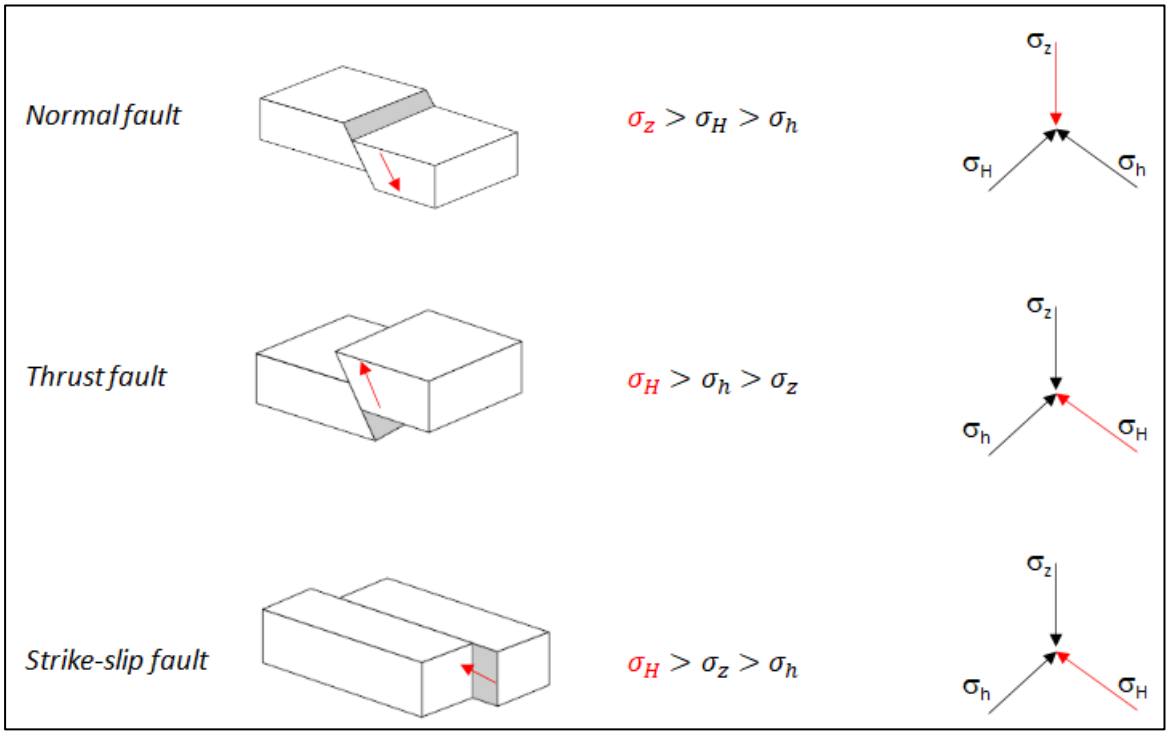

Figure 4.3: fault regimes and direction of in-situ stresses with qualitative stress magnitudes (modified from (Economides and Nolte, 2000)).

As discussed earlier, fracture propagates perpendicular to the least principal stress. Therefore, a vertical fracture is created in a vertical well when

$$\sigma_z > \sigma_H > \sigma_h$$

where σ_z: *vertical stress;* σ_H: *maximum horizontal stress and* σ_h: *minimum horizontal stress.*

But for horizontal wellbores, the situation is more complicated. Considering the normal stress distribution and wellbore along maximum or minimum horizontal stress fracture parallel or perpendicular to the wellbore can be created. If the wellbore is drilled along maximum horizontal stress, the minimum in-situ stress is perpendicular to the horizontal borehole and a corresponding parallel vertical fracture can be created. On the other hand, horizontal borehole along minimum horizontal stress will result in transverse fractures. Figure 4.4 shows different fracture orientations for vertical and horizontal boreholes. As can be observed from Figure 4.4b, drilling a well along maximum horizontal stress direction results in longitudinal fractures. Therefore, it is better to drill along minimum principal stress direction to create more transverse fractures along the same wellbore length leading to higher

stimulated reservoir volume (SRV). It should be noted that in-situ stress in the order of $\sigma_z > \sigma_H > \sigma_h$ is considered for Figure 4.4. Non-alignment of borehole with any of the principal stress direction further complicates the situation in horizontal boreholes (Fjær et al., 1992b; Fjær et al.,2008).

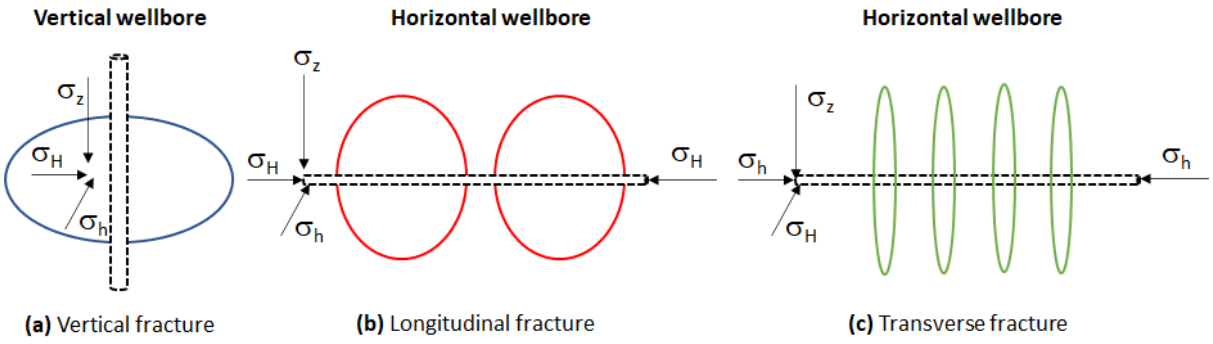

Figure 4.4: idealized fracture orientation for vertical and horizontal boreholes.

4.1.3 Fracture confinement

The difference in in-situ stresses especially horizontal stresses in different formations play a major role for fracture confinement. The vertical stress also called the overburden stress generally increases with depth; the horizontal stresses also depend upon the lithology. For instance, in rock salt the horizontal stresses can reach the lithostatic stress. On the other hand, sandstones have shown lower horizontal stresses compared to rock salt or clay stones. Fracture confinement in a single layer or propagation to other layers is also affected by properties such as rock strength and elastic parameters. The fracture is normally confined to a layer when the over and underlying layers have a sufficient stress contrast to the fractured formation. However, if the pressure rises above the minimum horizontal stress in confining layers, the fracture propagates into them.

Once the fracture is initiated, the pressure requirement is based upon keeping the fracture open, fluid flow in the fracture and the resistance at the fracture tip. Therefore, as the fracture length increases, the pressure requirements may increase. If a fracture is contained between confining layers, continued injection increases fracture width in addition to half-length. The injection pressure requirements are also not only highly dependent upon injection fluid properties such as viscosity, density, injection rate etc. but also on the proppant properties such as proppant density, size, concentration etc. In the case of pre-mature tip screen out, the pressure rises beyond the normal extension pressure. On the contrary, the fracture extension in zones of lower horizontal stress reduce the injection pressure requirements and fracture propagates easily (Fjær et al., 1992b; Fjær et al.,2008).

4.1.4 Fracture closure

Once the pressure in fracture is reduced below the minimum principal stress, it starts to close. Generally, this minimum principal stress can be considered as the closure stress. The closure stress can be estimated from shutin tests, flowback tests or mini-frac tests etc. it is important to note that fracture closure is not instantaneous. For shutin tests, the instantaneous shutin pressure can be considered as the upper limit of closure stress. Therefore, it should be determined by waiting until the fracture closure, ideally. Fluid and formation properties can have significant effect upon waiting time. In the case of flowback testing, fluid is injected at fracturing pressure and then flowed back until closure (Fjær et al., 1992b; Fjær et al.,2008).

4.1.5 Proppants

In hydraulic fracturing, once the injection is stopped, the pressure inside the fracture starts to decrease as the fluid leaks off to the formation. When the fracture pressure becomes lower than the minimum horizontal stress, it starts to close. To avoid complete fracture closure in hydraulic fracturing, proppants are transported into the fracture. They are used according to the fracture design and formation properties. Hydraulic fracturing can be divided into two stages i.e., pad stage and slurry stage. In the pad stage frac-fluid is injected without the proppants to initiate and extend the fracture. whereas in the slurry stage, proppant carrying slurry is injected. The slurries are designed according to the proppant properties such as density so that proppants can be transported till the fracture tip. The size of proppant depends upon the fracture aperture and should be 2-3 times less than the fracture width to avoid premature tip screen out. Although higher diameter proppants offer higher permeabilities but as the proppant size increases, the crush resistance decreases. Therefore, an important parameter for proppant design is the closure stress and proppants should have higher strength to avoid crushing. Generally, with increase in proppant strength, the proppant density also increases. Therefore, closure stress, fracture width, proppant size and density can be considered as most important parameters. Some of the commonly used proppants according to their strength are presented in Figure 4.5 (Liang et al., 2016).

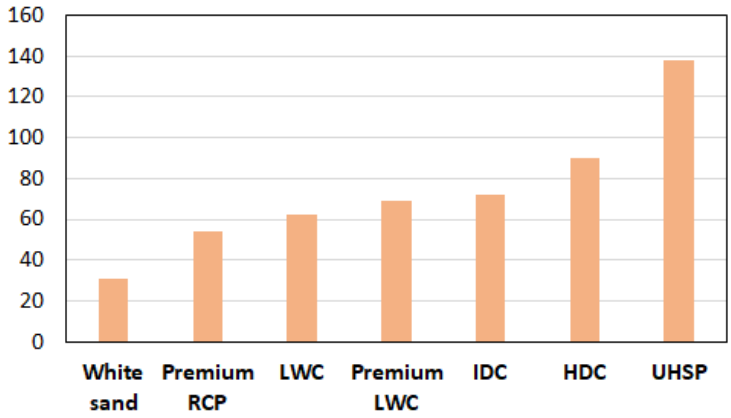

Figure 4.5: conductivity of 1750 md-ft for different proppants at corresponding stress [MPa]. RCP: resin coated proppant; LWC: light weight ceramic; IDC: intermediate density ceramic; HDC: high density ceramic; UHSP: ultra-high strength proppant (modified from (Liang et al., 2016)).

The higher density proppants fall to the bottom of the fracture especially when the gel breaks. This can lead to proppant settling at the bottom of fracture depriving the upper section of fracture of proppants. It can result in loss of hydraulic connection between fracture and injection level or perforations. Therefore, the fracture closes near the perforations leading to poor fracture job. Light weight proppants with suitable strength can solve this issue and due to lower density. Lower viscosity fluid may be required for transporting light weight proppants compared to higher density proppants. Resultantly, injection pressure requirements will be lowered. Figure 4.6 summarizes some information about light weight proppants (Bestaoui-Spurr and Li, 2018; Denney, 2012; Han et al., 2016; Jardim Neto et al., 2012; Liang et al., 2016; Myers et al., 2004; Parker et al., 2012; Rickards et al., 2006).

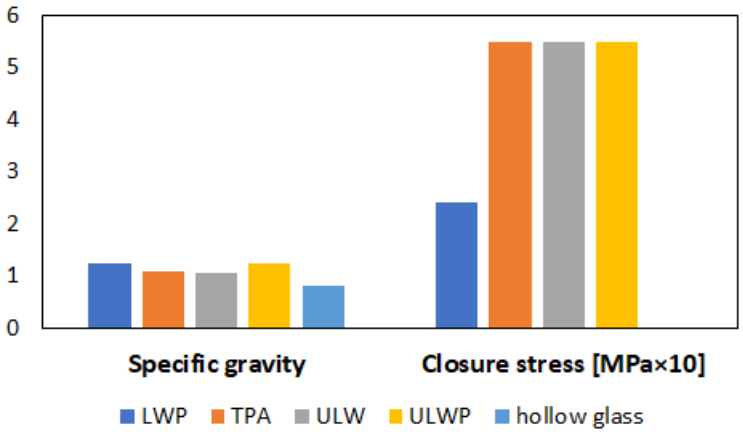

Figure 4.6: specific gravity and closure stress of some light-weight proppants. ULWP: ultra-light weight proppants; ULW: ultra-light weight; TPA: thermoplastic alloy; LWP: light weight proppant.

4.2 Mass and energy balance for flow in porous media

For MM flow of fluid in the pores, TMVOC formulation of popular TOUGH2 code is utilized (Pruess and Batistelli, 2002). The mass conservation for different components and phases can be written as:

$$\frac{\partial M^{\kappa}}{\partial t} = -\vec{\nabla} \cdot \left(\sum_{\beta} \vec{F}_{\beta} x_{\beta}^{\kappa} \right) + q^{\kappa} \qquad (4.3)$$

Where, M^{κ}: Mass accumulation term for component k; F: mass or heat flux; β: liquid/gas/NAPL phase; x_{β}^{κ}: component k's mole fraction in phase β; q: source or sink.

Therefore, the mass of a component *k* includes its share from all the phases in which it is present. Mass accumulation for formation (matrix) for different phases in the reservoir (water/gas) is based upon the following relation:

$$M^{\kappa} = \phi \sum_{\beta} S_{\beta} \rho_{\beta} x_{\beta}^{\kappa} \qquad (4.4)$$

Where, ϕ: porosity [-]; S_{β}: saturation of phase β [-]; ρ_{β}: density of phase β [mole/m^3].

For volatile oil components (VOC)/non-aqueous phase liquids (NAPL), sorption on the solid grains is also included as:

$$M^{\kappa} = \phi \sum_{\beta} S_{\beta} \rho_{\beta} x_{\beta}^{\kappa} + (1 - \emptyset) \sigma_r \sigma_w x_w^k k_d \qquad (4.5)$$

In this case, σ_r is the rock density; σ_w: is the water density; x_w^k: is the mole fraction of VOC in aqueous phase, and k_d: represents distribution coefficient for aqueous phase.

The fluid flow is governed by the Darcy's law. Therefore, the total flux is a sum of fluid flow of all the phases given by Equation (4.6).

$$F^k = \sum\nolimits_{\beta} x_{\beta}^k F_{\beta} \qquad (4.6)$$

Here, the fluid flow in terms of Darcy's law is given by:

$$\vec{F}_{\beta} = -k \frac{k_{r\beta} \rho_{\beta}}{\mu_{\beta}} \left(\vec{\nabla} P_{\beta} - \rho_{\beta} \vec{g} \right) \qquad (4.7)$$

where, k: absolute permeability [m^2]; $k_{r\beta}$: phase β relative permeability [-]; μ_{β}: phase β viscosity [Pa.s]; P_{β}: phase β fluid pressure and the capillary pressure [pa]; g: gravitational acceleration vector [m/s^2].

The above relation can be written as product of velocity and density as:

$$\vec{F}_{\beta} = \rho_{\beta} u_{\beta} = -k \frac{k_{r\beta} \rho_{\beta}}{\mu_{\beta}} \left(\vec{\nabla} P_{\beta} - \rho_{\beta} \vec{g} \right) \qquad (4.8)$$

Relative permeability and capillary pressure determination are of prime importance for fluid flow in the porous media. The relative permeability ranging between 0-1 determines the flowing ability of a fluid in the presence of other fluids. Whereas capillary pressure is the pressure between fluids arising due to

their interactions with the walls of porous media. TOUGH2MP has built in relative permeability and capillary pressure functions, one such function is the relative permeability and capillary pressure functions of Van Genuchten- Mualem for two-phase liquid-gas system (Genuchten, 1980; Mualem, 1976; Pruess et al., 1999).

$$k_{rl} = \sqrt{\frac{(S_l - S_{lr})}{(S_{ls} - S_{lr})}} \left\{ 1 - \left[1 - \left(\frac{(S_l - S_{lr})}{(S_{ls} - S_{lr})} \right)^{\frac{n}{n-1}} \right]^{1-\frac{1}{n}} \right\}^2 \quad (4.9)$$

If $S_{gr} = 0$, then $k_{rg} = 1 - k_{rl}$

If $S_{gr} > 0$, then according to Brooks and Corey (Brooks and Corey, 1964)

$$k_{rg} = \left[1 - \left(\frac{S_l - S_{lr}}{1 - S_{lr} - S_{gr}} \right) \right]^2 \left[1 - \left(\frac{S_l - S_{lr}}{1 - S_{lr} - S_{gr}} \right)^2 \right] \quad (4.10)$$

And the capillary pressure for two phase system is found as (Genuchten, 1980)

$$P_{cp} = -P_o \left[\left(\frac{(S_l - S_{lr})}{(S_{ls} - S_{lr})} \right)^{-\frac{n}{n-1}} - 1 \right]^{-\frac{1}{n}} \quad (4.11)$$

Where, k_{rl}: liquid phase relative permeability; k_{rg}: gas phase relative permeability; S_l: liquid saturation; S_{lr}: residual liquid saturation; S_{gr}: residual gas saturation; n: constant; P_{cp}: two phase capillary pressure.

For three-phase fluid flow where proposed fluid is injected in the presence of formation gas and water, three phase relative permeability is utilized. Modified version of Stone's relative permeability method is utilized in this work which is a built-in function in the TMVOC (Pruess and Battistelli, 2002; Stone, 1970).

$$k_{rg} = \left[\frac{S_g - S_{gr}}{1 - S_{wr}} \right]^n \quad (4.12)$$

$$k_{rw} = \left[\frac{S_w - S_{wr}}{1 - S_{wr}} \right]^n \quad (4.13)$$

$$k_{ra} = \left[\frac{1 - S_g - S_w - S_{ar}}{1 - S_g - S_{wr} - S_{ar}} \right] \left[\frac{1 - S_{wr} - S_{ar}}{1 - S_w - S_{ar}} \right] \left[\frac{(1 - S_g - S_{wr} - S_{ar})(1 - S_w)}{(1 - S_{wr})} \right]^n \quad (4.14)$$

The light alkaline saturation is defined as: $S_a = 1 - S_g - S_w$

For light alkane saturation near irreducible saturation, it is defined as: $S_{ar} \leq S_a \leq S_{ar} + 0.005$

And the relative permeability can be calculated as: $k'_{rn} = k_{rn} \frac{S_n - S_{nr}}{0.005}$

Where, k_{rg}: gas phase relative permeability; k_{rw}: water phase relative permeability; k_{ra}: alkane (n-heptane) phase relative permeability; S_g: gas phase saturation; S_w: water phase saturation; S_a: alkane (n-heptane) saturation; S_{gr}: irreducible gas saturation; S_{wr}: irreducible water saturation; S_{ar}: irreducible alkane (n-heptane) saturation.

Similarly, three phase capillary pressure function of Parker et al. (Parker et al., 1987; Pruess and Battistelli, 2002) is utilized to find the gas-alkane, alkane-water, gas-water capillary pressure.

$$P_{cga} = -\frac{\rho_w g}{\alpha_{ga}}\left[(\bar{S}_l)^{-1/n} - 1\right]^{1/m} \quad (4.15)$$

$$P_{cgw} = -\frac{\rho_w g}{\alpha_{aw}}\left[(\overline{S_w})^{-1/m} - 1\right]^{1/n} - \frac{\rho_w g}{\alpha_{ga}}\left[(\bar{S}_l)^{-1/m} - 1\right]^{1/n} \quad (4.16)$$

$$P_{caw} = P_{cgw} - P_{cga} \quad (4.17)$$

Where, $\overline{S_w} = \frac{(S_w - S_m)}{(1-S_m)}$, $\bar{S}_l = \frac{(S_w + S_n - S_m)}{(1-S_m)}$, $m = 1 - \frac{1}{n}$, P_{cga}: capillary pressure gas-light alkanes, P_{cgw}: capillary pressure gas-water.

The heat conservation is based upon conduction and convection. Conduction involves the internal energy exchange due to particle collisions and electron movement. The kinetic/potential energy is transferred between molecules in all phases. The heat conduction depends not only upon the temperature gradient but also on the conductive properties of the medium or the surface. Mathematically expressed as:

$$Heat\ conduction = -K_c \nabla T \quad (4.18)$$

Where, K_c: thermal conductivity [joule/°C/mole].

Convective heat transfer is the dominant means of heat transfer in fluids and involves the fluid motion as mechanism of heat transfer. It can be expressed as Equation (4.19):

$$Heat\ convection = \sum_{\beta} h_\beta\, \rho_\beta u_\beta = \sum_{\beta} h_\beta\, F_\beta \quad (4.19)$$

Therefore, total heat conservation can be defined based upon conduction and convection.

$$\frac{\delta M^h}{\delta t} = \nabla\left(-K_c \nabla T + \sum_{\beta} h_\beta\, F_\beta\right) + q \quad (4.20)$$

Whereas M^h: heat accumulation [joule/m^3]; q: source [joule/m^3/sec].

4.3 Space and time discretization

Solving the MM flow problems requires space discretization. Therefore, a model is divided into small discrete blocks and integral finite difference method is used for averaging. A discrete volume element (Vn) in the system is shown in Figure 4.7 bounded by closed surface Γ_n. The interface area between

blocks is represented by A. Therefore, surface integrals for mass or energy can be approximated by taking integral of Equation (4.3) as:

$$\int_{V_n} M^k \, dV_n = \int_{\Gamma n} F^k d\Gamma_n - \int_{V_n} q^k dV_n \tag{4.21}$$

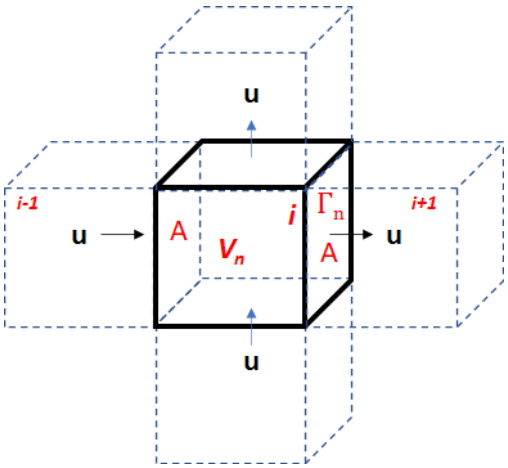

Figure 4.7: discrete element i in space discretization concept.

The time discretization for mass or energy conservation can be written in the form of first order partial differential equation. Applying the volume averages results in the following differential Equation (4.22) for the volume element Vn.

$$\frac{dM_n^k}{dt} = \frac{1}{V_n} \int_{\Gamma n} F^k d\Gamma_n + q^k \tag{4.22}$$

The solution of the above equation lies in solving the time as first order finite difference. Whereas the terms on the right side of the equation including flux and sink or source are evaluated at new time step t+Δt, known as fully implicit. At the new time step i.e., t+Δt, the unknown thermodynamic parameters express the flux and are explicitly defined in the resulting equations. Therefore, mass variation between the new and old time step can be explained as follows:

$$M_n^{k,t+\Delta t} - M_n^{k,t} = \frac{\Delta t}{V_n} \int_{\Gamma n} F^{k,t+\Delta t} d\Gamma_n + \Delta t q^{k,t+\Delta t} \tag{4.23}$$

The residuals equations are introduced to account for the change in quantities between new and old time steps. During the Newton-Raphson iterations, the residuals should remain below a certain defined limit for the successful completion of iteration and going to next time step until the completion of simulation. The residual for the component *k* can be found using Equation (4.24):

$$R_n^{k,t+\Delta t} = M_n^{k,t+\Delta t} - M_n^{k,t} - \frac{\Delta t}{V_n} \left[\sum_{\Gamma_n} F^{k,t+\Delta t} d\Gamma_n + V_n q_n^{k,t+\Delta t} \right] \tag{4.24}$$

4.4 Numerical model

4.4.1 Stress state

The stress tensor determines the stress state at a single point through three normal stresses and six shear stress in 3D space. The stresses in the directions of x, y and z-axis are denoted by σ_x, σ_y, and σ_z, respectively. Whereas the corresponding shear stresses can be written as τ_{xy}, τ_{yz} and τ_{zx}, respectively which have equal shear forces in the opposite direction. The stress tensor can be written in matrix form as in Equation (4.25) and presented in Figure 4.8 (Fjær et al., 1992a).

$$\begin{pmatrix} \sigma_x & \tau_{xy} & \tau_{xz} \\ \tau_{yx} & \sigma_y & \tau_{yz} \\ \tau_{zx} & \tau_{zy} & \sigma_z \end{pmatrix} \tag{4.25}$$

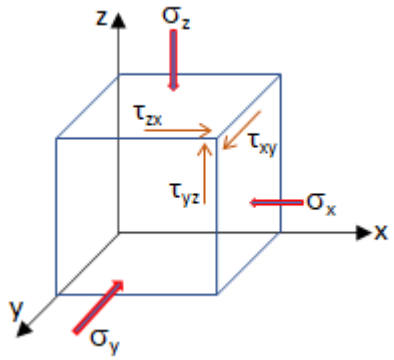

Figure 4.8: normal and shear stresses.

Where, σ_x, σ_y, and σ_z: normal stresses in three respective directions; τ_{xy}, τ_{yz} and τ_{zx}: shear stresses.

Due to application of stresses, displacements of u, v, and w are produced in x, y and z directions, respectively. Normal and shear strains are produced corresponding to the applied stresses as presented in Equation (4.26).

$$\begin{pmatrix} \varepsilon_x & \varepsilon_{xy} & \varepsilon_{xz} \\ \varepsilon_{yx} & \varepsilon_y & \varepsilon_{yz} \\ \varepsilon_{zx} & \varepsilon_{zy} & \varepsilon_z \end{pmatrix} \tag{4.26}$$

Where, $\varepsilon_x, \varepsilon_y \varepsilon_z$: normal strains; $\varepsilon_{xy,}$ ε_{yz}, ε_{zx}: shear strains.

There are total fifteen unknowns considering six stresses, six strains and three displacements. Therefore, three equations of equilibrium, six continuous condition geometric equations, and six equations of physical condition based upon Hook's law can help find these unknowns. Equilibrium condition based upon normal and shear stresses, and direction specific volume force is given by following equations:

$$\begin{cases} \dfrac{\partial \sigma_x}{\partial x} + \dfrac{\partial \tau_{xy}}{\partial y} + \dfrac{\partial \tau_{xz}}{\partial z} + V_{fx} = 0 \\ \dfrac{\partial \tau_{xy}}{\partial x} + \dfrac{\partial \sigma_y}{\partial y} + \dfrac{\partial \tau_{yz}}{\partial z} + V_{fy} = 0 \\ \dfrac{\partial \tau_{xz}}{\partial x} + \dfrac{\partial \tau_{yz}}{\partial y} + \dfrac{\partial \sigma_z}{\partial z} + V_{fz} = 0 \end{cases} \quad (4.27)$$

Where, x, y, z: co-ordinates, V_{fx}, V_{fy}, V_{fz}: volume forces.

The following geometry Equations (4.28) based upon the normal and shear strains define the continuous condition:

$$\begin{cases} \varepsilon_x = \dfrac{\partial u}{\partial x}, \quad \varepsilon_{xy} = \dfrac{1}{2}\left(\dfrac{\partial u}{\partial y} + \dfrac{\partial v}{\partial x}\right) \\ \varepsilon_y = \dfrac{\partial v}{\partial y}, \quad \varepsilon_{yz} = \dfrac{1}{2}\left(\dfrac{\partial w}{\partial y} + \dfrac{\partial v}{\partial z}\right) \\ \varepsilon_z = \dfrac{\partial w}{\partial z}, \quad \varepsilon_{xz} = \dfrac{1}{2}\left(\dfrac{\partial w}{\partial x} + \dfrac{\partial u}{\partial z}\right) \end{cases} \quad (4.28)$$

Where, u, v, w: displacements in x, y, z directions.

The constitutive equations relating stress and strain according to Hooke's law describe the strains as a function of stresses and material property i.e., elastic modulus and Poisson's ratio. The shear strains arising due to shear stress are described in terms of shear or rigidity modulus and expressed as Equation (4.29).

$$\begin{cases} \varepsilon_x = \dfrac{1}{E}\left[\sigma_x - \upsilon(\sigma_y + \sigma_z)\right], \quad \varepsilon_{xy} = \dfrac{\tau_{xy}}{G} \\ \varepsilon_y = \dfrac{1}{E}\left[\sigma_y - \upsilon(\sigma_x + \sigma_z)\right], \quad \varepsilon_{yz} = \dfrac{\tau_{yz}}{G} \\ \varepsilon_z = \dfrac{1}{E}\left[\sigma_z - \upsilon(\sigma_x + \sigma_y)\right], \quad \varepsilon_{zx} = \dfrac{\tau_{zx}}{G} \end{cases} \quad (4.29)$$

Where, $E: Young's modulus; v: Poisson's ratio.\ G\ (shear\ modulus): E/2(1+v)$.

4.4.2 Mechanical deformation

The changes in stress environment due to fluid injection or production are calculated by commercial FLAC3D software which uses finite difference method (FDM). However, since the fracture is a discontinuous media, therefore discontinuous displacement due to tensile failure needs to be modelled. The flow in the fracture can be considered between two parallel plates. Continued injection of fluid after fracture initiation leads to leakoff of fluid into the formation matrix from fracture. Therefore, the pressure in the fracture changes. A simple bi-wing fracture can be observed from Figure 4.9. Generally, the fracture width is more in the near injection zone which then reduces as the fracture propagates away from the wellbore. The fluid leakoff is a result of pressure difference between fracture and formation.

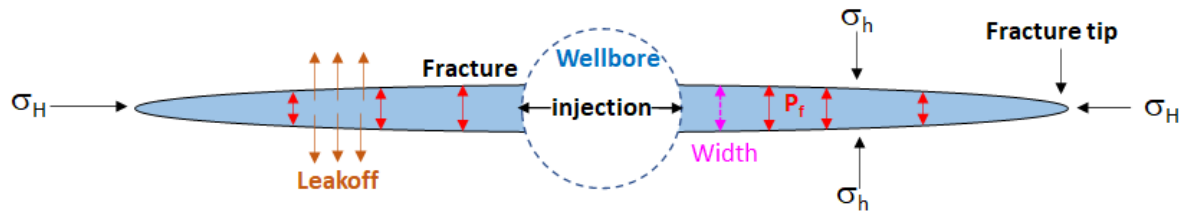

Figure 4.9: top view of a bi-wing fracture originating from wellbore.

In order to perform the mechanical calculations, FLAC3D^{plus} formulation is used which is based on the elasto-plasticity theory (Zhou and Hou, 2013, Zhou et al.,2014). In this regard, mainly the displacement increment in a time interval is determined by the solution of equation of motion (Equation (4.30)). The strain and stress increments can be determined using the continuum and constitutive equation (Equations (4.31) and (4.32)).

$$\sigma_{ij,j} + \rho(g_i - \frac{dv_i}{dt}) = 0 \qquad (4.30)$$

$$\Delta\varepsilon_{ij} = \frac{1}{2}(\Delta u_{i,j} + \Delta u_{j,i}) \qquad (4.31)$$

$$\Delta\sigma'_{ij} = D\Delta\varepsilon_{ij} \qquad (4.32)$$

where $\sigma = \sigma' - \alpha I P_m$, σ: stress [Pa]; ρ: density [kg/m³]; g_i: gravitational acceleration [m/s²]; v_i: velocity [m/s]; $\Delta\varepsilon$: strain increment [-]; $\Delta\sigma'$: effective stress increment [Pa]; α: Biot's-coefficient [-].

As the pressure inside the fracture changes, the fracture elements (residing in the host matrix elements) deform as a result. Hence, strain change perpendicular to fracture is induced. This strain change can be expressed as Equation (4.33)

$$\Delta\varepsilon_f = \frac{P_f(t+1) - \sigma_n(t)}{\alpha_1} \qquad (4.33)$$

Where, $\Delta\varepsilon_f$: normal strain increment of hydraulic fracture [dimensionless]; $\alpha_1 = K + 4G/3$; P_f: the pressure in fracture [Pa]; K: bulk modulus of rock [Pa]; G: shear modulus [Pa].

Considering the dimension of element perpendicular to the fracture small, the fracture width change can be expressed as follows

$$\Delta w = \frac{P_f(t+1) + \sigma_n(t)}{\alpha_1} l_c \qquad (4.34)$$

and

$$\Delta w = \Delta\varepsilon_f l_c \qquad (4.35)$$

Where Δw: fracture width increment [m]; l_c: zone length normal to fracture [m].

It implies that, if fracture pressure is higher than the normal stress, the width will increase. Conversely, the width will decrease. However, due to fracture surface roughness the width cannot be negative or zero. Therefore, it will remain higher than a residual width. In the case of propped fracture, the width will reduce until the fracture walls come in contact with the proppants, which requires the consideration of contact stress. The new strain increment then includes the current fracture pressure and previous step normal and contact stress. The contact stress only comes into effect once the fracture wall is in contact with the proppants (Equation (4.36)).

$$\Delta\varepsilon_f = \frac{P_f(t+1) + \sigma_{con}(t) + \sigma_n(t)}{\alpha_1} \tag{4.36}$$

Where,

$\sigma_{con}: contact\ stress \begin{cases} \sigma_{con}(t+1) = 0 & if\ \ C \leq 0.65\ and\ w \geq w_{res} \\ \sigma_{con}(t+1) = \sigma_{con}(t) + \alpha_1.\Delta\varepsilon_o & if\ \ C > 0.65\ and\ w < w_{res} \end{cases}$ [MPa];

$\Delta\varepsilon_o: over\ reduced\ strain\ [-]$

The new stress state on the host reservoir element due to width increment can be found from the following Equations (4.37) and (4.38):

$$\sigma_n(new) = \sigma_n(old) - \alpha_1\Delta\varepsilon_f \tag{4.37}$$

$$\sigma_{1,2}(new) = \sigma_{2,3}(old) - \alpha_2\Delta\varepsilon_f \tag{4.38}$$

Where $\sigma_{1,2}$: stress in other principal directions; α_2: material constant defined as $\alpha_2 = K - 2G/3$; and K, G: bulk and shear modulus, respectively.

4.4.3 Fracture propagation mechanism

As discussed earlier, if fracture pressure exceeds the normal stress and tensile strength of rock, the fracture propagates (Equation (4.39)). To model the propagation phenomenon, the elements are divided into fractured, partially fractured and unfractured elements (Figure 4.10). The tip element is further divided into sub-elements to increase accuracy. The tensile criterion as expressed by Equation (4.39) is satisfied for each sub-element. When adequate sub-elements are fractured, the whole element is converted and identified as fractured element. Then, the element next to the new fracture element becomes tip element and is divided into sub-elements. The process continues until the end of simulation.

$$P^{t+1} - \sigma_n^{t+1} > \sigma_{Tensile} \tag{4.39}$$

And, fraction of fractured element is given by, $F = \frac{no.of\ fractured\ sub\_elements}{total\ no.of\ sub\_elements}$

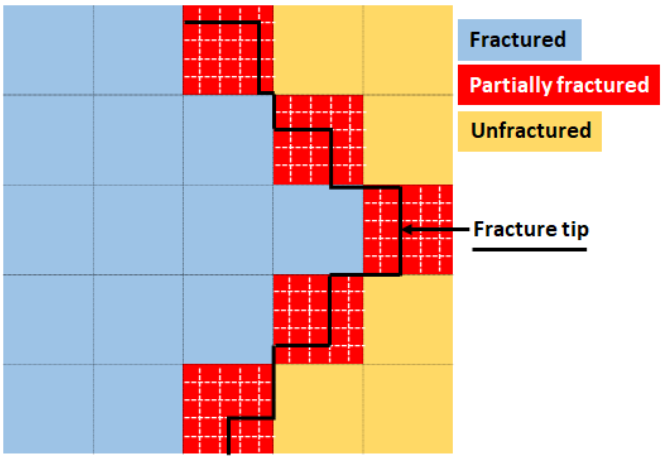

Figure 4.10: classification of different elements in the model based upon fractured, partially fractured and unfractured elements and fracture tip (Liao et al., 2019, Mehmood et al., 2021)).

4.4.4 MM fluid flow

The flow simulation can be characterized in three categories which include flow in fracture, flow exchange between fracture and matrix and matrix flow. The discrete elements are subdivided into matrix or reservoir elements and potential fracture elements. The matrix elements work as host elements for the fracture elements which bear separate identity. As discussed earlier, a discrete grid block is converted to fractured element when sufficient sub-elements in that element are fractured according to the tensile criteria. Darcy law governs the fluid flow in these elements, which can be written for a fluid phase β as:

$$\vec{F}_\beta = \rho_\beta u_\beta = -k\frac{k_{r\beta}\rho_\beta}{\mu_\beta}\left(\vec{\nabla}P_\beta - \rho_\beta \vec{g}\right) \tag{4.40}$$

In order to model flow of fluid in the matrix zones and fluid exchange between reservoir and fracture the average permeability of reservoir is used. However, for modeling the flow of fluid in the fracture elements, flow is considered between parallel plates i.e., walls of the fracture and permeability is approximated by the fracture width according to the following equation.

$$k = \frac{fw^2}{12} \tag{4.41}$$

Where, f: factor based on fracture roughness [-]; w: fracture width [m].

Since the simulation is to be carried out for compressible and incompressible fluids, the concept of mass conservation is utilized. For reservoir matrix element, it has already been discussed in section 4.2. However, for fracture elements, the mass conservation can be written by including the fracture width in Equation (4.42) as

$$F\frac{1}{w}\frac{\delta(wM^{k})}{\delta t} = -\vec{\nabla}\left(\sum_{\beta}\vec{u}_{\beta}x_{\beta}^{\kappa}\right) + q^{\kappa} \qquad (4.42)$$

Where, F: fraction of fractured sub-elements [-].

In the TOUGH2 code, Newton Raphson iterations are used to solve the mass conservation equation for all the components. The residual equation for any matrix element for a component *k* at new time step $t + \Delta t$ can be written as

$$R_{n}^{\kappa,t+\Delta t} = M_{n}^{\kappa,\,t+\Delta t} - M_{n}^{\kappa,\,t} - \frac{\Delta t}{V_{n}}\sum_{m} A_{nm}F_{nm}^{\kappa,t+\Delta t} + \Delta t q_{n}^{\kappa,t+\Delta t} = 0 \qquad (4.43)$$

Including the width of fracture element (*w*) and fraction of fractured element (*F*), the residual equation for fracture element at time $t + \Delta t$ is given by Equation (4.44)

$$R_{n}^{\kappa,\;t+\Delta t} = (FwM)_{n}^{\kappa,\;t+\Delta t} - (FwM)_{n}^{\kappa,\,t} - \frac{\Delta t}{A_{n}}\sum_{m} A_{nm}F_{nm}^{\kappa,t+\Delta t} + \Delta t w^{t+\Delta t} q_{n}^{\kappa,t+\Delta t} = 0 \qquad (4.44)$$

Once the residual equations for each component are solved and convergence takes place within the provided limits, the primary parameters such as pressure, temperature, component fraction in different phases etc. are updated. The simulation then continues for new time step until the end of simulation.

4.4.5 Proppant transport in fracture

In hydraulic fracturing, the injection of proppants to keep the fracture open is of paramount importance. As discussed earlier, the proppant properties are dependent upon stress state, formation properties, fracture aperture etc. Based upon the model developed by Zhou et al., the proppant carrying slurry velocity is dependent upon the fluid velocity and proppant velocity in a relation explained by Equation (4.45) (Zhou et al., 2014).

$$v_{slurry} = (1 - C_{p})v_{l} + C_{p}v_{p} \qquad (4.45)$$

Whereas v_{slurry}: proppant carrying slurry velocity [m/s]; C_{p}: proppant concentration [-]; v_{l}: fluid velocity [m/s]; v_{p}: proppant velocity [m/s].

The fluid velocity and gravity are the two driving forces for proppant transport in the fracture. Therefore, relative velocity models were developed. Liu's (Liu, 2006) corrections based upon experimental results with different fluids to the Gadde's model (Gadde et al., 2004) are described in terms of the ratio of proppant velocity and fluid velocity in Equation(4.46) which takes into account the ratio of proppant diameter to effective fracture width.

$$k_{wc} = {}^{v_p}/_{v_l} = \begin{cases} -0.826\left(\frac{d_p}{w_{eff}}\right)^2 + 0.0475\left(\frac{d_p}{w_{eff}}\right) + 1.2713, & \left(\frac{d_p}{w_{eff}}\right) < 0.93 \\ -7.71\left(\frac{d_p}{w_{eff}}\right) + 7.71, & \left(\frac{d_p}{w_{eff}}\right) \geq 0.93 \end{cases} \quad (4.46)$$

To include the effect of proppant concentration in retarding the relative velocity, effective fracture width concept is utilized in place of actual fracture width based upon wall analogy concept. It depends upon the fracture width, proppant diameter and concentration as given by the following Equation (4.47) (Zhou, 2014).

$$\frac{1}{w_{eff}} = \frac{1}{w^2} + 1.411\left(\frac{1}{{d_p}^2} - \frac{1}{w^2}\right) Cp^{0.8} \quad (4.47)$$

Where, k_{wc}: relative velocity; w_{eff}: effective fracture width [m]; w: actual fracture width [m]; d_p: proppant diameter [m].

Three forces i.e., Buoyancy, drag and gravitational act on the proppant. Normally the proppant density is higher than that of the fluid due to strength requirements to avoid proppant crushing and fracture closure. However, this higher density is also helpful in proppant settling under gravity to reach the perforations otherwise buoyant forces will dominate. The settling velocity of the proppants in lower and higher Reynold's number region i.e., for laminar and turbulent flow can be written in the form of Equation (4.48).

$$V_{settling} = \begin{cases} \frac{{d_p}^2(\rho_p - \rho_f)g}{18\mu_a} & if \quad RN_p < 2 \\ \frac{0.79132{d_p}^{1.14}(\rho_p - \rho_f)^{0.71}}{{\rho_l}^{0.29}{\mu_a}^{0.43}} & if \quad 500 > RN_p > 2 \end{cases} \quad (4.48)$$

Where, $V_{settling}$: proppant settling velocity [m/s]; ρ_p: proppant density [kg/m^3]; ρ_f: fluid density [kg/m^3]; μ_a: apparent viscosity [Pa.s]; RN_p: particle Reynold's number= $\frac{d_p v_p \rho_f}{\mu_a}$.

4.4.6 Apparent fluid viscosity

For the injection of pure fluid such as water, gases, non-aqueous phase liquids etc., the fluid viscosity can be calculated directly by the TMVOC simulator as the required properties are provided initially in the infile. For light alkanes, the fluid viscosity is calculated using the individual viscosity of the components in the NAPL phase (Pruess and Battistelli, 2002).

$$\mu_n = \prod_k \mu_k^{x_n^k} \quad (4.49)$$

μ_n: viscosity of NAPL phase [Pa.s]; $\mu_k^{x_n^k}$: viscosity of component k in NAPL (non-aqueous phase liquid) mixture [Pa.s].

However, gelling the fluids for proppant transport or reducing fluid loss to formation and addition of proppants affects the apparent viscosity of the fluid. Generally, guar gum is added to fluids as gelling agent (Hasan and Abdel-Raouf, 2018). The gelling agent concentration, fluid and surrounding temperature, shear rate affect the apparent viscosity of the fluid. For the guar gel fluid flow, based upon its dependency on guar concentration and temperature, following Equations (4.50) and (4.51) from Torres et al. (Torres et al., 2014) and Zhang et al. (Zhang et al., 2007) are utilized respectively:

$$\frac{\mu_{ap}}{\mu_0} = \frac{1}{1 + k\gamma^{(1-n)}} \tag{4.50}$$

$$\mu_0 = (a_1 b_1)^{ln(C_g)} exp\left[\left(\frac{Ea}{R}\right) \times \left(\frac{1}{T} - \frac{1}{T_0}\right)\right] \tag{4.51}$$

Where, μ_0: zero shear viscosity [Pa.s]; μ_{ap}: apparent viscosity [Pa.s]; γ: shear rate [1/s]; n: flow index; a_1, b_1, k, R: constants; E_a :acitivation energy of viscous flow, C_g: guar concentration in guar gel [g/l]; T: temperature [K].

To find the viscosity of the gelled fluid including the proppants, namely apparent viscosity μ_a (eq. 10) presented by Barre et al. (Barree and Conway, 1995) is utilized as follows:

$$\mu_{ap} = \mu_o(1 - \frac{C_p}{C_{pmax}})^{-a} \tag{4.52}$$

C_p: proppant concentration in the slurry; C_{pmax}: maximum proppant concentration; a: correlation coefficient.

To include the effect of shear rate on the fluid viscosity, Equations (4.50) and (4.52) are combined in Equation (4.53):

$$\mu_{ap} = \frac{\mu_0}{1 + k\gamma^{(1-n)}}(1 - \frac{C_p}{C_{pmax}})^{-a} \tag{4.53}$$

To make the numerical model suitable for apparent fluid viscosity of compressible as well as incompressible fluids in the presence of guar gel and proppants, Equations (4.49) and (4.51) are combined with Equation (4.53). Equation(4.54) presents the model to find the apparent viscosity in the presence of proppants (Pruess and Battistelli, 2002; Torres et al., 2014; Zhang et al., 2007).

$$\mu_{ap,\, \mu_k^{x_n^k}} = \left\{(a_1 b_1)^{ln(C_g)} exp\left[\left(\frac{Ea}{R}\right) \times \left(\frac{1}{T} - \frac{1}{T_0}\right)\right]\right\} \frac{1}{1 + k\gamma^{(1-n)}}(1 - \frac{C_p}{C_{pmax}})^{-a} \tag{4.54}$$

Where, $\mu_{ap,\, \mu_k^{x_n^k}}$: apparent viscosity of proppant carrying fluid (component *k*) in the NAPL phase [Pa.s]

The proppant velocity, apparent viscosity and proppant concentration are used in the proppant mass conservation equation as

$$\frac{\partial(wCp)}{\partial t} + \nabla \cdot \left(v_p wCp\right) + Cp_{inj} q_s \quad (4.55)$$

Where, Cp_{inj}: injected proppant concentration [-].

The details about the parameters a_1, b_1, E_a, R and verification of the apparent viscosity model can be found from (Liao, 2020).

4.4.7 Fluid leakoff

The fluid flow to the formation from fracture, called leakoff, during the fracturing operation is a major phenomenon in modeling the hydraulic fracturing operation. The pressure in the fracture is higher than the formation therefore this pressure differential causes fluid infiltration. It plays a major role in fracture propagation. If the leakoff rate is equal to the injection rate, the fracture cannot propagate further. This fluid interaction or flow exchange between fracture and formation can be numerically modelled at new time step t+Δt using Darcy law, mass conservation and pore pressure variation as (Equation (4.56)) (Gou et al., 2015; Zhou et al., 2014):

$$Q_{leak\,(t+\Delta t)} = A\frac{k_m}{\mu_{ap}} f\left[p_f(t) - p(t)\right] \quad (4.56)$$

Where, $Q_{leak\,(t+\Delta t)}$: exchange volume [m^3/s]; A: exchange area [m^2]; k_m: matrix permeability [m^2] μ_{ap}: apparent fluid viscosity [Pa.s]; f: infiltration coefficient [1/m]; p_f: pressure in fracture [pa]; p: pressure in formation [pa].

The models are implemented in FLAC3D^{plus}-TMVOC. The data sharing between software and specific calculations performed at a time step can be seen from Figure 4.11.

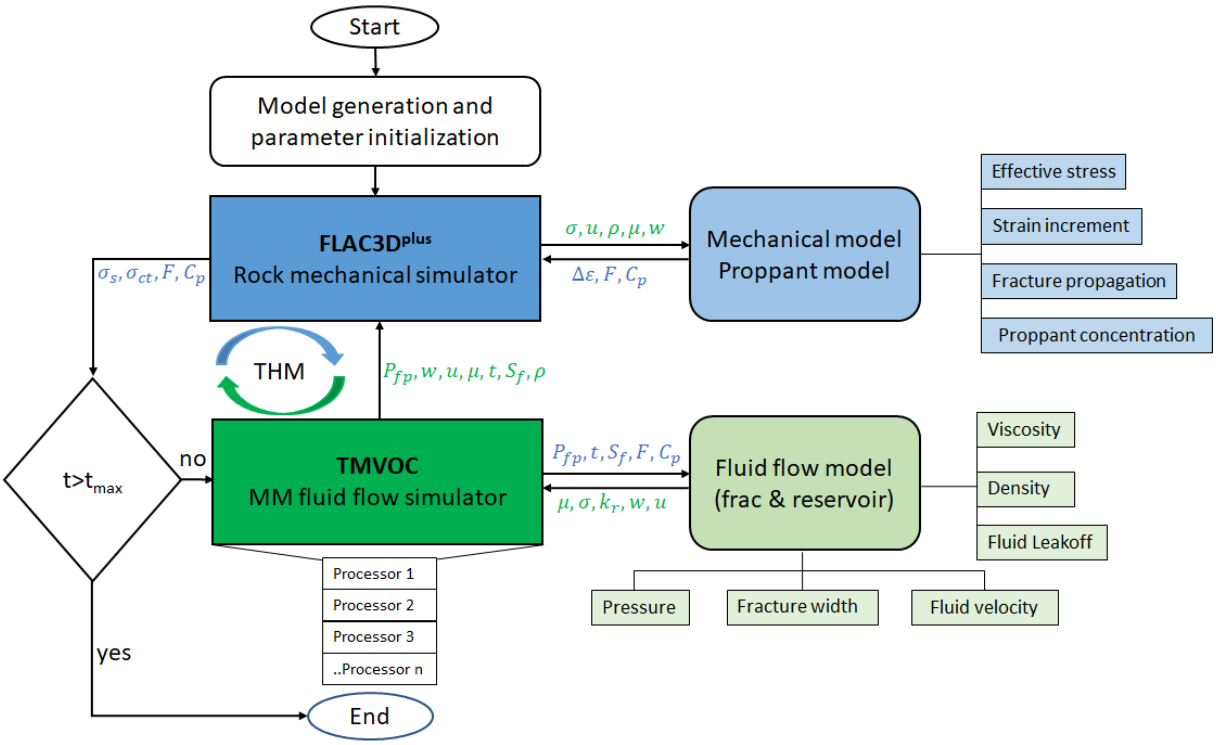

Figure 4.11: flow chart illustrating the functioning of the numerical model and data sharing between software (σ_s: stress state, u: fluid velocity, ρ: density, μ: viscosity, w: width, S_f: fluid saturation) (Mehmood et al., 2021).

5 Model verification and application

The verification of the model is divided into three parts as:

- Fracture initiation and propagation
- Isothermal MM flow verification
- Non-isothermal MM flow verification

5.1 Fracture initiation and propagation

Verification is done by matching the hydraulic fracturing results with already developed and published model for fracturing based upon FLAC3D^{plus}-TOUGH2MP (Li et al., 2018). The hydraulic fracturing was performed in the GeneSys (Generated Geothermal Energy Systems) project. Two wells were involved in this project however, for the purpose of verification one well Gross Buchholz Gt1 drilled in 2009was considered. Hydraulic fracturing was performed to create high permeability flow paths for heat production. Massive hydraulic fracturing treatment injecting 20,000 m^3 fresh water with five injection-shutin cycles was carried out to create fracture area of more than 0.5 km^2.

For the purpose of verifying the hydraulic fracturing ability of developed model, the first hour of injection was simulated and matched with published results, although 106 hours of injection were required to carry out the complete massive fracturing operation. The generated 3D quarter model in FLAC3D^{plus} based upon the geological data can be observed from Figure 5.1a. The model lies between the depth of -3424 m to -3773 m and has dimensions of 1700 m × 350 m in the xy plane, respectively. The reservoir pressure and stress state can be observed from Figure 5.1b. It was a high-pressure formation having reservoir pressure in excess of 60 MPa (Li et al., 2018; Tischner et al., 2013).

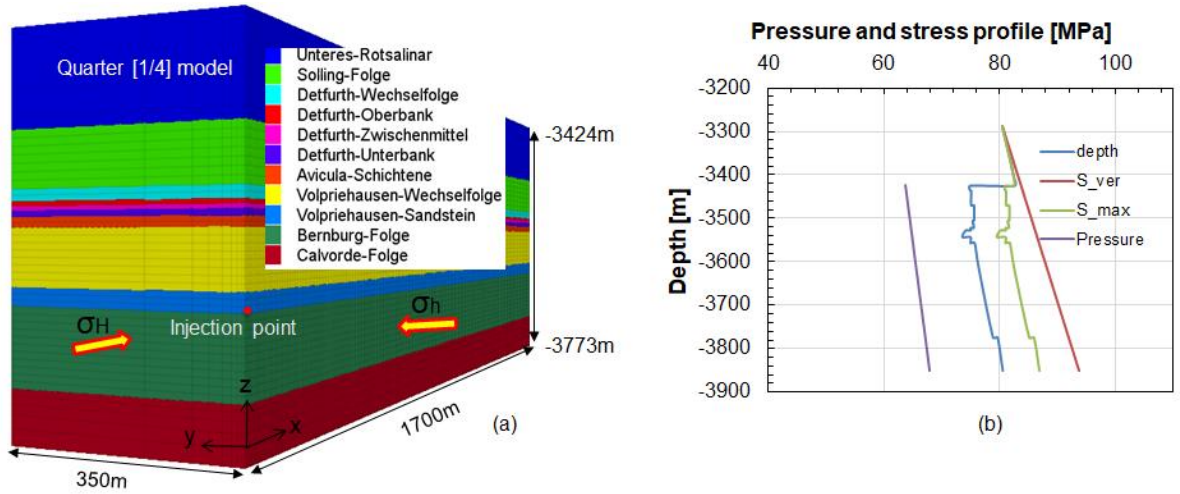

Figure 5.1: (a) 3D stratigraphic model (b) stress state and pressure profile.

The injection fluid (water) is injected for a period of one hour which resulted in fracture creation and propagation. The fracturing started with lower injection rates and then injection rate was increased. The simulated bottomhole fracture pressure is matched with published data (Li et al., 2018). The pressure

rises initially for creating the fracture by overcoming the mean stress and tensile strength of the rock and then normalize. However, it remained slightly higher than 80 MPa during the simulation time (Figure 5.2).

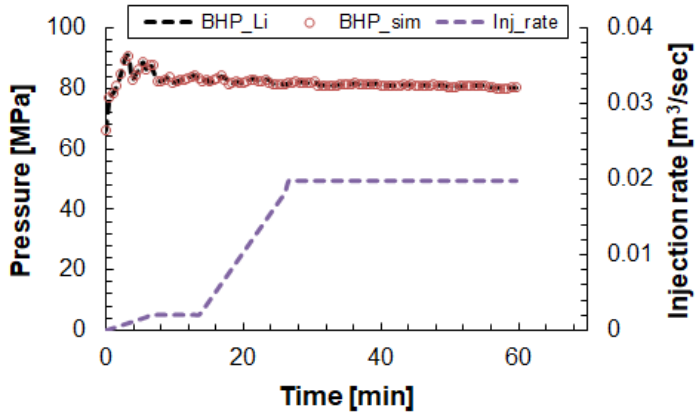

Figure 5.2: fracture pressure (at the end of injection) comparison for simulated and published data.

Figure 5.3, shows the fracture volume and half-width evolution with time for developed model and Li et al. (Li et al., 2018). The fracture half-width temporal evolution is shown for the injection zone. The rise and fall on the increasing width curve are due to the space discretization in small elements. The pressure decreases once an element is fractured and then increases when a new element starts to fracture.

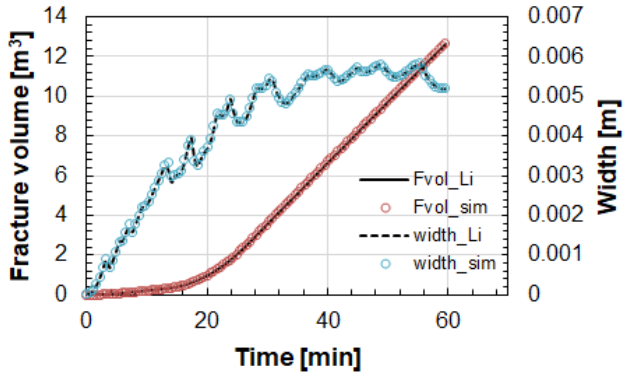

Figure 5.3: fracture half-width (injection zone) and fracture volume comparison for simulated and published data.

5.2 Isothermal MM flow verification

Multiphase multicomponent flow verification in an isothermal process with air displacement of non-aqueous phase liquids in a laboratory column is utilized to validate the developed model (Pruess and Battistelli, 2002). Isothermal process is simulated using the no. of equations (NEQ)= no. of components (NK) in the TMVOC. Flow is simulated in a sand column having a height of 18 cm which is equally divided into 18 elements. The model is generated in FLAC3D^{plus} and exported in the TMVOC infile (Figure 5.4a). Table 5.1 provides the properties of the model and the number and name of fluid components involved.

Table 5.1: properties of the model for isothermal flow.

5 components: O_2, N_2, water, o-xylene, toluene	
Permeability	8.4×E-11m^2
Porosity	35%
Pressure	1.01×E5 Pa
Temperature	20°C [293.15 °K]

Initially static equilibrium with gas as the initial existing phase is created in the column. The distribution of two gases is based upon 20.79 % and 78.21% mole fraction of oxygen and nitrogen, respectively. The 1% water also exists in the gaseous phase. In the next phase, the injection of NAPL i.e., o-xylene and toluene are injected in the column at an injection rate for the mixture of 1 ml/min for a period of 216 seconds. Three phase relative permeability correlation of Stone is utilized. The NAPL after injection distributes itself in the elements which is then displaced by injecting air at the bottom of sand column. Air flooding is done at rates of .7844×10^{-6} kg/sec and 9.2155×10^{-6} kg/sec for oxygen and nitrogen, respectively. The displacement is carried out for a period of 7200 seconds, at the end of which the volatile oil components or non-aqueous phase liquids are removed from the column.

The results for the topmost element are presented in Figure 5.4b. The green elements at the top and bottom are utilized for specific boundary conditions. A very good match with the appearance and disappearance of different components at different stages of the simulation can be observed.

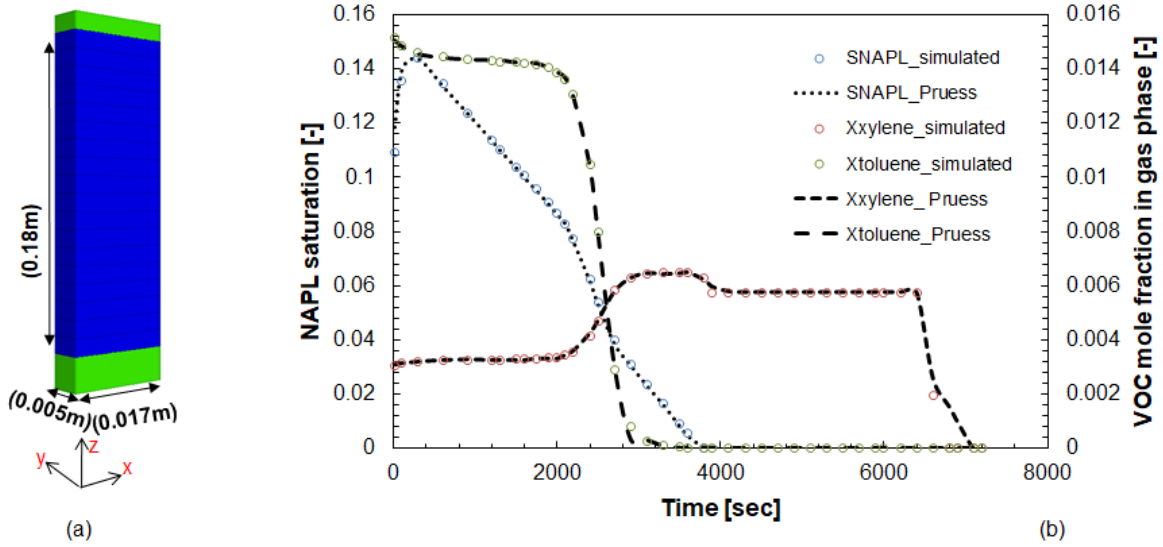

Figure 5.4: (a) 3D geometric model of laboratory column, (b) comparison between simulation results and published literature (Pruess and Battistelli, 2002). SNAPL: Saturation of NAPLs, Xxylene: mole fraction of xylene in gaseous phase, Xtoluene: mole fraction of toluene in gaseous phase.

Compared with xylene, toluene being more volatile is removed preferentially. After the removal of toluene due to air flooding in the fourth stage, xylene concentration in the NAPL (non-aqueous phase liquid) phase increases the vapour pressure and hence the xylene concentration in the gaseous phase also increases.

5.3 Non-isothermal MM flow verification

The non-isothermal simulation requires the setting of no. of equations (NEQ) = no. of components+1 (NK+1) in TMVOC infile to include heat as a component and model exchange between formation and fluid. Steam displacement of NAPL mixture (Pruess and Battistelli, 2002) is utilized to verify the model for non-isothermal flow ability. The model generated in FLAC3D^{plus} consisting of 50 grid blocks is exported to infile of TMVOC Figure 5.5a. Table 5.2 provides properties of the utilized model.

Two volatile oil components toluene and benzene are injected in a laboratory column for a period of 120 seconds at injection rates of 6.488×10^{-5} kg/sec, and 6.592×10^{-5} kg/sec, respectively. The column is then water flooded at an injection rate of 3.5382×10^{-5} kg/sec for a period of 18,162 seconds. The water flooding rate is then continued at a decreased rate of 9.4352×10^{-6} kg/sec for another 90,809 seconds. After the waterflood, 81.5% and 21.3% of benzene and toluene were removed, respectively. In the last phase, steam is injected at injection rate of 3.5341×10^{-5} kg/sec for 9000 seconds to displace the NAPLs or VOCs.

Table 5.2: properties of the column for non-isothermal flow verification.

4 components: water, air, toluene, benzene	
50 grid blocks	
Permeability	81.6×10^{-11} m^2
Porosity	38.5%
Pressure	1.013×10^{5} Pa
Temperature	22°C [295.15 K]

The simulation is performed with the developed model and the results are plotted in Figure 5.5b and Figure 5.6. The process starts with the injection of toluene and benzene followed by water flood and steam flood. Figure 5.5b presents the variations in saturations of gas, water and NAPL phases (three phase). Due to injection of water, the saturation of water increases. In addition, steam injection vaporizes the fluid. The NAPL bank is reduced to grid block 38 to 42. Additionally, due to high solubility, benzene is initially depleted. The effect on the temperature of laboratory column after 5000 seconds of steam injection can also be observed. The temperature in grid block 36 reached 100°C, whereas the temperature in grid block 45 is still at 22°C which was the original temperature of the column. Given sufficient time, the temperature change will reach all the grid blocks.

Moreover, the changes in NAPL saturation, as a function of vertical distance from top, before and after waterflood can be observed from Figure 5.6 for isothermal flow conditions. It can be seen that the initial high saturation of NAPL is changed and shifted downward in the column due to water injection (based on the first and second stage of the same problem). First stage involves the injection of NAPLs in the 15th grid block from the top in the laboratory column. In the second stage, water is injected from the top to displace the NAPLs. As can be observed, the maximum saturation of NAPLs reached about 40%

before the water-flood. But soon after the water-flood, the saturation of NAPLs kept on decreasing till the end of injection to below 5%.

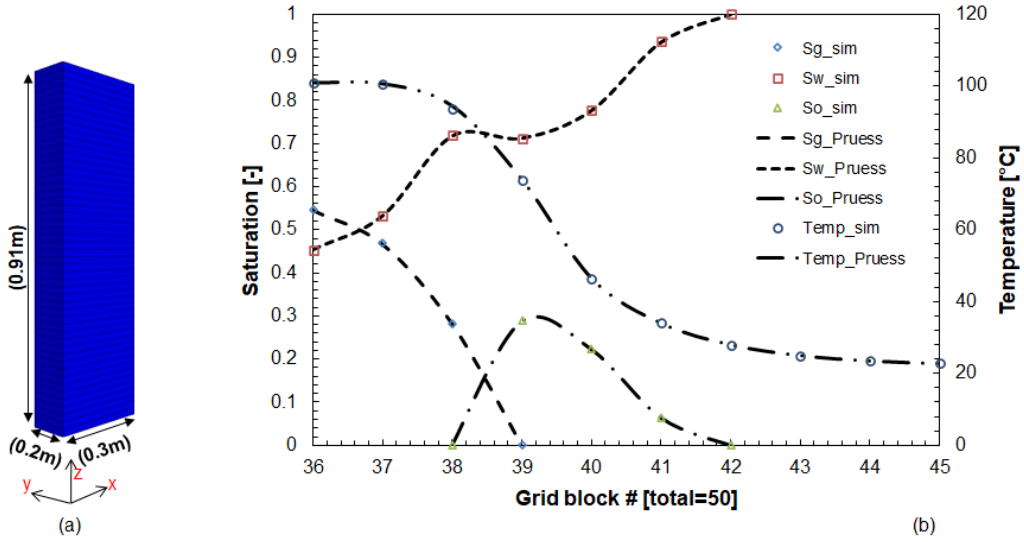

Figure 5.5: (a) 3D model of column for NAPL displacement with steam flood,(b) comparison between simulation results and published literature for non-isothermal conditions (Pruess and Battistelli, 2002). Sg: gas saturation, Sw: water saturation, So: NAPL saturation.

Furthermore, at 108971 seconds, the NAPL is displaced from the upper columns to lower columns as well. Initially they existed at distance between 20 and 33 cm but were shifted to between 30 and 57cm grid blocks region with substantial reduction in saturation.

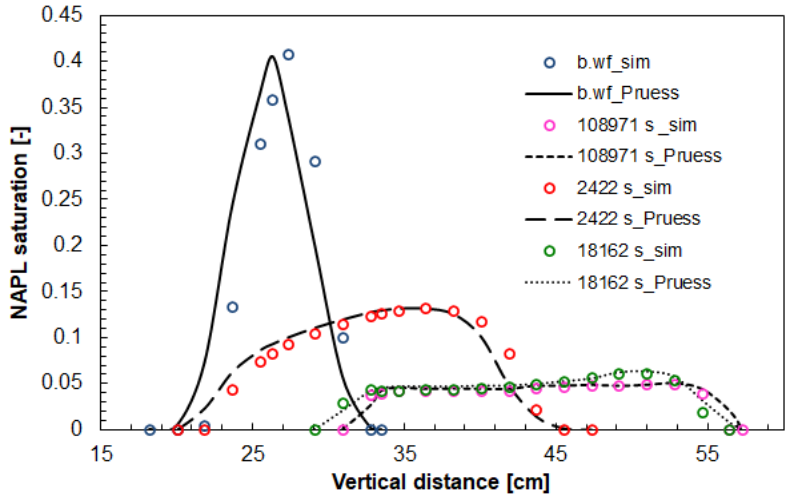

Figure 5.6: Comparison between simulation results and published literature for isothermal flow. b.wf: before waterflood.

The above performed simulations verify the (MM) fracturing and flow ability of the developed model. This model is utilized to simulate hydraulic fracturing in tight gas reservoirs with alternative fluid.

5.4 Hydraulic fracturing in McCully tight gas reservoir, New Brunswick, Canada

5.4.1 Introduction

McCully gas field comprising of low permeability sandstone and shale formations is an unconventional commercial gas field located in New Brunswick, Canada. In 2003, the production from Hiram Brook sandstone was initiated which was followed by full production in 2007. Whereas the production from underlying Frederick Brook shale began in 2008. A number of stimulation treatments were performed initially between 2005 and 2008, however well tests showed minimum contribution from fractures. Therefore, hydraulic fracturing with Liquified Petroleum Gas (LPG) was performed and the results were convincing in terms of better cleanup and improvement in well performance and stimulation (Leblanc et al., 2011).

The Hiram Brook sands and shales belong to the Lower Carboniferous Albert formation. The sandstone ranges from coarse-grained poorly sorted to fine grain well sorted in different layers with interbedded shale layers. Using TOUGHREACT, simulations were performed for water-based and propane-based fluid fractures and future performance predictions with varying parameters by Schwartz (Schwartz, 2017). Table 5.3 summarizes some properties of the gas field.

Table 5.3: McCully gas reservoir properties (Leblanc et al., 2011).

McCully Reservoir Properties	
Reservoir top depth	1800 m
Reservoir gross thickness	Up to 870 m
Porosity	4 - 8%
Initial water saturation	<10% - 30%
Gas saturation	90%
Reservoir temperature range	40°C – 60°C (313 °K – 333 °K)
Reservoir pressure range	20 MPa – 35 MPa

5.4.2 3D model and fracture design

In order to apply the developed model to fracturing operation, a 3D geometric model is generated in FLAC3D^{plus}, where the depths of the formation are approximated due to scarcity of available data. The height of the model is 1000 m starting at a depth of 1800 m. The interbedded sand and shale layers with overlying Sussex group and underlying shale can be observed from Figure 5.7a. From the full 1000m×1000m×1000m model, a section 300m×200m×275m is chosen for hydraulic fracturing operation with alternative fluids. The sandstone formation ‘sand5’ with overlying and underlying ‘shale2 and 3’ can be observed from Figure 5.7b. The injection point is located at 2300 m depth.

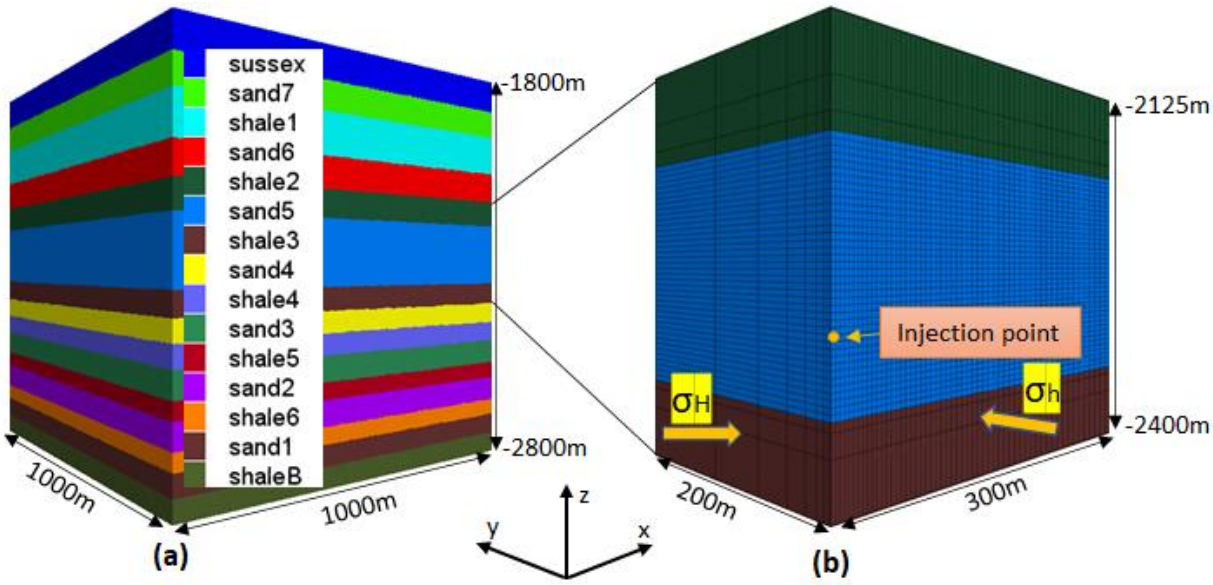

Figure 5.7: (a) 3D geometric model showing Hiram Brook sand with interbedded shale layers (b) target formation 'sand5' with location of injection point at 2300 m depth and stress directions (quarter model) (Mehmood et al., 2020).

The hydromechanical properties are averaged for sandstone and shale formations and presented in Table 5.4.

Table 5.4: utilized rock mechanical and physical properties (Séjourné, 2017).

Rock type	**Young's modulus [GPa]**	**Pisson's ratio [-]**	**Shear modulus [GPa]**	**Bulk modulus [GPa]**	**Permeability [m^2]**	**Porosity [%]**	**Density [kg/m^3]**
shale	39.7	0.25	19.1	40.4	9.87E-20	4	2737
sandstone	57.5	0.23	23.6	36.4	9.87E-18	8	2530

The stress and pressure profile of different wells is available for different wells such as E-67, G-41, P-66 etc., from the Geological Survey of Canada (Séjourné, 2017). Figure 5.8b shows the reported and used pressure and stress conditions in the 3D model. Assuming homogeneity, the generated model is a quarter model to reduce the number of calculations and simulation time.

The hydraulic fracturing is performed with different frac-fluids and compared. Water-based, propane-based and light alkane-based fluid are utilized to understand the efficiency of fracturing operation and advantages of alternative fluids. During the fracturing operations in McCully gas field, injection rates ranging from 4-7 m^3/min were utilized. Therefore, fluid for all the cases were injected at an average rate of 4.8 m^3/min in the simulation. The injection scheme of light alkanes i.e., proposed fluid was different from other fluids. In this case, hybrid fluid concept was utilized where the fracturing is initialized with water injecting about 30m^3 in the first seven minutes and then continue with light alkanes which in this case was selected to be n-heptane (C_7H_{16}). This hybrid fluid concept has an added

advantage of initiating fracture with water which has higher density thus avoiding excessive surface injection pressures and conducting fracturing with available surface equipment. The proppant injection starts at 45 minutes from the beginning of fracturing operation and continues for 30 minutes. Therefore, hydraulic fracturing is conducted for a period of 75 minutes injecting around 56 tons proppant having density of 2700 kg/m^3. The proppant size utilized is 30/50 mesh. The fluid and proppant injection schedule can be observed from Figure 5.8a.

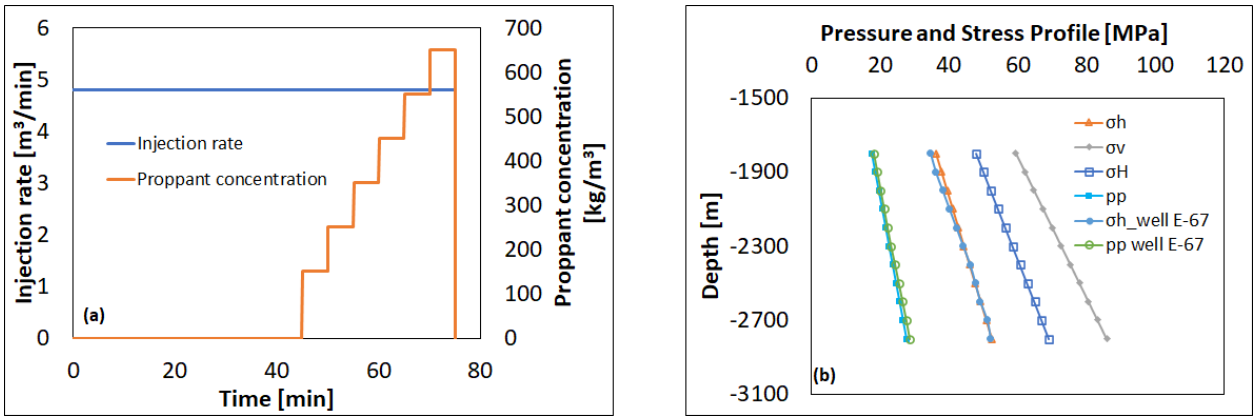

Figure 5.8: (a) injection rate and proppant schedule for stimulation, (b) formation pore pressure and stress profile applied in 3D model (Séjourné, 2017).

5.4.3 Analysis of fracturing with different fluids

Different fracture geometries are created as different frac-fluids are used. The density, viscosity etc., lead to different fluid leakoff, different fracture rates and overall geometry. Considering a fracture width with at least three proppants, fractures with fracture height of 143 m, 151 m, and 151 m and half-lengths of 76 m, 85 m and 81 m are created for propane (LPG) based, water-based and C7-hybrid fluid, respectively. In addition to simulated cases, fracture half-length of 79m of well L-38 with propane-based fluid is also plotted in Figure 5.9.

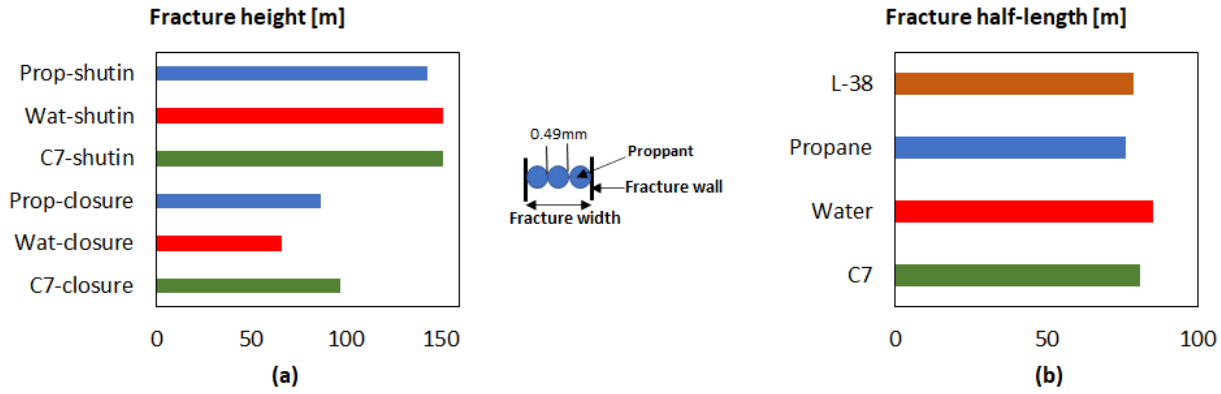

Figure 5.9: (a) simulated fracture heights for different frac-fluids at shutin and closure, (b)simulated fracture half-lengths for different fluids (well L-38 with propane-based fluid fracture half-length also plotted). Prop: Propane, Wat: water, C7: n-heptane.

The maximum fracture half-width of 6.1 mm, 7.8 mm, and 7.2 mm for propane-based, water-based and proposed fluid fracturing are obtained. The main difference is the viscosity of the fluids. The heat capacity of the fluids is different, therefore due to lower heat capacity the change in the temperature of propane is quick followed by heptane and water. Therefore, the leakoff of propone is more leading to lower created fracture width. Hence maximum fracture width is created for water-based fluid Figure 5.9.

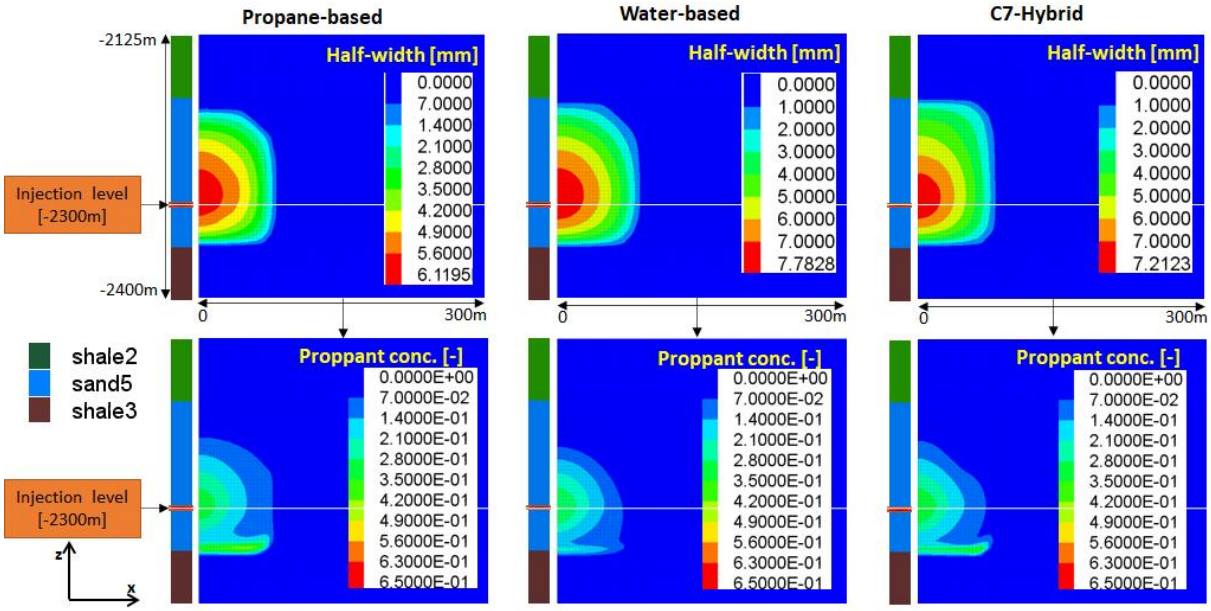

Figure 5.10: fracture half-width and proppant distribution at the end of injection for propane-based, water-based and C7-hybrid fluid.

In order to observe the proppant settling, simulation is continued after the fluid injection is stopped. When the fluid injection is stopped, the pressure inside the fracture starts to decrease and fluids leaks off to the formation due to pressure difference between fracture and formation. As discussed earlier, the viscosity decrease or gel break on the base of fluid heat capacity will be quick for propane and other light alkanes compared to water. Therefore, the leakoff of fluid to formation will be quickest for propane and then for heptane. Hence, at 600 minutes, complete fracture closure can be observed for propane and heptane, however for water-based fluid the fracture closure is slow. Therefore, although the proppants have settled to the bottom, the fracture in the upper half has not closed (Figure 5.11). Therefore, although the initial fracture height for water-based fluid was 151 m, the propped fracture height has reduced to only 66 m due to slow fracture closure. In comparison, the fracture closure for propane and heptane-based fluid is quick, leading to higher propped fracture heights of 87 m and 97 m, respectively (Figure 5.9a).

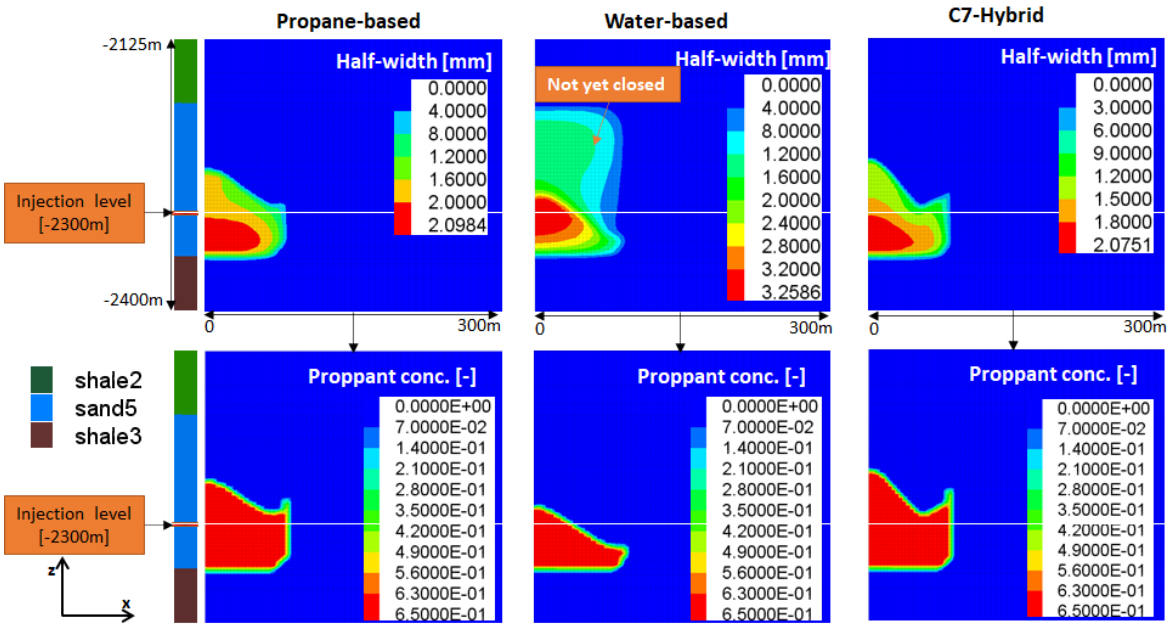

Figure 5.11: fracture half-width and proppant distribution at 600 minutes for propane-based, water-based and C7-hybrid fluid.

The previous discussion shows that water-based fluid will result in fracture with highest initial volume followed by heptane and propane creating 197 m^3, 173 m^3 and 150 m^3, respectively. The time required for fracture closure depends upon fluid leakoff. The fracture clsoure is quickest for propane-based fluid and then for hybrid-n-heptane fluid but after shutin it takes longer for water-based fluid to leak-off. Water-based fluid fracture closure took place 320 minutes after the n-heptane case (Figure 5.12). Therefore, proppants are retained in the upper half of fracture for propane and heptane-based fluid. On the other hand, more propped fracture width at the bottom of fracture due to proppant settlement at the bottom for water-based fluid is observed which causes partial connection between fracture and injection level. The propped fracture height for proposed fluid will maintain contact with more formation area which can have a significant impact upon the ultimate recovery. Figure 5.13 shows the difference in fracture half-width profile for different fluids at the end of injection and closure along the borehole wall.

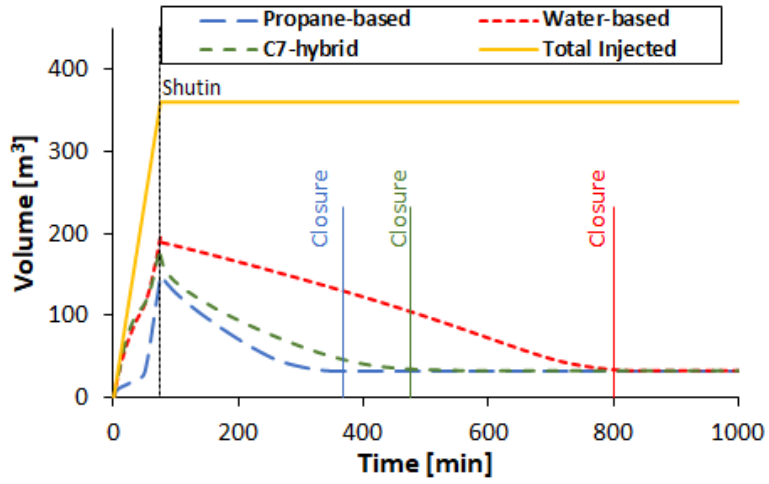

Figure 5.12: fracture volume vs time and difference between fracture closure for different fluids.

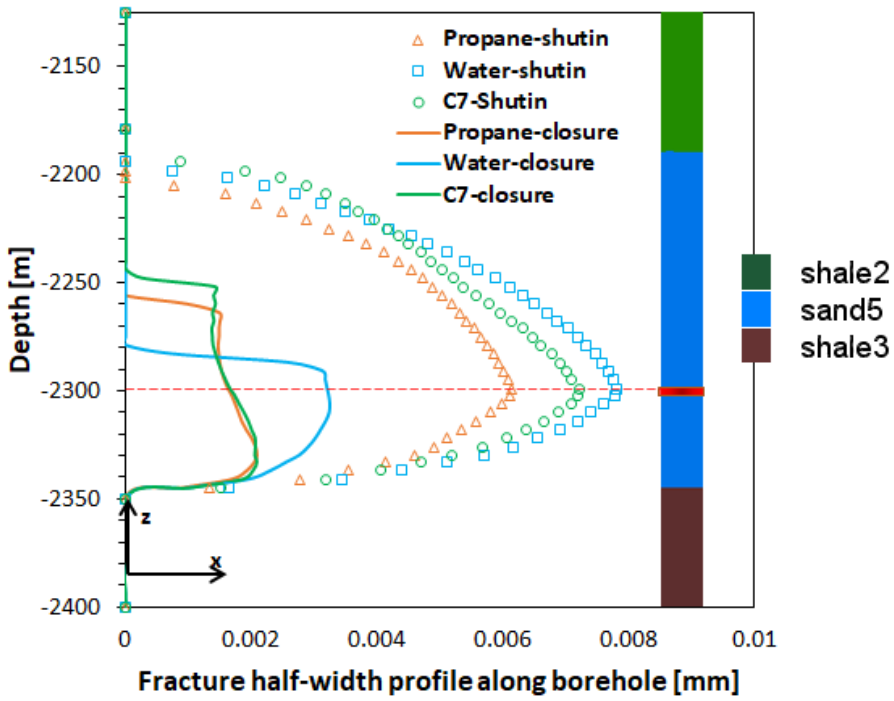

Figure 5.13: fracture halfwidth profile for different fluids at shutin and closure along z-axis at borehole.

A similar behavior for injection zone pressure profile can be observed from Figure 5.14. the pressure rises initially until breakdown and then decreases during fracture propagation phase and then rises due to high viscosity proppant carrying slurry. After shutin, the pressure normalization to reservoir level is the quickest for propane-based followed by C7-hybrid fluid. whereas, water-based fluid gel breaks later as discussed earlier, which requires more time to leakoff to formation and pressure reduction to initial reservoir pressure level.

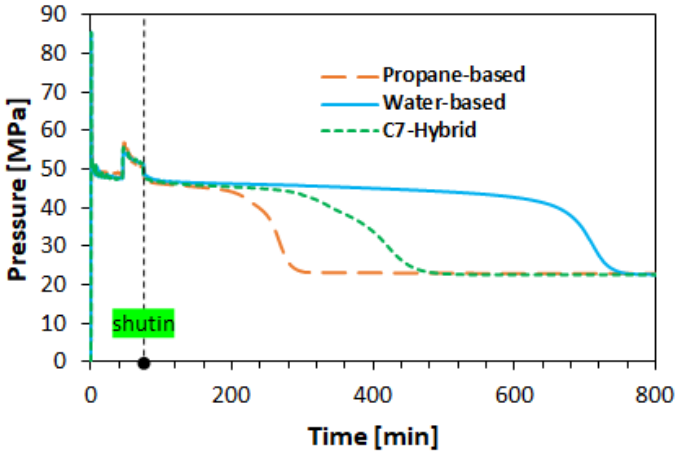

Figure 5.14: injection zone pressure profile for different fluids till complete closure.

The settling behavior of proppants for the fluids at different time points is presented in Figure 5.15. In the light of previous discussion, the proppants settle under the influence of gravity since their density is higher than the fluid density. The fracture closure for light alkanes is quick, therefore more propped

fracture height is created since the proppants come in contact with the walls of fracture as it closes under the influence of closure stress. For water-based fluid the initial fracture width was more, the fracture closure was slow due to lower leakoff rate. The fracture closes slowly giving more time to proppants to settle hence reduced fracture height.

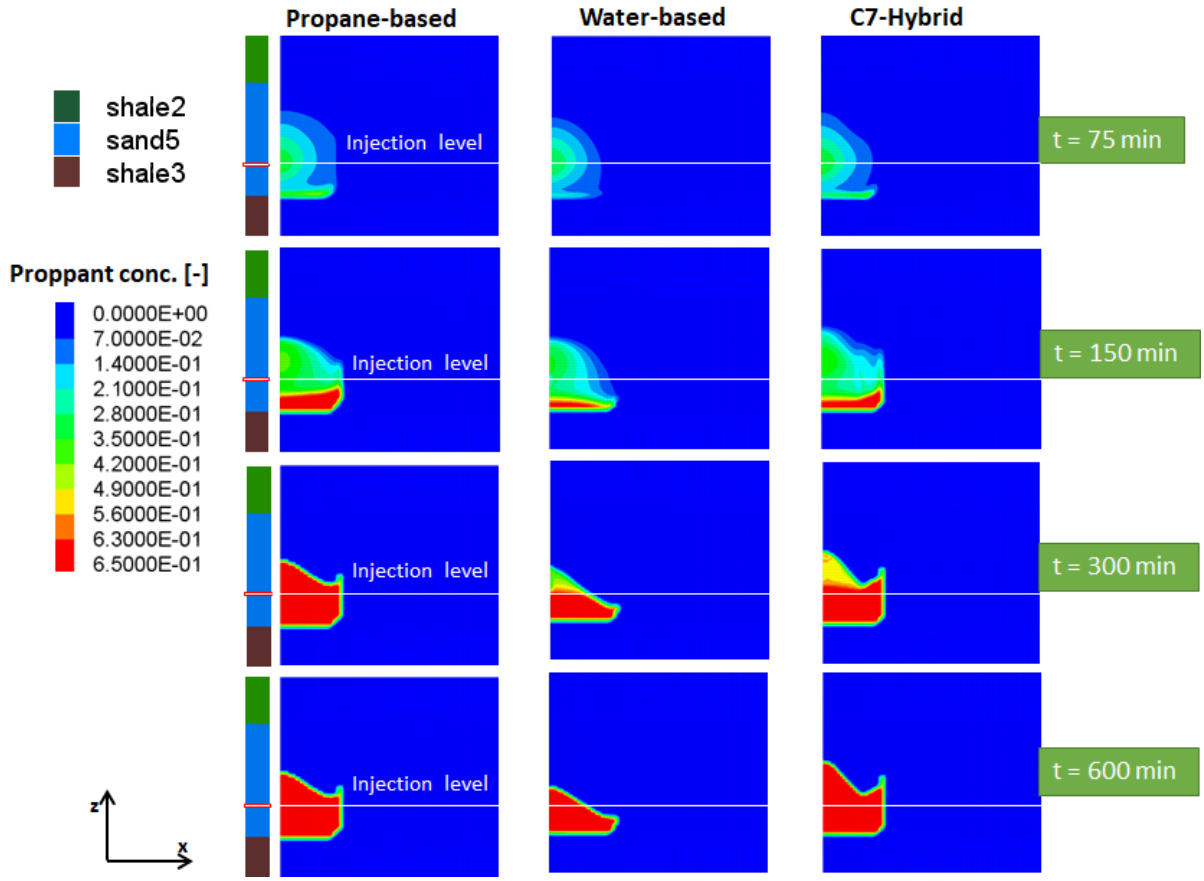

Figure 5.15: proppant settling behavior for different fluids (Mehmood et al., 2020).

5.4.4 Frac-fluid flowback

In hydraulic fracturing operations, after the creation of fractures and proppant placement, the next big task is the flowback of injected fluid. In the case of formations having sub reducible water saturations and clay swelling problems, the injected water is retained in the pores reducing the effective permeability to reservoir fluids. It seriously damages the effectiveness of fracturing operation and desired productivity leading to poor recoveries. Therefore, to observe the flowback behavior of different fluids, simulation is continued for seven days to allow the fluid to flow back. The results are presented in Figure 5.16. At the end of fracturing operation, the reservoir gas is completely displaced by the injected fluid. When the flowback starts, the fluid properties such as density and viscosity play a major role in recovering the fluid. At the end of seven days, propane being lightest and bearing lower viscosity flows back preferentially from propped zone leading to 90% gas saturation in the fracture zone with proppants. Similarly, C7-hybrid fluid (also the proposed fluid) is removed from the propped fracture

zone resulting in maximum gas saturation of 90% reservoir gas in the near perforation zone and more than 70% away from the injection zone. This behavior is due to presence of small volume of water which was utilized in the initiation of fracture and then displaced further by heptane. Considering the advantages of using a small volume of water initially, the obtained results are very attractive from practical application point of view of proposed fluid in hydraulic fracturing with available surface equipment. Having a look at the flowback performance of water-based fluid, it can be seen that most of the injected fluid remains in the reservoir. This is also true for the propped fracture zone. The injected water saturation remained higher than 40% and in excess of 90% for most of the created fracture. This is a serious drawback, hindering the flow of reservoir fluid reducing ultimate recovery. It can take even several months to flowback which can nullify the effect of fracturing operation leading to loss of production, time, effort, and economics.

The cost of light alkanes is more than water. The quick flowback and recovery at the surface of alternative proposed fluid and subsequent reuse can help reduce costs of the operation.

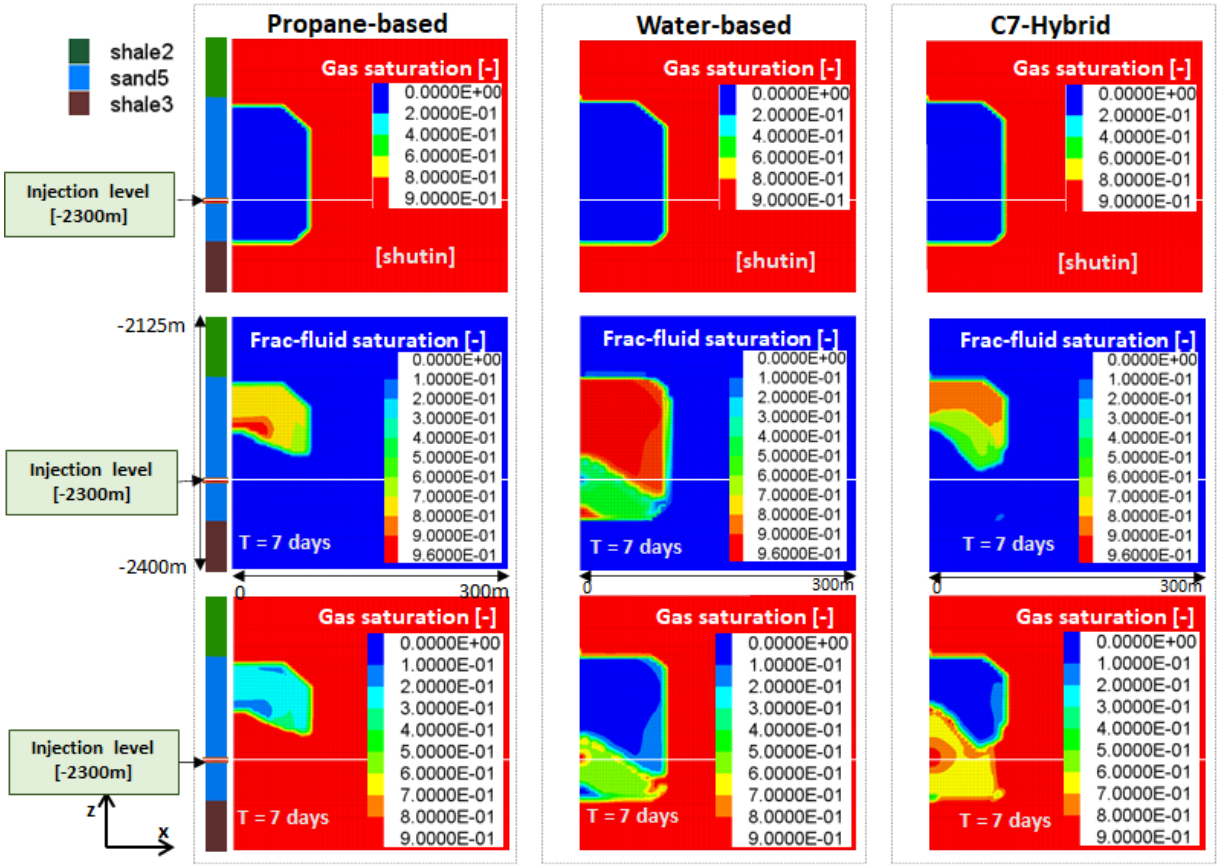

Figure 5.16: reservoir gas and frac-fluid saturations for different fluids at shut-in and seven (07) days.

5.4.5 Production forecast

The production for three scenarios i.e., propane-based, water-based and no-frac cases for a period of five years was presented (Leblanc et al., 2011). To match the production forecast, simulation was

performed for production from the simulated fractures based upon developed model. The results are plotted in Figure 5.17 along with the production forecast from published literature. It can be observed that, 40.5 million m^3 can be recovered with propane-based single fracture compared to 27 million m^3 production from water-based fluid single fracture. However, with proposed fluid, due to better fracture performance and maintaining more contact area of fracture with the formation, around 45 million m^3 of gas in place can be recovered which is 11% more than propane-based fracture.

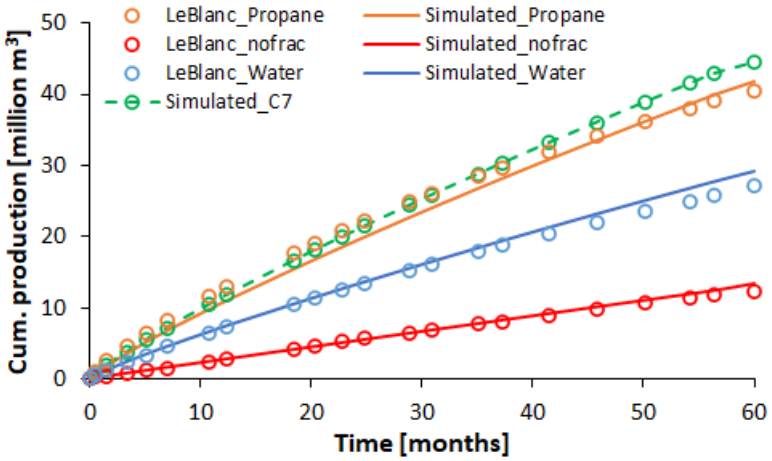

Figure 5.17: production forecast match for propane-based fluid frac, water-based fluid frac and no-frac cases. The forecast for C7-hybrid fluid is also plotted.

6 Hydraulic fracturing optimization in a tight gas reservoir of Germany

6.1 Introduction

In this section, a wellbore yx1, in tight gas reservoir yxz in which hydraulic fracturing operation was performed in 2000, is considered for optimization of fracturing operation with the proposed fluid. The location of wellbore in the reservoir yxz can be observed from Figure 6.1. The reservoir consists of Wustrow, Dethlingen and Mirow formations. The top of reservoir lies at 4551m TVD and the base lies at a depth of 4757 m TVD.

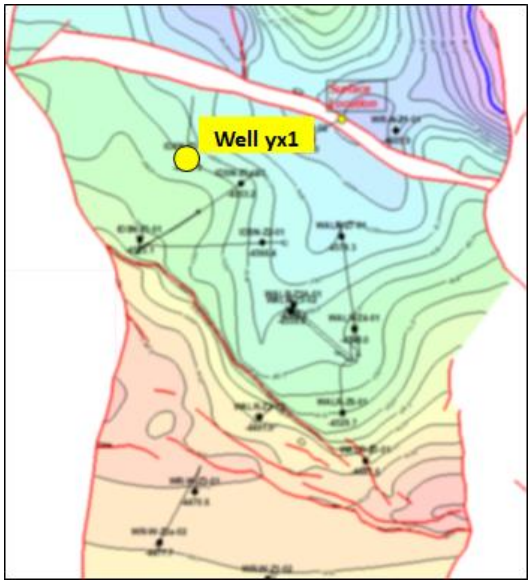

Figure 6.1: location of wellbore yx1 in tight gas reservoir yxz.

Some important information about the reservoir can be seen in the following Table 6.1.

Table 6.1: important information of the reservoir.

General properties	
Reservoir top	4551.3 m
Reservoir base	4757.4 m
Gross sand thickness	205.7 m
Porosity	11.3%
Permeability (in situ)	<0.01 mD
Permeability (core data)	0.2-29 mD
Bottomhole temperature	146.5 °C (420 K)
Gas composition (%) and related properties	
Methane	88.32
Propane	2.004

Butane	0.1033
Isobutane	0.0248
n-Butane	0.0158
N_2	8.2
Formation volume factor at 67MPa [sm^3/rm^3]	312.2
Wobbeindex [kWh/m^3]	13.08

The wellbore yx1 was completed in the year 2000 and started production. However, due to lower productivity, the production was stopped in the year 2001. Total production of only 2.016 million m^3 could be obtained at that time. According to the P/Z analysis, gas reserves of 645 million m^3 were present (Figure 6.2). However, due to low permeability as is the case with tight gas reservoirs, the commercial production is not possible. Therefore, hydraulic fracturing is performed to create artificial flow paths for a better productivity. However, the fracturing operation did not improve the productivity to sufficiently increase the natural gas production. Therefore, the production was halted after only 2.016 million m^3 cumulative production. The production started in July 2000 and continued with intermittent periods of production and shutin until April 2001. The reasons for lower productivity will be discussed in later section.

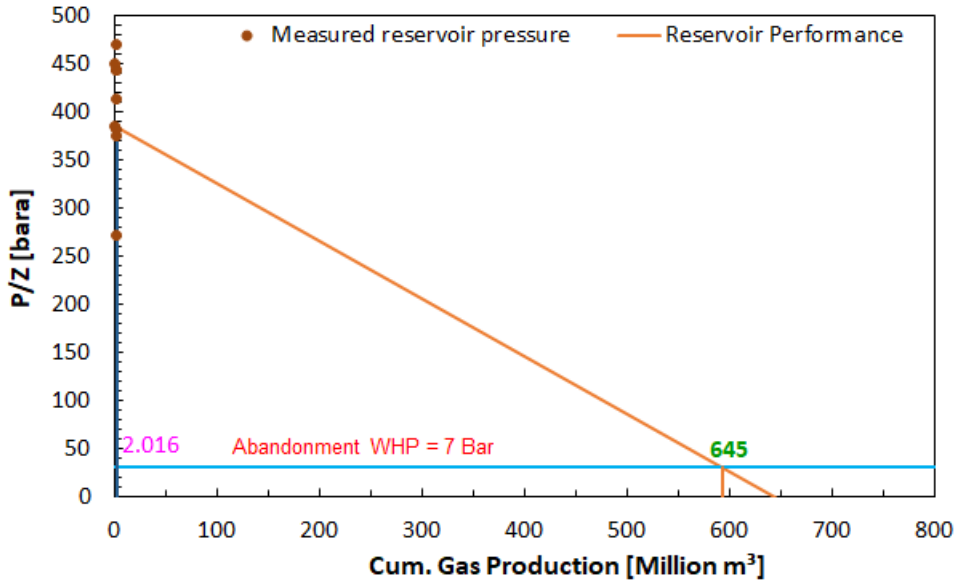

Figure 6.2: gas reserves based upon P/Z analysis.

Figure 6.3 shows the pressure profile of wellbore yx1 during production period and after shutin until 2013 and the pressure has returned to its initial reservoir pressure conditions as there was no production since May 2001.

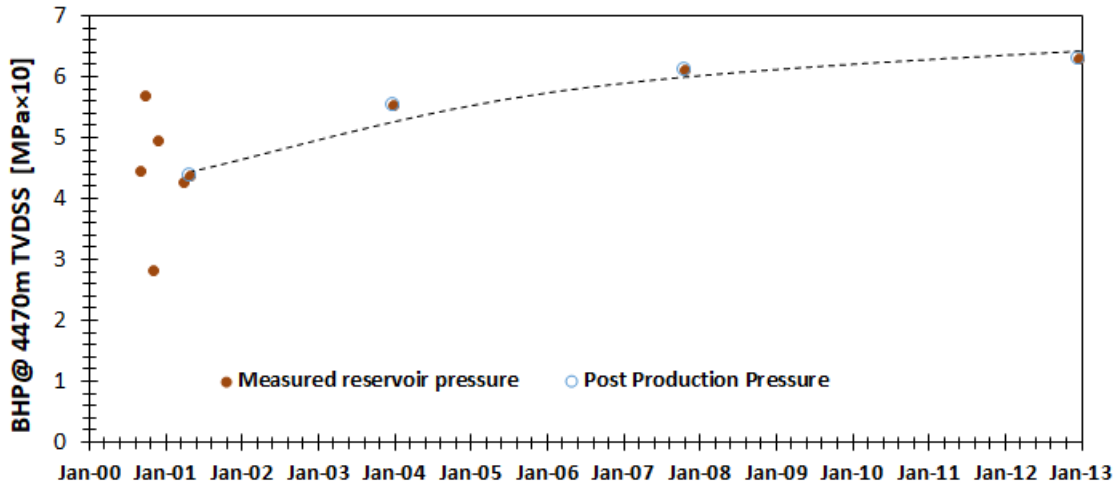

Figure 6.3: pressure profile during production and post-production period.

The previous hydraulic fracturing job was conducted in July 2000 creating a single fracture in the reservoir with water-based fluid using the perforations at a depth of 4671 m TVD. The well bore has 9 5/8" liner casing until 3175 m, 7" liner from 3069 m – 4651 m and 4 1/2" liner from 4454 m – 4851 m. The reservoir formations properties based upon core analysis and well logging can be found from the following Table 6.2.

Table 6.2: formation properties.

Formation	**Top depth [m]**	**Young's modulus [Pa]**	**Poisson's ratio [-]**	**Porosity [-]**	**Permeability [m^2]**	**Density [kg/m^3]**
Z1-An	4490	2.90E+10	0.275	0.041	9.720E-21	2940
Z1-Rk	4535.18	2.85E+10	0.253	0.044	4.84E-17	2840
Kupfe	4538.6	2.89E+10	0.260	0.059	3.15E-19	2715
He-Me	4540	2.94E+10	0.255	0.040	1.05E-16	2705
Mu-Me	4553.76	3.06E+10	0.206	0.068	2.78E-16	2655
Ni-Me	4573.86	3.72E+10	0.220	0.001	1.00E-21	2750
Da-Me	4598.38	3.31E+10	0.230	0.081	1.154E-16	2574
Ba-Me	4608.7	3.01E+10	0.197	0.110	1.165E-16	2500
Wu-Me	4626.81	2.93E+10	0.2025	0.110	4.887E-16	2493
Eb-Me	4653.75	2.76E+10	0.200	0.110	8.430E-16	2707
De-fo	4669.9	2.65E+10	0.1975	0.113	5.79E-16	2668
Ha-Sa	4722.72	2.61E+10	0.2267	0.113	9.504E-16	2668
Al-Su	4816.19	2.92E+10	0.25	0.064	1.067E-20	2750

The breakdown/stepdown tests were performed to determine the breakdown gradient, fracture gradient and friction gradient and tortuosity. Whereas closure stress and fluid efficiency were determined

through the minifrac test. The closure stress was found to be around 81 MPa. the breakdown and fracture gradients were determined to be 0.0213 MPa/m and 0.0175 MPa/m. After gathering necessary data, hydraulic fracturing was performed. The injection rate remained very low initially and then was increased to 4.8 m^3/min after injecting 16 m^3 injection fluid. Once the tubing pressure dropped, crosslinked fluid was injected. After the initiation of fracture, proppant slug was injected to minimize the tortuosity. Proppant injection was continued only for a few minutes and then discontinued and then continued again at a later stage until the end of fracturing operation. According to the pumping schedule a total of about 424.592 m^3 fluid and 120-ton Sinterball 20/40 SBC 3465 kg/m^3 density proppant was injected. The fracturing operation continued for a period of 150 min (2.5 hours). Figure 6.4 shows details of the main fracturing job performed.

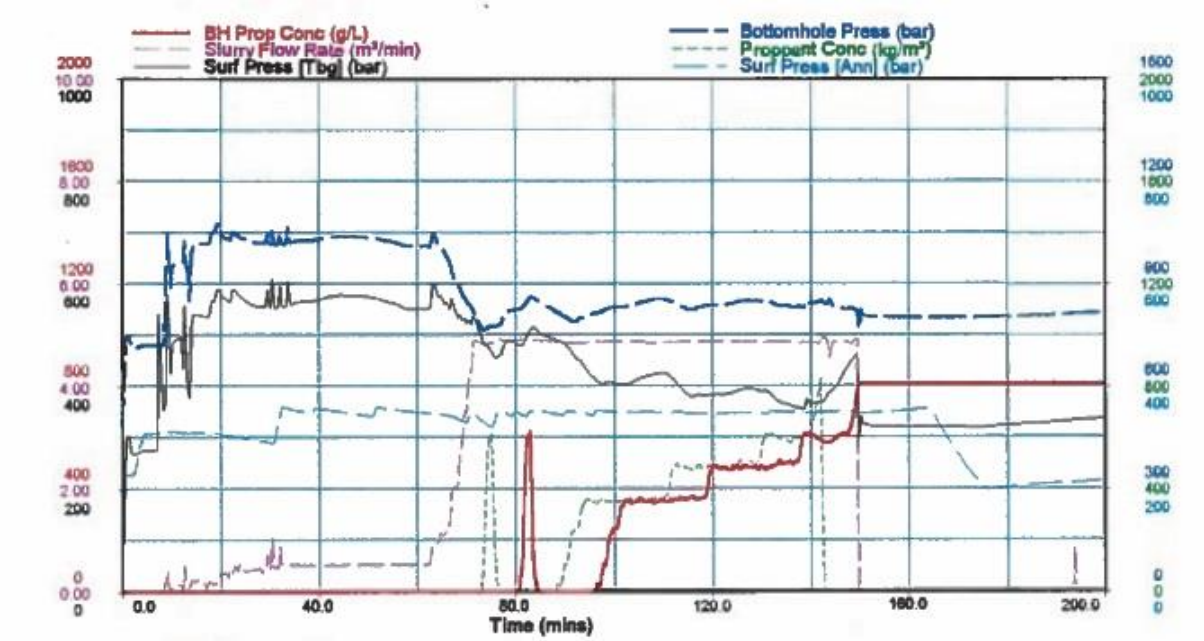

Figure 6.4: fluid injection and proppant schedule, measured bottomhole and surface pressures during the hydraulic fracturing treatment.

6.2 Model generation and verification

In order to perform stimulation tests in wellbore yx1, first 3D quarter model of the field is generated in FLAC3D according to the stratigraphy. The model is verified by pressure history matching with the previously conducted fracturing operation. Figure 6.5 presents the quarter model and pressure and stress profile of the developed model. The stress state is based on log derived data. The model is assigned hydromechanical properties as per Table 6.2. The injection schedule of fluid as well as proppant was followed during the simulation using the gelled fluid model including proppant transport as presented in Figure 6.4.

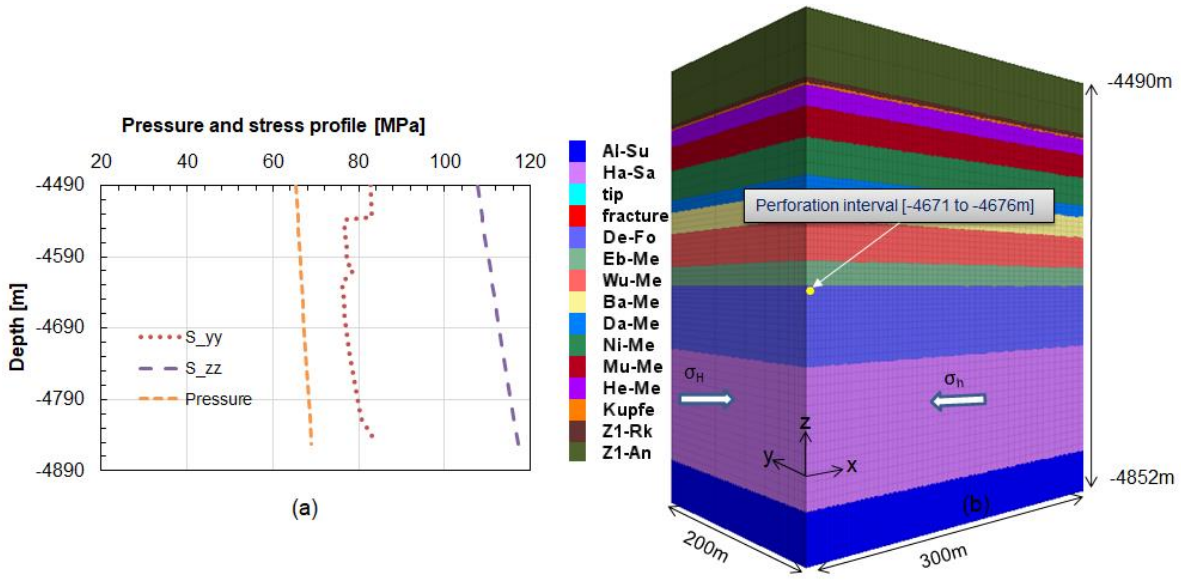

Figure 6.5: (a) pressure and stress in the model, (b) 3D geometric (1/4) model with stress directions.

The pressure history match can be observed from Figure 6.6. The injection of high viscosity gelled fluid was simulated along with proppant transport. The injection rate remained low for the initial one hour but then increased and was maintained at 4.89 m^3/min. Due to some technical problems, the initial one hour showed very high tubing pressures and for this reason the injection rate was kept low (Figure 6.6 section A). After the pressure normalization, the injection rate increased flowed by proppant injection (Figure 6.6 section B). The increase in injection rate can also be observed from increase in simulated pressure. It can be observed that a reasonable pressure match between measured and simulated cases is obtained during the main injection period when most of the injection fluid was injected. However, in section A, the pressure match cannot be made due to high pressure values obtained as a result of initial presence of cross-linked fluid in the well. The initial spike in the simulated pressure at the beginning is due to the breakdown of formation by overcoming the effective minimum stress and tensile strength of the rock. Once the fracture is initiated, the fracture pressure reduces, however it remained above 80 MPa during the course of operation.

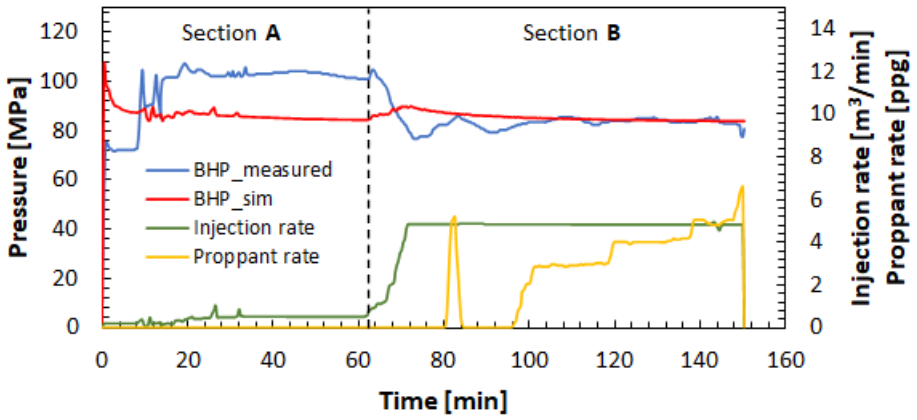

Figure 6.6: history match with measured BHP during the main-frac job (injection rate and proppant schedule are also plotted). sim: simulated.

At the end of fracturing operation, fracture with half-length of 130 m is created which is close to the results of Fracpro program of 118 m half-length fracture. Figure 6.7 shows the temporal development of fracture half-length along with injection rate and comparison with Fracpro results. The increasing rate of fracturing can be matched with the increasing injection rate.

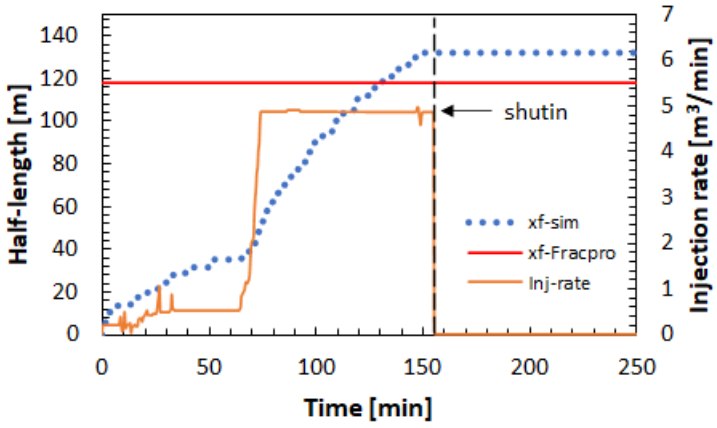

Figure 6.7: temporal development of fracture half-length.

Once the injection stops, the fracture starts to close under the influence of closure stress because the pressure inside the fracture reduces. During this time, the proppants settle and come in contact with the walls of the fracture due to reduction of fracture width. Therefore, to observe fracture closure, the simulation was continued until 10 hours. Figure 6.8 presents the fracture geometry at shutin and closure. The shutin corresponds to the time when injection was stopped. At shutin an average fracture width of 11 mm is created which is around 0.43 inches close to the predicted value of 0.41 inches by Fracpro. During the closure process, the maximum initial fracture half-width reduced from 7 mm to 2.4 mm. The maximum fracture width zone during the fracturing operation is located near the perforations due to high pressure in these zones, but then shifts to the zones having maximum proppant distribution i.e., the zones with maximum proppant kg/m^2. The proppants settle under the influence of gravity and hence settle at the bottom of fracture. This reduces the propped fracture height depriving the upper fractured

zones of proppants and loosing valuable fracture conductivity in those zones. In the current case, the proppants fall to the perforation level. However, due to lower proppant distribution [kg/m^2] in the near injection zone, a fracture half-width of only about 1 mm is retained. This can be a major reason behind the lower productivity.

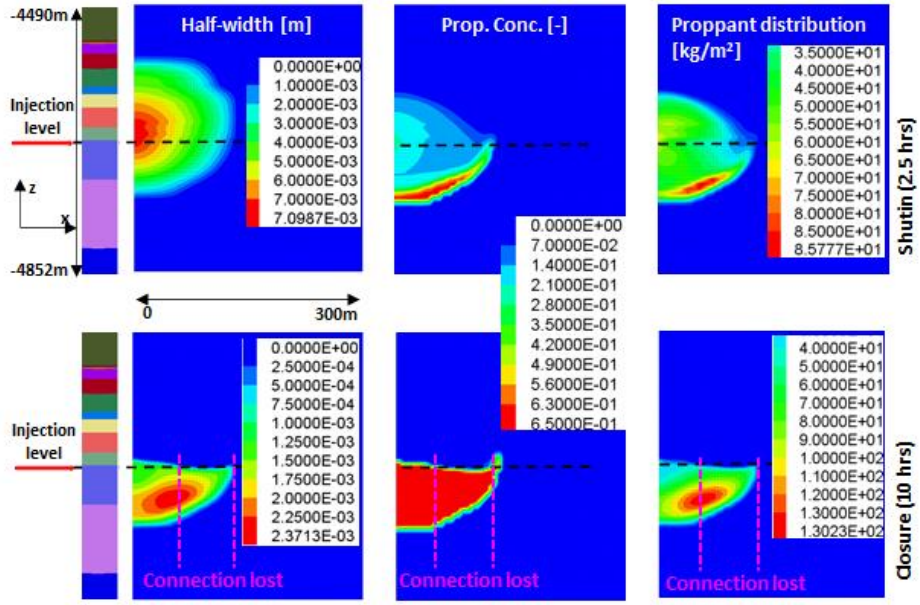

Figure 6.8: fracture half-width, proppant concentration and distribution at shutin and closure (dotted line shows perforation level).

The fracture volume rises during the injection period as long as the leakoff rate is less than the fracturing rate. Generally higher injection rates and fluid viscosity create larger fracture volumes. Figure 6.9 shows the evolution of fracture volume until shutin and then decline. Initial fracture volume of 280 m^3 is created until shutin, however after injection is stopped the fracture closure and fluid fluid leak reduce the volume which in this case reduced to 56 m^3.

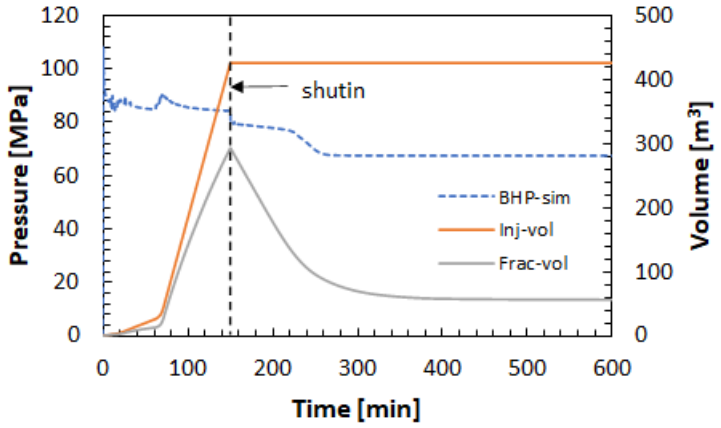

Figure 6.9: injection and fracture volume (simulated BHP trend is also plotted).

Fluid viscosity plays an important role in the geometry of the fracture. The fluids are gelled and crosslinked so that they can retain viscosity for proppant transport and avoiding large fluid losses. Once

the injection is stopped, the proppants settle and gel breaks. The temperature of the reservoir is very high ranging between 418-423 K (145-150 °C). therefore, as the gel breaks the fluid starts to leak-off to formations and fracture closure starts. Temperature is one of the major factors controlling viscosity. The viscosity and temperature profile are presented in Figure 6.10 at shutin and closure. Due to injection of fluid at lower temperature compared to reservoir, the temperature of the reservoir drops as can be observed from temperature contour at the shutin. But since the reservoir temperature is very high, the fluid temperature rises gradually due to heat transfer between formation and fluid. As the fluid temperature rises, the viscosity of the fluid decreases and it reduced to about 0.02 Pa.s from initial viscosity of more than 0.2 Pa.s.

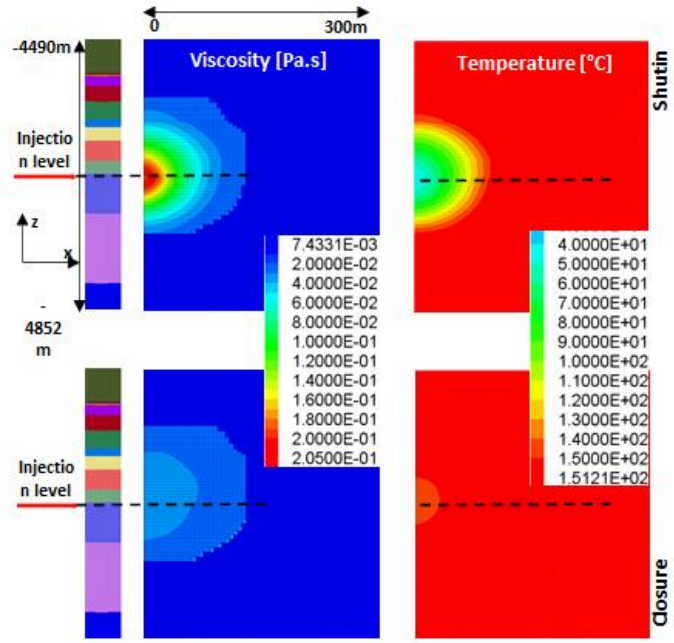

Figure 6.10: viscosity and temperature profile at shutin and closure.

6.3 Production history match

The production from wellbore yx1 remained low and only 2.016 million m^3 could be recovered and then closed. However, the initial reserves showed 645 million m^3 in place gas. Since it is a tight gas reservoir therefor, hydraulic fracturing was performed which could not provide with the desired results. As discussed in the previous section, the problem may be due to poor hydraulic connection between propped fracture and injection zone. Due to very low fracture aperture in the near perforation zone, the productivity remained low. The production was not continuous, and the well was shutin for many times during this period.

In this section, the production history match is performed after the fracture creation. Producing from the formation changes the pressure distribution which leads to stress redistribution. However, as the production was low, the possibility of stress change is less. According to the space discretization, the

matrix zone hosts the fracture zone, therefore the permeability of these zones can be found from the following correlations (Figure 6.11) (Li, 2018):

$$k_x = \frac{x_1 k_1 + w_f k_f}{x_1 + w_f} \tag{6.1}$$

$$k_y = \frac{x_1 + w_f}{\frac{x_1}{k_2} + \frac{w_f}{k_f}} \tag{6.2}$$

$$k_z = \frac{x_1 k_3 + w_f k_f}{x_1 + w_f} \tag{6.3}$$

Where:

k_x, k_y, k_z: zone permeability containing fracture [m^2]; k_f: propped zone permeability [m^2]; k_1, k_2, k_3: matrix permeability in x, y and z directions [m^2]; x_1: width of matrix zone [m] and w_f: fracture width [m].

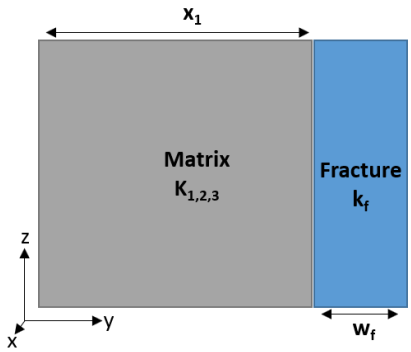

Figure 6.11: fracture zone permeability calculation (modified from (Li, 2018)).

At the closure after fracking, the fracture properties are exported from FLAC3D^{plus} and provided in the infile of TMVOC. The measured BHP are specified in the infile, which TMVOC then sends to FLAC3D^{plus} during simulation. The stress redistribution because of reduced pressure is calculated in FLAC3D^{plus}. The results of production simulation and its comparison with measured data is presented in Figure 6.12

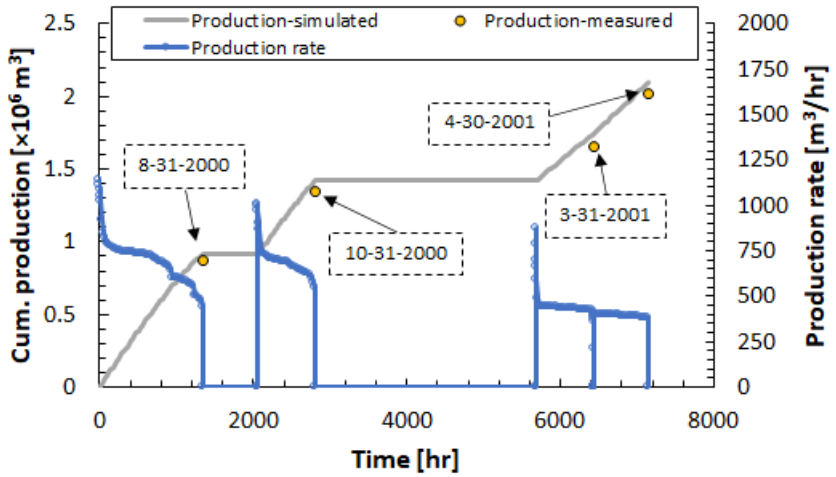

Figure 6.12: simulated cumulative production and production rates comparison with data points from measured production.

The hydraulic fracturing operation was performed in July 2000 and production started same month after it. The production remained low and was stopped at the end of April 2000. During this period, production was taken only in the months of July, August, October 2000 and March-April 2001. Figure 6.13 presents the results according to the measured bottomhole pressure during production phase.

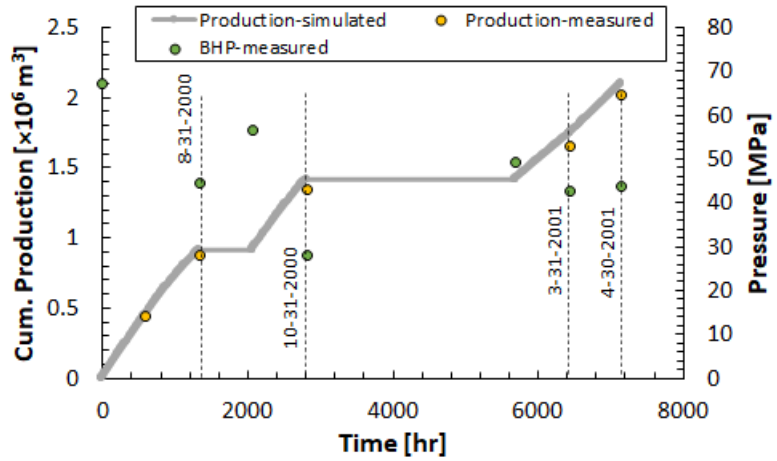

Figure 6.13: production history match against BHP with measured data.

For the designing of hydraulic fracturing operation with proposed fluid, the pressure current pressure situation needs to be understood. Therefore, the pressure profile from the initial fracturing operation until 2019 is simulated. The results are presented for different time points of production and shutin in the Figure 6.14. Due to lower fracture conductivity, formation permeability and lower production, the pressure response remained in the near wellbore zone.

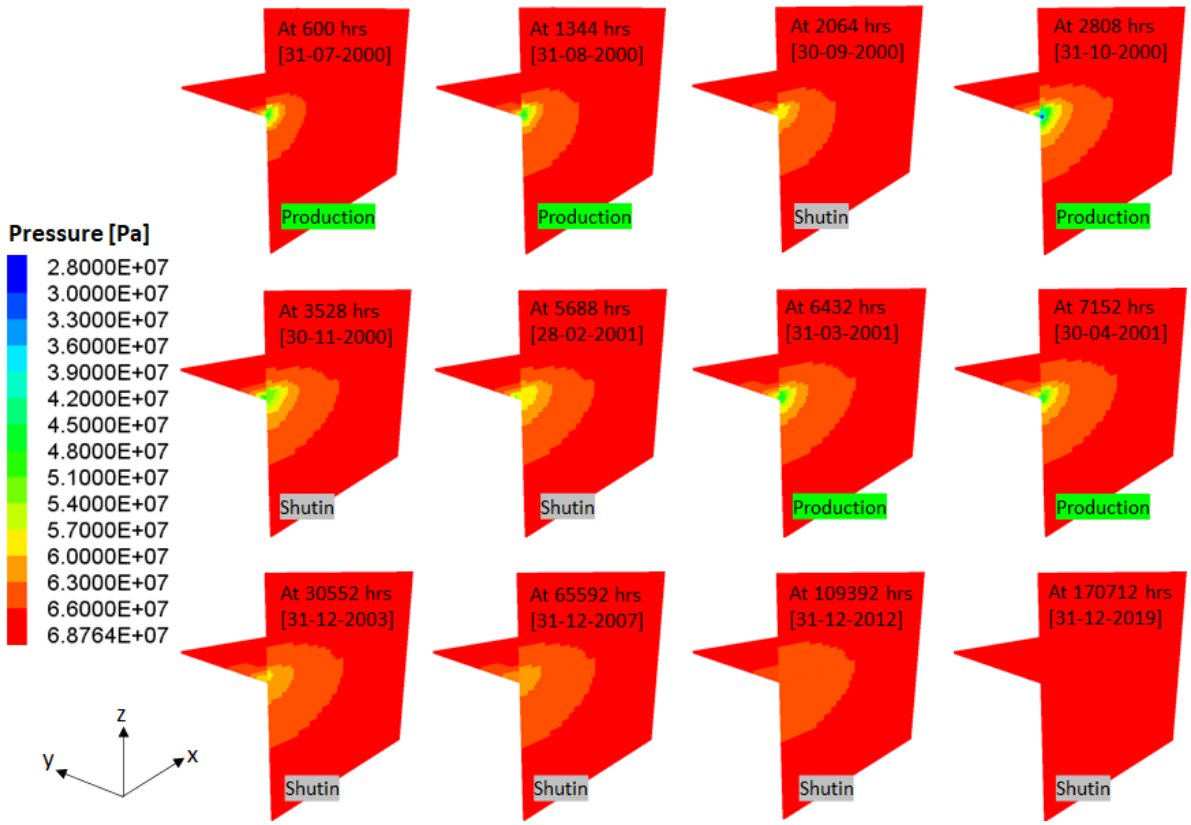

Figure 6.14: reservoir pressure profile at different times of production and shutin.

The pressure profile in Figure 6.15 suggests that if stimulation is performed now, the reservoir will be at its initial stress state.

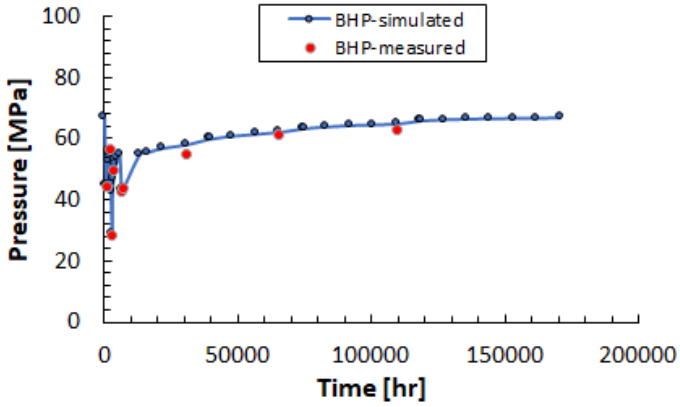

Figure 6.15: simulated BHP profile until December 2019 and its comparison with measured BHP.

6.4 Stress state

To carry out the hydraulic fracturing operation at this stage, it is important to consider the current stress state in the reservoir and direction of principal stresses. considering normal fault conditions, if the difference between the maximum and minimum horizontal stress is small, then due to mechanical and poroelastic effects the stress orientation may change. The hydraulic fracture propagates perpendicular to the least principal stress, therefore the minimum principal stress increases. If the difference between

minimum and maximum horizontal principal stress is small, the minimum horizontal principal stress exceeds the maximum horizontal principal stress. Therefore, the direction of the least principal stress reverses in the region of influence. This region of influence is called the stress reversal region. The poroelastic effects on stress reorientation can be observed due to production from a reservoir. This happens due to more pressure depletion parallel to the fracture than in the perpendicular direction. Due to the stress reorientation due to mechanical or poroelastic effects, the re-fracture propagates in a different direction compared to the initial fracture direction in the region of stress change which starts at the wellbore (Figure 6.16) (Hagemann et al., 2013; Li et al., 2019; Lu et al., 2020; Radwan and Sen, 2020; Roussel and Sharma, 2012; Zhang and Chen, 2010; Zhou et al., 2015).

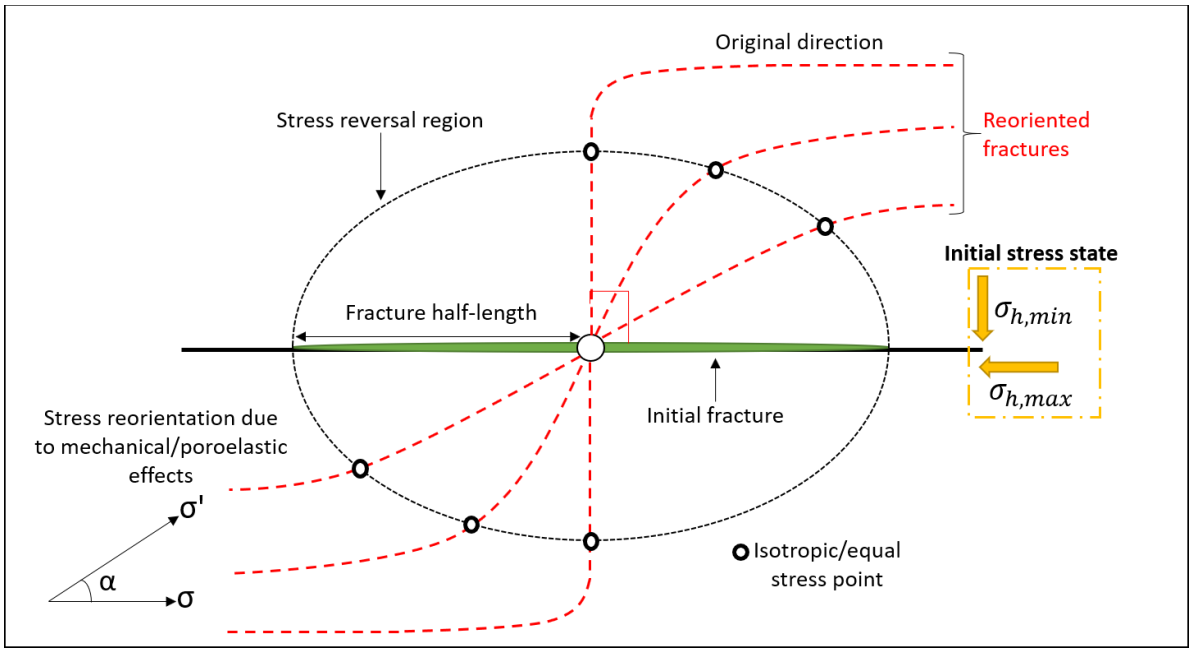

Figure 6.16: concept of stress reversal region due to mechanical and poroelastic effects.

Based upon the hydraulic fracturing and production history match performed in previous sections, the stress reorientation at different at different times of production after fracturing was determined for wellbore yx1 (Figure 6.17).

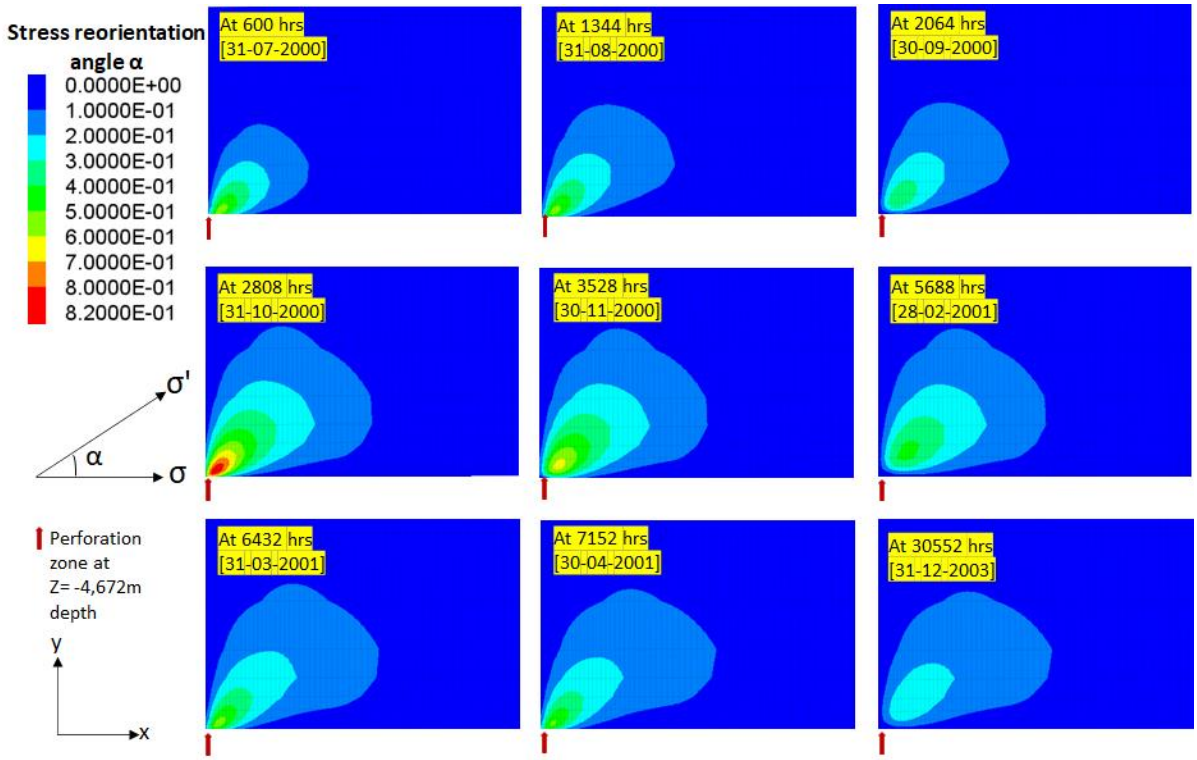

Figure 6.17: angle of stress reorientation during and after production until 2003.

The hydraulic fracturing was performed almost twenty years before and the production of only about 2 million m^3 could be taken. Therefore, the mechanical and poroelastic effect upon the stress reversal are minimum which could be observed from Figure 6.17, where a maximum angle of stress reorientation of only 0.82° during production in October 2000 was created. The production was followed by shutin, therefore by the end of 2003, the stress orientation can be considered negligible for all practical purposes. This leads to the conclusion that, refracturing operation now will follow the path of initial fracture. Therefore, the reservoir can be considered at its initial stress state and pressure conditions.

6.5 Important parameter analysis

The injection fluid properties such as injection fluid viscosity, injection rate, injection volume and proppant properties are crucial for the success of hydraulic fracturing design and operation (Daneshy, 2010; Duan et al., 2018). As discussed in the previous sections, if injection rate is higher than the leakoff rate, the fracture propagates. It takes longer to induce fracture at lower injection rates. However, at higher injection rates, higher pressure requirements and fracturing speeds are observed. Difference in injection rates also lead to different fracture geometries (Duan et al., 2018; Morgan et al., 2017). Fluid viscosity has a significant bearing not only on fracture initiation, propagation, and geometry but also on the fluid infiltration rate. Higher viscosity fluids increase the injection pressure requirements for formation breakdown but are needed for proppant transport and avoiding excessive fluid loss into the matrix from fracture (Barati and Liang, 2014; Duan et al., 2018; Shimizu et al., 2011; Zoback et al., 1977).

To design the fracture treatment schedule with hybrid-intelligent fluid, initially simulation was performed for a period of 75 minutes with 4, 6 and 8 m^3/min injection rates. The fracturing started with water-based fluid to avoid excess surface injection pressure requirements due to lower density of light alkanes compared to water. The process was followed by n-Heptane (light alkane) injection from 8-30 minutes and then with gelled n-heptane (0.15 Pa.s) from 30-45 minutes. The PVT behavior of n-heptane (C_7H_{16}) was already presented in Figure 3.11.

This analysis was performed to help understand the effect of pure and gelled fluid for different injection rates on fracture propagation in the presence of formation fluids.

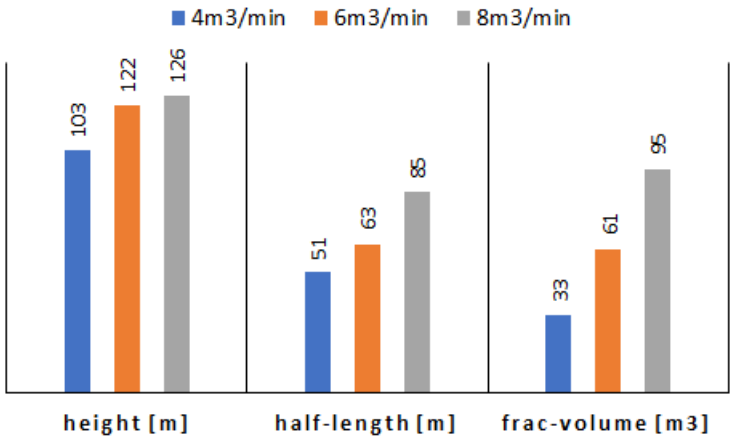

Figure 6.18: fracture height, half-length and volume because of different injection rates.

Based upon the performed simulations, the results are presented in Figure 6.18 and Figure 6.19. Although the injection time was same but due to different injection rates 300, 450 and 600 m^3 fluid was injected for 4, 6 and 8 m^3/min rates. Higher fracturing rates with higher injection rates and more fracture volume are to be expected compared to lower injection rates for the same time period. Therefore, fracture height of 103, 122 and 126 m, fracture half-length of 51, 63 and 85 m, and volume of 33, 61 and 95 m^3 are created with the applied injection rates of 4, 6 and 8 m^3, respectively. The results are as expected however, the fluid leakoff is high (Figure 6.18). The higher injection rate not only led to higher fracture height and half-length, but also more fracture width compared to lower injection rate cases. With the current injection strategy maximum fracture width of 1.06 cm can be created with highest injection rate simulated Figure 6.19.

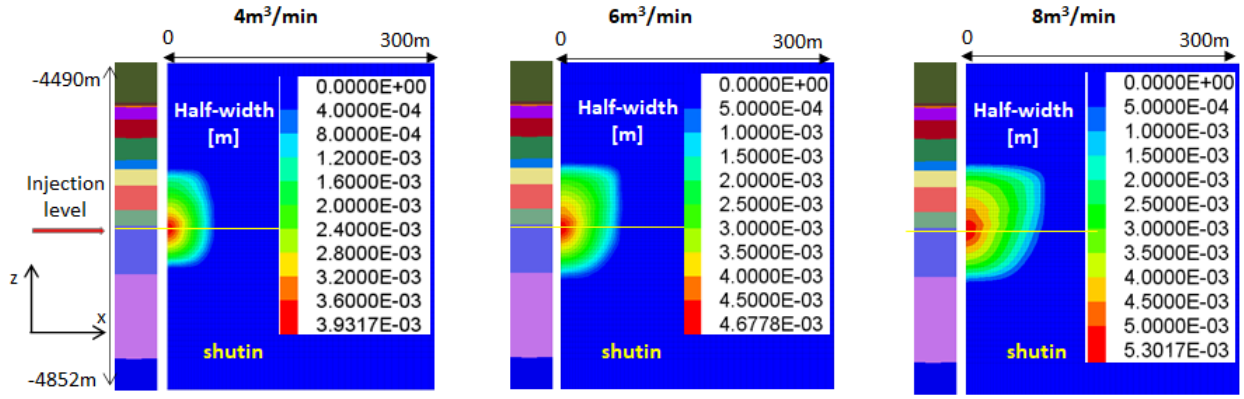

Figure 6.19: fracture geometry for different injection rates at the end of injection.

Although, the increase in fracture width is observed for increasing injection rate, the fracture half-lengths for the corresponding injection volumes are low. This is due to high leakoff to surrounding formation during the injection of pure frac-fluid without any gelling. The fracture volume evolution profile can be observed for the three cases from Figure 6.20. For the first thirty minutes of injection, the fracture volume is a little above 0 m^3 which shows that the fluid leakoff is very high and the injection rate is a little higher than the fluid infiltration rate. This high leakoff is due to lower viscosity of pure n-heptane which is only 0.00035 Pa.s at standard conditions. The reservoir temperature is in excess of 418.15 K (145 °C), and when the fluid comes in contact with the formations, the viscosity further decreases due to heat exchange between formation and injected fluid. After the initial half an hour of injection, high viscosity fluid is injected, and it increases the fracture volume due to lower leakoff of gelled fluid.

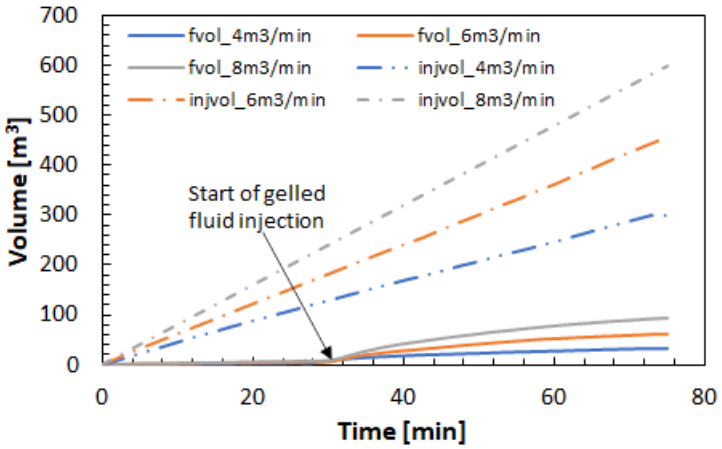

Figure 6.20: comparison of fracture volume for different cases (fvol: fracture volume, injvol: injection volume).

Similar behavior can be observed for the fracture width evolution where the width remained low during the pure fluid injection and then increased immediately in the injection zone when the high viscosity fluid injection started. Figure 6.21 is divided into two sections A and B, section A corresponds to pure

fluid and section B belongs to high viscosity fluid injection. The rise in fracture pressure in the beginning of section B represents the high viscosity fluid injection.

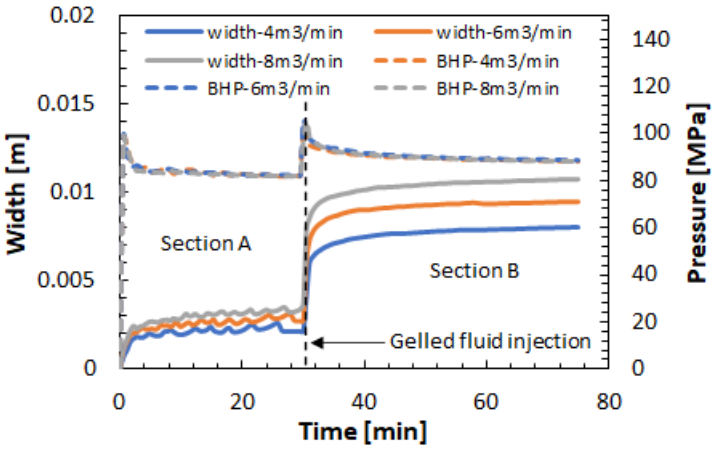

Figure 6.21: fracture width and pressure profile of injection zone until shutin.

The permeability of the reservoir zone lies in the range of 4.88×10^{-16}-9.5×10^{-16} m^2, which cannot be regarded as ultra-tight reservoir. Therefore, injecting pure fluid will create a thin fracture and excessive leakoff. Hence it is recommended to use higher viscosity gelled fluid from the beginning. In addition, injection rates of 6-8 m^3/min can generate better fracture geometries compared to lower injection rates with proposed fluid. Since no chemical additives are used, therefore, at such a high reservoir temperature, the reduction of fluid viscosity/gel break will be quick. In order to optimize the injection strategy, sensitivity analysis is performed for important parameters including:

- Fluid viscosity and injection rate
- Injection time
- Reservoir permeability

6.5.1 Fluid viscosity and Injection rate

Numerous simulations were performed for stimulation with proposed fluid to analyze the effect of injection rate and fluid viscosity on fracture geometry, fracture pressure, fracture height, half-length and aperture. The reservoir temperature is in excess of 418 K which is much higher than the boiling point of injection fluid hence upon full back the proposed fluid will have reduced viscosity, density and may change its face if appropriate conditions are met. To make detailed analysis injection rates off 4 to 8 m^3/min and fluid viscosity 0.15 to 0.45 Pa.s was utilized. Although the leak of in this reservoir with proposed fluid is more requiring higher injection rate then 4 m^3/min but to investigate the effect of varying fluid viscosity lower injection rate is also simulated. Once again, the concept of hybrid fluid is utilized in which water is injected for the initial 8 minutes at a maximum injection rate of 4 m^3/min followed by the gelled n-heptane injection. The total injection period was 75 minutes without proppant

injection. It should be noted that the non-isothermal flow simulations were carried out in all cases to observe the effect of heat exchange between formation and fluid on fluid viscosity.

The results for different injection rates and injection viscosities for fracture height, half-length, volume, aperture etc., are plotted together to analyze their influence. The smallest fracture geometry is obtained for lowest injection rate and viscosity combination and the fracture dimensions increase as they are increased. For the case of 4 m^3/min injection rate at 0.35 Pa.s, fracture half-length of 63 m and 53 m^3 volume are obtained which is considerably less than other cases. For the case of 6 m^3/min and 8m^3/min injection rates at 0.15 Pa.s viscosity , the corresponding half-length and fracture volume are 76 m and 95 m and 75 m^3 and 112 m^3, respectively. Similarly, the fracture heights are also noticeably more for higher injection rates than the lower injection rate of 4 m^3/min. Increasing the fluid viscosity from 0.15 to 0.45 Pa.s results in higher half-length and volume of 85 m and 101 m^3 for 6 m^3/min case and 105 m and 155 m^3 for 8 m^3/min injection rate case (Figure 6.22).

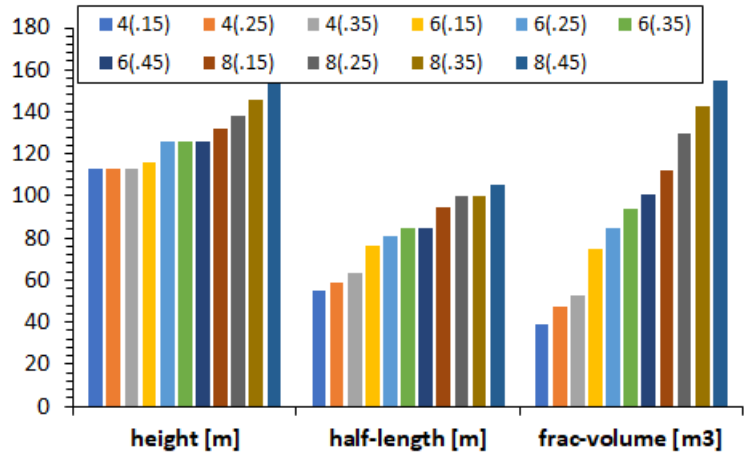

Figure 6.22: fracture height, half-length and volume for different viscosity fluids at injection rates of 4, 6 and 8 m^3/min at the end of injection.

The fracture width increases with time as injection continues. Increasing the injection rate creates more fracture volume as the difference between injection rate and leakoff rate increases. Increasing the viscosity lowers the fluid leakoff. For the low injection rate of 4 m^3/min, the leakoff is more and maximum fracture width is less than 1 cm. Increasing the injection rate to 6-8 m^3/min and increasing the viscosity from 0.15 to 0.45 Pa.s increases the fracture width. And with these combinations, fractures with maximum half-widths around 1 cm to 1.34 cm can be created in addition to better half-length and more height fractures. Figure 6.23 presents the fracture geometry for 6 and 8 m^3/min injection rates at the end of injection. With water-based fluids more fracture width can be created but that is not the objective as thin fracture is more suitable for better proppant placement especially at the upper half of fracture.

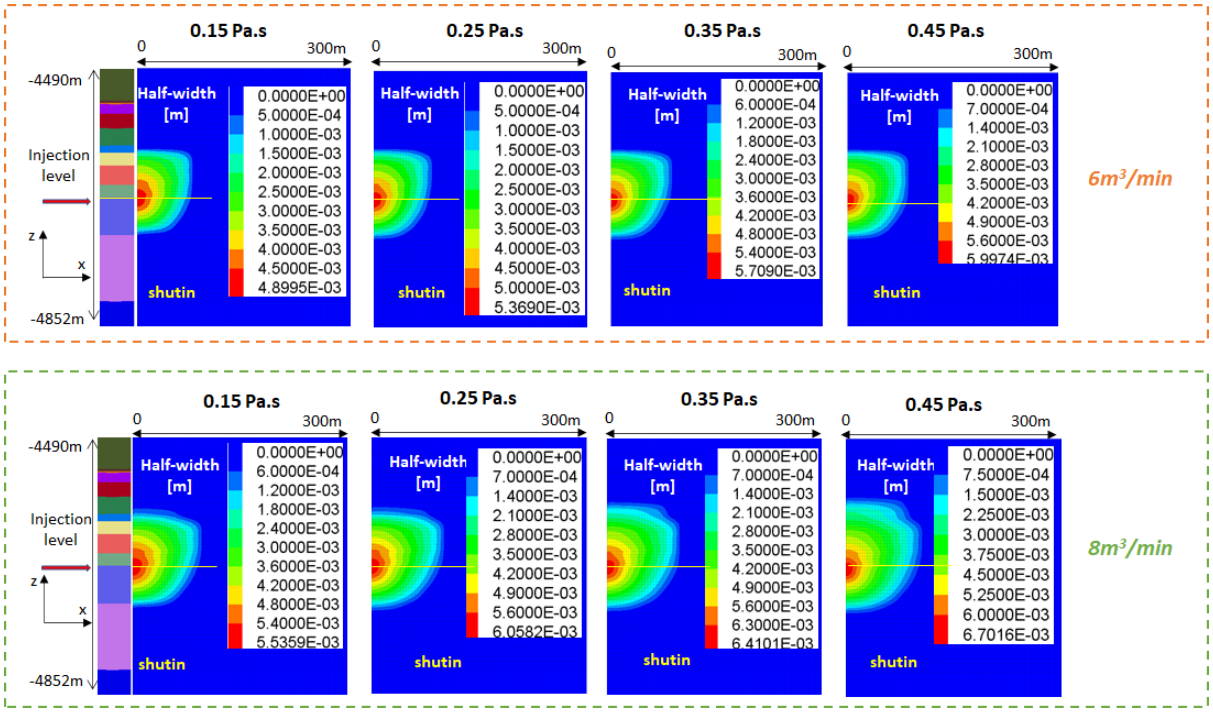

Figure 6.23: fracture geometry for different viscosity fluids at injection rates of 6 and 8 m³/min.

The reason behind lower fracture volume is excessive leakoff of frac-fluid to formation. Since, no chemical additives are utilized to keep the fluid gelled under high reservoir temperature conditions, therefore, as the temperature of fluid rises, the viscosity decreases, and fluid is leaked to the surrounding formation. Also, the rate of penetration is low at lower injection rates, so fluid gets more time to leakoff.

The gel break of fluid is dependent upon the surrounding temperature; therefore, the proposed fluid's viscosity decreases quickly compared to water-based fluid which has higher heat. The fluid leakoff however is desirable and higher injection rates can result in optimum fracture geometry and fracture aperture which is sufficient for proppant transport during injection. The fracture volume evolution for 4, 6 and 8 m^3/min at different viscosities ranging from0.15 to 0.45 Pa.s can be observed from Figure 6.24. Increasing the injection rate lowers the leakoff rate and frac-fluid spends more time in the fracture, thereby increasing the volume. Therefore, for fluid viscosity of 0.15 Pa.s, the fracture volume is 13%, 17.3% and 19.7% of the injected volume of 300 m^3, 432 m^3 and 567 m^3 for 4, 6 and 8 m^3/min injection rate. Whereas, 17.7%, 21.8% and 25.2% is the ratio of fracture to injected fluid volume when the viscosity is increased to 0.35 Pa.s for 4, 6 and 8 m^3/min injection rates, respectively.

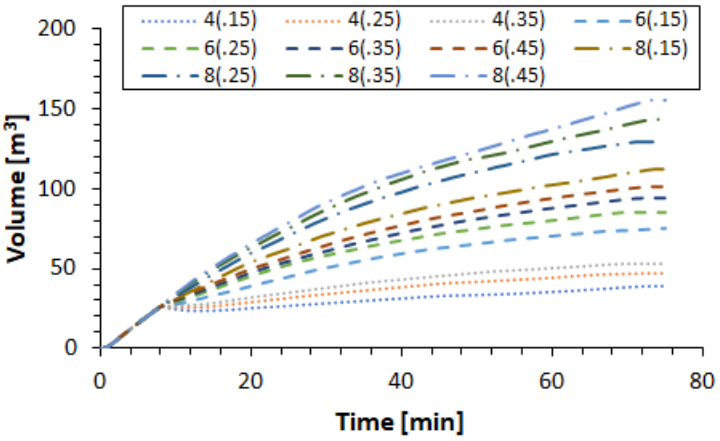

Figure 6.24: fracture volumes for varying viscosities at injection rates of 4, 6 and 8 m^3/min.

The fracture aperture or width i.e., the distance between the walls of the fracture is an important design parameter especially with reference to proppant transport. The diameter of the proppant should be 2-3 times smaller than the fracture width so that the proppants can be placed efficiently until the tip of fracture and avoiding premature tip screen out. Therefore, a reasonable width creation is important for effectiveness of the fracture job. As discussed earlier, increasing the injection rate and fluid viscosity increase the fracture aperture. Hence, maximum fracture aperture is created with 8 m^3/min injection rate and viscosity of 0.45 Pa.s. The fracture width temporal evolution in the injection zone for different sensitivity cases can be seen from Figure 6.25.

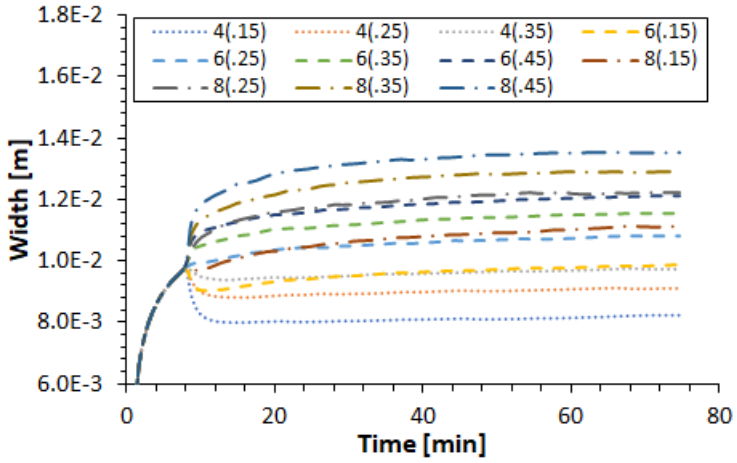

Figure 6.25: fracture width evolution in the injection zone for different viscosity fluid at 4, 6 and 8 m^3/min injection rate.

6.5.2 Injection time

In the previous section, it was found that higher injection rates (6-8 m^3/min) can create better fractures in this reservoir. However, it is important to understand the influence of different injection times on the hydraulic fracture propagation and geometry. Previously, simulation time for fluid injection was 75 minutes (1.25 hours) for all the cases. Therefore, to perform injection time sensitivity analysis, injection

periods were varied from 1.25 hours to 2 hours and 6 and 8 m^3/min injection rates. Increasing injection time increases the injection volume but can further improve the fracture conductivity. The viscosity was varied between 0.15 Pa.s and 0.35 Pa.s. The results are plotted in Figure 6.26.

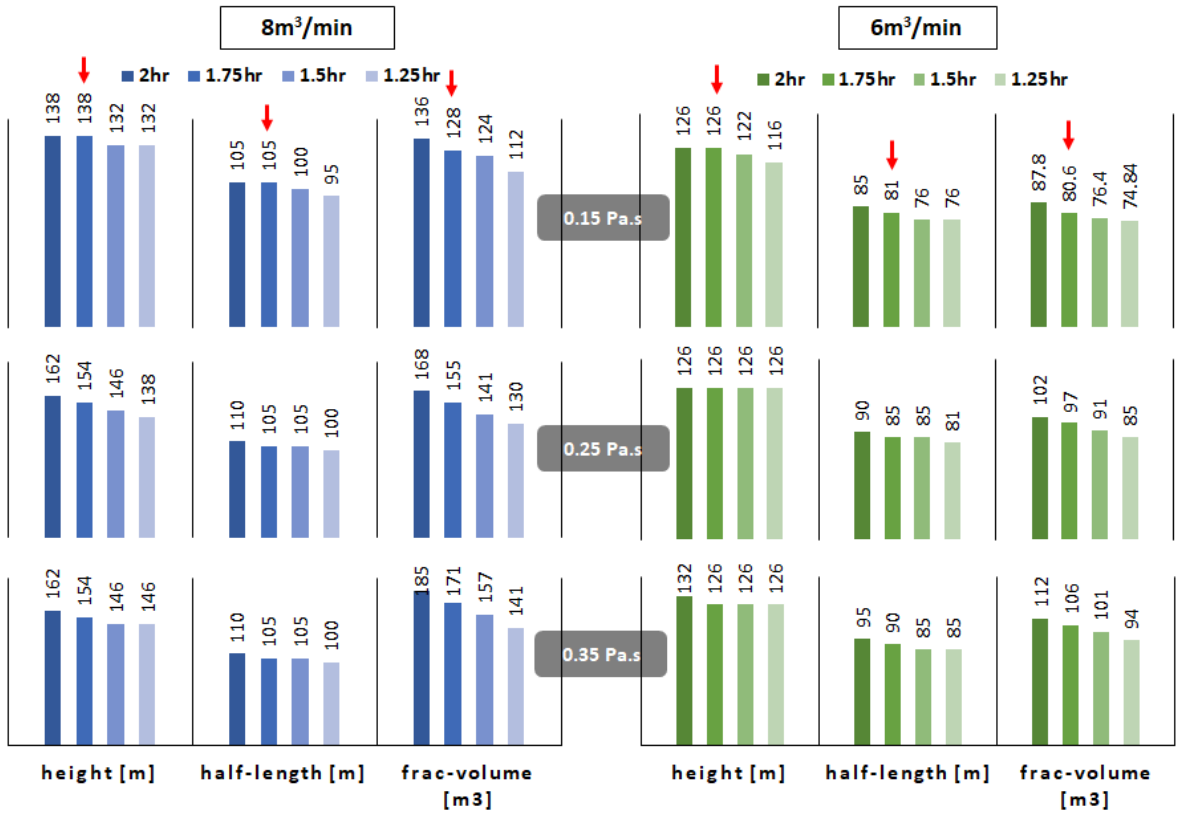

Figure 6.26: fracture heights, half-lengths and volumes for different injection times for 0.15 Pa.s, 0.25 Pa.s and 0.35 Pa.s fluids at 6 and 8 m^3/min injection rates.

It can be noted that higher rate and more time for fluid injection at more viscosity can generate attractive fracture geometry. But on the other hand, can increase the expenses. Therefore, optimum injection strategy is chosen from the obtained results and is marked with red arrows on Figure 6.26. An injection time of 1.75 hours (105 minutes) for 0.15 Pa.s fluid viscosity with 6-8 m^3/min injection rates can yield satisfactory results. For 6 m^3/min, a fracture with half-length of 81 m and height of 126 m can be created. Whereas 8 m^3/min injection rate should be utilized if desired half-length is more than 100 m.

6.5.3 Reservoir permeability

Wellbore yx1 with permeability range from 4.88e-16 to 9.5e-16 cannot be regarded as ultra-tight. Therefore, simulation is performed to observe the performance of proposed fluid for varying permeability by a factor of 0.01 and utilizing different hybrid fluid design scenarios. Table 6.3 summarizes different design parameters.

Table 6.3: details of fracture job design for different cases.

75 min (300 m^3 injected)		
Case-1	Original permeability	Water+light alkane+gelled fluid (0.15 Pa.s)
Case-2	Original permeability	Gelled fluid (0.15 Pa.s)
Case-3	Permeability × 0.01	Water+light alkane+gelled fluid (0.15 Pa.s)

Fracture volumes of 33 m^3, 39 m^3 and 200 m^3 were created for cases 1, 2 and 3, respectively. A significant increase of more than five times in the fracture volume for case-3 (lower permeability case) shows the major influence of reservoir permeability on fracture propagation with proposed fluid. Whereas, 51 m, 55m and 149 m half-length fractures were generated for the three cases, respectively. Almost three times increase in fracture half-length (Figure 6.27) is seen while injecting clean fluids for the first thirty minutes and then continuing with higher viscosity fluid. The fracture height is also larger for case-3 compared to other cases.

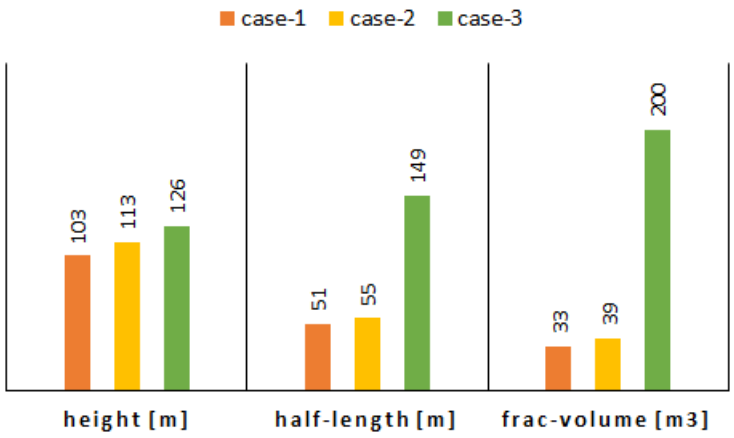

Figure 6.27: fracture height, half-length and volume for different cases.

Fracture geometry can be observed from Figure 6.28. A significant difference between the created fractures is evident. Case-3 with lower permeability shows a marked improvement in fracturing efficiency. Maximum fracture half widths of 3.9 mm, 4.0 mm and 5.3 mm for cases1, 2 and 3, respectively, are generated. The lower leakoff due to ultra-tight reservoir in case-3 resulted in creating a wider fracture aperture.

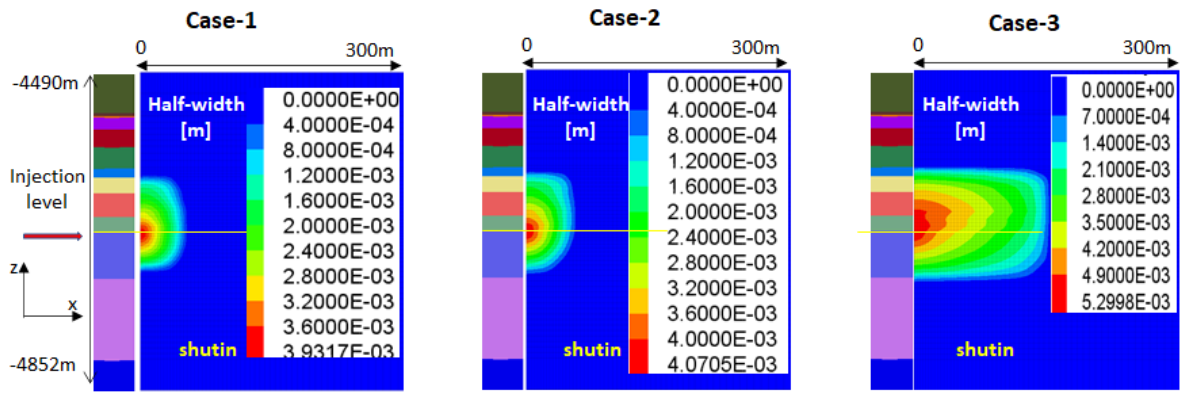

Figure 6.28: fracture geometry for different cases.

Figure 6.29 shows the comparison between injection and fracture volume for the discussed cases. Although the injection fluid design for case-3 is similar to case-1, the fluid leak for case-3 is minimum compared to other cases, whereby 89%, 87% and 33% fluid leakoff were observed for cases 1, 2 and 3, respectively. It shows that pure fluid injection can create sufficient conductivity fractures in ultra-tight reservoirs even at high temperatures.

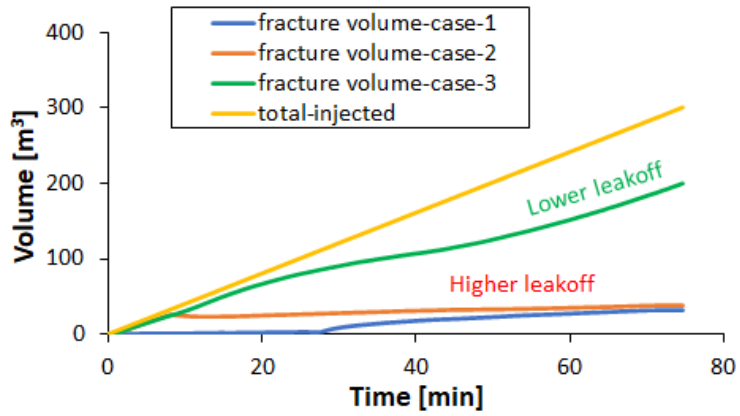

Figure 6.29: fracture volumes for different cases.

Based upon the sensitivity analysis, formation permeability is one of the most important parameters, but it is an uncontrollable factor. Therefore, the parameters such as injection rate and fluid viscosity can be controlled in a manner to optimize the fracture geometry. The proposed injection rates for the reservoir in question are 6-8 m^3/min with fluid viscosity of 0.15 Pa.s. The reason of choosing this viscosity value is based upon the efficiency of proppant placement and added advantage of lower surface injection pressure requirements. Lower viscosity will create a comparatively thin fracture. When the injection is stopped, the fracture closure will be quick as discussed in the previous sections. Therefore, the proppants will come in contact quickly with the walls of the fracture and will be retained at upper half of the fracture rather than falling to the bottom under the gravitational forces, which may disconnect the hydraulic connection between fracture and perforation level.

6.6 Frac-fluid flowback

To understand the flowback behavior of proposed fluid, hydraulic fracturing simulation was performed with proposed and water-based fluid. The injection schedule is presented in Table 6.4 and can also be observed from Figure 6.30 with details of proppant injection schedule.

Table 6.4: injection schedule for water-based and proposed hybrid fluid.

1. Conventional (375 m^3)				**2. Hybrid-fluid (375 m^3)**			
	Injection fluid	Total injected (m^3)	Injection time (min)		Injection fluid	Total injected (m^3)	Injection time (min)
Stage-1	Water	195	0-40	**Stage-1**	Water	30	0-6
Stage-2	Slurry	180	40-77	**Stage-2**	n-heptane	166	6-40
				Stage-3	Slurry	179	40-77

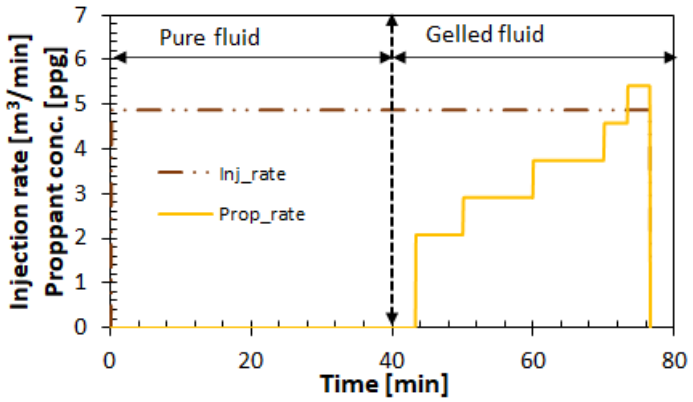

Figure 6.30: injection schedule (w: water-based fluid, hf: hybrid n-heptane).

Figure 6.31 shows the fracture and injection volume of the fracking operation. The fracture closure for water-based fracture takes place at about 400 minutes whereas, fracture closed at 150 minutes for n-heptane.

After the fracture closure and proppant placement, simulation is carried out to observe the fluid flowback for both the cases. The obtained results for one day and seven days can be seen from Figure 6.32. The lower density and viscosity of proposed fluid greatly help in the flow back compared to water based fluid. At the end of seven days, more than 90% of the n-heptane from the propped fracture zone has been recovered whereas, most of the water-based fluid remains in the reservoir. The saturation contour of reservoir gas at one and seven days of flowback is also very interesting to note. For the n-heptane case, the propped fracture zone is completely occupied by the reservoir gas as injected fluid has been recovered. The reservoir fluid production can start as early as the first day of flow back and continue to increase and reach maximum production within one week of fracturing operation.

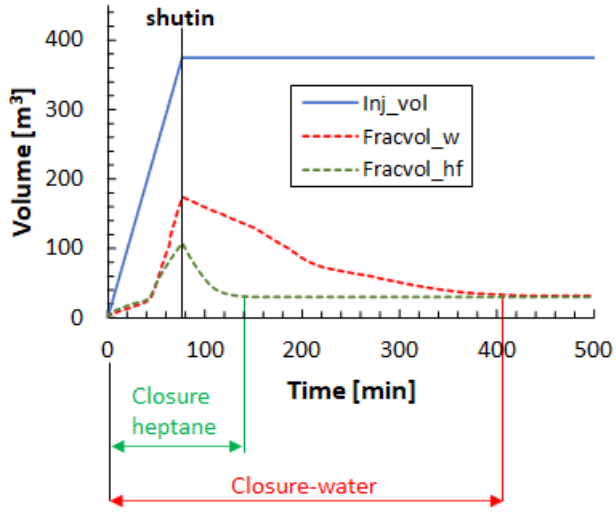

Figure 6.31: difference between fracture volume and closure times for the two cases, w: water-based, hf: n-heptane hybrid fluid.

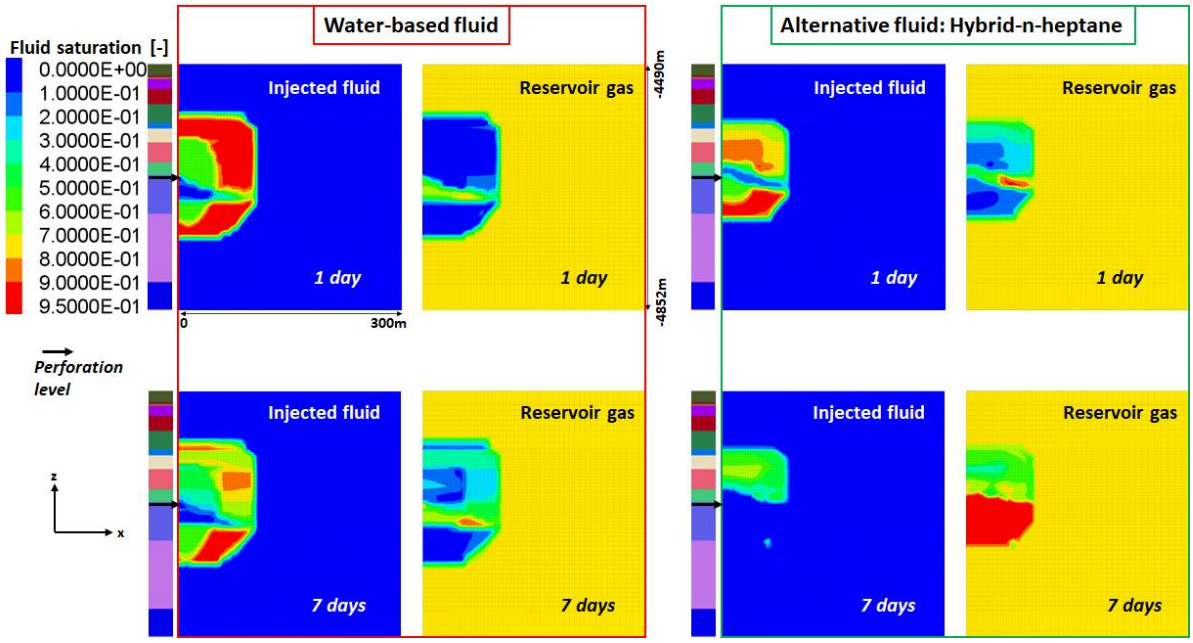

Figure 6.32: saturation contours of reservoir gas and injection fluids after 1 and 7 days of flowback (Mehmood et al., 2021).

6.7 Design proposals

The hydraulic fracture design is generally based upon the conductivity of the created fracture. The higher the conductivity, the better the production performance after fracturing. The fracture conductivity F_c given by Equation (6.4) is simply the ability of created fracture to transmit the reservoir fluid to wellbore which is a product of fracture permeability with fracture aperture (Economides and Nolte, 2000). Whereas, in tight reservoirs a more realistic approach is to include the potential of reservoir to feed the fracture in the fracture conductivity F_c making it dimensionless fracture

conductivity F_{cd} (Equation (6.5)). This idea was introduced by Prats and is analogous to Highway concept where the numerator '$k_f w$' is similar to capacity of Highway and the denominator 'kx_f' is the traffic joining the Highway from feeder roads (Economides and Nolte, 2000; Prats, 1961).

$$F_c = k_f w \tag{6.4}$$

$$F_{cd} = \frac{k_f w}{k x_f} \tag{6.5}$$

The above approaches have been vastly utilized in the petroleum industry for designing hydraulic fracturing operations. However, they cannot identify the situation of hydraulic connection between fracture and perforations. Therefore, a better technique would be to include the position and concentration of proppants with reference to injection/production zone in fracture conductivity. Hou et al., presented the weighted fracture conductivity (Equation (6.6)) which includes the position and concentration of proppants which can better predict the dimensionless fracture conductivity for fracture design. However, it can be considered as a conservative approach (Hou et al., 2020).

$$F_{CD,weighted} = \frac{\sum_{i=1}^{n} \frac{w_i k f_i}{d_i} A_i \frac{c_p}{c_{max}}}{\sum_{i=i}^{n} \frac{1}{d_i} A_i \frac{c_p}{c_{max}}} \times \frac{1}{k x_f} \tag{6.6}$$

where, w:fracture width [m]; kf: fracture permeability [m^2]; d: distance between fracture element and perforation; A: fracture element area [m^2]; c_p: proppant concentration [-]; c_{max}: maximum proppant concentration; k: reservoir permeability [m^2] and x_f: fracture half-length [m] and n: total fracture elements [-].

Several simulations were performed and evaluated to arrive at best proposals for hydraulic fracture design in wellbore yx1. Two of the proposed designs using 6 and 8 m^3/min injection rates are presented in the following section.

6.7.1 Proposal 1

The design schedule is based on the injection of hybrid fluid concept. After initiation of fracture the injection is continued with gelled n-heptane at an injection rate of 6 m^3/min. The proppant injection starts at 40 minutes of fracturing operation. The total injection period is 1.75 hours (105 minutes) during which 614 m^3 fluid and 90 ton proppant are injected. The proppant injection was gradually increased until the end of injection (Figure 6.33).

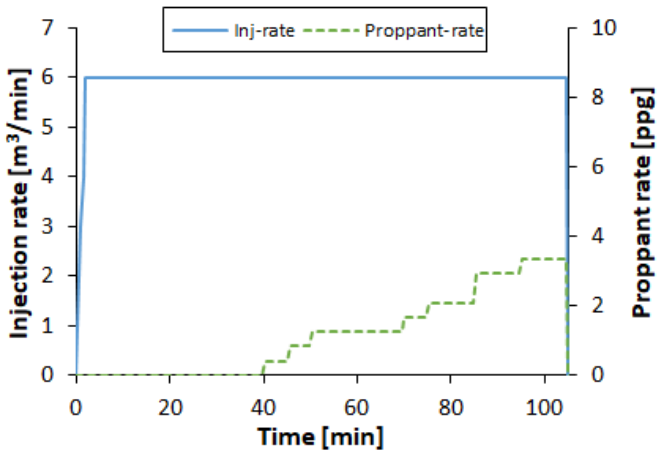

Figure 6.33: fluid and proppant injection schedule for proposal 1.

The fracture profile at the end of injection and closure can be observed from Figure 6.34, which displays contours of fracture half-width and proppant distribution. At shutin, fracture with maximum half-width of 4.91 mm is created which then reduces to 4.69 mm at closure under the closure stress and proppants coming in contact with the walls of fracture. The proppant distribution shows good proppant placement not only in the lower half but also the upper half of fracture creating good hydraulic connection between fracture and perforation level.

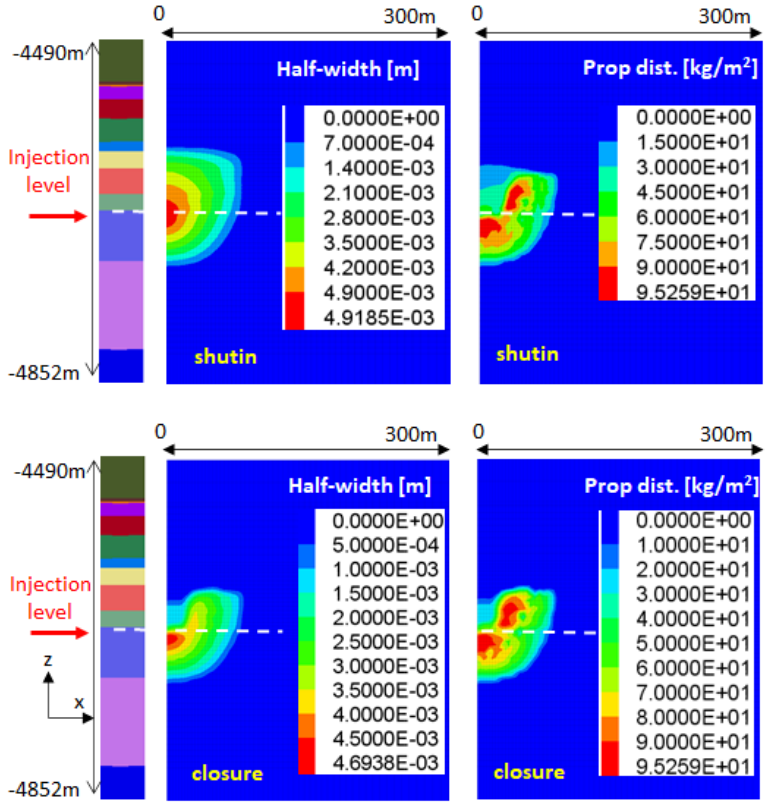

Figure 6.34: contours of fracture half-width and proppant distribution at shutin and closure.

The temperature and injected fluid viscosity profile can be noted from Figure 6.35. Fluid with initial viscosity of 0.15 Pa.s is injected which when comes in contact with formation having higher temperature

(in excess of 418 K), shows maximum viscosity of 0.128 Pa.s. After shutin, as fluid spends more time in the fracture, the temperature of fluid rises due to heat exchange between formation and fluid. The rise in temperature breaks the gel and reduces the fluid viscosity.

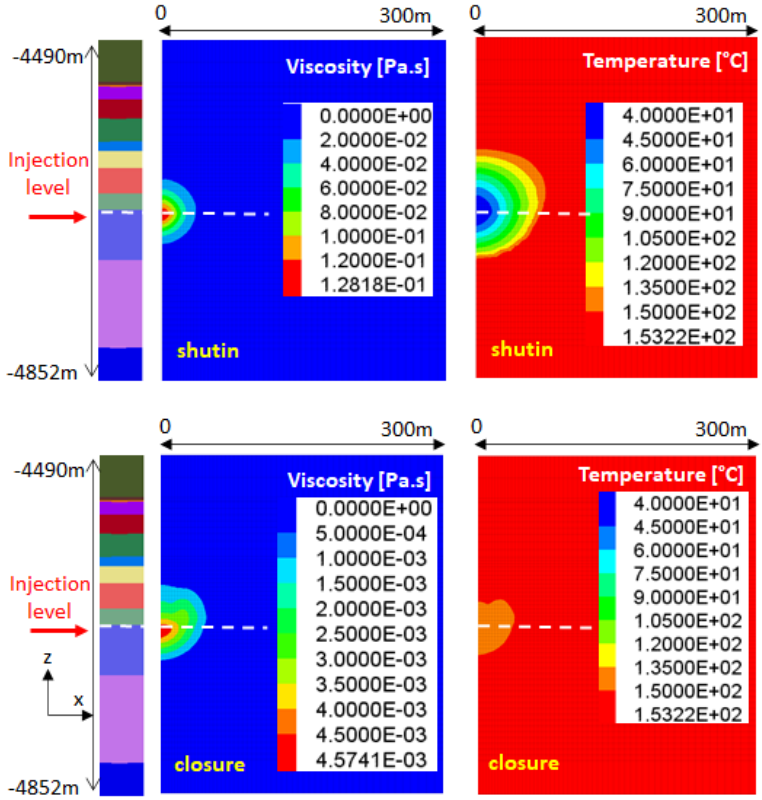

Figure 6.35: contours of injection fluid viscosity and reservoir temperature at shutin and closure.

The injection zone pressure profile and hydraulic fracture volume at shutin and closure are presented in Figure 6.36. The pressure rose initially to more than 100 MPa initiates the fracture. Pressure decline at about 8 minutes shows the starts of injection of proposed fluid whose density and viscosity are different from that of water-based fluid. At shutin, 81 m^3 fracture volume is created which then reduces until the proppants come in contact with the fracture walls due to fracture closure and fluid leakoff. The fracture closure is quick due to reduction in fluid viscosity as a result of temperature difference between fluid and formation. The fracture volume decreases during this phase and is reduced to 52 m^3 at closure.

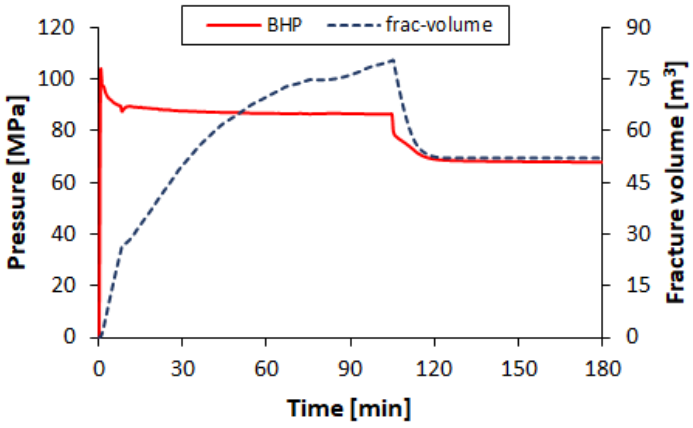

Figure 6.36: fracture pressure profile and fracture volume for proposal 1 from start of injection until 180 minutes.

To show that a good hydraulic connection is maintained at closure between fracture and perforation level, the injection zone fracture width and proppant concentration profile is plotted in Figure 6.37. The fracture width increases as water-based fluid is initially injected which then decreases a little due to n-heptane injection. The width then continues to increase due to injection. At the end of fluid injection, the injection zone width reached 10 mm which then reduced to 8.25 mm due to closure in the presence of proppants. The proppant diameter is about 0.667 mm which means at least 10 proppant layers are present in the width of fracture. A fracture with weighted dimensionless fracture conductivity $F_{cd,weighted}$*: 30* is created, which when evaluated according to dimensionless fracture conductivity F_{cd}*: 123* (Hou et al., 2020; Prats, 1961).

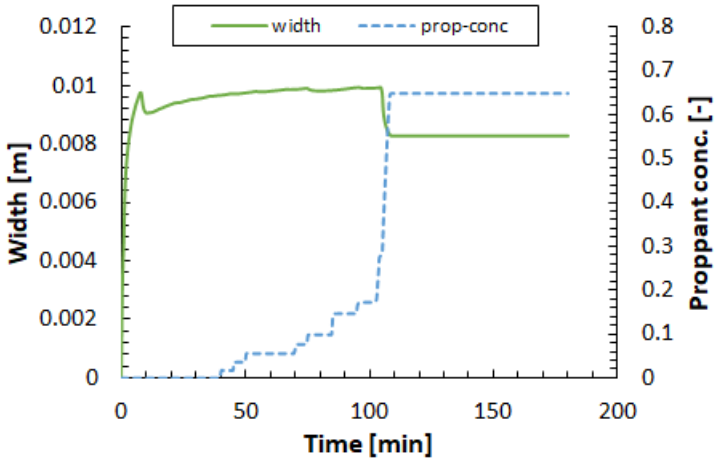

Figure 6.37: fracture width and proppant concentration in the injection zone.

6.7.2 Proposal 2

Similar to previous proposal, hybrid fluid concept is utilized. After initial water-based fluid injection, fracturing is continued with gelled n-heptane at an injection rate of 8 m^3/min. The proppant injection starts at 40 minutes of fracturing operation. The total injection period is 1.75 hours (105 minutes) during

which 808 m^3 fluid and 134 ton proppant are injected. The proppant injection was gradually increased, and it reached maximum concentration of 5.42 ppg (Figure 6.38).

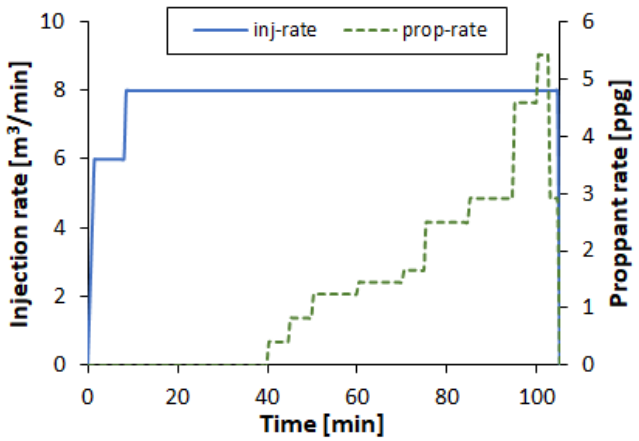

Figure 6.38: fluid injection rate and proppant schedule for proposal B.

Figure 6.39 shows a fracture geometry better than proposal 1. Due to higher injection rate, maximum half-width of 5.58 mm is created which then reduces to 5.35 mm at closure. The maximum proppant concentration in proposal 2 is 116 kg/m^2 which is higher than 95 kg/m^2 maximum proppant concentration in proposal 1. An excellent hydraulic connection exists between fracture and injection zone.

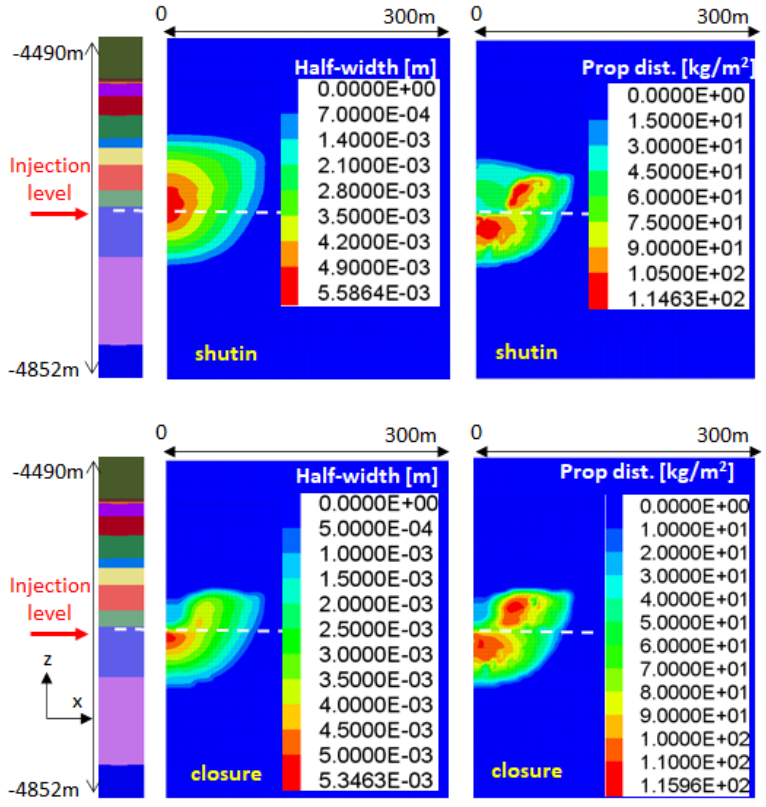

Figure 6.39: contours of fracture half-width and proppant distribution at shutin and closure for proposal 2.

Since the heat capacity of alkanes is less compared to water, the rise in fluid temperature is quick. This leads to quicker gel break of fluid. Though more reservoir volume is contacted in this case, the viscosity and temperature profile are similar in trend to previous case (Figure 6.40).

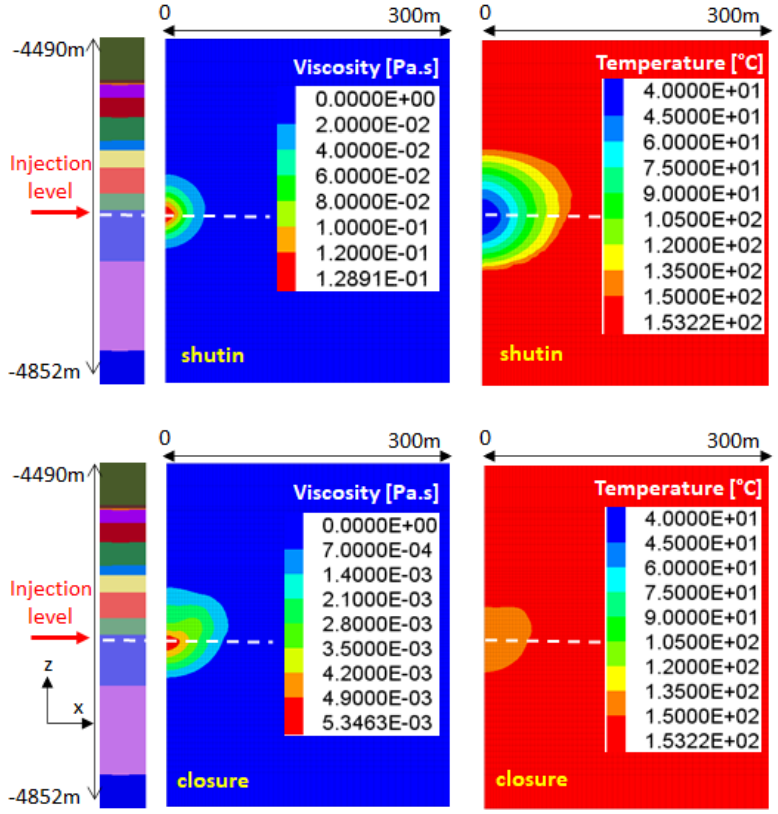

Figure 6.40: contours of injection fluid viscosity and reservoir temperature at shutin and closure for proposal 2.

The injection zone pressure profile and hydraulic fracture volume at shutin and closure are presented in Figure 6.41. Pressure decline at about 8 minutes shows the starts of injection of proposed fluid whose density and viscosity are different from that of water-based fluid, however this decline is less than the proposal 1, because in this case the injection rate is high although fluid viscosity and density are similar. Fracture volume of about 130 m^3 was created initially which then reduced to 80 m^3.

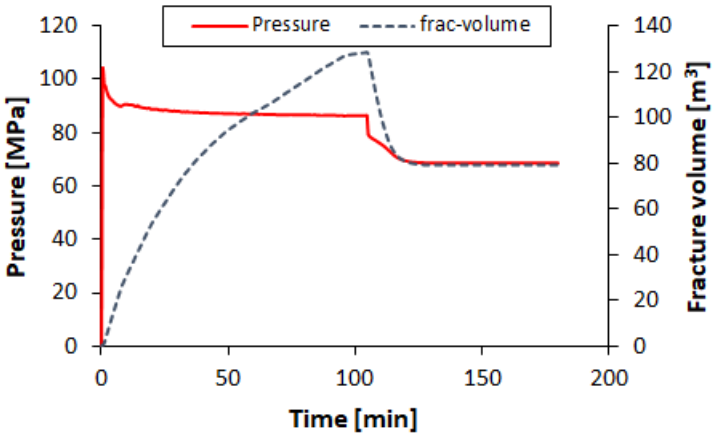

Figure 6.41: fracture pressure profile and fracture volume for proposal B.

Better hydraulic connection exists between the fracture and perforations in this case as is evident from the injection zone fracture width and proppant concentration profile in Figure 6.42. The decrease in the fracture width at the start of n-heptane injection after water-based fluid injection is less in comparison with proposal 1 due to higher injection rate. At shutin, the injection zone width reached 11.2 mm which then reduced to 9.3 mm. Even higher weighted dimensionless fracture conductivity $F_{cd,weighted}$*: 44* is created in proposal 2, which when measured according to dimensionless fracture conductivity is F_{cd}*: 180* (Hou et al., 2020; Prats, 1961).

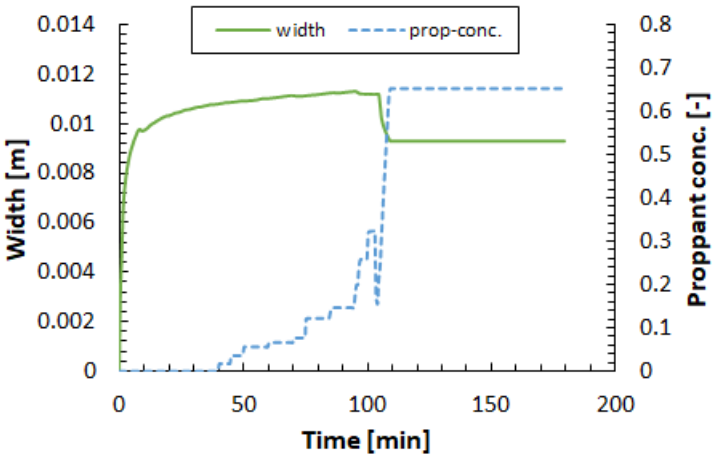

Figure 6.42: fracture width and proppant concentration in the injection zone.

6.8 Comparison with previous fracture job

The results of proposed design with alternative frac-fluid are encouraging when compared with previous fracture job performed with water-based fluid. The details of fracture design based upon type of fluid, injection volume and proppant can be seen from Table 6.5.

Table 6.5: fracture job design comparison of proposed and previous job.

	Details	**Fluid**	**Injection volume [m^3]**	**Proppant [ton]**
Case-1	Proposal 1	Hybrid-C7 (n-heptane)	615	90
Case-2	Proposal 2	Hybrid-C7 (n-heptane)	808	134
Case-3	Previous fracture job	Conventional water-based	425	121

Although more injection fluid is required due to more leakoff in case of proposed designs, a much better fracture geometry with better fracture heights and significantly improved hydraulic connection between fracture and perforation levels can be attained. The propped fracture volume is in the order case2>case3>case1. Having a look at the results for propped fracture height, 112 m fracture height for proposal 2 is the highest. The reservoir thickness is around 205 m. Therefore, better propped fracture heights will be beneficial for ultimate recovery. For fracture height, the order is case2>case1>case3. Half-length of more than 100 m can be created with injection rate of 8 m^3/min. A high contrast in maximum fracture width at closure exist for the proposed and previous fracture job design in the order case2>case1>case3. Table 6.6 summarizes the comparison.

Table 6.6: fracture geometry for proposals and its comparison with previous frac-job.

	Fracture volume at shutin [m^3]	**Fracture volume at closure [m^3]**	**Initial Fracture height [m]**	**Propped fracture height [m]**	**Fracture half-length [m]**	**Max. propped frac. width [mm]**
1	81	52	125	96	81	9.4
2	148	83	162	112	105	10.8
3	285	56	180	83	132	4.74

The two proposed designs have been presented after performing numerous simulations for sensitivity analysis with most important parameters. A comparison between proposed designs and previous fracture job in terms of fracture geometry, proppant distribution and fluid viscosity contours can be observed from Figure 6.43. Due to higher viscosity of water-based fluid, which is in excess of 0.2 Pa.s, in the previous fracture job, more fracture volume with higher initial fracture aperture was created.

Higher viscosity and heat capacity of water-based fluid result in lower leakoff and late gel break of fluid. On the other hand, a fluid viscosity of 0.15 Pa.s is chosen for alternative fluid. The lower viscosity compared to previous fracture job and lower heat capacity of light alkanes results in quicker rise in fluid temperature in the target reservoir. It leads to reduction in fluid viscosity and more leakoff leading to a thinner initial fracture aperture, which is still close to 1 cm (maximum width) for proposal 1 and more than 1 cm (maximum width) for proposal 2.

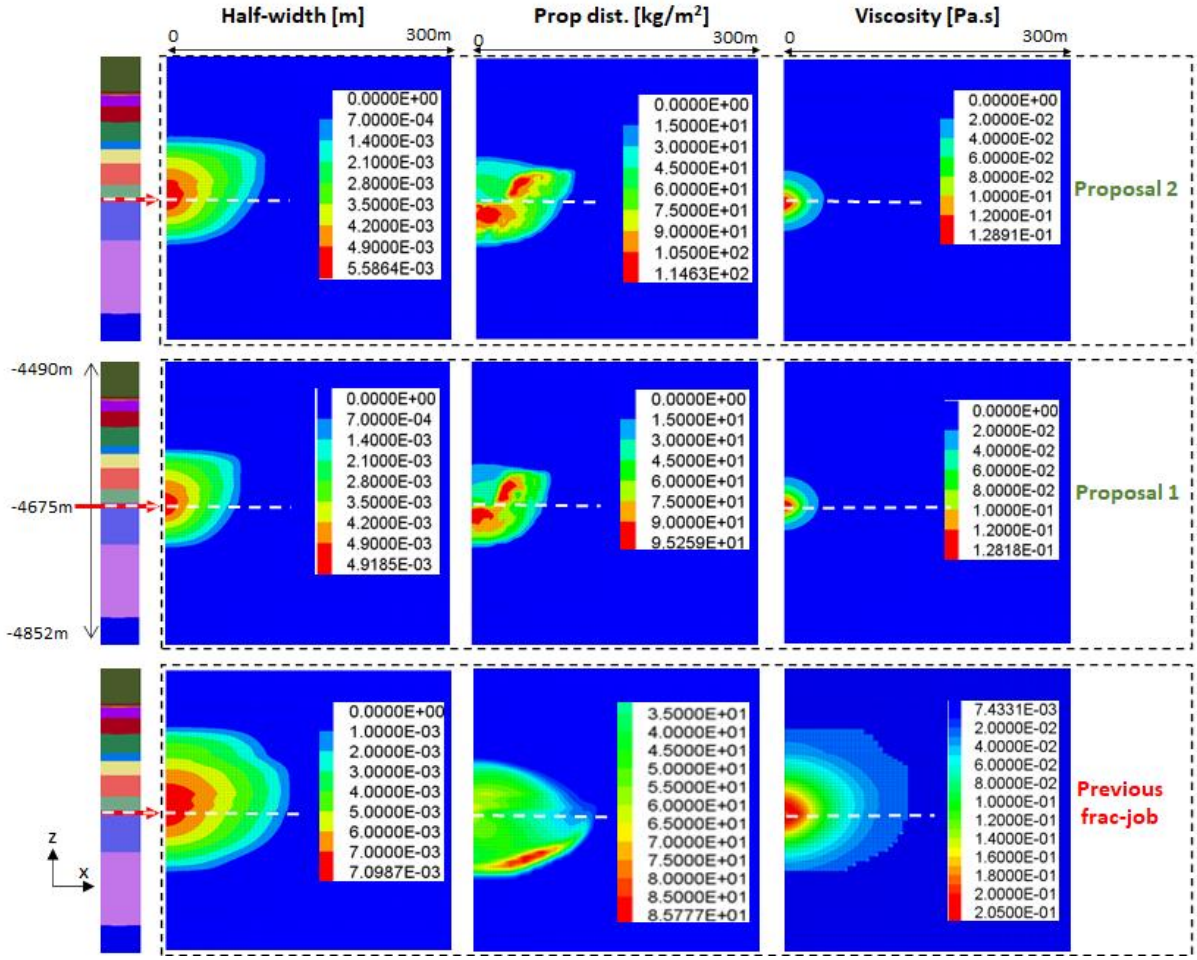

Figure 6.43: comparison between different proposed designs and previous fracture job at shutin for fracture half-width, proppant distribution and fluid viscosity.

However, having a look at the fracture geometry contours at closure clarifies the picture and the idea behind proposed designs (Figure 6.44). After shutin, the fracture starts to close due to closure stress. During this time, the proppants settle, and the fracture aperture reduces until it comes in contact with the proppant. As can be observed from Figure 6.44, fractures with better conductivity can be generated with proposed designs. In addition, better hydraulic connection between fracture and formation with proposed fluid can be created. The presence of proppants in the upper half of fracture shows that it will contribute towards production in addition to lower half. Therefore, the proposed designs if implemented can generate better productivity of fractured well and increase the ultimate recovery.

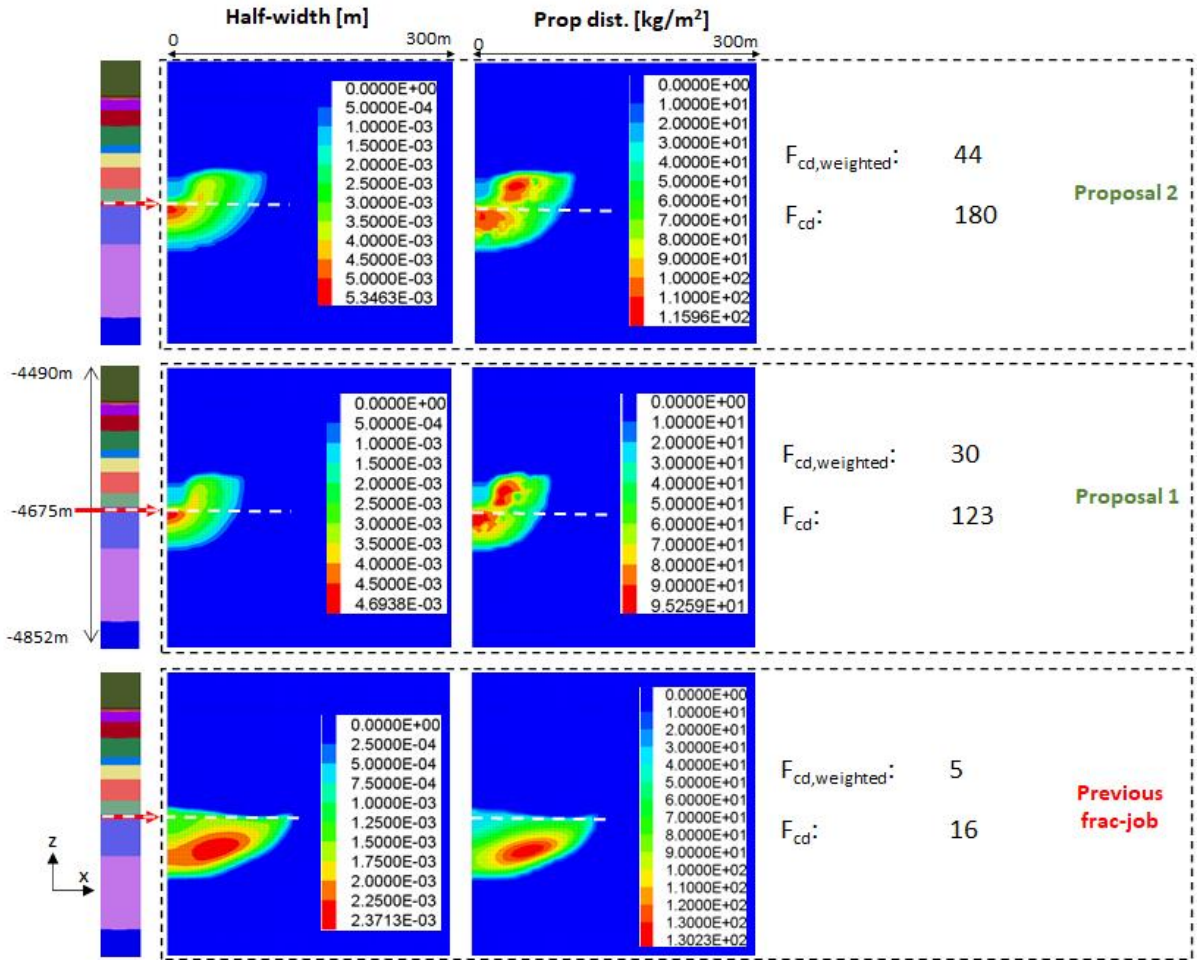

Figure 6.44: fracture geometry profile at closure for different proposals and previous frac job with details about fracture conductivity.

7 Rod-shaped proppants

7.1 Introduction

One of the most important part of a hydraulic fracturing operation is proppant transport and placement in the fracture to keep it open once the fluid injection is stopped. If proppants are not injected, the fracture will ultimately close under the influence of closure stress. The same is true for the fracture zones where proppants cannot reach or have reached but migrated to other zones such as settling under the influence of gravity to lower half of the fracture. Proppants, compared to rock grains, are large diameter particles and their purpose is not only to keep a fracture open but also provide sufficient porosity and permeability to reservoir fluid so that commercial production becomes possible.

The first hydraulic fracturing operation performed in 1947 utilized silica sand proppants. Since then, many materials such as natural sand, ceramic, resin coated sand, sintered bauxite, kaolin etc., have been utilized for proppants. Generally sand and ceramic proppants have been utilized (Hellmann et al., 2009; Liang et al., 2016; Montgomery and Smith, 2010). These proppants have their own strengths depending upon the material. They can be categorized into low strength, medium strength, high strength proppants. Mostly, spherical proppants have been utilized in millions of hydraulic fracturing operations worldwide and their sphericity is dependent upon roundness of particle. The larger the size of proppant, the higher the conductivity. Fracture conductivity is the measure of propped fracture ability of how well it can transmit reservoir fluid during production. Factors such as proppant composition, strength, grain size distribution, roundness, density, pack permeability, proppant degradation over time etc., affect the fracture conductivity. Discussion about different types of spherical proppants can be found in section 4.1.5. Proppants are available in many sizes ranging between 105 µm to 2.38 mm. In petroleum industry, they are characterized according to the mesh size such as 16/30, 20/40, 30/50, 40/80 (Economides and Nolte, 2000; Liang et al., 2016). They are utilized according to a particular job design and formation characteristics.

As discussed earlier, spherical proppants have been utilized extensively over the last decades and much research has been done in increasing the fracture conductivity based upon different proppant composition, densities, particle size distribution, material strength etc. Since conductivity is dependent upon permeability which in turn depends upon porosity of proppant pack, changing the shape of proppant can make a significant difference. Rod-shaped proppants, which are cylindrical in shape, can provide range of packing arrangements much wider than conventional proppants. In comparison to spherical proppants, up to three times higher conductivity fractures can be created with rod-shaped proppants. A unique consolidated proppant pack can be created due to their cylindrical shape which can resist the proppant flowback. Spherical proppants are isotropic with respect to shape which leads to lower space between particles due to higher compaction. However, a large number of packing arrangements are possible for rod-shaped proppants due to shape anisotropy. In comparison to the

diameter of spherical proppants, the concept of aspect ratio i.e., length to diameter ratio of proppant is utilized for cylindrical proppants. As the aspect ratio increases, the porosity and permeability of proppant pack increases. Cylindrical proppant with aspect ratio of 3 can generate volume which is equivalent to spherical proppant whose diameter is 40% more. Another added advantage is the mobility increase of high viscosity slurry, which can help in quick fracture cleanup due to higher available permeability. Rod-shaped proppants have been successfully applied in petroleum reservoirs (Schlumberger, 2013; Jia et al., 2019; Li et al., 2015; Osiptsov, 2017). Figure 7.1 presents spherical and rod-shaped proppants and proppant packed in a fracture.

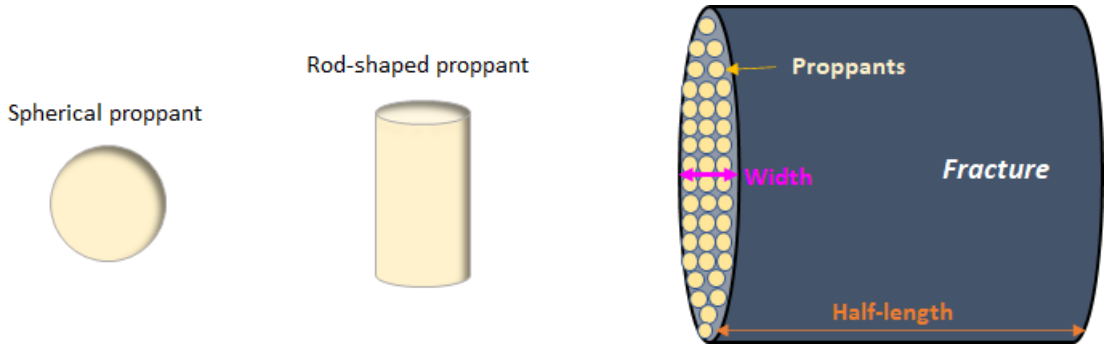

Figure 7.1: spherical and rod-shaped (cylindrical) proppants and propped fracture (proppant dimensions not to scale).

According to Osiptsov, periodical packing of cylinders having aspect ratio 5 yielded 23% more porosity than spherical proppants. The numerical simulation results with different proppants showed maximum porosity and permeability for cylindrical proppant packs (Osiptsov, 2017). Compared to conventional proppants, the initial and retained conductivity are enhanced using rod-shaped proppants. Successful field trials have demonstrated that existing wellsite equipment can perform the fracturing operation with this proppant even at high volumes of 100,000 lbm per job. These proppants not only reduce friction pressure which lowers surface injection pressure but also significantly enhanced the productivity index compared to conventionally fractured wells (McDaniel et al., 2010).

Longer effective fracture half-lengths due to better and quicker cleanup and higher conductivity of rod-shaped proppants increased the cumulative production by at least 12% after six months production period compared to hydraulic fracturing with conventional proppants (Carpenter, 2016). Combination of channel fracturing technique with rod-shaped proppants have increased the well productivity in the depleted Devonian formations in Orenburg region Russia. Due to their shape, rod-shaped proppants can hold each other through mechanical means whereas, for conventional proppants such as resin coated, the proppant pack stability is based on chemical bonds which in turn depend on temperature or time of activation. Therefore, rod-shaped proppant injection especially at the final stage of fracturing not only provides high conductivity in the near wellbore region but also minimize proppant flowback problem (Wilson, 2015). Similarly, application of high strength ceramic rod-shaped proppant during hydraulic

fracturing operation in a petroleum field in Indonesia lifted production adding valuable reserves (Soetikno et al., 2014). It is important to note that due to shape anisotropy of rod-shaped proppants, the resulting geometry can result in three-point bending stress on proppant. Therefore, high strength cylindrical proppants such as ceramic bauxite, ceramic corundum etc., can be used to avoid localized failure of pellets under high stress conditions (McDaniel et al., 2010; Osiptsov, 2017). Figure 7.2 shows rod-shaped proppant geometry which results in more porosity and restricts proppant flowback.

Figure 7.2: rod-shaped proppant geometry (2D and 3D) restricting mobility of proppant and increasing porosity (modified from (McDaniel et al., 2010; Wilson, 2015)).

7.2 Fracture conductivity

The long-term fracture conductivity depends upon the proppant embedment and deformation. The proppant-formation and proppant-proppant interaction can lead to proppant embedment and deformation. Therefore, mechanical properties of formation and proppant such as elastic modulus and Poisson's ratio are critical. The effective stress determines the load on the proppants under closure conditions to keep the walls of fracture apart. Therefore, it is imperative that the strength of proppants is sufficient to sustain the applied stress otherwise fracture conductivity can be significantly reduced due to proppant crushing. In soft formations, high contrast between proppant and formation strength may lead to higher proppant embedment which reduces the fracture conductivity. The proppant-proppant interaction can cause proppant deformation. Therefore, the reduction in fracture aperture due to proppant embedment, deformation/crushing will have direct impact on fracture conductivity and productivity of a stimulated well. 20% reduction in fracture width can reduce the recovery efficiency as low as 50-60% in weakly consolidated formations (Lacy et al., 1998, 1997; Li et al., 2015).

Therefore, it is imperative to understand the influence of proppant embedment and deformation to model the performance of different proppants in the life of a hydraulically fractured well. In doing so, the effect of factors such as strength contrast of proppant and target formation, effective stress, proppant diameter, aspect ratio etc. need to be considered. The impact of proppant embedment and deformation on fracture conductivity for spherical proppants have been investigated by many researchers (Arshadi et al., 2017; Chen et al., 2018; H. Li et al., 2017; Li et al., 2015; Luo et al., 2020; Xu et al., 2019). However, Jia et al. presented mathematical model for the investigation of embedment and deformation of rod-shaped proppant in consideration of proppant-formation mechanical properties and closure stress

and their influence on fracture aperture and conductivity and verified their model with the experimental results (Jia et al., 2019; Osiptsov, 2017).

7.3 Numerical model

In order to simulate the effect of different proppants on production, the mathematical models developed by Jia et al. (Jia et al., 2019) and Li et al. (Li et al., 2015) have been incorporated in FLAC3D^{plus}-TMVOCMP framework in this work. The concept of change in fracture conductivity due to reduction of fracture aperture because of proppant embedment and deformation based upon elastic modulus, Poisson's coefficient, proppant diameter and aspect ratio and effective stress is applied. Figure 7.3 describes the concept of change in fracture width due to proppant embedment and deformation, where 'wd' and 'we' represent changed fracture width due to deformation and embedment, respectively.

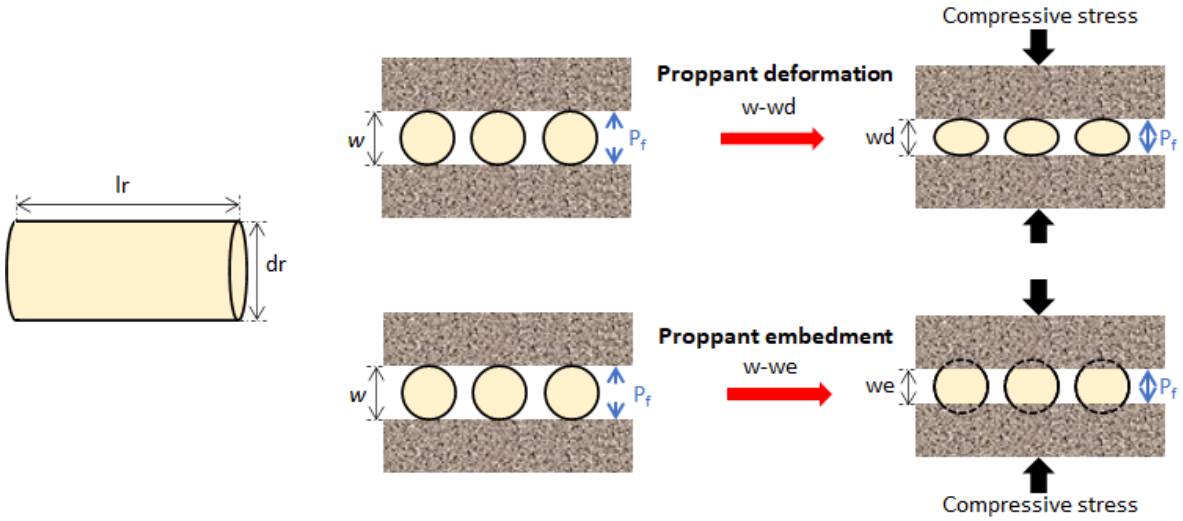

Figure 7.3: rod-shaped proppant dimensions (diameter and length) and fracture width change concept due to proppant embedment and deformation under the effective stress.

The proppant embedment and deformation are dependent upon the effective stress, the strength of proppant and formation and the aspect ratio of proppants (Jia et al., 2019). The proppant embedment, dependent upon proppant and formation properties, on one wall of fracture or on one side is given by the following Equation (7.1).

$$E^{"} = \sigma' d_{r1}\left[V_2\left[1 + ln\left\{\frac{2l_r^2}{(V_1+V_2)\sigma'}\left(\frac{1}{d_{r1}}\right)^2\right\}\right] - V_1 ln\left(\frac{V_1+V_2}{V_1}\right)\right] \quad (7.1)$$

Whereas proppant deformation due to proppant-formation and proppant-proppant interaction residing in the fracture aperture can be mathematically written as

$$D^{"} = \sigma' w_i V_1\left[1 + ln\left\{\frac{2l_r^2}{V_1\sigma'}\left(\frac{1}{d_{r1}}\right)^2\right\}\right] \quad (7.2)$$

V_1 and V_2 are proppant and formation properties dependent given by Equations (7.3) and (7.4).

$$V_1 = (1 - v_1^2)/\pi E_1 \quad (7.3)$$

$$V_2 = (1 - v_2^2)/\pi E_2 \quad (7.4)$$

Where, $E^{"}$: proppant embedment [mm]; $D^{"}$: proppant deformation; σ': effective stress [MPa]; v_1:Poisson's ratio of proppant [-]; v_2: Poisson's ratio of formation [-]; E_1: elastic modulus of proppant [MPa]; E_2: elastic modulus of formation [-]; l_r: proppant length [mm]; d_r: proppant diameter [mm]; w_i: initial fracture width [mm].

For rod-shaped proppants, the aspect ratio which is the ratio of proppant length to diameter (Equation (7.5)) is used instead of proppant diameter only.

$$aspect\ ratio = \frac{l_r}{d_r} \quad (7.5)$$

Adding the proppant embedment and deformation will give the change in fracture aperture on one side ($C^{"}$) of fracture wall as

$$C^{"} = E^{"} + D^{"} \quad (7.6)$$

Therefore, the total change in fracture aperture at a particular time during production under effective stress can be found by subtracting the total change in fracture aperture from initial width (Equation (7.7)). Equation (7.6) provides with the fracture width change on one wall or one side of fracture therefore it is multiplied by a factor of two to provide with width reduction on both walls of fracture.

$$w = w_i - 2C^{"} \quad (7.7)$$

Where, w is the updated fracture width after fracture width reduction.

To determine the fracture conductivity, fracture permeability needs to be determined which is based upon the proppant porosity. Therefore, the permeability is defined in terms of porosity using commonly used formula based upon the Kozeny-Carman model and mathematically expressed by Equation (7.8) (Jia et al., 2019; Li et al., 2017; Li et al., 2015).

$$k_f = \frac{\emptyset r^2}{8\tau^2} \quad (7.8)$$

Where, k_f: permeability of propped fracture [µm^2]; $\emptyset$: porosity [-]; r: radius of pore throat [µm]; τ; pore tortuosity [-].

For spherical proppants, the porosity, pore throat radius and tortuosity relations were presented by Li et al. (Li et al., 2015) as presented by Equations (7.9), (7.10) and (7.11).

$$\emptyset = \frac{w_i \emptyset_i - 2D}{w_i - 2D} \quad (7.9)$$

$$r = \left[\frac{w_i - 2D}{w_i}\right] 1000 \times \frac{2\sqrt{3} - 3}{6} d_r \quad (7.10)$$

$$\tau = \sqrt{\left[\frac{w_i - 2D}{w_i}\right]^2 [\tau_0^2 - 1] + 1} \tag{7.11}$$

Where, $\emptyset_i$: initial porosity when effective stress is zero [-]; D: spherical proppant deformation [mm]; τ_0: tortuosity when effective stress is zero [-].

However, for the rod-shaped proppants the concept of equivalent diameter is utilized as follows

$$d_e = 1.14(d_r)^{0.67}(l_r)^{0.33} \tag{7.12}$$

Where, d_e: equivalent diameter of proppant [mm]; for spherical proppant $d_e = d_r$.

Therefore, utilizing the concept of equivalent diameter in terms of aspect ratio, the relations for loose packing porosity for rod-shaped proppants i.e., when closure pressure or effective stress is zero, can be written as

$$\emptyset_i = 1 - \frac{8.97}{\frac{l_r}{d_r} + \frac{d_r}{l_r} + 13.325} \tag{7.13}$$

And the pore throat radius (r_i) at the beginning when closure stress is zero can be found as

$$r_i = 1000 \times \frac{2\sqrt{3} - 3}{6} \times 1.14(d_r)^{0.67}(l_r)^{0.33} \tag{7.14}$$

When the injection is stopped at the end of fracturing operation, the fluid pressure inside the fracture reduces until it becomes less than the closure stress and the fracture start to close. Therefore, the fracture width begins to reduce as the closure stress increases. Also, due to production the pressure depletes in the reservoir which increases the effective stress. So, the close packing of proppants under compaction takes place and the porosity can be determined using the concept of change in fracture aperture at the corresponding effective stress as

$$\emptyset = \frac{w_i\left(1 - \frac{8.97}{\frac{d_r}{l_r} + \frac{l_r}{d_r} + 13.325}\right) - 2D^{"}}{w_i - 2D^{"}} \tag{7.15}$$

And based upon the previous discussion on the correlation between permeability and porosity Equation (7.8), the permeability of fracture can be written as Equation (7.16).

$$k_f = 11.067 \frac{\left[w_i\left(1 - \frac{8.97}{\frac{d_r}{l_r} + \frac{l_r}{d_r} + 13.325}\right) - 2D^{"}\right]\left(w_i - 2D^{"}\right)^2 d_r^{4/3} l_r^{2/3}}{w_i^2(w_i - 2D^{"})\left[0.5\left(\frac{w_i - 2D^{"}}{w_i}\right)^2 + 1\right]} \tag{7.16}$$

The porosity and permeability correlations for spherical proppants are defined by Equations (7.17) and (7.18) (Li et al., 2015).

$$\emptyset = \frac{w_i \emptyset_i - 2D}{w_i - 2D} \tag{7.17}$$

$$k_f = 498.58 d_r^2 \left[\frac{\emptyset_i w_i - 2D}{w_i - 2D}\right] \tag{7.18}$$

Where, D: spherical proppant deformation [mm].

The fracture conductivity can be defined as the ability of fracture to transmit fluids to the wellbore and mathematically expressed as (Economides and Nolte 2000; Prats 1961)

$$F_c = k_f w_i \tag{7.19}$$

For tight reservoirs, a more realistic approach is to add the ability of reservoir to feed the fracture to conductivity term (Eq. (10)) making it dimensionless fracture conductivity F_{cd} (Eq. (11)) (Economides and Nolte 2000).

$$F_{cd} = \frac{k_f w_i}{k x_f} \tag{7.20}$$

However, to investigate the effect of hydraulic connection between fracture and perforations, the effect of position and proppant concentration with reference to injection zone were added to Eq. (11) by Hou et al. (2021) to make it weighted fracture conductivity.

$$F_{cd,weighted} = \frac{\sum_{j=1}^{n} \frac{w_{ij} k f_j}{d_i} A_j \frac{c_p}{c_{max}}}{\sum_{j=1}^{n} \frac{1}{d_j} A_j \frac{c_p}{c_{max}}} \times \frac{1}{k x_f} \tag{7.21}$$

Where, w_i: initial fracture width [m]; kf: fracture permeability [m^2]; d: distance between fracture element and perforation; A: fracture element area [m^2]; c_p: proppant concentration [-]; c_{max}: maximum proppant concentration; k: reservoir permeability [m^2] and x_f: fracture half-length [m] and n: total fracture elements [-].

To find out the decreased fracture conductivity due to fracture aperture reduction after production, following correlations (Eq. (13)) can be used

$$\begin{cases} F_c' = k_f\left(w_i - 2C^{"}\right) \\ F_{cd}' = \dfrac{k_f\left(w_i - 2C^{"}\right)}{k x_f} \\ F_{cd,weighted}' = \dfrac{\sum_{j=1}^{n} \dfrac{\left(w_i - 2C^{"}\right)_j k f_j}{d_i} A_j \dfrac{c_p}{c_{max}}}{\sum_{j=1}^{n} \dfrac{1}{d_j} A_j \dfrac{c_p}{c_{max}}} \times \dfrac{1}{k x_f} \end{cases} \tag{7.22}$$

These models are implemented into the FLAC3D^{plus}-TMVOC. Where after the hydraulic fracturing operation, the created fracture geometry is assigned porosity and permeability according to the proppant selection i.e., the diameter is specified in case of spherical proppant and diameter and length in case of rod-shaped proppant. The proppant strength parameters are supplied. Then the initial permeability and porosity is calculated and the initial fracture conductivity according to the choice of proppant. The permeability of the fracture zone can then be determined based on the principle of superposition as discussed in section 6.3, where the fracture zone permeability is calculated by the new model and host reservoir zone permeability is based on the reservoir data provided initially. After performing these calculations in FLAC3D^{plus}, the simulation starts for production from a fractured reservoir. The data such as porosity, permeability stress etc., is sent to TMVOC where the pressure, fluid flow, phase saturations etc. are determined. This data is then sent back to FLAC3D^{plus} where new fracture width is determined based upon the change in effective stress and the resultant proppant embedment and deformation. The simulation continues to next time step once the convergence is made. Figure 7.4 presents the detailed working of the developed production model for different proppants.

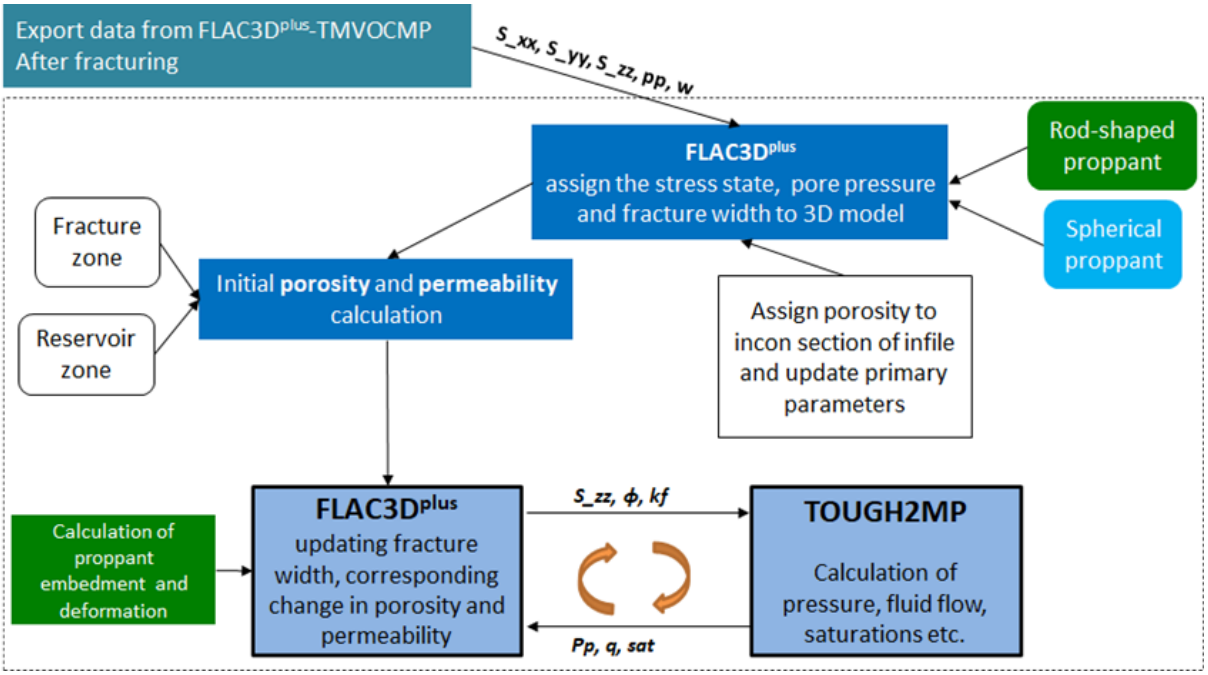

Figure 7.4: flowchart showing different steps involved in developed production model and data sharing between software. S_zz: stress, ϕ: porosity, Pp: pore pressure, q: flowrate, sat: fluid saturation in different phases.

7.4 Sensitivity analysis

In order to understand the influence of important factors such as proppant aspect ratio, strength contrast with formation, effective stress etc., on fracture permeability, conductivity and long-term production performance, simulations were performed in a generic model. Therefore, a 3D quarter model for a gas reservoir is generated and properties are assigned to it according to the data presented in Gou et al. (Gou

et al., 2015). The model (Figure 7.5a) was generated in FLAC3D^{plus} and properties such as porosity, permeability, e-modulus, Poisson's ratio were applied according to Table 7.1. The stress state and pressure can be observed from Figure 7.5c. The hydraulic fracturing was conducted according to the plan presented in Figure 7.5b and the resulting fracture geometry at shutin and closure can be seen from Figure 7.5d.

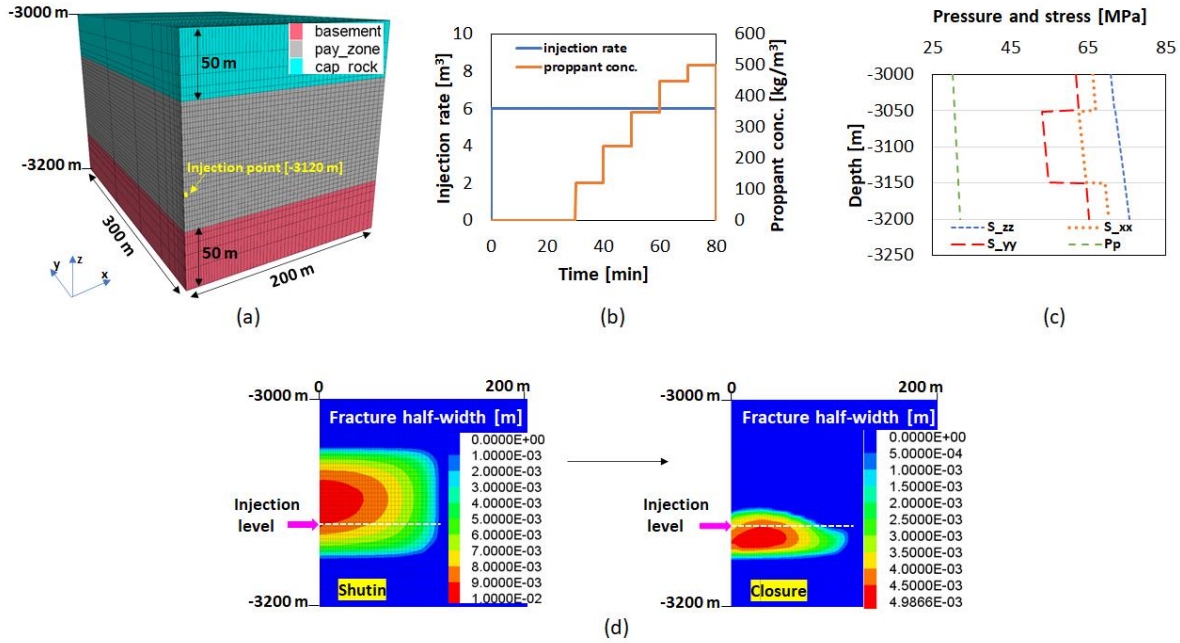

Figure 7.5: (a) 3D generic model (Gou et al. 2015), (b) injection schedule for hydraulic fracturing, (c) pressure and stress profile and (d) fracture geometry at shutin and closure in terms of half-width.

Table 7.1: formation properties.

Formation type	**Porosity [-]**	**Permeability [m^2]**	**E-modulus [GPa]**	**Poisson ratio [-]**	**Density [kg/m^3]**
Cap_rock	0.025	4e-17	25	0.3	2650
Pay_zone	0.1	4e-15	30	0.25	2600
Basement	0.025	4e-17	25	0.3	2650

7.4.1 Fracture permeability and conductivity

After the hydraulic fracturing operation is performed. The data including stress state, reservoir pore pressure, fracture geometry etc., is exported to the developed production model where sensitivity analysis is performed for rod-shaped proppants with different aspect ratios and strength properties and compared with spherical proppants. Considering the fracture width at closure as in Figure 7.5d, the generated porosity and permeability can be observed from Figure 7.6. Increasing the aspect ratio of rod-shaped proppant significantly increases the porosity and permeability of fracture. For the rod-shaped proppant with aspect ratio of 1, the porosity and permeability are more compared to spherical proppant having same diameter.

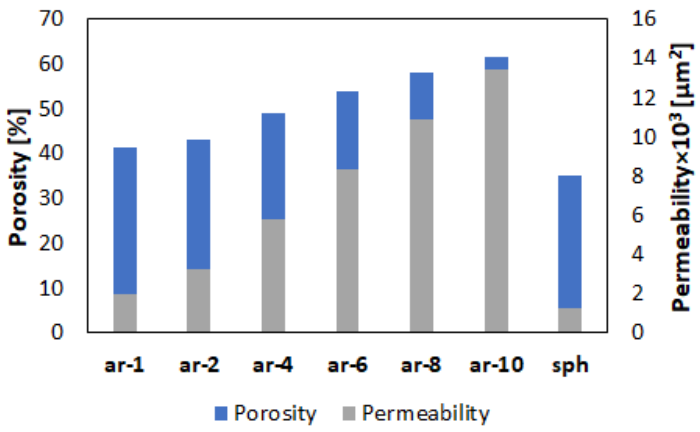

Figure 7.6: porosity and permeability of rod-shaped (ar: aspect ratio: 1-10) and spherical proppants.

Similarly, the fracture conductivity will be higher for rod-shaped proppants compared to spherical proppants. The fracture conductivity for proppants according to weighted dimensionless conductivity ($F_{cd\ (weighted)}$), dimensionless conductivity (F_c)and conductivity (F_c) can be observed from Figure 7.7. Identical trends to the permeability behavior can be observed for fracture conductivity as the aspect ratio of proppants is increased. It shows that higher aspect ratio proppants are attractive from the point of view of higher fracture conductivity. On the other hand, the higher aspect ratio proppant may undergo more proppant deformation or failure under stress.

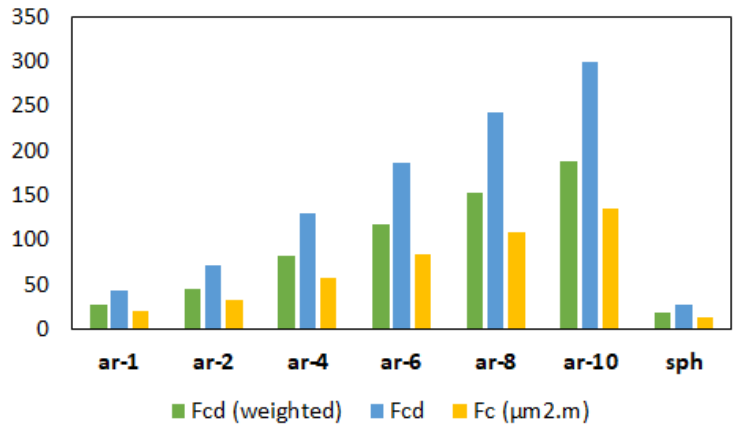

Figure 7.7: fracture conductivity of rod-shaped (ar: aspect ratio: 1-10) and spherical proppants.

7.4.2 Proppant deformation and embedment

The proppants deform under compaction. The compressive stress on proppants increases, as the reservoir pressure depletes due to production. To analyze the effect of pressure depletion and rising effective stress on fracture aperture due to proppant-proppant and proppant-formation interaction, production was performed for a period of one year where the bottomhole pressure was reduced to 15 MPa. The pressure and stress profile during this production phase can be observed from Figure 7.8.

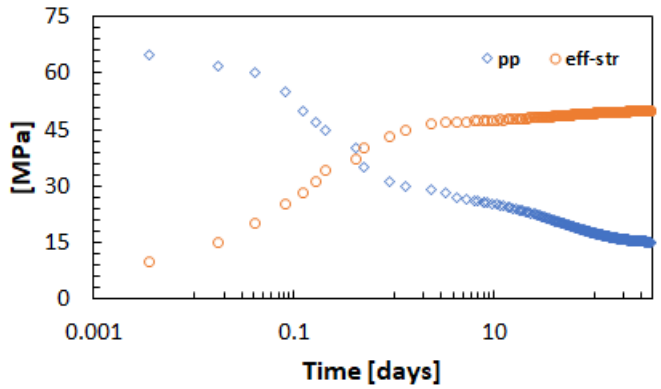

Figure 7.8: stress and pressure profile for a production period of one year.

After one year of pressure depletion to 15 MPA, the zone width change under the combined effect of embedment and deformation can be observed from Figure 7.9. The decrease in fracture aperture can be observed from Figure 7.9b where the change in width contour can be seen after one year. Whereas Figure 7.9a shows the fracture width profile along a-a', at the end of injection (blue circles), after one year depletion (gray circles) and difference in fracture width between these two time points (red circles). It can be observed from the trend of Δw, that more reduction in fracture aperture occurs where the initial fracture width was more due to more layers of proppants undergoing deformation.

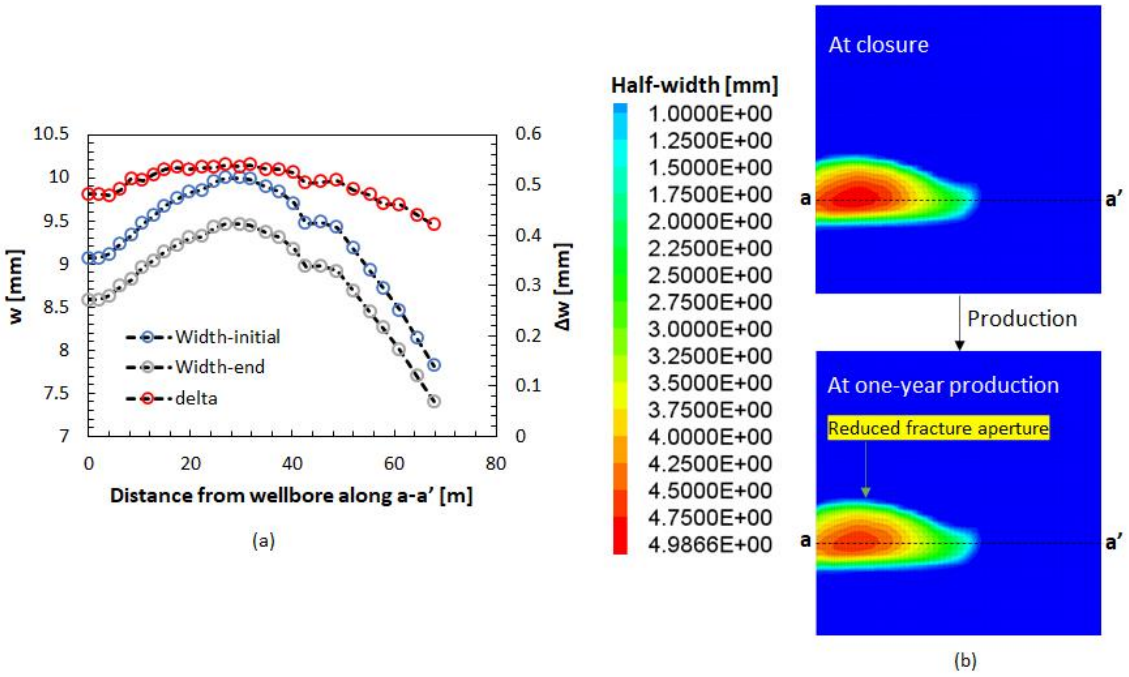

Figure 7.9: (a) change in fracture width at horizontal distance from borehole along a-a'. (b) reduced fracture aperture after one year of depletion and line a-a' at horizontal distance from wellbore.

7.4.3 Strength contrast between proppant and formation

Using the same depletion time of one year and pressure and stress profile (Figure 7.8), the effect of strength contrast between proppant and formation is analyzed. The results in terms of change in fracture

aperture are plotted for different cases in Figure 7.10. Two different cases are presented where for the cases e1, the formation Young's modulus is kept constant at 20 GPa and proppant elastic modulus is changed from 7 GPa to 15 GPa for the three cases α1, α2 and α3, respectively. Whereas, for the e2 cases, the proppant strength is kept constant at 20 GPa and formation modulus is changed from 10 GPa to 20 GPa. It can be inferred that the if proppant e-modulus is less than the formation e-modulus, the reduction in fracture aperture will be more due to more deformation than embedment.

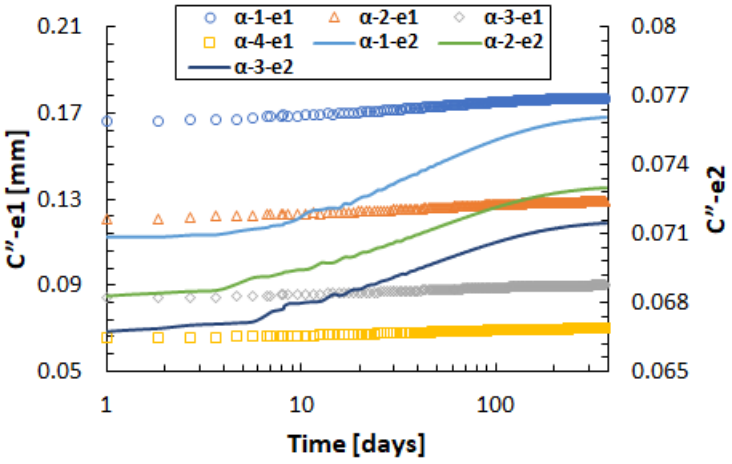

Figure 7.10: sensitivity analysis of strength contrast between proppant and formation. e1 cases represent changing elastic modulus of proppant and e2 cases represent changing elastic modulus of formation.

7.4.4 Bottomhole production pressure

To account for the effect of selecting bottomhole production pressure on fracture aperture, simulations were performed with different production pressures and results were obtained which are plotted for a period of one year in Figure 7.11. Lowering the bottom hole pressure (BHP) increases the stress on proppants therefore more reduction in fracture aperture occurs. Four different cases with producing BHPs of 25 MPa, 20 MPa, 15 MPa and 5 MPa are presented. Although lower BHP can lead to higher injection rates, but long-term productivity can be reduced due to reduced fracture conductivity because of reduced aperture (Figure 7.11a). The relation between fracture aperture reduction and BHP can be observed from Figure 7.11b.

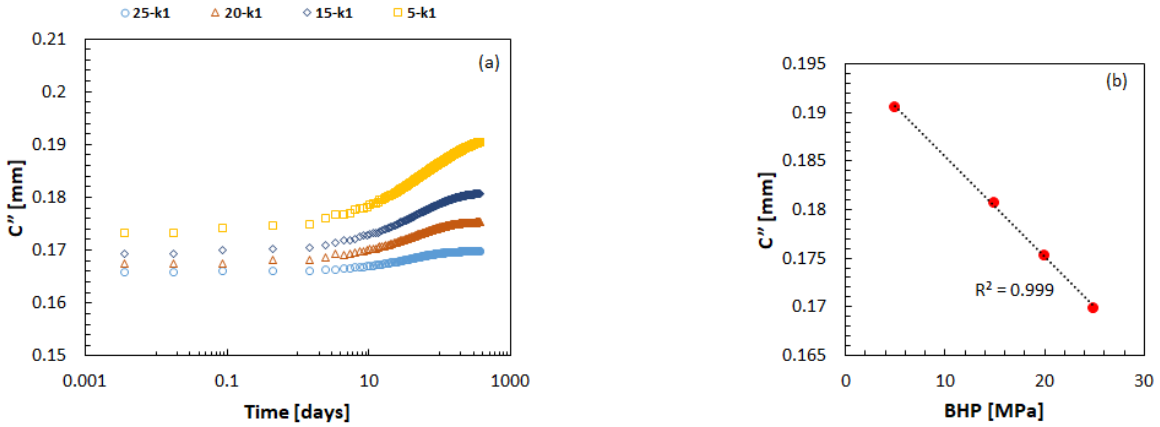

Figure 7.11: (a) effect of producing bottomhole pressure on reduction in fracture aperture (b) relation between change in fracture aperture and BHP.

In order to observe the long-term production performance of these proppants, simulation is performed for a period of ten years. All the conditions are kept similar for these simulations except the proppant shape and aspect ratio. The production rates and cumulative production for four cases are presented in Figure 7.12. The results are encouraging as around 13% more production can be achieved if the aspect ratio of proppant is increased from 1 to 10. 7% more recovery can be achieved by rod-shaped proppants of aspect ratio 1 compared to spherical proppants having similar diameter.

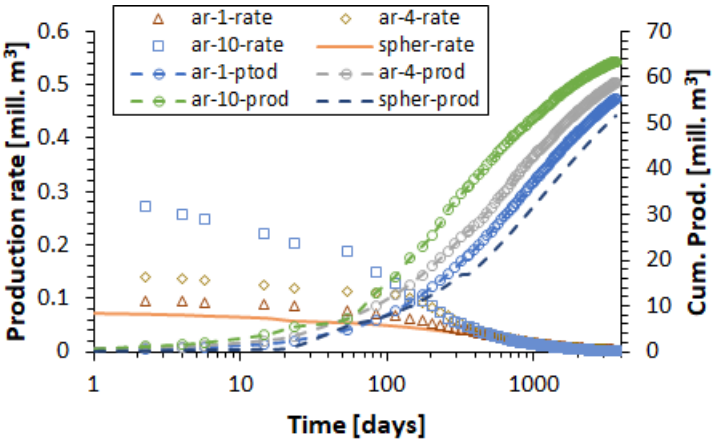

Figure 7.12: production rates and cumulative production using rod-shaped (ar: aspect ratio) and spherical proppants over a period of ten years.

Due to production, the reservoir pressure depletes with time which increases the stress on the proppants. Therefore, the proppants embed and deform according to stress conditions and strength contrast with the formation. The simulation results for the four cases are presented in Figure 7.13. The bottomhole pressure during production is decreased from initial pressure to 3 MPa. This means, the load shared by pore pressure is increasingly shared by the proppant during the production life. This leads to change in fracture aperture which reduces continuously as the stress increases under pressure depletion conditions. The higher aspect ratio or size proppants suffer more deformation under same stress conditions.

Therefore, around 38% more deformation of aspect ratio 10 proppant compared to aspect ratio one proppant is noticed. For aspect ratio 10 proppant, the fracture aperture reduces by about 1 mm in this case.

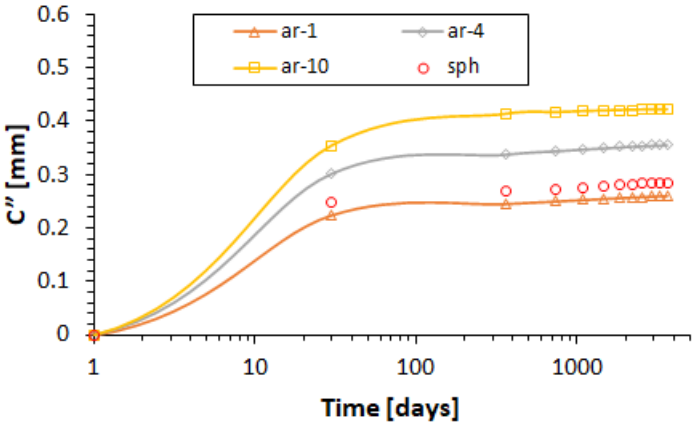

Figure 7.13: change in fracture aperture for rod-shaped (ar: aspect ratio) and spherical proppants over a period of ten years.

7.5 Application

The developed model is applied to wellbore yx1 to investigate the effect of change in proppant shape and size on recovery. The fractures created in Proposals 1 and 2 are used to perform sensitivity analysis. Due to higher porosity of rod-shaped proppant pack, more permeability and conductivity is offered compered to spherical proppants. Figure 7.14 shows the fracture conductivity based on different proppant shapes and sizes for design proposals. It can be noted that increasing the proppant aspect ratio increases the conductivity therefore, aspect ratio 7 proppant can result in maximum productivity. On the other hand, spherical proppants give lower fracture conductivity when compared with aspect ratio 1 rod-shaped proppant which has the same diameter as spherical proppant but different shape. The reason for different conductivities for proposal 1 and 2 is due to the difference between fracture widths therefore, proposal B can be a better choice due to higher conductivity fracture.

Due to higher conductivity, rod-shaped proppants can further enhance the production from wellbore yx1. The production forecast over a period of ten years for rod-shaped and spherical proppants has been performed to analyze their effect on recovery. The forecast for proposal 1 and 2 with different proppants are presented in Figure 7.15 and Figure 7.16 and also tabulated (Table 7.2).

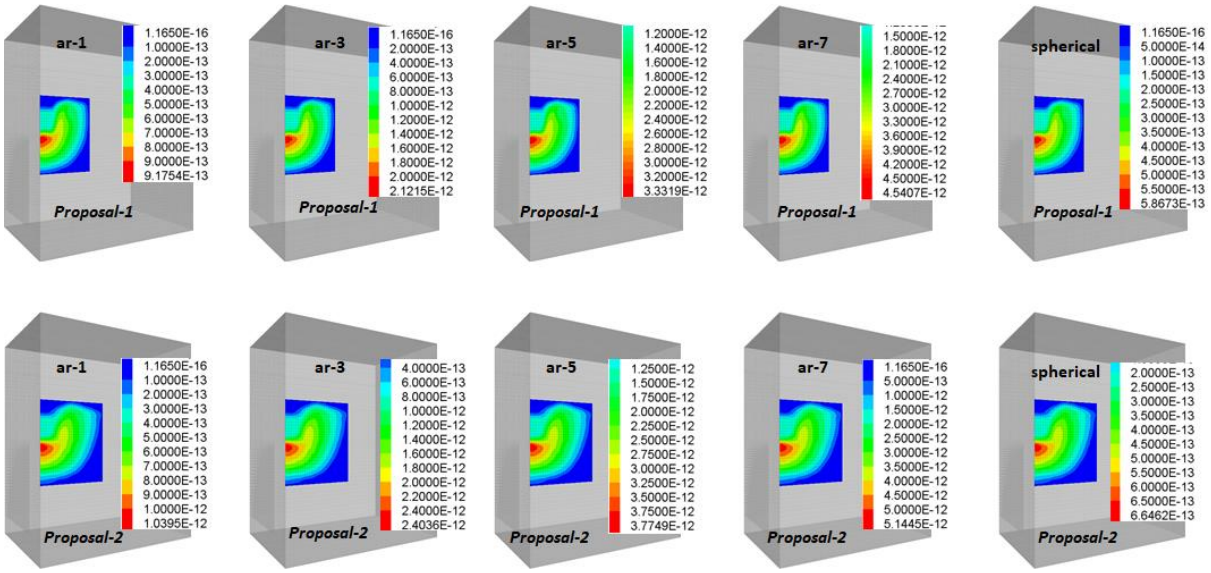

Figure 7.14: fracture conductivity kf.w (m^2.m) for proposals 1 and 2 using different aspect ratio rod-shaped proppants and comparison with spherical proppants.

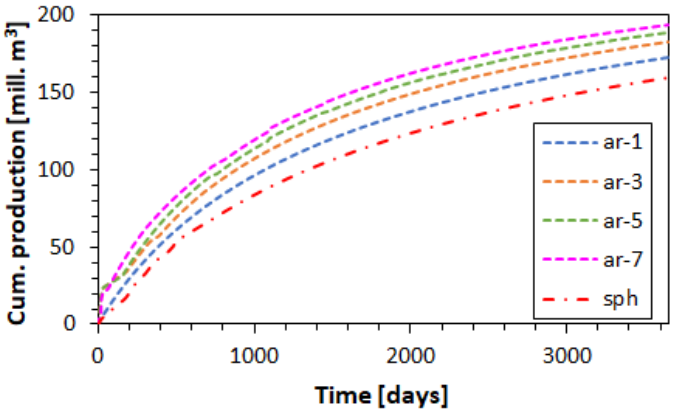

Figure 7.15: production forecast for proposal 1 with different proppants. ar: aspect ratio of rod-shaped proppant, sph: spherical proppant.

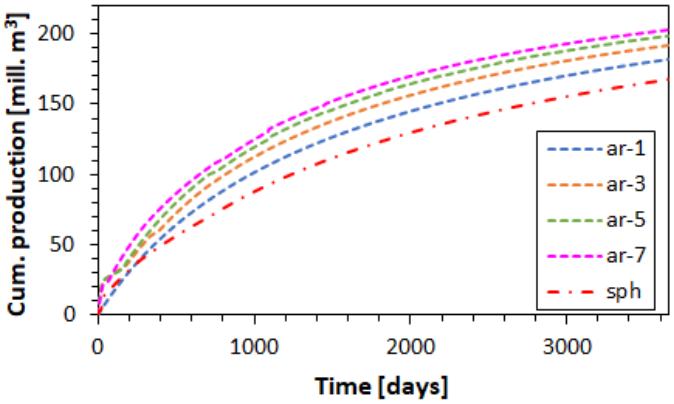

Figure 7.16: production forecast for proposal 2 with different proppants. ar: aspect ratio of rod-shaped proppant, sph: spherical proppant.

Compared to the previous fracture job, excellent recoveries can be made using either of the proposals with conventional spherical proppants. However, the use of rod-shaped proppants can further enhance the recovery. More than 7% recovery increase is observed when using rod-shaped proppant of aspect ratio 1 which has the same diameter as that of spherical proppant. Increasing the aspect ratio of proppant significantly increases recovery. The difference in the production while changing proppants from aspect ratio 1, 3, 5 and 7 is approximately 5.5%, 3.1% and 2.59%. Therefore, increasing the proppant size increases production, however the increase in production ratio decreases with it.

Table 7.2: 10 years production forecast with different proppants.

Proppant type and dimensions		**Production forecast (million sm^3)**	
		Proposal-1	*Proposal-2*
Rod-shaped (aspect ratio: 1)	l_r: *0.6mm* d_r: *0.6mm*	172	181
Rod-shaped (aspect ratio: 3)	l_r: *1.8mm* d_r: *0.6mm*	182	192
Rod-shaped (aspect ratio: 5)	l_r: *3.0mm* d_r: *0.6mm*	188	199
Rod-shaped (aspect ratio: 7)	l_r: *4.2mm* d_r: *0.6mm*	193	204
Spherical	d_r: *0.6mm*	160	168

During the production period, the pressure in the fracture decreases which increase the effective stress on the proppants leading to proppant deformation and embedment. This reduces the fracture aperture resulting in lowering the fracture permeability (Figure 7.17). it can be seen that the higher aspect ratio proppant results in more fracture aperture reduction and higher decline in permeability. Therefore, aspect ratio of proppant should be chosen carefully to avoid proppant damage. High strength proppants having e-modulus of 300 GPa were chosen for this case study to avoid proppant damage and deformation in high stress environment. The fracture width reduction is not very high; therefore, the fracture can produce for a longer period of time.

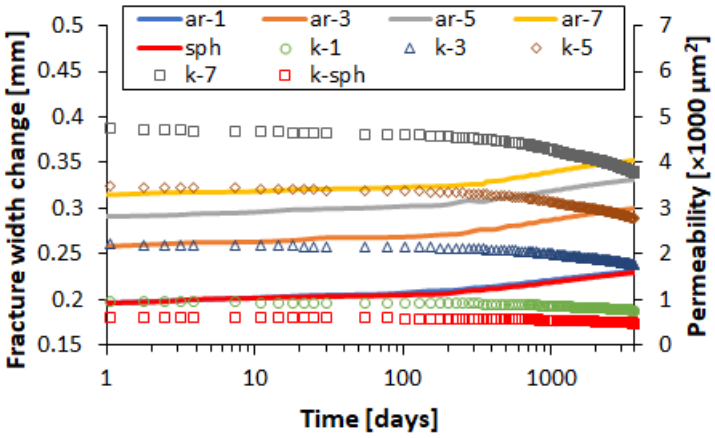

Figure 7.17: reduction in fracture aperture and resulting decrease in permeability due to production.

The reservoir pressure contour after ten years production can be observed from Figure 7.18. Due to higher permeability in the fracture zone, the pressure reduction wave travels quickly in the fracture compared to the lower permeability surrounding formation. The initial reservoir pressure was around 65 MPa which then reduced to around 20 MPa in the near wellbore fracture zone surrounding the perforation interval.

Based upon the analysis of obtained results and considering proppant shape and size, it is recommended to use rod-shaped proppants. In addition, to avoid sizeable damage, smaller size proppants are a better choice. To avoid proppant failure due to three point bending stress condition in rod-shaped proppant pack, high strength proppant should be utilized especially in higher stress environments such as encountered in this field. Therefore, rod-shaped proppants having aspect ratio 3 are recommended for an optimum recovery from this reservoir.

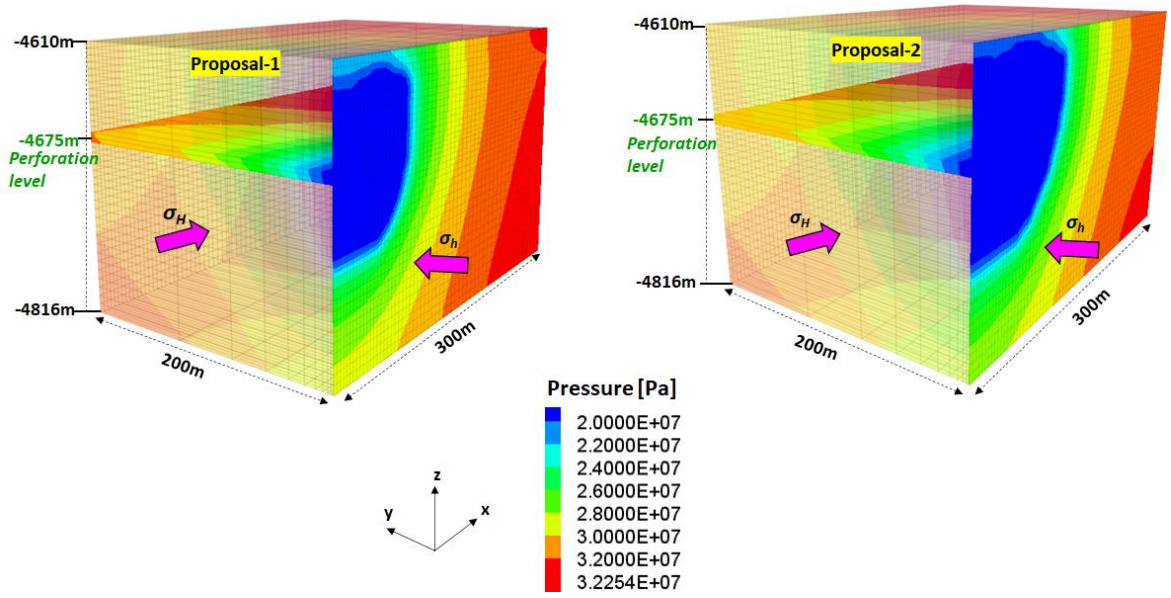

Figure 7.18: pressure profile of different proposals at the end of ten-year production period.

8 Conclusions

Light alkanes as alternative frac-fluid can be the solution to address the technical and environmental issues associated with water-based fluids. The use of proposed fluid can save millions of barrels of water utilized in hydraulic fracturing operation. It may also pave the way for public acceptance towards fracturing operation. In comparison with spherical proppants, rod-shaped proppants can provide higher fracture porosity, and resultant permeability and conductivity. Therefore, unconventional fluid and unconventional proppants are recommended for better productivity from unconventional reservoirs.

The conventionally used water-based fluid and its chemical additives were discussed in detail. The environmental hazards associated with water-based fluid are grave. In addition, the issues of delayed closure, slow flowback, partial or complete loss of borehole-fracture connection, clay swelling and phase entrapment especially in water sensitive formations and formations with sub reducible water saturations damage the efficiency of hydraulic fracturing operation. Although the issue of induced seismicity involves produced water in addition to flowback water, the use of light alkanes can at least reduce the amount of wastewater reinjection by that amount. The water remaining in the reservoir due to poor flowback reduces the permeability to reservoir gas. The injected water, if remains in reservoir lowers the productive capacity and if returns to surface creates surface handling and environmental issues. Many available alternative frac-fluids such as foam-based, oil-based, gas-based etc., have been discussed with their advantages and disadvantages. However, the objectives of this work cannot be achieved with them. The intended use of proposed fluid can help address these issues. The use of single component fluid or mixture based on reservoir-to-reservoir conditions can provide with better proppant placement and flowback. This leads to better conductivity and resultant ultimate recovery. The phase behavior shows that the fluid can be handled as liquid at surface conditions and even change its phase to gas upon flowback if appropriate conditions are met (especially for n-pentane). Simulation in a fictive model using TMVOC was performed to understand the performance of proposed fluid in reservoir conditions and appearance and disappearance of components in the liquid and gaseous phase.

To perform hydraulic fracturing with alternative frac-fluid, popular THM code FLAC3D-TOUGH2MP/TMVOC was utilized. The model development was discussed in detail for mechanical deformation, fracture initiation and propagation, MM fluid flow in fracture and reservoir element, proppant transport in fracture, apparent fluid viscosity due to shear rate and temperature change and fluid leakoff to surrounding formation. After that, the verification of the model with three case studies for fracture initiation and propagation, MM fluid flow in porous media in isothermal and non-isothermal conditions was performed.

The verified model was then applied to a case study from McCully Gas Field, New Brunswick Canada. A hybrid fluid concept was utilized for fracturing with proposed fluid whereby about 30 m^3 water was injected to initiate fracturing, followed by n-heptane injection. Since the density of proposed fluid

ranges between 626 kg/m^3 – 730 kg/m^3, which is considerably less than water. Resultantly, surface injection pressure requirement will increase. Initiating hydraulic fracturing with a small volume of water (30-40 m^3) can help avoid large surface pressure requirements. Therefore, due to this hybrid fluid concept, hydraulic fracturing can be performed with proposed fluid through available surface equipment. In the case study, fracturing was performed for three different fluids, i.e., water-based, propane-based and hybrid-n-heptane. The fracture geometry and proppant settling behavior for different cases were discussed in detail. The fracture closure for water-based fluid took the longest and resulted in proppant settling to the bottom of fracture and partial hydraulic connection between fracture and perforation was created. Maximum propped fracture height of about 100 m was generated for proposed fluid whereas only 66 m height remained for water-based fluid after proppant settlement. The flowback behavior for the proposed fluid was excellent compared to water-based fluid and comparable with gas-based fluid. Within seven days of flowback, almost all the n-heptane flowed back from the propped fracture zone similar to propane-based fluid. However, at the same time most of the water-based fluid remained in the fracture. Therefore, with proposed fluid the reservoir gas production can start earlier. The production forecast for five years showed that 10% and 35% more recovery can be obtained with proposed fluid compared to propane-based and water-based fluid over a period of five years, respectively.

Moreover, simulations of hydraulic fracturing using proposed fluid for optimization of wellbore yx1 in tight gas reservoir yxz Germany were performed, after the verification of generated 3D geologic model in FLAC3D by making pressure history match with the previous fracture job using water-based fluid. The results showed that although a fracture having more than 100 m half-length was created, the proppants fall to the bottom leading to partial hydraulic connection between fracture and injection level. The lower productivity even after stimulation can be due to insufficient borehole-fracture connection. Numerous simulations were performed with hybrid n-heptane fluid concept to reach at design optimization for better conductivity fractures. N-heptane, with a boiling point of 371.85 K, when injected in a reservoir having temperature of more than 418 K undergoes gel break due to quick rise in its temperature because of heat exchange. Therefore, upon flowback the fluid will have reduced viscosity and density as the reservoir temperature is higher than its boiling point even if it remains in liquid phase due to higher pressure conditions. Sensitivity analysis were performed for most important parameters such as fluid viscosity, injection rate and time. It was also found that because of higher fluid leakoff, it is better to use gelled fluid from the beginning of fracturing operation. Larger fracture apertures due to higher viscosity fluid can lead to proppant settling at the bottom of fracture under the effect of gravity, depriving the upper half of fracture of proppants. This leads to unpropped fracture zones and in severe cases ends in loss of hydraulic connection between fracture and perforations. Therefore, although increased fracture aperture leads to increased fracture volume, better proppant placement constraints the use of higher viscosity fluids.

Hydraulic fracturing designs with injection rates of 6 and 8m^3/min and 0.15 Pa.s viscosity fluid were proposed to create fractures having weighted dimensionless conductivities of 30 and more while maintaining sufficient hydraulic connection between perforation level and fracture due to better proppant placement. Frac-fluid flowback analysis showed that n-heptane flow back performance was excellent in this case study compared to conventional water-based fluid. Most of the fluid can flowback which when used for subsequent fracturing operation can make the project economically attractive.

Spherical proppants have been utilized extensively over the last decades and much research has been done in increasing the fracture conductivity based upon different proppant composition, densities, particle size distribution, material strength etc. Since conductivity is dependent upon permeability which in turn depends upon porosity of proppant pack, changing the shape of proppant can make a significant difference. Rod-shaped proppants, which are cylindrical particles can provide range of packing much wider than conventional proppants. In comparison to spherical proppants, up to three times higher conductivity fractures can be created with rod-shaped proppants. A unique consolidated proppant pack can be created due to their cylindrical shape which can resist the proppant flowback. A new production model for different types of proppants was integrated into FLAC3D-TMVOC. The production forecast in consideration of change in fracture aperture and conductivity due to closure stress during production phase and resultant proppant embedment and deformation can be modelled. Higher aspect ratio rod-shaped proppants are desirable for more conductivity and productivity however, proppant deformation increases with increasing size. The bottomhole production pressures should be kept in a suitable range to avoid higher effective stress on the proppants. Further sensitivity analysis with proposed designs for wellbore yx1 with rod-shaped and spherical proppants were performed for production forecast over a period of ten years. Considerable improvement in recovery of 7% was observed by using rod-shaped proppants (aspect ratio 1) compared to spherical proppants having similar diameter. For future research, the proppant transport and settling model for rod shaped proppants can be developed and implemented in the FLAC3D-TMVOC framework.

9 References

Abaa, K., Wang, J.Y., Ityokumbul, M.T., 2013. Parametric study of fracture treatment parameters for ultra-tight gas reservoirs. J Petrol Explor Prod Technol 3, 159–168. https://doi.org/10.1007/s13202-013-0058-x

Alexander, T., Baihly, J., Boyer, C., Clark, B., Waters, G., Jochen, V., 2011. Shale Gas Revolution. Oilfield Review 16.

API, 2016. Tech Data Book 10. American Petroleum Institute.

Arshadi, M., Zolfaghari, A., Piri, M., Al-Muntasheri, G.A., Sayed, M., 2017. The effect of deformation on two-phase flow through proppant-packed fractured shale samples: A micro-scale experimental investigation. Advances in Water Resources 105, 108–131. https://doi.org/10.1016/j.advwatres.2017.04.022

Bahadori, A., 2014. Chapter 1 - Overview of Natural Gas Resources, in: Bahadori, A. (Ed.), Natural Gas Processing. Gulf Professional Publishing, Boston, 1–22. https://doi.org/10.1016/B978-0-08-099971-5.00001-5

Bahrami, H., Rezaee, R., Clennell, B., 2012. Water blocking damage in hydraulically fractured tight sand gas reservoirs: An example from Perth Basin, Western Australia. Journal of Petroleum Science and Engineering, Unconventional hydrocarbons exploration and production Challenges 88–89, 100–106. https://doi.org/10.1016/j.petrol.2012.04.002

Barati, R., Liang, J.-T., 2014. A review of fracturing fluid systems used for hydraulic fracturing of oil and gas wells. Journal of Applied Polymer Science 131. https://doi.org/10.1002/app.40735

Barbot, E., Vidic, N.S., Gregory, K.B., Vidic, R.D., 2013. Spatial and temporal correlation of water quality parameters of produced waters from Devonian-Age shale following hydraulic fracturing. Environ. Sci. Technol. 47, 2562–2569. https://doi.org/10.1021/es304638h

Barree, R.D., Conway, M.W., 1995. Experimental and numerical modeling of convective proppant transport. Journal of Petroleum Technology 47, 216–222. https://doi.org/10.2118/28564-PA

Bennion, D.B., Thomas, F.B., Bietz, R.F., Bennion, D.W., 1999. Remediation of water and hydrocarbon phase trapping problems in low permeability gas reservoirs. Journal of Canadian Petroleum Technology 38. https://doi.org/10.2118/99-08-01

Bennion, D.B., Thomas, F.B., Bietz, R.F., Bennion, D.W., 1996. water and hydrocarbon phase trapping in porous media-diagnosis, prevention and treatment. Journal of Canadian Petroleum Technology 35. https://doi.org/10.2118/96-10-02

Bestaoui-Spurr, N., Li, C., 2018. Ultra-light weight proppants for better placement. Presented at the SPE Annual Technical Conference and Exhibition, Society of Petroleum Engineers. https://doi.org/10.2118/191585-MS

Borchardt, D., Ewen, C., Richter, S., Hammerbacher, R., 2012. Information and dialog process on the safety and environmental compatibility of fracking technology (Informations- und Dialogprozess zur Sicherheit und Umweltverträglichkeit der Frackingtechnologie). Wasser und Abfall 6(12):10–14

Boudet, H., Clarke, C., Bugden, D., Maibach, E., Roser-Renouf, C., Leiserowitz, A., 2014. "Fracking" controversy and communication: Using national survey data to understand public perceptions of hydraulic fracturing. Energy Policy 65, 57–67. https://doi.org/10.1016/j.enpol.2013.10.017

BP, 2020. Statistical Review of World Energy. British Petroleum, 69th edition, 68.

Brooks, R.H., Corey, A.T., 1964. Hydraulic properties of porous media. Hydrology Papers, Colorado State University, 37.

Bundesgesetzblatt, 2016. Zur Änderung wasser- und naturschutzrechtlicher Vorschriften zur Untersagung und zur Risikominierung bei den Verfahren der Fracking-Technologie. Bundesgesetzblatt, Teil I Nr. 40, ausgegeben zu Bonn, 1972.

Caineng, Z.O.U., Zhi, Y., Rukai, Z.H.U., Guosheng, Z., Lianhua, H.O.U., Songtao, W.U., Shizhen, T. a. O., Xuanjun, Y., Dazhong, D., Yuman, W., Lan, W., Jinliang, H., Shufang, W., 2015. Progress in China's Unconventional Oil & Gas Exploration and Development and Theoretical Technologies. Acta Geologica Sinica - English Edition 89, 938–971. https://doi.org/10.1111/1755-6724.12491

Cander, H., 2012. What Are Unconventional Resources? a simple definition using viscosity and permeability, #80217.

Carpenter, C., 2016. Rod-shaped-proppant fracturing boosts production and adds reserves. Journal of Petroleum Technology 68, 70–98. https://doi.org/10.2118/0316-0070-JPT

Chen, M., Zhang, S., Liu, M., Ma, X., Zou, Y., Zhou, T., Li, N., Li, S., 2018. Calculation method of proppant embedment depth in hydraulic fracturing. Petroleum Exploration and Development 45, 159–166. https://doi.org/10.1016/S1876-3804(18)30016-8

Clark, C.E., Horner, R.M., Harto, C.B., 2013. Life Cycle Water consumption for shale gas and conventional natural gas. Environ. Sci. Technol. 47, 11829–11836. https://doi.org/10.1021/es4013855

Clark, J.B., 1949. A hydraulic process for increasing the productivity of wells. Journal of Petroleum Technology 1, 1–8. https://doi.org/10.2118/949001-G

Dai, J., Ni, Y., Wu, X., 2012. Tight gas in China and its significance in exploration and exploitation. Petroleum Exploration and Development 39, 277–284. https://doi.org/10.1016/S1876-3804(12)60043-3

Daneshy, A., 2010. Hydraulic fracturing to improve production. The Way Ahead 06, 14–17. https://doi.org/10.2118/0310-014-TWA

Denney, D., 2012. Ultralightweight proppants for long horizontal gravel packs. Journal of Petroleum Technology 64, 152–156. https://doi.org/10.2118/1012-0152-JPT

Die Bundesregierung, 2017. No fracking in Germany. https://www.bundesregierung.de/breg-en/issues/sustainability/no-fracking-in-germany-391340 (accessed 11-06-2021).

Doglioni, C., 2018. A classification of induced seismicity. Geoscience Frontiers, Reliability Analysis of Geotechnical Infrastructures 9, 1903–1909. https://doi.org/10.1016/j.gsf.2017.11.015

Duan, K., Kwok, C.Y., Wu, W., Jing, L., 2018. DEM modeling of hydraulic fracturing in permeable rock: influence of viscosity, injection rate and in situ states. Acta Geotech. 13, 1187–1202. https://doi.org/10.1007/s11440-018-0627-8

Economides, M.J., Martin, T., 2007. Modern Fracturing: Enhancing Natural Gas Production. Energy Tribune Publishing.

Economides, M.J., Hill, A.D., Ehlig-Economides, C., 1994. Petroleum Production Systems. PTR Prentice Hall.

Economides, M.J., Nolte, K.G., 2000. Reservoir Stimulation. Wiley.

ecorpStim. URL http://ecorpstim.com/technology/ (accessed 10.6.20).

ecorpStim. LAS and light alkanes and amorphous boro-silica proppant. URL http://ecorpstim.com/technology/light-alkanes-stimulation/ (accessed 10.6.20).

EFSA, 2012. Scientific opinion on mineral oil hydrocarbons in food. Europian Food Safety Authority. EFSA Journal 10, 2704. https://doi.org/10.2903/j.efsa.2012.2704

Elliott, E.G., Ettinger, A.S., Leaderer, B.P., Bracken, M.B., Deziel, N.C., 2017. A systematic evaluation of chemicals in hydraulic-fracturing fluids and wastewater for reproductive and developmental toxicity. Journal of Exposure Science & Environmental Epidemiology 27, 90–99. https://doi.org/10.1038/jes.2015.81

FAO/WHO, 2012. Compendium of food additive specifications: joint FAO/WHO Expert Committee on Food Additives: 76th meeting 2012. Joint FAO/WHO Expert Committee on Food Additives, Food and Agriculture Organization of the United Nations, World Health Organization FAO JECFA monographs. Food and Agriculture Organization of the United Nations, Rome.

Feng, W., Were, P., Li, M., Hou, Z., Zhou, L., 2016. Numerical study on hydraulic fracturing in tight gas formation in consideration of thermal effects and THM coupled processes. Journal of Petroleum Science and Engineering 146, 241–254. https://doi.org/10.1016/j.petrol.2016.04.033

Fisher, M.K., Warpinski, N.R., 2012. Hydraulic-fracture-height growth: real data. SPE Production & Operations 27, 8–19. https://doi.org/10.2118/145949-PA

Fjær, E., Holt, R.M., Horsrud, P., Raaen, A.M., Risnes, R. (Eds.), 1992a. Chapter 1 Elasticity, in: Developments in Petroleum Science, Petroleum Related Rock Mechanics. Elsevier, 1–46. https://doi.org/10.1016/S0376-7361(09)70187-6

Fjær, E., Holt, R.M., Horsrud, P., Raaen, A.M., Risnes, R. (Eds.), 1992b. Chapter 11 Fracturing, in: Developments in Petroleum Science, Petroleum Related Rock Mechanics. Elsevier, 269–286. https://doi.org/10.1016/S0376-7361(09)70197-9

Fjær, E., Holt, R.M., Horsrud, P., Raaen, A.M., Risnes, R. (Eds.), 1992c. Chapter 2 Failure mechanics, in: Developments in Petroleum Science, Petroleum Related Rock Mechanics. Elsevier, 47–88. https://doi.org/10.1016/S0376-7361(09)70188-8

Fjær, E.H. and RM, H., P., Raaen, AM and Risens, R.,1992. Petroleum Related Rock Mechanics. Developments in Petroleum Science, 33.

Fjær, E., Holt, R.M., Horsrud, P., Raaen, A.M., Risnes, R., 2008. Chapter 11 Mechanics of hydraulic fracturing, in: Developments in Petroleum Science, Petroleum Related Rock Mechanics. Elsevier 2nd edition (53), 369–390.

Gadde, P.B., Liu, Y., Norman, J., Bonnecaze, R., Sharma, M.M., 2004. Modeling proppant settling in water-fracs. Presented at the SPE Annual Technical Conference and Exhibition, Society of Petroleum Engineers. https://doi.org/10.2118/89875-MS

Gallegos, T.J., Varela, B.A., 2015. Trends in hydraulic fracturing distributions and treatment fluids, additives, proppants, and water volumes applied to wells drilled in the United States from 1947

through 2010—Data analysis and comparison to the literature. US Geological Survey Scientific Investigations Report 2014-5131.

Gallegos, T.J., Varela, B.A., Haines, S.S., Engle, M.A., 2015. Hydraulic fracturing water use variability in the United States and potential environmental implications. Water Resources Research 51, 5839–5845. https://doi.org/10.1002/2015WR017278

Gandossi, L., Estorff, U.V., 2015. An overview of hydraulic fracturing and other formation stimulation technologies for shale gas production - Update 2015. JRC Science for Policy Report, European Commission, 62.

Genuchten, M.T. van, 1980. A closed-form equation for predicting the hydraulic conductivity of unsaturated soils. Soil Science Society of America Journal 44, 892–898. https://doi.org/10.2136/sssaj1980.03615995004400050002x

Gou, Y., Zhou, L., Zhao, X., Hou, Z., Were, P., 2015. Numerical study on hydraulic fracturing in different types of georeservoirs with consideration of H2M-coupled leak-off effects. Environ Earth Sci 73, 6019–6034. https://doi.org/10.1007/s12665-015-4112-5

Grantham, C.K., McLaurine, H.C., 1986. Thixotropy without viscosity: a new approach to rheology control of oil muds. Presented at the SPE Annual Technical Conference and Exhibition, Society of Petroleum Engineers. https://doi.org/10.2118/15415-MS

Gregory, K.B., Vidic, R.D., Dzombak, D.A., 2011. Water management challenges associated with the production of shale gas by hydraulic fracturing. Elements 7, 181–186. https://doi.org/10.2113/gselements.7.3.181

Guo, B., Lyons, W.C., Ghalambor, A., 2007. Petroleum Production Engineering: A Computer-assisted Approach. Gulf Professional Pub.

Guo, J., Gou, B., 2015. Design philosophy and practice of asymmetrical 3D fracturing and random fracturing: A case study of tight sand gas reservoirs in western Sichuan Basin. Natural Gas Industry B 2, 174–180. https://doi.org/10.1016/j.ngib.2015.07.007

Gupta, D.V.S., 2009. Unconventional fracturing fluids for tight gas reservoirs. Presented at the SPE Hydraulic Fracturing Technology Conference, Society of Petroleum Engineers. https://doi.org/10.2118/119424-MS

Hagemann, B., Wegner, J., Ganzer, L., 2013. Investigation of hydraulic fracture re-orientation effects in tight gas reservoirs.

Han, J., Pirogov, A., Li, C., Hurt, R., Sookprasong, A., Min Kim, J., 2016. Maximizing productivity with ultra-lightweight proppant in unconventional wells: simulations and field cases. Presented at the SPE Asia Pacific Hydraulic Fracturing Conference, Society of Petroleum Engineers. https://doi.org/10.2118/181849-MS

Harris, P.C., 1987. Dynamic fluid-loss characteristics of CO2-foam fracturing fluids. SPE Production Engineering 2, 89–94. https://doi.org/10.2118/13180-PA

Harris, P.C., 1985. Dynamic fluid loss characteristics of foam fracturing fluids. Journal of Petroleum Technology 37, 1,847-1,852. https://doi.org/10.2118/11065-PA

Hasan, A.M.A., Abdel-Raouf, M.E., 2018. Applications of guar gum and its derivatives in petroleum industry: A review. Egyptian Journal of Petroleum 27, 1043–1050. https://doi.org/10.1016/j.ejpe.2018.03.005

Hedelin, A., 2013. Mineral oil – Origin, production and composition. Conservation of Clean Air and Water in Europe CONCAWE.

Hellmann, J.R., Scheetz, B.E., Luscher, W.G., Hartwich, D.G., Koseski, R.P., 2009. Engineering ceramics for stimulation of unconventional energy resources. American Ceramic Society Bulletin 93.

Hincks, T., Aspinall, W., Cooke, R., Gernon, T., 2018. Oklahoma's induced seismicity strongly linked to wastewater injection depth. Science 359, 1251–1255. https://doi.org/10.1126/science.aap7911

Holditch, S.A., 2006. Tight gas sands. Journal of Petroleum Technology 58, 86–93. https://doi.org/10.2118/103356-JPT

Holditch, S.A., 1979. Factors affecting water blocking and gas flow from hydraulically fractured gas wells. Journal of Petroleum Technology 31, 1,515-1,524. https://doi.org/10.2118/7561-PA

Hornbach, M.J., Jones, M., Scales, M., DeShon, H.R., Magnani, M.B., Frohlich, C., Stump, B., Hayward, C., Layton, M., 2016. Ellenburger wastewater injection and seismicity in North Texas. Physics of the Earth and Planetary Interiors, Microseismicity from all scales 261, 54–68. https://doi.org/10.1016/j.pepi.2016.06.012

Hou, M.Z., Mehmood, F., 2018. Numerical simulation of innovative fracking without water or chemical additives. Eurogeologists 46, 17-23.

Hou, M.Z., Li, M., Gou, Y., Feng, W., 2020. Numerical simulation and evaluation of the fracturing and tight gas production with a new dimensionless fracture conductivity (FCD) model. Acta Geotech. https://doi.org/10.1007/s11440-020-01079-4

Howarth, R.W., Ingraffea, A., Engelder, T., 2011. Should fracking stop? Nature 477, 271–275. https://doi.org/10.1038/477271a

Hughes, J.D., 2013. A reality check on the shale revolution. Nature 494, 307–308. https://doi.org/10.1038/494307a

IARC, 2012. Chemical Agents and Related Occupations. International Agency for Research on Cancer (IARC) Monographs, 100F.

IEA, 2020. Global Energy Review 2019: The latest trends in energy and emissions in 2019. International Energy Agency. https://doi.org/10.1787/90c8c125-en

Itasca, 2009. Fast Lagrangian Analysis of Continua in 3 Dimensions, Version 4.0. Itasca Consulting Group Inc., Minneapolis, USA.

Jacobs, T., 2014. Energized fractures: shale revolution revisits the energized fracture. Journal of Petroleum Technology 66, 48–56. https://doi.org/10.2118/0614-0048-JPT

Jardim Neto, A.T., Prata, F.G.M., Gomez, J.R., Pedroso, C.A., Martins, M. de O., Silva, D.N., 2012. Ultra-lightweight proppant technology: best practices for long horizontal gravel packs offshore Brazil. Presented at the North Africa Technical Conference and Exhibition, Society of Petroleum Engineers. https://doi.org/10.2118/150581-MS

Jia, C., 2017. Breakthrough and significance of unconventional oil and gas to classical petroleum geology theory. Petroleum Exploration and Development 44, 1–10. https://doi.org/10.1016/S1876-3804(17)30002-2

Jia, L., Li, K., Zhou, J., Yan, Z., Wan, F., Kaita, M., 2019. A mathematical model for calculating rod-shaped proppant conductivity under the combined effect of compaction and embedment. Journal of Petroleum Science and Engineering 180, 11–21. https://doi.org/10.1016/j.petrol.2019.05.034

Johnson, K., French, K., Fichter, J.K. and Oden, R., 2008, March. Use of microbiocides in Barnett Shale gas well fracturing fluids to control bacteria related problems. Paper presented at the CORROSION, New Orleans, Louisiana.

Kakati, A., Sangwai, J.S., 2018. Wettability alteration of mineral surface during low-salinity water flooding: role of salt type, pure alkanes, and model oils containing polar components. Energy & Fuels, 32(3), 3127–3137.

Kargbo, D.M., Wilhelm, R.G., Campbell, D.J., 2010. Natural gas plays in the Marcellus shale: challenges and potential opportunities. Environ. Sci. Technol. 44, 5679–5684. https://doi.org/10.1021/es903811p

Khilar, K.C., Fogler, H.S., 1983. Water sensitivity of sandstones. Society of Petroleum Engineers Journal 23, 55–64. https://doi.org/10.2118/10103-PA

Koehler, M., 2005. Productivity of frac stimulations in the German Rotliegend: theoretical considerations and practical results. In SPE Europec/EAGE Annual Conference Madrid, Spain. doi: https://doi.org/10.2118/94250-MS

Kondash, A., Vengosh, A., 2015. Water footprint of hydraulic fracturing. Environ. Sci. Technol. Lett. 2, 276–280. https://doi.org/10.1021/acs.estlett.5b00211

Kondash, A.J., Lauer, N.E., Vengosh, A., 2018. The intensification of the water footprint of hydraulic fracturing. Science Advances 4, eaar5982. https://doi.org/10.1126/sciadv.aar5982

Kong, B., Wang, S., Chen, S., 2017. Minimize formation damage in water-sensitive Montney formation with energized fracturing fluid. SPE Reservoir Evaluation & Engineering 20, 562–571. https://doi.org/10.2118/179019-PA

Koplos, J., Tuccillo, M.E., Ranalli, B., 2014. Hydraulic fracturing overview: How, where, and its role in oil and gas. Journal AWWA 106, 38–46. https://doi.org/10.5942/jawwa.2014.106.0153

Labinger, J.A., Bercaw, J.E., 2002. Understanding and exploiting C–H bond activation. Nature, 417(6888), 507–514.

Lacy, L.L., Rickards, A.R., Ali, S.A., 1997. Embedment and fracture conductivity in soft formations associated with HEC, borate and water-based fracture designs. Presented at the SPE Annual Technical Conference and Exhibition, Society of Petroleum Engineers. https://doi.org/10.2118/38590-MS

Lacy, L.L., Rickards, A.R., Bilden, D.M., 1998. Fracture width and embedment testing in soft reservoir sandstone. SPE Drilling & Completion 13, 25–29. https://doi.org/10.2118/36421-PA

Lashkarbolooki, M., Ayatollahi, S., Riazi, M., 2017. Mechanistical study of effect of ions in smart water injection into carbonate oil reservoir. Process Safety and Environmental Protection, 105, 361–372.

Leblanc, D.P., Martel, T., Graves, D.G., Tudor, E., Lestz, R., 2011. Application of propane (LPG) based hydraulic fracturing in the McCully Gas Field, New Brunswick, Canada. Presented at the North

American Unconventional Gas Conference and Exhibition, Society of Petroleum Engineers. https://doi.org/10.2118/144093-MS

Lei, X., Huang, D., Su, J., Jiang, G., Wang, X., Wang, H., Guo, X., Fu, H., 2017. Fault reactivation and earthquakes with magnitudes of up to Mw4.7 induced by shale-gas hydraulic fracturing in Sichuan Basin, China. Scientific Reports 7, 7971. https://doi.org/10.1038/s41598-017-08557-y

Leimkuhler, J., Leveille, G., 2012. Unconventional resources. The Way Ahead 08, 27–28. https://doi.org/10.2118/0112-026-TWA

Li, G., Li, X.-S., Li, C., 2017. Measurement of permeability and verification of Kozeny-Carman equation using statistic method. Energy Procedia, Proceedings of the 9th International Conference on Applied Energy 142, 4104–4109. https://doi.org/10.1016/j.egypro.2017.12.332

Li, H., Lu, Y., Zhou, L., Han, S., Gou, Y., 2017. A new constitutive model for calculating the loading-path dependent proppant deformation and damage analysis of fracture conductivity. Journal of Natural Gas Science and Engineering 46, 365–374. https://doi.org/10.1016/j.jngse.2017.08.005

Li, J., Dong, S., Hua, W., Yang, Y., Li, X., 2019. Numerical simulation on deflecting hydraulic fracture with refracturing using extended finite element method. Energies 12, 2044. https://doi.org/10.3390/en12112044

Li, K., Gao, Y., Lyu, Y., Wang, M., 2015. New mathematical models for calculating proppant embedment and fracture conductivity. SPE Journal 20, 496–507. https://doi.org/10.2118/155954-PA

Li, M., 2018. Optimization of multistage hydraulic fracturing treatment for maximization of the tight gas productivity (Dissertation). Clausthal University of Technology. Cuvillier Verlag Göttingen, Germany.

Li, M., Hou, M. Z., Zhou, L., Gou, Y., 2018. Numerical study of the hydraulic fracturing and energy production of a geothermal well in Northern Germany. Geomechanics and Geodynamics of Rock Masses: Selected Papers from the 2018 European Rock Mechanics Symposium. CRC Press.

Li, S., Zhang, D., 2019. How effective is carbon dioxide as an alternative fracturing fluid? SPE Journal 24, 857–876. https://doi.org/10.2118/194198-PA

Liang, F., Sayed, M., Al-Muntasheri, G.A., Chang, F.F., Li, L., 2016. A comprehensive review on proppant technologies. Petroleum 2, 26–39. https://doi.org/10.1016/j.petlm.2015.11.001

Liao, J., 2020. Development of coupled THM models for reservoir stimulation and geo-energy production with supercritical CO2 as working fluid (Dissertation). Clausthal University of Technology. Cuvillier Verlag Göttingen, Germany.

Liao, J., Hou, M.Z., Mehmood, F., Feng, W., 2019. A 3D approach to study the interaction between hydraulic and natural fracture. Environ Earth Sci 78, 681. https://doi.org/10.1007/s12665-019-8699-9

Liu, Y., 2006. Settling and hydrodynamic retardation of proppants in hydraulic fractures (Dissertation). The University of Texas at Austin, USA.

Liu, Y., Leung, J.Y., Chalaturnyk, R., 2018. Geomechanical simulation of partially propped fracture closure and its implication for water flowback and gas production. SPE Reservoir Evaluation & Engineering 21, 273–290. https://doi.org/10.2118/189454-PA

Lu, M., Su, Y., Zhan, S., Almrabat, A., 2020. Modeling for reorientation and potential of enhanced oil recovery in refracturing. Advances in Geo-Energy Research 4, 20–28.

Luo, Z., Zhang, N., Zhao, L., Liu, F., Liu, P., Li, N., 2020. Modeling of pressure dissolution, proppant embedment, and the impact on long-term conductivity of propped fractures. Journal of Petroleum Science and Engineering 186, 106693. https://doi.org/10.1016/j.petrol.2019.106693

Mac Kinnon, M.A., Brouwer, J., Samuelsen, S., 2018. The role of natural gas and its infrastructure in mitigating greenhouse gas emissions, improving regional air quality, and renewable resource integration. Progress in Energy and Combustion science, 64, 62–92.

Mahadevan, J., Sharma, M.M., Yortsos, Y.C., 2007. Capillary wicking in gas wells. SPE Journal 12, 429–437. https://doi.org/10.2118/103229-PA

McDaniel, G.A., Abbott, J., Mueller, F.A., Anwar, A.M., Pavlova, S., Nevvonen, O., Parias, T., Alary, J., 2010. Changing the shape of fracturing: new proppant improves fracture conductivity. Presented at the SPE Annual Technical Conference and Exhibition, Society of Petroleum Engineers. https://doi.org/10.2118/135360-MS

Mehmood, F., Hou, M.Z., Liao, J., 2020. Alternative frac-fluids: A step towards efficient and environment friendly fracking. Oil Gas European Magazine 46, 33–40.

Mehmood, F., Hou, M.Z., Liao, J., Haris, M., Cao, C. Luo, J., 2021. Multiphase multicomponent numerical modeling for hydraulic fracturing with n-heptane for efficient stimulation in a tight gas reservoir of Germany. Energies, 14(11), 3111.

Mena-Carrasco, M., Oliva, E., Saide, P., Spak, S.N., de la Maza, C., Osses, M., Tolvett, S., Campbell, J.E., Molina, L.T., 2012. Estimating the health benefits from natural gas use in transport and heating in Santiago, Chile. Science of the Total Environment, 429, 257–265.

Middleton, R.S., Carey, J.W., Currier, R.P., Hyman, J.D., Kang, Q., Karra, S., Jiménez-Martínez, J., Porter, M.L., Viswanathan, H.S., 2015. Shale gas and non-aqueous fracturing fluids: Opportunities and challenges for supercritical CO2. Applied Energy 147, 500–509. https://doi.org/10.1016/j.apenergy.2015.03.023

Montgomery, C.T., Smith, M.B., 2010. Hydraulic fracturing: history of an enduring technology. Journal of Petroleum Technology 62, 26–40. https://doi.org/10.2118/1210-0026-JPT

Morgan, S.P., Li, B.Q., Einstein, H.H., 2017. Effect of injection rate on hydraulic fracturing of Opalinus clay shale. Presented at the 51st U.S. Rock Mechanics/Geomechanics Symposium, American Rock Mechanics Association.

Mualem, Y., 1976. A new model for predicting the hydraulic conductivity of unsaturated porous media. Water Resources Research 12, 513–522. https://doi.org/10.1029/WR012i003p00513

Myers, R., Potratz, J., Moody, M., 2004. Field Application of new lightweight proppant in appalachian tight gas sandstones. Presented at the SPE Eastern Regional Meeting, Society of Petroleum Engineers. https://doi.org/10.2118/91469-MS

Olsson, O., Weichgrebe, D., Rosenwinkel, K.H., 2013. Hydraulic fracturing wastewater in Germany: composition, treatment, concerns. Environmental earth sciences, 70(8), 3895–3906.

Ortiz, J., McLane, J.E., 1986. Low-pH methanol: an alternative for stimulation in water-sensitive, tight, dirty sandstones. SPE Production Engineering 1, 195–202. https://doi.org/10.2118/12502-PA

Osiptsov, A.A., 2017. Hydraulic fracture conductivity: effects of rod-shaped proppant from lattice-Boltzmann simulations and lab tests. Advances in Water Resources 104, 293–303. https://doi.org/10.1016/j.advwatres.2017.04.003

Pang, W., Du, J., Zhang, T., Ehlig-Economides, C.A., 2016. Actual and optimal hydraulic-fracture design in a tight gas reservoir. SPE Production & Operations 31, 60–68. https://doi.org/10.2118/168613-PA

Parker, J.C., Lenhard, R.J., Kuppusamy, T., 1987. A parametric model for constitutive properties governing multiphase flow in porous media. Water Resources Research 23, 618–624. https://doi.org/10.1029/WR023i004p00618

Parker, M.A., Ramurthy, K., Sanchez, P.W., 2012. New proppant for hydraulic fracturing improves well performance and decreases environmental impact of hydraulic fracturing operations. Presented at the SPE Eastern Regional Meeting, Society of Petroleum Engineers. https://doi.org/10.2118/161344-MS

Petex. PVTp; IPM Suite of petroleum Engineering Software. Petroleum Experts, Petex House, 10 Logie Mill, Edinburgh EH7 4HG, United Kingdom.

Poling, B.E., Prausnitz, J.M., O'Connell, J.P., 2001. The properties of gases and liquids, 5th ed. McGraw-Hill, New York.

Prats, M., 1961. Effect of vertical fractures on reservoir behavior-incompressible fluid case. Society of Petroleum Engineers Journal 1, 105–118. https://doi.org/10.2118/1575-G

Prud'homme, A., 2013. Hydrofracking: What Everyone Needs to Know. Oxford University Press, Incorporated, Cary, United States.

Pruess, K., Battistelli, A., 2002. TMVOC, A numerical simulator for three-phase non-isothermal flows of multicomponent hydrocarbon mixtures in saturated-unsaturated heterogeneous media. Lawrence Berkeley National Laboratory, Berkeley, CA 94720, U.S.A., 204.

Pruess, K., Oldenburg, C., Moridis, G., 1999. TOUGH2 user's guide, version 2. Lawrence Berkeley National Laboratory, Earth Sciences Division, University of California, LBNL-43134, 210.

Radwan, A., Sen, S., 2020. Stress path analysis for characterization of in situ stress state and effect of reservoir depletion on present-day stress magnitudes: reservoir geomechanical modeling in the Gulf of Suez Rift Basin, Egypt. Nat Resour Res. https://doi.org/10.1007/s11053-020-09731-2

Rahm, D., 2011. Regulating hydraulic fracturing in shale gas plays: The case of Texas. Energy Policy 39, 2974–2981. https://doi.org/10.1016/j.enpol.2011.03.009

Reid, R.C., Prausnitz, J.M., Poling, B.E., 1987. The properties of gases and liquids.

Rickards, A.R., Brannon, H.D., Wood, W.D., 2006. High strength, ultralightweight proppant lends new dimensions to hydraulic fracturing applications. SPE Production & Operations 21, 212–221. https://doi.org/10.2118/84308-PA

Rogelj, J., Den Elzen, M., Höhne, N., Fransen, T., Fekete, H., Winkler, H., Schaeffer, R., Sha, F., Riahi, K. and Meinshausen, M., 2016. Paris Agreement climate proposals need a boost to keep warming well below 2 C. Nature, 534(7609), 631–639.

Rojo, F., 2009. Degradation of alkanes by bacteria. Environmental microbiology, 11(10), 2477–2490.

Roussel, N.P., Sharma, M.M., 2012. Role of stress reorientation in the success of refracture treatments in tight gas sands. SPE Production & Operations 27, 346–355. https://doi.org/10.2118/134491-PA

Rubinstein, J.L., Mahani, A.B., 2015. Myths and facts on wastewater injection, hydraulic fracturing, enhanced oil recovery, and induced seismicity. Seismological Research Letters 86, 1060–1067. https://doi.org/10.1785/0220150067

Ruidiaz, E.M., Winter, A. and Trevisan, O.V., 2018. Oil recovery and wettability alteration in carbonates due to carbonate water injection. Journal of petroleum exploration and production technology, 8(1), 249–258.

Rutqvist, J., 2011. Status of the TOUGH-FLAC simulator and recent applications related to coupled fluid flow and crustal deformations. Computers & Geosciences, 2009 Transport of Unsaturated Groundwater and Heat Symposium 37, 739–750. https://doi.org/10.1016/j.cageo.2010.08.006

Rutqvist, J., Rinaldi, A.P., Cappa, F., Moridis, G.J., 2013. Modeling of fault reactivation and induced seismicity during hydraulic fracturing of shale-gas reservoirs. Journal of Petroleum Science and Engineering 107, 31–44. https://doi.org/10.1016/j.petrol.2013.04.023

Rutqvist, J., Wu, Y.-S., Tsang, C.-F., Bodvarsson, G., 2002. A modeling approach for analysis of coupled multiphase fluid flow, heat transfer, and deformation in fractured porous rock. International Journal of Rock Mechanics and Mining Sciences, Numerical Methods in Rock Mechanics 39, 429–442. https://doi.org/10.1016/S1365-1609(02)00022-9

Sanaei, A., Shakiba, M., Varavei, A., Sepehrnoori, K., 2018. Mechanistic modeling of clay swelling in hydraulic-fractures network. SPE Reservoir Evaluation & Engineering 21, 96–108. https://doi.org/10.2118/180372-PA

Schlumberger, 2013. RodPROP: High-aspect ratio proppant. www.slb.com/stimulation.

Schwartz, M.O., 2017. Modelling the performance of liquefied petroleum gas fracking versus water fracking. International Journal of Petroleum Engineering, 2(3), 163 – 181.

Séjourné, S., 2017. Caprock integrity of the Carboniferous Frederick Brook Shale analyzed by oil and gas well logs: McCully gas field and Elgin area, New Brunswick (No. 8203). https://doi.org/10.4095/299664

Shimizu, H., Murata, S., Ishida, T., 2011. The distinct element analysis for hydraulic fracturing in hard rock considering fluid viscosity and particle size distribution. International Journal of Rock Mechanics and Mining Sciences 48, 712–727. https://doi.org/10.1016/j.ijrmms.2011.04.013

Smith, K.W., Persinski, L.J., 1997. Preparation of hydrocarbon gels from ferric sources, polycarboxylic acid compounds, and optional amines, in combination with phosphate esters. US5647900A.

Soetikno, L., Artola, P.D., Guimaraes, C., 2014. Novel rod-shaped proppant fracturing boosts production and adds recoverable reserves in Indonesia during hydraulic fracturing field revival campaign. Presented at the International Petroleum Technology Conference. https://doi.org/10.2523/IPTC-18086-MS

Stone, H.L., 1970. Probability model for estimating three-phase relative permeability. Journal of Petroleum Technology 22, 214–218. https://doi.org/10.2118/2116-PA

Struchtemeyer, C.G., Elshahed, M.S., 2012. Bacterial communities associated with hydraulic fracturing fluids in thermogenic natural gas wells in North Central Texas, USA. FEMS microbiology ecology, 81(1), 13–25.

Tischner, T., Krug, S., Pechan, E., Hesshaus, A., Jatho, R., Bischoff, M., Wonik, T., 2013. Massive hydraulic fracturing in low permeable sedimentary rock in the GeneSys Project. In Proceedings, Thirty-Eights Workshop on Geothermal Reservoir Engineering, SGP-TR-198, Stanford University, Stanford, California, 11.

Torres, M.D., Hallmark, B., Wilson, D.I., 2014. Effect of concentration on shear and extensional rheology of guar gum solutions. Food Hydrocolloids 40, 85–95. https://doi.org/10.1016/j.foodhyd.2014.02.011

Tudor, E.H., Nevison, G.W., Allen, S., Pike, B., 2009. 100% Gelled LPG fracturing process: an alternative to conventional water-based fracturing techniques. Presented at the SPE Eastern Regional Meeting, Society of Petroleum Engineers. https://doi.org/10.2118/124495-MS

US EIA, 2019. International Energy Outlook 2019 with projections to 2050. U.S. Energy Information Administration, Office of Energy Analysis, U.S. Department of Energy, Washington, DC 20585, 85.

US EIA. How much carbon dioxide is produced when different fuels are burned? Independent Statistics & Analysis, U.S. Energy Information Administration. https://www.eia.gov/tools/faqs/faq.php?id=73&t=11 (accessed 02 July 2021).

US EPA, 2004. Evaluation of Impacts to Underground Sources of Drinking Water by Hydraulic Fracturing of Coalbed Methane Reservoirs. Office of water.

US EPA, 2009. Provisional Peer-Reviewed Toxicity Values for White Mineral Oil (CASRN 8012-95-1 and 8020-83-5), 34.

US EPA, 2015. Analysis of hydraulic fracturing fluid data from the FracFocus Chemical Disclosure Registry 1.

US EPA, 2016. Hydraulic fracturing for oil and gas: impacts from the hydraulic fracturing water cycle on drinking water resources in the United States (Final Report). National Center for Environmental Assessment, US Environmental Protection Agency, EPA/600/R-16/236F.

US EPA. White mineral oil (petroleum). Substance Registry Services (SRS), URL https://sor.epa.gov/sor_internet/registry/substreg/searchandretrieve/advancedsearch/externalSearch.do?p_type=CASNO&p_value=8042-47-5 (accessed 2.11.21).

Vengosh, A., Jackson, R.B., Warner, N., Darrah, T.H., Kondash, A., 2014. A critical review of the risks to water resources from unconventional shale gas development and hydraulic fracturing in the United States. Environ. Sci. Technol. 48, 8334–8348. https://doi.org/10.1021/es405118y

Wang, J., Bentley, Y., 2020. Modelling world natural gas production. Energy Reports 6, 1363–1372. https://doi.org/10.1016/j.egyr.2020.05.018

Wang, W., Shao, Z., 2013. Enzymes and genes involved in aerobic alkane degradation. Front Microbiol 4: 116.

Wilson, A., 2015. Unconventional proppant combined with channel fracturing increases effectiveness. Journal of Petroleum Technology 67, 89–93. https://doi.org/10.2118/0315-0089-JPT

Xu, J., Ding, Y., Yang, L., Liu, Z., Gao, R., Yang, H., Wang, Z., 2019. Effect of proppant deformation and embedment on fracture conductivity after fracturing fluid loss. Journal of Natural Gas Science and Engineering 71, 102986. https://doi.org/10.1016/j.jngse.2019.102986

Yakimov, M.M., Timmis, K.N. and Golyshin, P.N., 2007. Obligate oil-degrading marine bacteria. Current opinion in biotechnology, 18(3), 257–266.

Yang, J., Dong, Z., Dong, M., Yang, Z., Lin, M., Zhang, J., Chen, C., 2016. Wettability alteration during low-salinity waterflooding and the relevance of divalent ions in this process. Energy & Fuels, 30(1), 72–79.

Zhang, D., Yang, T., 2015. Environmental impacts of hydraulic fracturing in shale gas development in the United States. Petroleum Exploration and Development 42, 876–883. https://doi.org/10.1016/S1876-3804(15)30085-9

Zhang, G.Q., Chen, M., 2010. Dynamic fracture propagation in hydraulic re-fracturing. Journal of Petroleum Science and Engineering 70, 266–272. https://doi.org/10.1016/j.petrol.2009.11.019

Zhang, J., Zhu, D., Hill, A.D., 2016. Water-induced damage to propped-fracture conductivity in shale formations. SPE Production & Operations 31, 147–156. https://doi.org/10.2118/173346-PA

Zhang, L.-M., Kong, T., Hui, P.S., 2007. Semi-dilute solutions of hydroxypropyl guar gum: Viscosity behaviour and thixotropic properties. Journal of the Science of Food and Agriculture 87, 684–688. https://doi.org/10.1002/jsfa.2769

Zhang, X., Myhrvold, N.P., Hausfather, Z., Caldeira, K., 2016. Climate benefits of natural gas as a bridge fuel and potential delay of near-zero energy systems. Applied Energy, 167, 317–322.

Zhou, L., 2014. New numerical approaches to model hydraulic fracturing in tight reservoirs with consideration of hydro-mechanical coupling effects (Dissertation). Clausthal University of Technology. Cuvillier Verlag Göttingen, Germany.

Zhou, L., Gou, Y., Hou, Z., Were, P., 2015. Numerical modeling and investigation of fracture propagation with arbitrary orientation through fluid injection in tight gas reservoirs with combined XFEM and FVM. Environ Earth Sci 73, 5801–5813. https://doi.org/10.1007/s12665-015-4051-1

Zhou, L., Hou, M.Z., 2013. A new numerical 3D-model for simulation of hydraulic fracturing in consideration of hydro-mechanical coupling effects. International Journal of Rock Mechanics and Mining Sciences 60, 370–380. https://doi.org/10.1016/j.ijrmms.2013.01.006

Zhou, L., Hou, M.Z., Gou, Y., Li, M., 2014. Numerical investigation of a low-efficient hydraulic fracturing operation in a tight gas reservoir in the North German Basin. Journal of Petroleum Science and Engineering 120, 119–129. https://doi.org/10.1016/j.petrol.2014.06.001

Zhou, Q., Dilmore, R., Kleit, A., Wang, J.Y., 2016. Evaluating fracture-fluid flowback in Marcellus using data-mining technologies. SPE Production & Operations 31, 133–146. https://doi.org/10.2118/173364-PA

Zoback, M.D., Rummel, F., Jung, R., Raleigh, C.B., 1977. Laboratory hydraulic fracturing experiments in intact and pre-fractured rock. International Journal of Rock Mechanics and Mining Sciences & Geomechanics Abstracts 14, 49–58. https://doi.org/10.1016/0148-9062(77)90196-6

Zou, C., Yang, Z., Zhang, G., Hou, L., Zhu, R., Tao, S., Yuan, X., Dong, dazhong, Wang, Y., Guo, Q., Wang, L., Bi, H., Li, D., Wu, N., 2014. Conventional and unconventional petroleum “orderly

accumulation": Concept and practical significance. Petroleum Exploration and Development 41, 14–30. https://doi.org/10.1016/S1876-3804(14)60002-1

Zou, C., Zhang, G., Yang, Z., Tao, S., Hou, L., Zhu, R., Yuan, X., Ran, Q., Li, D., Wang, Z., 2013. Concepts, characteristics, potential and technology of unconventional hydrocarbons: On unconventional petroleum geology. Petroleum Exploration and Development 40, 413–428. https://doi.org/10.1016/S1876-3804(13)60053-1

Zou, C., Zhao, Q., Zhang, G., Xiong, B., 2016. Energy revolution: From a fossil energy era to a new energy era. Natural Gas Industry B 3, 1–11. https://doi.org/10.1016/j.ngib.2016.02.001

Zou, C.N., Yang, Z., Tao, S.Z., Yuan, X.J., Zhu, R.K., Hou, L.H., Wu, S.T., Sun, L., Zhang, G.S., Bai, B., Wang, L., Gao, X.H., Pang, Z.L., 2013. Continuous hydrocarbon accumulation over a large area as a distinguishing characteristic of unconventional petroleum: The Ordos Basin, North-Central China. Earth-Science Reviews 126, 358–369. https://doi.org/10.1016/j.earscirev.2013.08.006

Appendix A

Critical properties and viscosity and density trends of different light alkane mixtures with and without propane (LPG) using API correlations (API, 2016).

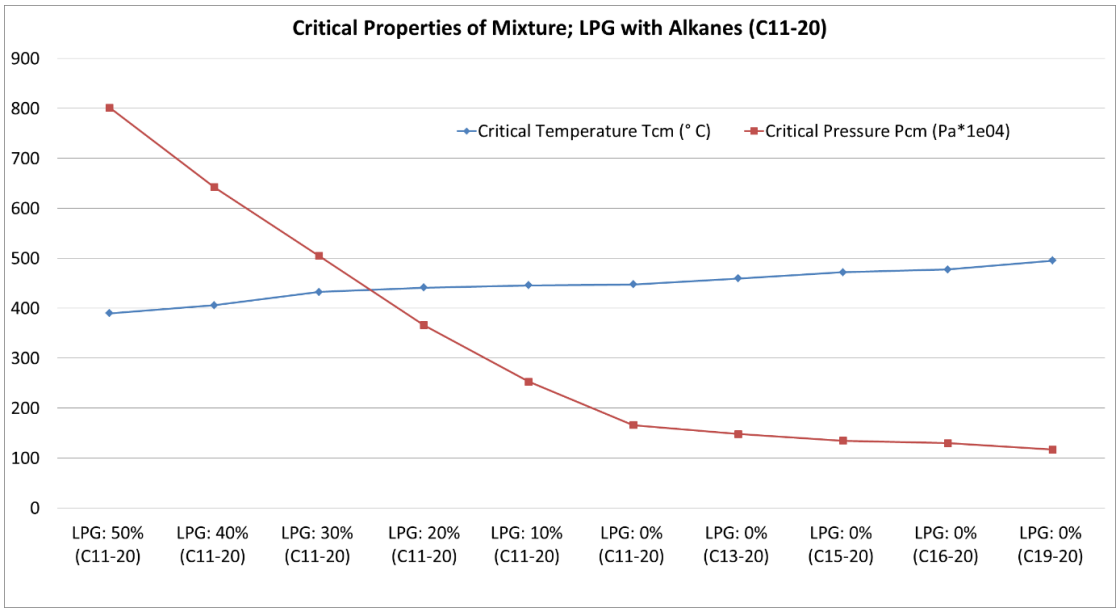

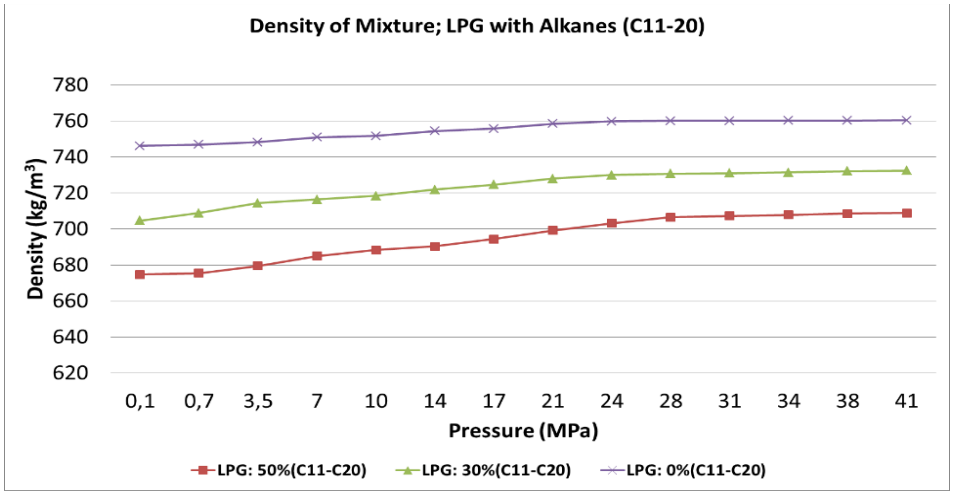

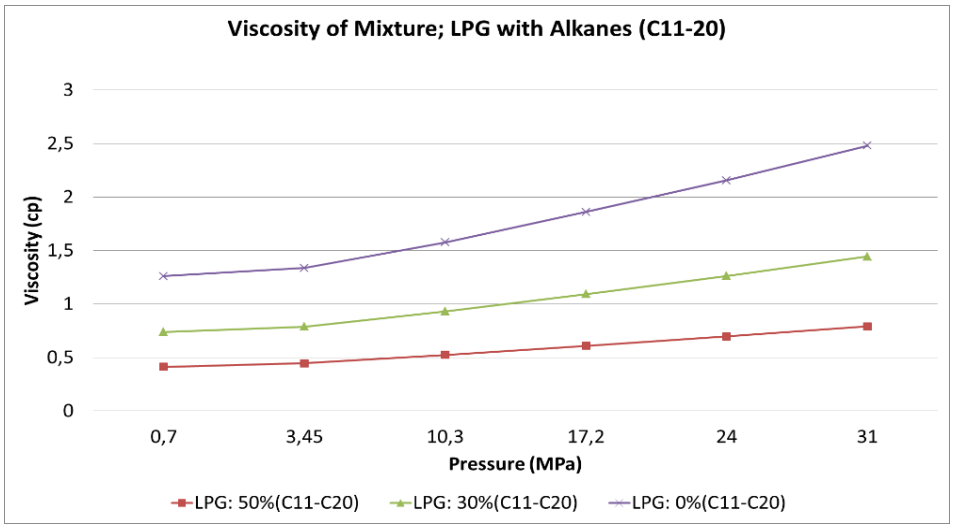

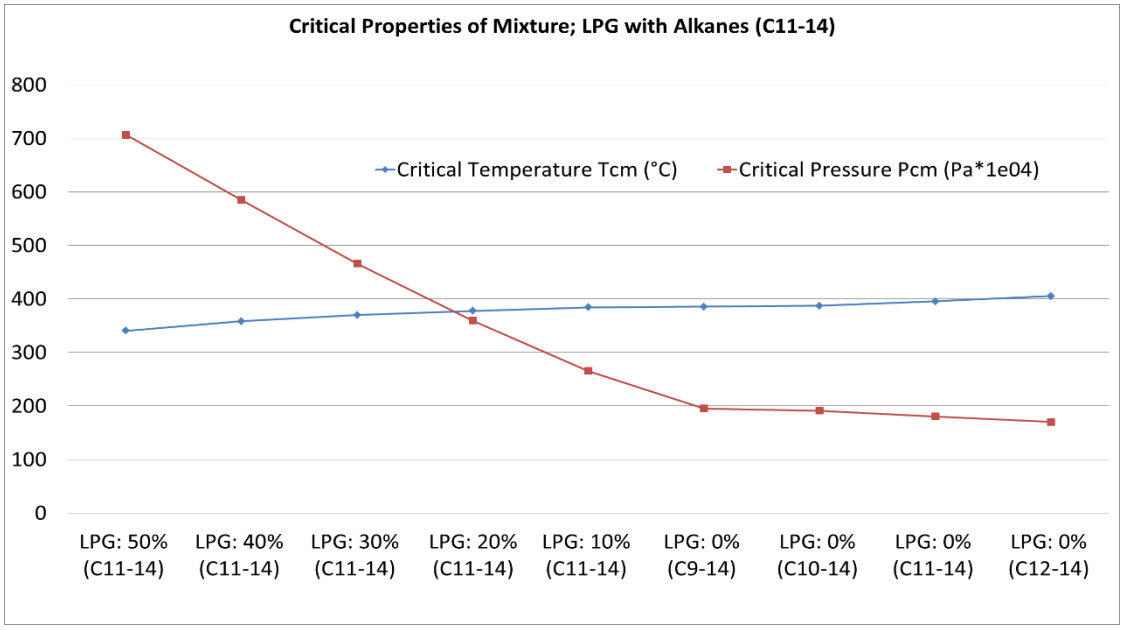
Critical Properties of Mixture; LPG with Alkanes (C11-14)
800
700
600
500
400
300
200
100
0
Critical Temperature Tcm (°C)
Critical Pressure Pcm (Pa*1e04)
LPG: 50% (C11-14)
LPG: 40% (C11-14)
LPG: 30% (C11-14)
LPG: 20% (C11-14)
LPG: 10% (C11-14)
LPG: 0% (C9-14)
LPG: 0% (C10-14)
LPG: 0% (C11-14)
LPG: 0% (C12-14)

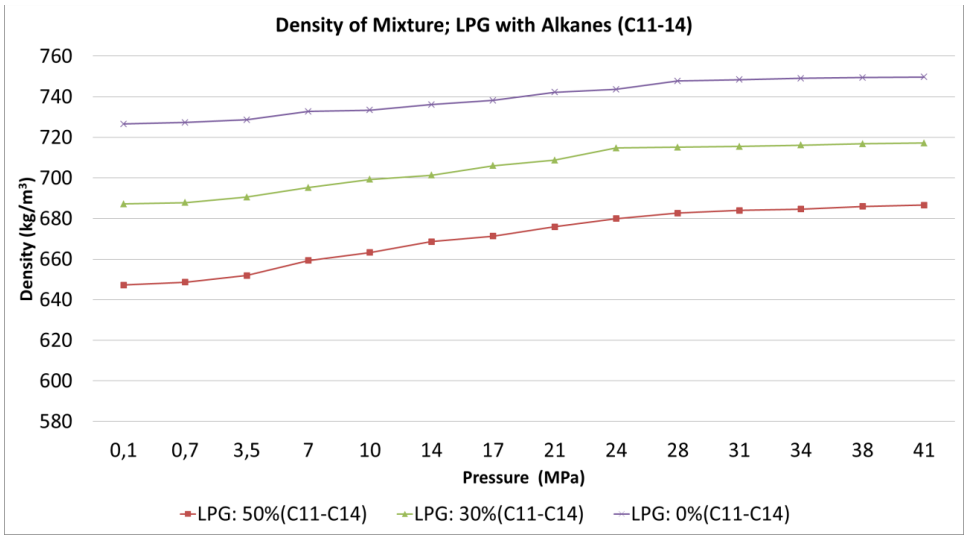
Density of Mixture; LPG with Alkanes (C11-14)
Density (kg/m³)
760
740
720
700
680
660
640
620
600
580
0,1
0,7
3,5
7
10
14
17
21
24
28
31
34
38
41
Pressure (MPa)
LPG: 50%(C11-14)
LPG: 30%(C11-14)
LPG: 0%(C11-14)

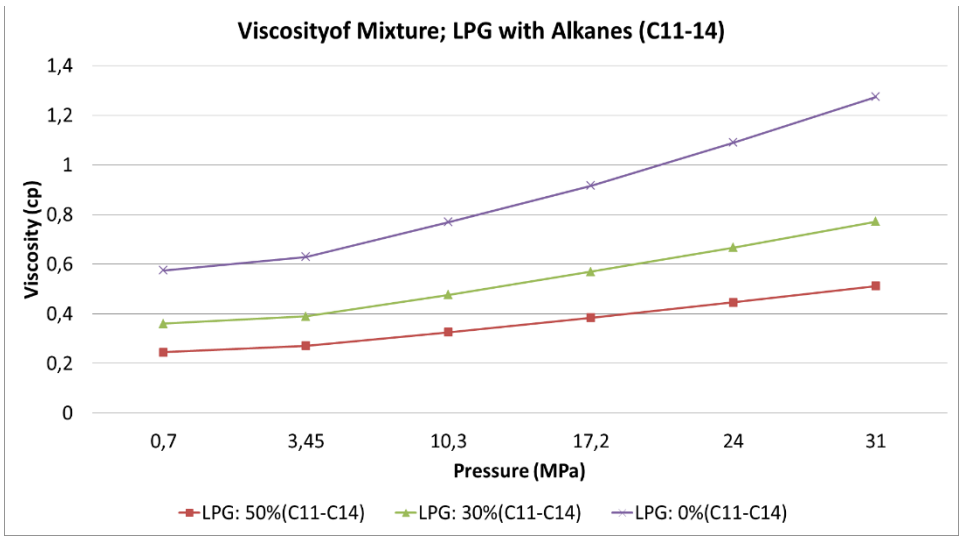
Viscosityof Mixture; LPG with Alkanes (C11-14)
Viscosity (cp)
1,4
1,2
1
0,8
0,6
0,4
0,2
0
0,7
3,45
10,3
17,2
24
31
Pressure (MPa)
LPG: 50%(C11-14)
LPG: 30%(C11-14)
LPG: 0%(C11-14)

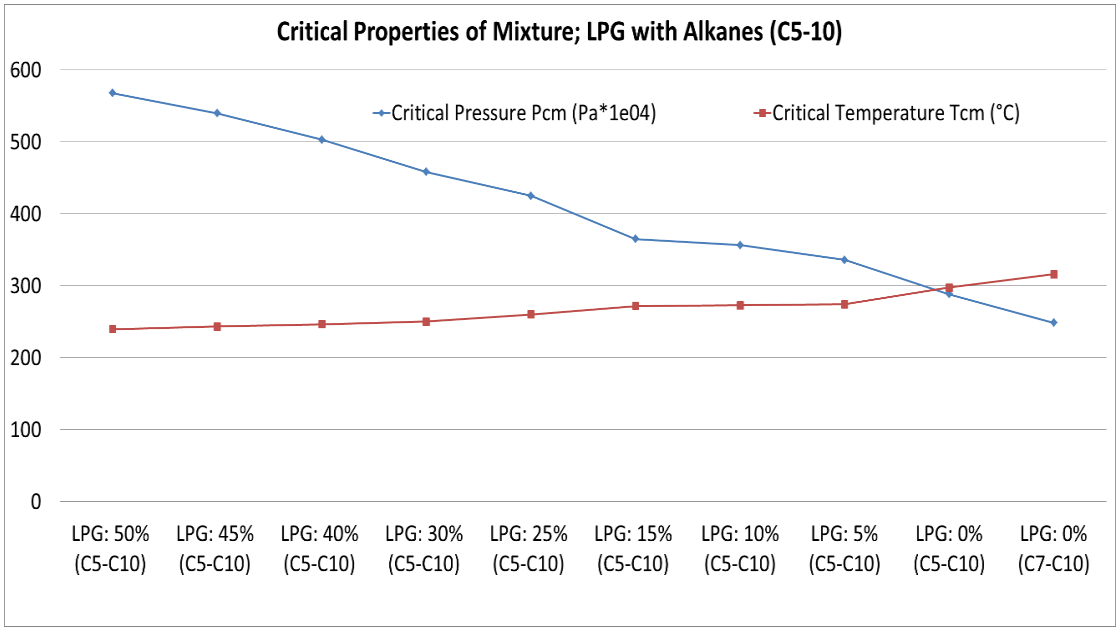
Critical Properties of Mixture; LPG with Alkanes (C5-10)
600
500
400
300
200
100
0
Critical Pressure Pcm (Pa*1e04)
Critical Temperature Tcm (°C)
LPG: 50% (C5-C10)
LPG: 45% (C5-C10)
LPG: 40% (C5-C10)
LPG: 30% (C5-C10)
LPG: 25% (C5-C10)
LPG: 15% (C5-C10)
LPG: 10% (C5-C10)
LPG: 5% (C5-C10)
LPG: 0% (C5-C10)
LPG: 0% (C7-C10)

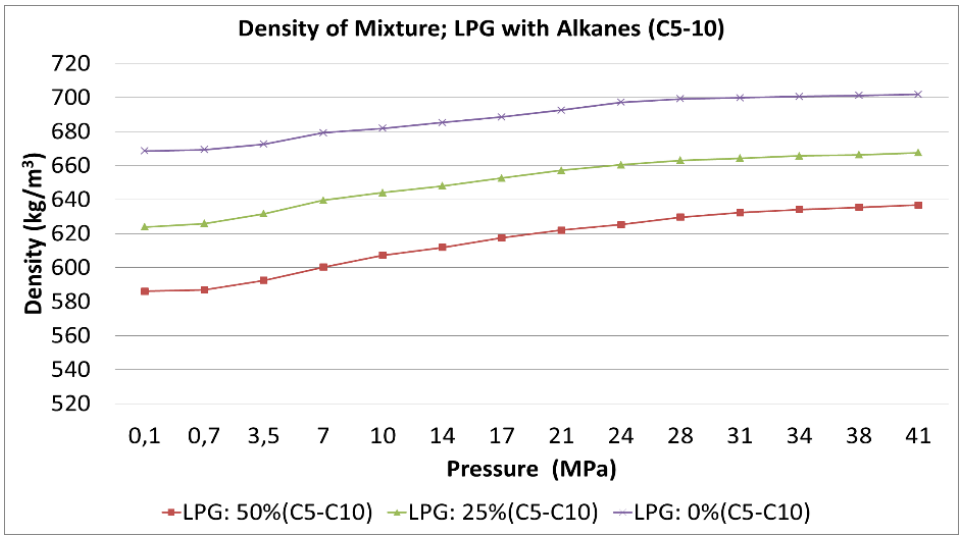
Density of Mixture; LPG with Alkanes (C5-10)
Density (kg/m³)
720
700
680
660
640
620
600
580
560
540
520
0,1 0,7 3,5 7 10 14 17 21 24 28 31 34 38 41
Pressure (MPa)
LPG: 50%(C5-C10)
LPG: 25%(C5-C10)
LPG: 0%(C5-C10)

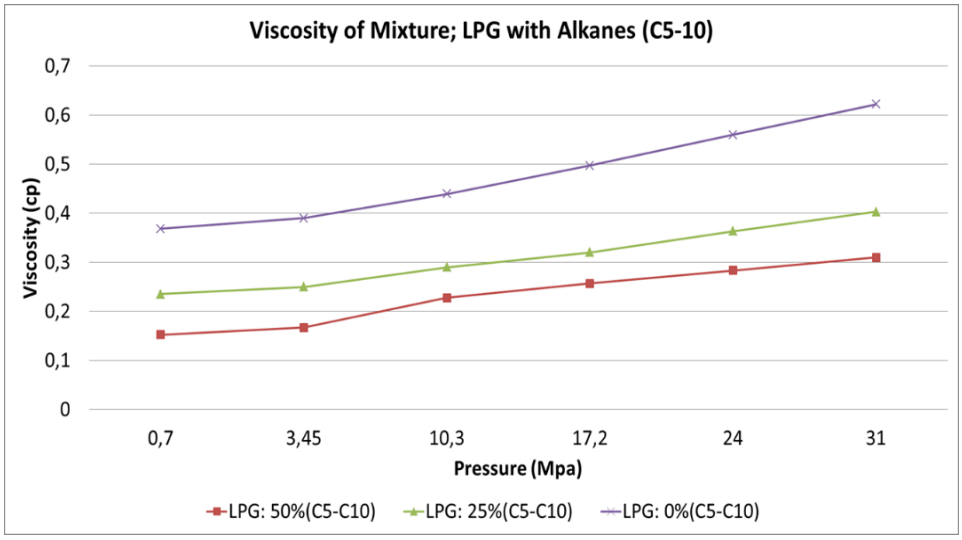
Viscosity of Mixture; LPG with Alkanes (C5-10)
Viscosity (cp)
0,7
0,6
0,5
0,4
0,3
0,2
0,1
0
0,7 3,45 10,3 17,2 24 31
Pressure (Mpa)
LPG: 50%(C5-C10)
LPG: 25%(C5-C10)
LPG: 0%(C5-C10)